Kelemen, P.B., Kikawa, E., Miller, D.J., et al., 2004
Proceedings of the Ocean Drilling Program, Initial Reports Volume 209

3. Site 1268[1]

Shipboard Scientific Party[2]

OPERATIONS SUMMARY

Port Call: Rio de Janeiro

Leg 209 began at 0956 hr on 6 May 2003 as the first line ashore at Berth 3, Porto Praça Maua, Rio de Janeiro, Brazil, ended Leg 208. Pacing items for the port call included resupply of fuel and drill mud bulk, loading casing scheduled for deployment during Leg 210, and installation of a remote diagnostic system for the active heave compensation (AHC) system. A complete overhaul and test of the drawworks transmission was also completed during the port call.

Two power outages, traced to a faulty transformer, occurred on the *JOIDES Resolution* early on the morning of 10 May. Repairing the transformer ultimately became the primary port call pacing item and resulted in a 1-day delay in our scheduled departure. After rotating the ship 180° to load a new spool of drilling cable on the starboard side, mooring lines were released and the last line was brought aboard at 0912 hr on 12 May. The pilot departed at 0954 hr and the vessel got under way at full speed for the 2627-nmi transit to our first site.

Transit to Site 1268

Transit speed over our first 4 days at sea averaged 11.3 nmi/hr. During the transit, an air sampling system for airborne microbial study was modified and mounted at the water table level of the derrick.

At 0925 hr on 15 May, the ship's master was informed that the Overseas Drilling Ltd. Electrical Supervisor required medical evacuation. At 0946 hr we changed course to 328° and steamed toward the port of Aracaju, Brazil, 109 nmi away. At 1654 hr we arrived at our rendezvous location (11°18′S latitude, 36°45′W longitude) and proceeded at reduced speed until arrival of a medivac helicopter. Brazilian police helicopter

---

[1] Examples of how to reference the whole or part of this volume.
[2] Shipboard Scientific Party addresses.

PT-HVA was on board by 1726 hr and departed at 1731 hr. We immediately resumed full speed, changed course to 055°, and proceeded up the eastern coast of Brazil. Overall impact to the leg for the medivac operation was an additional ~60 nmi steaming, or ~5 hr.

During the next 6 days of our transit we averaged 11.7 nmi/hr, until a wind heading change and the Equatorial Countercurrent slowed our speed. We arrived on Site 1268 at 0500 hr the morning of 22 May. Our transit totaled 2680 nmi at an average speed of 11.4 nmi/hr.

Site 1268

The planned location of Site 1268 was revised during transit from Rio de Janeiro after detailed review of the video tapes from the 1998 *Shinkai* 6500 Dive 427 (Fig. F1). Site 1268 was to be drilled in thin sediments at ~3011 meters below sea level (mbsl), overlying a flat, planar outcrop of serpentinized peridotite (probably a fault surface) visible a few meters downslope. Upon arrival at the planned location, the precision depth recorder (PDR) in the underway geophysics laboratory indicated a depth of ~2896 meters below rig floor (mbrf) (2885 mbsl), quite different from the expected depth. Given that submersible dive navigation can be uncertain, we undertook a PDR survey of the seafloor to the southeast (downslope). While making up the drilling assembly, the rig crew discovered a significant crack in the stress relief groove of the pin thread at the first 8¼-in drill collar. This collar was laid aside and we decided to magnaflux inspect the remaining eight drill collars in the bottom-hole assembly. No other cracks were found during the inspection.

F1. Track of *Shinkai* Dive 427 and bathymetry for Site 1268, p. 53.

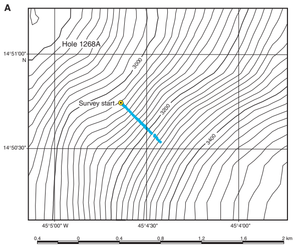

While running the drill pipe, we chose a position ~600 m southeast of the originally planned location, with a PDR depth of ~3040 mbsl, to start a camera survey (Fig. F1). However, when the camera depth was at ~3080 m, the sonar on the camera sled still could not detect bottom within 100 m. At this point, the ship began moving slowly northwest toward the originally planned site location. Bottom was first detected at ~3180 mbsl at a position ~500 m southeast of the originally planned location. Bathymetry determined during the camera survey conformed closely to bathymetry based on *Shinkai* 6500 Dive 427 at the same latitude and longitude, so we decided that the PDR depths were probably incorrect. At this point, the drill string and camera sled were raised to a bit depth of ~3008 m, and the originally planned location for Site 1268 was slowly approached. Again, bathymetry determined from the camera survey at the originally planned location conformed closely to that observed during *Shinkai* 6500 Dive 427 (Fig. F2), confirming the theory that dive navigation in this case was accurate and PDR depths were incorrect. The close equivalence between camera survey and dive bathymetry indicated that we were very near the originally planned location. Push tests indicated that sediment thickness was ~4 m, slightly thicker than anticipated but within acceptable limits. The positioning beacon was released from the vibration-isolated television (VIT) frame ~20 m away from the identified spud location prior to recovering the VIT frame.

F2. Comparison of depth data, p. 56.

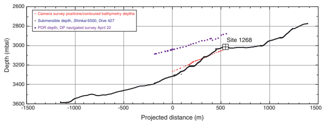

Hole 1268A

Before initiating coring we deployed the Water Sampling Temperature Probe (WSTP) to obtain a temperature and a seawater sample for a microbiology contamination baseline analysis. Hole 1268A was spudded at 0620 hr on 23 May. After cutting Core 1R, AHC was discontinued due to erratic performance. AHC performance data and coring parameters were recorded in the newly installed Maritime Hydraulics diagnostic computer and the Texas A&M University TruVu rig instrumentation system. TruVu was running in the 1-s capture mode. Marine Hydraulics–Norway remotely accessed their diagnostic computer and downloaded the data for analysis. Initial reports indicated a possible problem with the AHC motion reference unit.

Core 1R advanced to 14.0 meters below seafloor (mbsf) (Table T1), allowing the bit to stay in the hole during the next connection. A standard rotary core barrel was used without a core liner. All subsequent cores were taken using nonmagnetic chrome-plated inner diameter core barrels. In order to improve recovery, we opted to retrieve cores nominally every 5 m (half-cores).

T1. Site 1268 coring summary, p. 155.

Sepiolite mud sweeps (10 bbl) were circulated every 10 m, and the hole remained stable through Core 28R (145.1 mbsf) (Table T1) with no fill or overpull during connections. After making a connection before cutting Core 29R, the driller noted elevated torque and ~1.0 m of fill in the bottom of the hole. All drilling parameters returned to normal after pumping a pair of 20-bbl sepiolite mud sweeps. While cutting Core 29R, drilling parameters indicated the hole had collapsed, stalling the top drive and preventing any further rotation or axial movement of the drill string. After an unsuccessful attempt to free the pipe, we decided to sever the drill string above the bottom-hole assembly. The mate to the severed pipe joint cleared the rig floor at 1930 hr, ending Hole 1268A and drilling operations at Site 1268. The average penetration rate for the hole was 3.9 m/hr.

IGNEOUS AND MANTLE PETROLOGY

Large exposures of residual mantle harzburgite at active mid-ocean ridges are generally interpreted to be the uppermost portion of the lithospheric mantle, whereas gabbroic rocks emplaced into the harzburgite likely crystallized from magmas that intruded this mantle section. Each set of rocks potentially records a complicated history that includes high-temperature processes and lower-temperature alteration and/or deformation. (Here we restrict our attention to high-temperature processes. Although most of the ultramafic rocks have been converted to serpentine and/or talc, in this section we refer to them simply by their protolith name.)

The rocks recovered from Hole 1268A fall into two distinct categories, ultramafic rocks and gabbroic rocks. Most of the ultramafic rocks are harzburgites with large modal variations of orthopyroxene that may reflect variable amounts of partial melting, variable source compositions, and/or variable amounts of melt/rock interaction such as dissolution or precipitation. Dunites are the second most abundant lithology and may reflect reaction of harzburgite with basaltic liquids that passed through them. Very minor amounts of pyroxene-rich ultramafic rocks (orthopyroxenites and harzburgite that contain coarse orthopyroxene layers) were also recovered. Variations in the textures and mineralogies of the gabbroic rocks may provide insight into melting/crystallization processes in the underlying mantle and crystallization conditions in the recovered mantle section.

In describing and interpreting these rocks we first document the stratigraphic distribution of lithologies and divide the core into major lithologic units. Next, the rock textures and mineralogy are characterized.

Finally, we use these observations to discuss the high-temperature history of the rocks recovered from Hole 1268A.

Lithology and Stratigraphy

Hole 1268A consists of 29 cores recovered from 147.6 m of penetration below the seafloor. The distribution of rock types defines four major lithologic units. From the top of the core down, these are Unit I: harzburgite/dunite, Unit II: intrusion breccia, Unit III: harzburgite/dunite, and Unit IV: gabbronorite/harzburgite (Fig. F3).

F3. Lithology and stratigraphy, Hole 1268A, p. 57.

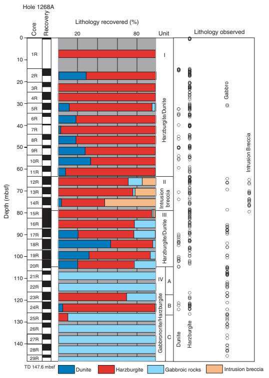

Unit I

Interval: Sections 209-1268A-1R-1 through 12R-1
Depth: 0–63.2 mbsf
Lithology: harzburgite/dunite

Unit I is composed almost exclusively of harzburgite (86%) and dunite (13.5%) with minor gabbro (0.5%). Clasts of various lithologies including aphyric basalt were sampled in the first core (Section 209-1268A-1R-1), but these probably correspond to a mixed rubble horizon and are not part of the stratigraphic sequence. Unit I is cut by a few small gabbroic intrusions (typically ~1 cm thick). Small intervals of less altered harzburgite with a small amount of clinopyroxene (classified as clinopyroxene-bearing harzburgite) were found in Sections 209-1268A-3R-1 and 3R-2 between 22.5 and 23.5 mbsf. Unit I shows an overall increase in the amount of dunite recovered with increasing depth.

Unit II

Interval: base of Section 209-1268A-12R-1 through base of 15R-1
Depth: 63.2–79.2 mbsf
Lithology: intrusion breccia

Unit II is characterized by an anastomosing network of gabbroic material that locally forms intrusion breccias within the harzburgite and dunite host rock. Unit II is bounded above and below by shear zones that contain a mixture of gabbroic and ultramafic material with fault breccias below the shear zones (Fig. F4). The intrusion breccias are distinguished from the fault breccias based on the presence of gabbroic material between the clasts (or inferred presence of gabbroic material based on mineral pseudomorphs in the case of severely altered examples). Harzburgite (65.5%) is the dominant lithology recovered in this section with intrusion breccia (27.5%), gabbro (5.5%), and dunite (1.5%) present in decreasing abundance. The percentage of intrusion breccia is somewhat arbitrary, as it is a function of the clast size defined by the network of injected material. Where the injections crosscut the core the observed clast sizes are smaller and the rocks are readily classed as an intrusion breccia. Where they are subparallel to the drilling direction the brecciated nature of the rock is less apparent.

F4. Upper and lower contacts of Unit II, p. 58.

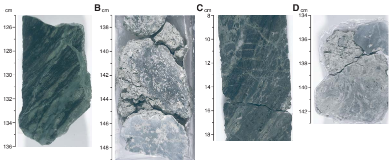

Unit III

Interval: base of Section 209-1268A-15R-1 to 20R-2
Depth: 79.2–104.38 mbsf
Lithology: harzburgite/dunite

Unit III is another interval with abundant harzburgite (68%) and the most dunite (23%) of any unit; the remainder is gabbro (9%). Unit III had the highest recovery of all units, >90% of the cored interval logged. The excellent recovery allowed us to identify gradational changes in the orthopyroxene mode from harzburgites to dunites. The base of Unit III is defined by a contact between dunite and gabbro at Section 209-1268A-20R-2, 135 cm (104.38 mbsf). The gabbro has distinctive elongate pyroxene crystals that appear to have nucleated and grown perpendicular to the margin (Fig. F5). This texture suggests a high temperature for the wallrock upon intrusion of the magma and/or some amount of water dissolved in the magma.

F5. Pyroxene crystals along a contact with dunite, p. 59.

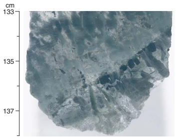

Unit IV

Interval: Sections 209-1268A-20R-2 to 29R-1
Depth: 104.38–147.6 mbsf
Lithology: gabbronorite/harzburgite

Unit IV is composed primarily of gabbronorite and gabbro (75.5%) with an interval of harzburgite (23.5%) and dunite (1%). For the purposes of the discussion below, we have additionally subdivided Unit IV into three subunits.

Subunit IVA

Interval: Sections 209-1268A-20R-2 to 23R-2
Depth: 104.38–118.12 mbsf
Lithology: gabbro and gabbronorite that varies substantially in mode and texture

Subunit IVB

Interval: Sections 209-1268A-23R-2 to 25R-1
Depth: 118.12–126.33 mbsf
Lithology: almost exclusively harzburgite with only a small amount of dunite

Subunit IVC

Interval: Section 209-1268A-25R-1 to total depth
Depth: 126-33–147.6 mbsf
Lithology: gabbronorite

Unit IVC is modally uniform with 60%–70% plagioclase, 20%–30% clinopyroxene, and 10%–15% orthopyroxene in most samples. Despite the uniform mineralogy, there are significant, but gradational, textural variations. Based primarily on the similarities of the mineralogy, we suggest that Subunit IVC could have formed as a single cooling unit but caution that additional work is required to understand the origin of the textural variations that could also indicate multiple intrusive events.

Lithologic Characterization

Harzburgites

Various aspects of the harzburgites are more readily observed depending upon the type and amount of alteration (low-temperature metamorphism and/or serpentinization), but all have fundamentally similar primary textures and mineral assemblages. Based on the nature of the alteration mineral phases and pseudomorphs, the major primary minerals were reconstituted as olivine (60–90 vol%) and orthopyroxene (10–40 vol%). Spinel (1–3 vol%) is mostly fresh and always present. Minor clinopyroxene (1–3 vol%), partially fresh, is observed with certainty in a very few thin sections and is thought to have been present in some other thin sections. Olivine and orthopyroxene are ubiquitously altered to secondary low-temperature minerals. In most samples, however, the grain boundaries between these two minerals are still preserved, providing information on the microstructure and texture and allowing us to roughly estimate their modal amounts. In some examples the alteration preserves small-sized (0.2–0.5 mm) polygonal neoblasts of serpentinized olivine that result from the recrystallization of coarser crystals. The original size of the primary olivine grains cannot be determined with confidence but appears to have been on the order of a centimeter, based on the olivine/orthopyroxene grain boundaries. Orthopyroxene can be as large as 1.5 cm but is generally 0.7–1.2 cm. Primary grains of orthopyroxene are anhedral with ragged boundaries (Fig. **F6**) and amoeboidal extensions between olivine grains (Fig. **F6F**), and ragged, thin grains commonly form interstitial patches in the serpentinized matrix (Fig. **F7**). The general outline of the orthopyroxene crystals is elongate, defining high-temperature lineations and layering. The primary texture can thus be defined as coarse-grained protogranular, although the orthopyroxene has an anhedral interstitial shape, unusual in abyssal peridotites. In many examples, orthopyroxene grains have recrystallized into 1- to 5-mm subgrains (Fig. **F8**), leading to clear porphyroclastic textures. Study of a single relatively fresh sample (65% serpentinization instead of the usual >99%) confirms that the texture is protogranular-porphyroclastic (Fig. **F9**). Where observed, clinopyroxene is present as small (<1 mm) crystals, commonly found at boundaries and junctions of orthopyroxene subgrains or along olivine/orthopyroxene and orthopyroxene/orthopyroxene grain boundaries or as interstitial grains in the serpentinized olivine matrix (Fig. **F10**). Small interstitial or rounded altered pyroxenes could have been former clinopyroxene based on analogy with similar textured clinopyroxene in other harzburgites (Fig. **F11**). In one thin section (Sample 209-1268A-13R-2, 3–6 cm), a cluster of altered pyroxenes could have been former clinopyroxene crystals. The outline of the cluster differs from that of former orthopyroxene porphyroclasts, supporting this interpretation. Spinel grains define two major textural types. One is associated with orthopyroxene and preferentially occurs at its margins, commonly forming wormy intergrowths (Fig. **F12**) that can be up to several millimeters in size (average generally = 0.5 mm) and interstitial to orthopyroxene neoblasts (Fig. **F12**). The second type of spinel grain is smaller (<0.1–0.3 mm), commonly euhedral to subhedral, and oval or rounded, although anhedral to interstitial grains are also present. This type of spinel is disseminated in the serpentinized olivine matrix where it may enclose olivine neoblasts; it is also associated with interstitial clinopyroxenes (Fig. **F10**). Both types are frequently flattened and may be aligned in trains or layers parallel to orthopyroxene-rich bands.

The amount of orthopyroxene varies between 13% and 22% in 64% of the ultramafic samples. About 27% of the ultramafic rocks are poorer in orthopyroxene and are classified as dunites (Fig. **F13**). True dunites with <8%–10% orthopyroxene form 12% of the ultramafic rocks. At the other end of the compositional range, harzburgites with >22% orthopyroxene constitute 9% of the ultramafic rocks, including 3% having 30%–40% orthopyroxene (28 pieces).

F6. Primary orthopyroxene morphologies, p. 60.

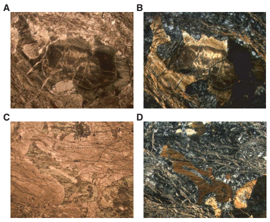

F7. Altered orthopyroxene crystals in serpentinized olivine, p. 62.

F8. Orthopyroxene porphyroclast recrystallized into subgrains, p. 63.

F9. Protogranular to porphyroclastic textures in harzburgite, p. 64.

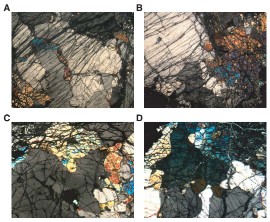

F10. Spinel and clinopyroxene near recrystallized orthopyroxene, p. 65.

Dunite

Two different types of dunite were sampled. The first type cuts the high-temperature fabrics of the harzburgites at a high angle. Traces of spinel and orthopyroxene can be observed as relics in the dunite (e.g., Section 209-1268A-20R-2 [Piece 5]). However, most dunites do not have clear-cut contacts with the harzburgites. They form a second type that occurs as bands or patches poorer in orthopyroxene (e.g., Section 209-1268A-17R-3 [Piece 7, 69 cm]). The orthopyroxene is smaller (maximum = 5 mm) but has the same anhedral to interstitial shape as in the harzburgites. Spinel in dunites also falls into the two textural groups defined above for spinel in harzburgites. However, because of the smaller amount of orthopyroxene, the spinel mainly occurs as small euhedral to subhedral crystals.

Orthopyroxenite and Orthopyroxene-Rich Bands

Interval 209-1268A-18R-4 (Pieces 10 and 11, 83–96 cm) represents a 13-cm fragment of orthopyroxenite (Sample 18R-4, 88–91 cm). The rock is composed of orthopyroxene (86 vol%), olivine (8 vol%), minor clinopyroxene (2 vol%), and spinel (4 vol%) that are only slightly altered (~5% serpentinization). The texture suggests that the rock was a coarse-grained granular orthopyroxenite that underwent high-temperature deformation and recrystallization and partial annealing. Orthopyroxene forms a heterogranular (0.2–12 mm) assemblage of anhedral to polygonal crystals (Fig. **F14**). Olivine, clinopyroxene, and most of the spinel are smaller (0.5–1, 0.05–0.2, and 0.1–5.0 mm, respectively) and are thought to have formed during subsolidus deformation, recrystallization, and equilibration. Primary spinel may have been present, as suggested by the larger crystals and inclusions in orthopyroxene (Fig. **F14**). Contacts with the surrounding harzburgite wallrock were not recovered.

Coarse orthopyroxene forms 0.5- to 1.5-cm-thick bands in several other places in the harzburgite. These bands are boudinaged and composed of >90 vol% orthopyroxene. The orthopyroxene was formerly present as crystals as large as 1.5 cm but recrystallized into 0.5- to 1-mm subgrains. The remaining ~10% of the bands is composed of spinel and olivine. The olivine may, however, belong to the host harzburgite (Samples 209-1268A-12R-2, 93–98 cm, and 18R-1, 61–63 cm). These orthopyroxene-rich bands are parallel to the high-temperature fabric of the harzburgite, and some of the spinel grains are also flattened along this direction. These bands could be orthopyroxene segregations in the harzburgite or may have formed as a consequence of injections of magma intruded into the harzburgite followed by flattening and transposition into the high-temperature foliation. Three observations support their origin as thin injections into the harzburgite:

1. Their locations do not seem to be random. Two bands are present close to gabbroic intrusions (Sections 209-1268A-12R-1 [Pieces 7 and 17]). Three other bands are present in a section rich in gabbroic injections, in the vicinity of the orthopyroxenite body (Sections 209-1268A-17R-2 [Piece 7] and 18R-1 [Piece 1B, 20–41 cm]). Another cluster of three bands is present in Sections 209-1268A-23R-3 (Piece 1A and Piece 2, 43–46 cm) and 24R-2 (Piece 11). These are located between two thick gabbroic sections.

F11. Altered clinopyroxene crystals, p. 66.

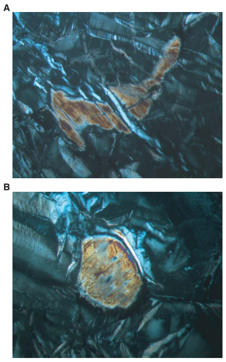

F12. Orthopyroxene/spinel textural relations, p. 67.

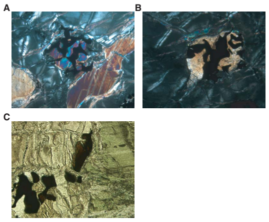

F13. Altered pyroxene in harzburgites and dunites, p. 68.

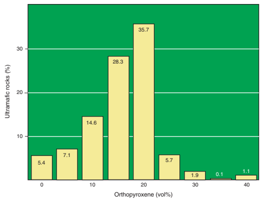

F14. Textures in recrystallized orthopyroxenite, p. 69.

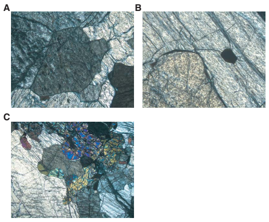

2. The host harzburgite is not enriched in orthopyroxene.
3. Inclusions of euhedral spinel (Sample 209-1268A-18R-1, 61–63 cm) are present in some orthopyroxene grains, and those are not observed in orthopyroxene from harzburgite. On the other hand, the orthopyroxene grains locally display embayments filled with olivine, as in harzburgite.

Gabbro/Gabbronorite

The gabbros and gabbronorites are interpreted to reflect at least four separate intrusive events. There is little evidence for crosscutting relationships between different gabbroic intrusions, which suggests that the gabbroic rocks nearest the seafloor are the oldest or that the intrusions were emplaced by lateral injections relative to the orientation of the drilling. Given the near-vertical orientation of some of the smaller gabbroic bodies, we favor an age/position relation and so discuss the gabbroic rocks from the top of the core downward, possibly corresponding to oldest to youngest.

The first significant occurrence of gabbroic rocks in the core is in Unit II where gabbroic material forms an anastomosing network around pieces of harzburgite, resulting in an intrusion breccia (Fig. **F15**). The injected material is almost completely altered so its original mineralogy and textures are uncertain, but pseudomorphs of plagioclase and clinopyroxene indicate that they were gabbroic. The alteration has obliterated any crosscutting relationships, so we cannot say if the intrusion breccia of Unit II formed in a single event or as a progression of many small injections.

F15. Intrusion breccia typical of Unit II, p. 70.

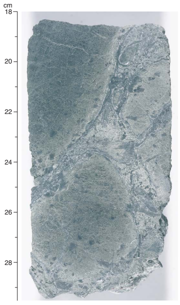

The next significant gabbroic intrusion is found in Unit III, Sections 209-1268A-16R-4 (86.61 mbsf) and 17R-1, with a maximum thickness of only 0.67 m. This gabbro has a variable texture, ranging from pegmatitic to microgabbroic over tens of centimeters. The microgabbroic texture could be related to rapid cooling at the intrusion margins, but the contacts were not recovered. Alternatively, this range of textures could indicate that this gabbro was relatively water rich. Upon emplacement it crystallized large grains, but a sudden rupture of the system decreased the partial pressure of H_2O and fine-grained microgabbros formed, by analogy to pegmatites and aplites in granitic systems thought to form via a "pressure quench" process. In thin section it can be seen that the clinopyroxene in this gabbro is completely altered, whereas ~50% of the original plagioclase remains. This large extent of alteration makes it impossible to determine whether primary amphibole or minor phases were present.

Another pegmatitic textured gabbro marks the upper boundary of Unit IV and extends to 107.16 mbsf (Section 209-1268A-21R-1). Like the gabbro described above, it has large elongate clinopyroxene crystals (Fig. **F16**) along contacts between gabbro and harzburgite, indicating that no quenching or rapid undercooling of the basaltic magma took place. Although it is coarse grained, the gabbro beneath this contact has significant textural and modal variations that may represent more than one injection and crystallization event.

F16. Pegmatitic textured gabbro, p. 71.

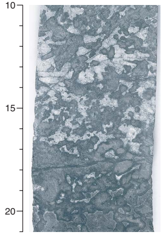

The lowest intrusive gabbroic unit is composed of variably textured gabbronorite that makes up the bulk of Subunit IVA and all of Subunit IVC. The orthopyroxene in these rocks has been completely altered and is identified based on its larger grain size and subophitic texture. In contrast, the clinopyroxene is smaller, subeuhedral, and can be >90% fresh even adjacent to completely altered orthopyroxene grains. The contact between the pegmatitic gabbro described above and the underlying gabbronorite was not recovered. The significant amount of low-temperature alteration and brittle deformation of the uppermost section of the gabbronorite suggests that the two are in fault contact. Below the horizon of alteration and deformation associated with the fault zone, the textures of the gabbronorite vary from coarse grained (orthopyroxene = 15 mm) with a weak primary magmatic foliation to medium grained (orthopyroxene = 6 mm) and massive. The plagioclase in these rocks is 90% fresh and records evidence of modest high-temperature deformation (e.g., bent plagioclase twins, strain twinning, and broken crystals) from which the plagioclase grain boundaries have partly recovered. Little or no evidence of this deformation is recorded by the pyroxenes, suggesting they may have behaved rigidly while the plagioclase accommodated the strain. A high-temperature shear zone was also logged at 136.66 mbsf (Section 209-1268A-27R-1 [Piece 8C]). It shows no alteration but has significant grain-size reduction and more abundant plagioclase than the surrounding gabbronorite.

Discussion

The recovered rocks provide some insight into the high-temperature processes operating at slow-spreading ridges in the uppermost mantle. A key observation is that there is a continuous decrease in the number of samples with a given proportion of modal orthopyroxene from harzburgites to dunitic rocks (Fig. F13). This distribution is not typical in oceanic mantle rocks, in which there is commonly a bimodal distribution of harzburgite with >15% orthopyroxene and dunite with <5% orthopyroxene and a discrete gap in the abundance of rocks with modal percentages of orthopyroxene in between. Samples with less than ~2.5% orthopyroxene are present in much greater abundance than expected based on the decreasing trend in orthopyroxene mode from harzburgites to dunites (Fig. F13). We suggest that two different processes are responsible for generating rocks with less than ~2.5% orthopyroxene. One of these processes corresponds to the first type of dunite described, which crosscuts the harzburgite fabric at a high angle. These dunites are found in relatively small discrete intervals with sharp boundaries. The other dunites are less easily understood and seem to have formed as an end-member in the process that produced the regular decrease in modal orthopyroxene in the harzburgites. In addition to the unusual gradation between the harzburgites and dunites, the textures of the orthopyroxenes are unusual in that they have irregular grain boundaries and locally extend between olivine grains, similar to how the pseudopods of amoebas extend beyond the main mass. The shape of the orthopyroxene suggests progressive dissolution of the orthopyroxene that may explain the continuous variation in observed mode. There is also a large proportion of harzburgite (35.7%) with ~20% orthopyroxene compared to that with ~25% orthopyroxene (~8.8% of harzburgites), suggesting that the orthopyroxene-rich harzburgites are different from the bulk of the harzburgites (Fig. F13). Orthopyroxene-rich harzburgites are spatially associated with some or all of the following: orthopyroxene-rich or orthopyroxenite bands in harzburgite, orthopyroxenites, and gabbroic intrusions (Fig. F17). A potential explanation for the high modal orthopyroxene in these rocks is that they represent tectonically disaggregated orthopyroxene-rich rocks (a kind of mechanical homogenization).

F17. Stratigraphic distribution of modal orthopyroxene, p. 72.

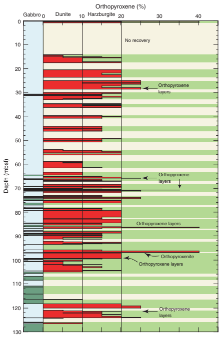

The several different generations of gabbroic rocks attest to a potentially extended history of magmatism in this section of the shallow mantle. The liquid that formed the intrusion breccia of Unit II must have had relatively low viscosity and/or intruded into relatively hot harzburgite to form such a network. The stockwork character of the breccias suggests that this liquid was relatively evolved and water rich, such as might be derived from a fractionating intrusion at depth. The fact that the gabbroic rocks below the intrusion breccia are not cut by similar intrusions likely discounts them as a source of this liquid. The pegmatitic textures of the gabbros in the lower parts of Unit III and in Subunit IVA are also consistent with the idea that hydrous basaltic liquids were present. This hypothesis may ultimately prove difficult to test because the rocks are highly altered (especially in Unit II). The gabbronorites in Subunits IVA and IVC appear very similar, especially with regard to their mineralogy. It may be that they formed during a single intrusive event and that the intervening mantle material in Subunit IVB represents either a xenolith or roof pendant near the top of the gabbronorite. However, the textural variations seen in both Subunits IVA and IVC are significant and could be interpreted to indicate that, although modally similar, this apparently massive gabbronorite is actually a composite intrusion with individual units on the scale of a meter or less, similar to the scale of the gabbros in the lower part of Unit III.

The atypical character of the mantle rocks recovered, both in terms of the progressive decrease in orthopyroxene from harzburgite to dunites and with regard to the textures of the orthopyroxene, may reflect the role of reaction with migrating hydrous melt in this mantle section. The idea that substantial H_2O was available during the high-temperature modification of this mantle sections finds support in the apparent importance of H_2O contents during the crystallization of the gabbroic rocks.

METAMORPHIC PETROLOGY

The 147.6-m-long section drilled at Site 1268 is composed of completely altered harzburgite and dunite intersected by mylonitic shear zones, late-stage magmatic dikes, and gabbronorite bodies that are moderately to completely altered. The high core recovery rate in Hole 1268A (53.3%) provides a unique opportunity to link the metamorphic evolution of the shallow mantle to tectonic and magmatic events. The most important first-order observation is that two alteration events have affected the rocks: (1) pervasive serpentinization and (2) pervasive talc alteration overprinting serpentinization in some sections. Both serpentinization and talc alteration were static and apparently unrelated to the intensity of crystal-plastic deformation. Cataclastic deformation and veining correlate with the intensity of gabbro alteration.

The basement at Site 1268 is heavily veined, with a remarkably high abundance of sulfide and sulfide oxide–bearing talc and serpentine veins. Sulfides and oxides are also abundant (up to a few percent of individual cores) in the halos along these metamorphic veins as well as along gabbroic dikes and veins. Different generations of serpentine veins are developed throughout Hole 1268A. These are early microscopic chrysotile + magnetite veins and later wispy chrysotile veins that were overprinted by talc alteration and are, hence, only preserved in the green serpentinites. The main stage of sulfide veining postdates the talc alteration. Late, usually subvertical serpentine veins are developed in all lithologies; although they may be transformed into talc veins, they intersect talc-altered rocks. The relative timing of crosscutting talc and serpentine veins is uncertain, but they both appear late in the sequence of veining.

Hydrothermal Alteration

Alteration of Ultramafic Rocks

During serpentinization, harzburgite and dunite are completely altered (secondary minerals = >95%) to dark green to green serpentinite consisting of serpentine ± magnetite ± pyrite (completely replacing both olivine and orthopyroxene) (Fig. **F18;** Table **T2**). Cr spinel is fresh in most instances, although minor alteration to magnetite and rare ferritchromite is present locally. The microtextures of serpentinized harzburgite and dunite range from pseudomorphic mesh and hourglass textures (Fig. **F19**) to transitional ribbon textures to nonpseudomorphic interlocking textures with serrate chrysotile veins (Fig. **F20**).

Talc alteration is common in the recovered drill core. Talc-altered dunite is massive and gray; macroscopic primary textures and serpentinite textures are variably preserved in pervasively talc-altered rock. Dissolution of orthopyroxene in talc-altered harzburgite imposed a vuggy appearance to the rock, with vuggy orthopyroxene pseudomorphs lined with talc (Fig. **F21**). Talc-altered harzburgites reveal variable replacement of serpentine and bastite by talc (Fig. **F22**). In talc-altered rock with complete bastite replacement, dark green millimeter-wide rims of relict serpentine of unusually intense green color and high birefringence outline the original shape of the orthopyroxene (Fig. **F23**). Macroscopic and thin section observations show that serpentine is replaced by talc in the talc-altered rocks. Incipient replacement of serpentine by talc is initiated along serpentine bands defining ribbon textures and mesh rims (Fig. **F24**). Even in highly talc-altered rock the original serpentinite microtexture is commonly preserved (Fig. **F25**). In some completely talc-altered rocks recrystallization resulted in coarse-grained nonpseudomorphic talc patches. Textural evidence shows that talc alteration postdates serpentinization, early chrysotile + magnetite veining, pyrite + serpentine veining, and later generations of chrysotile veins (Figs. **F20, F23, F26**). Hence, talc alteration is overprinting advanced serpentinization. Talc-altered rocks generally have lower oxide contents than the serpentinite precursors. Sulfides are also generally less abundant in talc-altered rock. However, talc-altered rock is locally enriched in sulfide, particularly along talc-oxide-sulfide veins.

In rare incompletely altered harzburgites and orthopyroxenites, olivine is replaced by serpentine and magnetite along mesh rims and hourglass cells and orthopyroxene is partly altered to serpentine and minor amounts of talc and tremolite. A sample of a highly altered orthopyroxenite (Sample 209-1268A-18R-4, 88–91 cm) has relict primary sulfide (pyrrhotite/pentlandite) and incipient breakdown products (heazlewoodite[?] and millerite[?]), indicating reducing conditions during the early stages of serpentinization.

Alteration of Mylonitic Shear Zones

Mylonitic shear zones formed under granulite facies conditions (see **"Structural Geology,"** p. 20) and are statically altered under greenschist facies conditions. The mylonitic shear zone with highest intensi-

F18. Photograph/XRD of a serpentinized harzburgite, p. 73.

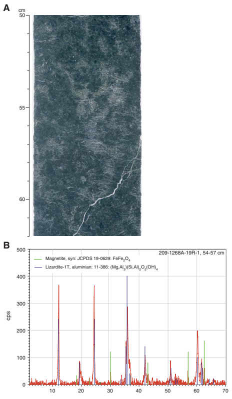

T2. XRD results, Hole 1268A, p. 156.

F19. Serpentinized harzburgite, p. 74.

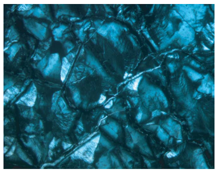

F20. Interlocking texture in a serpentinized harzburgite, p. 75.

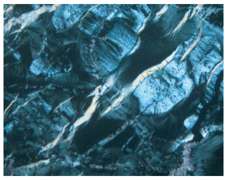

F21. Photograph/XRD of talc-altered serpentinized harzburgite, p. 76.

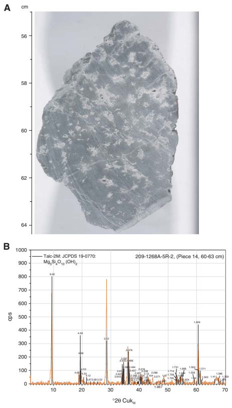

ties of crystal-plastic deformation is between 75 and 80 mbsf. At 78.6 mbsf this rock is pervasively altered, with amphibole, quartz, chlorite, oxides, and sulfides making up a significant fraction of the rock along with serpentine and varying proportions of talc (cf. thin section description of Sample 209-1268A-15R-1, 75–77 cm; see **"Site 1268 Thin Sections"**). The abundance of amphibole in the mylonite, as well as significant proportions of Fe-Ti oxides and apatite, suggests the presence of evolved magmatic material in this shear zone. The shear zone could represent a mylonitized gabbro-veined harzburgite or high-temperature metamorphic mineralization (e.g., brown amphibole) in harzburgite.

A mylonitized harzburgite at 75.6 mbsf lacks mafic and oxide-rich material and shows static alteration to almost pure serpentinite with minor amounts of magnetite (cf. thin section description of Sample 209-1268A-14R-2, 130–133 cm; see **"Site 1268 Thin Sections"**). Protomylonites and rare mylonites in other sections of Hole 1268A do not differ in alteration style or intensity from their undeformed analogs.

Alteration of Mafic Rocks

Crosscutting features interpreted as completely altered gabbroic dikes or veins are common, in particular between 60 and 100 mbsf. They are composed of talc, chlorite, amphibole, biotite, and white mica (Fig. **F27**). Gabbroic material also seems to be represented by heavily talc-altered rocks with a brecciated appearance that are distinguished from serpentinized harzburgites by the presence of pseudomorphs after large pyroxene and plagioclase crystals and/or a relict fine-grained texture. There is some suggestion, in particular for the section below 50 mbsf, that talc alteration is spatially associated with the presence of gabbroic veins (Fig. **F28**), small (meter scale) gabbro intrusions (Fig. **F29**), and contacts of large (tens of meters scale) gabbro intrusions. One possible explanation for this relationship is that silica-rich fluids, generated by gabbro-seawater interaction, metasomatized the surrounding serpentinites, causing the formation of talc at the expense of serpentine (see **"Silica Metasomatism of Serpentinites,"** p. 18, in "Discussion").

The large gabbroic intrusions appear to be gabbronorite in which orthopyroxene is completely altered to talc ± chlorite, while clinopyroxene is partly to completely altered to green amphibole and chlorite (Figs. **F30, F31**). Replacement of plagioclase and pyroxene by chlorite and amphibole along grain boundaries has created pronounced dark coronas (Figs. **F32, F33**). Plagioclase is variably altered to albite, quartz, and chlorite (Fig. **F34;** Table **T2**). The intensity of hydrothermal alteration of gabbronorite decreases downsection (Fig. **F35**). With decreasing alteration intensity, the relative proportion of chlorite in the secondary mineral assemblages decreases whereas that of amphibole increases. The lowermost gabbronorite unit has abundant fresh clinopyroxene and plagioclase, whereas orthopyroxene is completely altered in gabbroic rock throughout the entire hole. There appears to be a positive correlation between alteration intensity and intensity of cataclastic deformation as well as vein abundance (Fig. **F36;** see **"Structural Geology,"** p. 20). Although alteration of the gabbros is static, this relationship may indicate that large fractures had some control on alteration intensity by providing pathways for fluids that then penetrated the rock along microcracks and caused the moderate to complete alteration. A remarkable difference between gabbros from Hole 1268A and the gabbros and gabbroic veins drilled or dredged at other sites of mantle exposure on the seafloor (e.g., Bideau et al., 1991; Früh-Green et al.,

F22. Talc-altered serpentinite with serpentine pseudomorphs, p. 77.

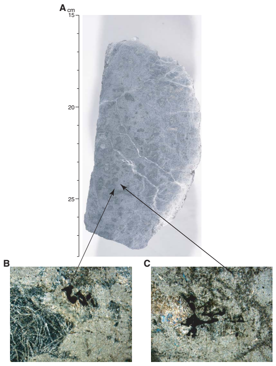

F23. Orthopyroxene pseudomorphed by talc and pyrite, p. 78.

F24. Serpentine partly replaced by talc + pyrite veinlets, p. 79.

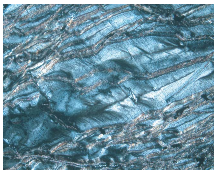

F25. Talc-altered rock with original serpentinite microtexture, p. 80.

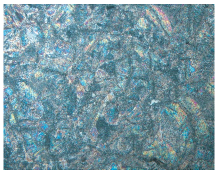

F26. Talc veins replacing serpentinite and crosscutting chrysotile veins, p. 81.

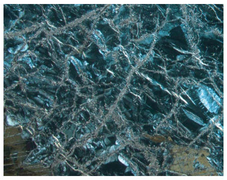

1996; Dilek et al., 1997b) is the complete lack of any Ca metasomatic and zeolite facies overprints in the gabbronorites and gabbroic veins in Hole 1268A.

A <1-cm-thick, highly altered amphibolite band is developed at 23.2 mbsf (cf. thin section description of Sample 209-1268A-3R-3, 6–9 cm; see **"Site 1268 Thin Sections"**). Apart from a few percent of relict brown amphibole, the amphibolite is completely altered to green amphibole, chlorite, serpentine, and white mica. This amphibolite is sandwiched in a centimeter-wide zone of highly altered orthopyroxene-rich harzburgite that shows significant amounts of weakly deformed relict olivine and orthopyroxene.

Metamorphic Veins

In the following sections we discuss the mineralogy of the veins as well as their characteristic macroscopic features and crosscutting relationships in the harzburgites, dunites, and gabbroic lithologies in Hole 1268A.

As part of the visual core description, we estimated the volumetric fraction of the core that is composed of different vein minerals (talc, serpentine, oxides, sulfides, and chlorite) (see the **"Supplementary Material"** contents list). Figure F36 illustrates the relationships between vein volume, composition, and lithology. Vein volume is low in zones of relatively high crystal-plastic deformation, as is the vein density (cf. **"Crystal-Plastic Deformation,"** p. 20, in "Structural Geology"). Sulfide veins are volumetrically important in Unit I between 20 and 30 mbsf, in the intrusion breccia zone (Unit II), and locally in Unit III. Oxide abundance in veins shows a similar distribution, but there is an overall trend of decreasing vein oxide downsection. Talc veins and serpentine veins exhibit spiky downhole distribution patterns that correlate with deformation intensity (lows in both serpentine and talc) and intensity of background talc alteration (highs in talc vein volume).

The distribution of the constituent minerals in different vein populations identified visually and verified by shipboard X-ray diffraction (XRD) analyses and thin section observations is shown in Figure F37. Figure F38 shows the different (a) shapes, (b) textures, (c) structures, and (d) connectivities of the identified vein populations. The percentage of the recovered core is shown in Table T3 along with breakdowns of the relative contribution of each vein population to this total. The distribution of various vein minerals among the vein populations and their relative contributions to the volume of core recovered is also calculated in Table T3.

Veins in Harzburgite and Dunite

The rocks of Hole 1268A have experienced a complex history of subseafloor metamorphism and associated vein alteration. Four distinct populations of veins are present within the harzburgite and dunite lithologies. These are described in more detail in the following sections. Chlorite and other populations of veins are subsidiary to these four.

Massive Sulfide Veins

Veins composed entirely of sulfides with varying proportions (as much as 50%) of iron oxides (dominantly magnetite and hematite) are described here as massive, referring to their dominant texture (Fig. F38A). This vein type commonly has irregular or sigmoidal shapes (Fig.

F27. Completely serpentinized harzburgite with magmatic dikes, p. 82.

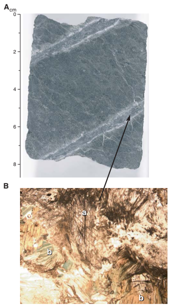

F28. Intrusion breccias, p. 83.

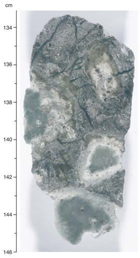

F29. Intrusion of gabbro into serpentinized harzburgite, p. 84.

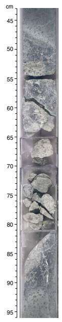

F30. Moderately altered gabbro, p. 85.

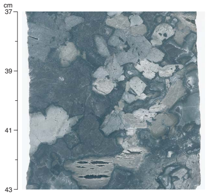

F31. Two pyroxenes in gabbro, p. 86.

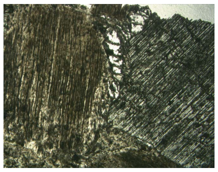

F38B) and composite or uniform structures (Fig. F38C). Relative to other vein populations, the massive sulfide veins show the highest connectivity (Fig. F38D). Mineralogically, they are dominated by pyrite, magnetite, and hematite, although traces of chalcopyrite and millerite are also present. Hematite is easily identified because of its reddish contrast against the dark background alteration. In thin section it appears that this red oxide is intergrown hematite and magnetite. Finely anastomosing sulfide veinlets are so abundant in places (e.g., Sections 209-1268A-2R-2 [Pieces 4A, 4B] and 19R-1 [Pieces 2A, 2B, 2C]) that they grade into the pervasive background alteration. A similar network of sulfide veinlets is present in the halos around pyroxenite of Section 209-1268A-13R-1 (Pieces 6A, 9). These sulfide veins crosscut chrysotile veins that were subsequently altered to talc (Fig. F39A). The sum of sulfide and iron oxide contents of the massive sulfide veins and the talc pyrite veins accounts for 10.6% of vein mineralization and ~0.9% of the entire core (for summaries of the relative proportions of veins and their mineralogy see Table T3; Figs. F38, F40).

Talc-Pyrite Veins

Talc veins with as much as 40% disseminated pyrite and iron oxides (mostly hematite) dominate the vein alteration at this site. The shape of the talc veins is irregular and occasionally sigmoidal, whereas the texture is massive and the internal structure is uniform. Half of this vein generation is nonbranched and the other half is composed of locally branched veins. Volumetrically, talc veins compose 4.2% of the core and talc itself accounts for 48% of all vein mineralogy (see Table T3). The talc is usually white or light green and contains irregular clusters of sulfide minerals (pyrite, rare marcasite, and millerite) and minor oxide (hematite and rare magnetite). Talc-pyrite veins cut both the serpentinized harzburgite/dunite and talc-altered lithologies. However, in proximity to areas of heavy talc alteration the connectivity of the veins drops (see Fig. F40C, F40D) and the pyrite and hematite content diminish over a short distance (several centimeters) to the point where the veins are composed solely of talc. This phenomenon is particularly well developed in intervals 209-1268A-4R-1, 80–116 cm, and 4R-2, 74–81 cm. Conversely, in serpentinized harzburgite/dunite lithologies the modal proportion of pyrite ± hematite increases when talc-pyrite veins crosscut relict orthopyroxene grains, commonly to the point where talc is absent. The relationships observed in Section 209-1268A-3R-2 suggest that two separate generations of this type of vein may be present because crosscutting relationships between talc veins with differing modal percentages of sulfide ± hematite are present here. Talc-pyrite veins crosscut massive sulfide veins (see Fig. F39), and in Sections 209-1268A-12R-3 and 22R-1 they crosscut chrysotile veins. Talc-pyrite veins also crosscut the gabbroic veins or dikes of Section 209-1268A-24R-2.

Massive Talc Veins

A generation of massive talc veins with only traces of sulfide cuts the earlier generations of talc-pyrite and massive sulfide veins. Massive talc veins are dominantly of irregular shape (Fig. F38B). Commonly, they have a uniform or composite structure (Fig. F38C) and a dominantly massive texture (Fig. F38B). In contrast to the massive sulfide and talc-pyrite veins, they exhibit cross and slip fibers. The connectivity ranges from single to branched (Fig. F38D). Crosscutting is particularly well developed in Sample 209-1268A-11R-1 (Piece 24, 126–137 cm) and in Section 16R-2, where the massive talc veins cut earlier vein generations.

F32. Coronas along boundaries of plagioclase and pyroxene, p. 87.

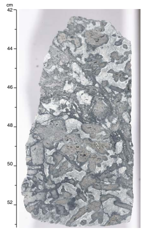

F33. Green amphibole and chlorite in gabbronorite, p. 88.

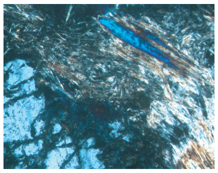

F34. Plagioclase replaced by chlorite and quartz, p. 89.

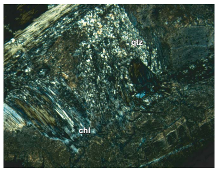

F35. Variation of alteration intensity, Hole 1268A, p. 90.

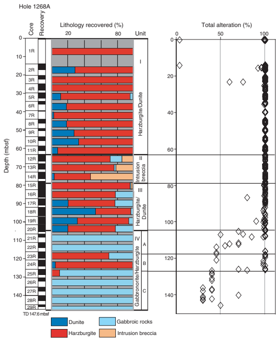

F36. Abundance of metamorphic veins, p. 91.

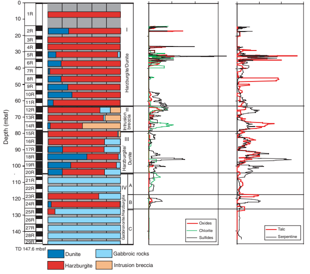

Notably, talc overprints chrysotile veins (Fig. **F39B**) and talc veins generally cut chrysotile veins. In Section 209-1268A-24R-2 massive talc veins contain small amounts of pyrite, hematite, and trace proportions of needlelike millerite. This is the only section in Hole 1268A where significant amounts of sulfides and iron oxides could be observed within the massive talc veins. Massive talc veins cross lithologic boundaries between serpentinized harzburgite/dunite and talc-altered ultramafics. They also crosscut talc-pyrite veins and, in some examples, may be associated with normal faulting (Fig. **F40D**). Therefore, this generation of veining was probably late in the sequence of alteration events that occurred at Site 1268.

Serpentine Veins

After talc, serpentine is the most abundant vein mineral in Hole 1268A. It constitutes 39.1% of the vein mineralization, which in turn represents 3.4% of the core volume (see Table **T3;** Figs. **F38, F40**). Monomineralic serpentine veins that range from white through light to dark green are seen throughout Hole 1268A. This vein population occurs with irregular, sigmoidal, and straight shapes (Fig. **F38B**), a dominantly uniform structure (Fig. **F38C**), and mostly massive textures (Fig. **F38A**), as well as cross- and slip-fiber types. Serpentine veins are either single or show connectivities ranging from branched to nonbranched (Fig. **F38C**). They are generally sigmoidal and run subparallel to lithologic boundaries in poorly connected or unconnected semicontinuous en echelon arrays. For example, they are subparallel to the lithologic boundary between harzburgite and dunite in Sections 209-1268A-13R-2 (Pieces 4, 12, 19, 20) and are often present adjacent to the talc-altered transition zones between harzburgite/dunite and various igneous intrusions (e.g., Section 209-1268A-15R-2 [Piece 2B, 34 cm]). In many cases these veins have been replaced by talc (e.g., Section 209-1268A-3R-1 [Piece 21]) and are crosscut by talc-pyrite veins (e.g., Section 22R-1). Talc overprinting of chrysotile veins is identified by the powdery, weathered look of some chrysotile veins that only locally retain patches of their former fibrous nature. Elsewhere, however (e.g., in Section 209-1268A-18R-2), chrysotile veins of this type crosscut talc-pyrite veins, supporting the hypothesis that at least one of these vein types has multiple generations.

Serpentine and magnetite veins occur throughout the dunite-rich section between 90 and 105 mbsf and constitute a significant fraction of the magnetite present in this lithologic unit (0.2 vol% of veins and 0.02 vol% of the recovered core, not including magnetite present in background serpentinite alteration).

A final generation of serpentine veins crosscuts both talc-pyrite veins and talc veins, suggesting that the serpentine veins probably represent the last significant alteration and veining event at Site 1268. Sulfide is not usually present in these veins; however, chalcopyrite is present in Section 209-1268A-18R-3. This serpentine vein system is usually branching with individual veins >1 cm wide. It is present in substantial volumes of core within areas of serpentinized dunite (e.g., Sections 209-1268A-24R-1 and 24R-2). Rotated clasts of former chrysotile veins and angular rock fragments are commonly enclosed within these veins, so some of these vein systems are associated with minor cataclastic deformation. The serpentine veins in Section 209-1268A-24R-2 were identified by XRD analysis as lizardite.

F37. Abundance and distribution of minerals in veins, p. 92.

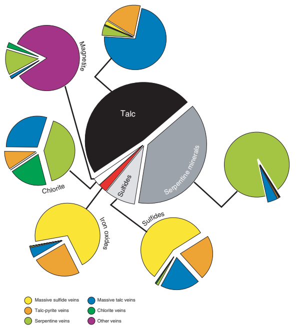

F38. Vein texture, shape, and structure in peridotites, p. 93.

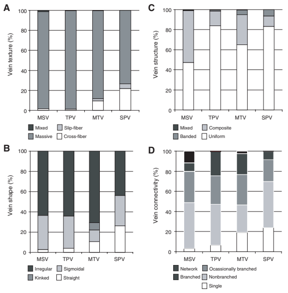

T3. Mineralogy of metamorphic veins, Hole 1268A, p. 157.

F39. Crosscutting between different generations of veins, p. 94.

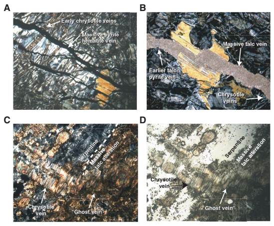

F40. Crosscutting between different generations of veins, p. 95.

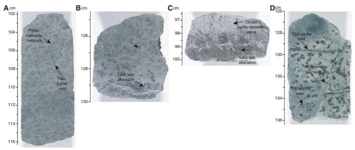

Chlorite-Rich Veins

Chlorite veins, or veins containing a significant proportion of chlorite, compose only 2% of the total volume of the veins logged and only 0.14% of the volume of core recovered (Table T3). Rare, small, wispy veins thought to be composed of chlorite are present in areas of dunite (particularly in Section 209-1268A-18R-4). Chlorite is also present in small mixed talc-chrysotile veins in Section 209-1268A-8R-1 (Piece 30).

Veins in Talc-Altered Lithologies

Talc Veins

Talc veins dominate areas of serpentinized harzburgite/dunite that were subsequently overprinted by pervasive talc alteration. These veins can be traced into areas of serpentinized peridotites and dunites where the talc overprint is absent. They exhibit increasing modal proportions of sulfide and hematite with distance away from the zones of talc alteration. We interpret this to indicate that sulfide was preferentially precipitated in areas of serpentinized harzburgite. Alternatively, talc alteration was superimposed upon a preexisting generation of sulfide-rich talc veins, mobilizing sulfide and reprecipitating it in areas away from the talc alteration front.

Serpentine Veins

Small, wispy, sigmoidal chrysotile veins are present in some areas of heavy talc alteration. These are usually subparallel single or semicontinuous en echelon fibrous chrysotile veins. Their orientation is commonly parallel to the leading edge of the talc alteration front.

Veins in Gabbroic Lithologies

The occurrence and frequency of veins in the gabbroic units is low, and crosscutting relationships are rare, making the construction of an alteration history for this lithology difficult.

Rare small talc veins are present throughout the massive gabbros and are volumetrically insignificant. Small talc veins crosscut clasts of gabbro within the gabbroic intrusion breccias and are present within the gabbro from Section 209-1268A-22R-2 downhole. Further, a small chlorite-amphibole-serpentine vein network is developed in Section 209-1268A-20R-3.

Serpentine veins run subparallel to, or split, gabbro veins or dikes and gabbroic intrusion breccias, contributing to their extensive and multistage hydrothermal alteration. In Sections 209-1268A-16R-1 and 18R-4, serpentine veins crosscut gabbroic veins or dikes at a high angle. Cross fractures typically associated with gabbro veinlets are filled with serpentine. Serpentine veins in intrusion breccias do not cut peridotite clasts. This type of relationship is also seen in the gabbroic veins of Section 209-1268A-16R-2, where serpentine veins within the gabbro terminate at the gabbro/harzburgite contact.

A single pyrite-chalcopyrite-hematite vein is present in Section 209-1268A-18R-3, which hosts a large aggregate of chalcopyrite.

Veins in Pyroxenite

Pyroxenite is present only in very small volumes in cores from Hole 1268A, and accordingly, the veins within this lithology account for an insignificant volume of the whole core. A halo surrounding the pyroxenite in Section 209-1268A-13R-1 contains a small network of pyrite-hematite veins similar to those that are well developed in the serpentinized harzburgite/dunite. Chrysotile veins crosscut the pyroxenite in Section 209-1268A-18R-1, whereas in Section 18R-4 small serpentine-chlorite-amphibole veins are present.

Discussion

Timing and Conditions of Alteration and Vein Formation

The rocks recovered from Site 1268 have experienced a complex history of veining and hydrothermal alteration, as is demonstrated by the variety of veins present and their complex crosscutting relationships. Recognizing that the succession of alteration and veining events follows a systematic trend toward more oxidizing conditions, we have grouped the veins simply as early, main, and late stages of vein formation. A simplified overview of the relative timing of alteration and veining is provided in Figure **F41.**

F41. Timing of alteration and veining events, p. 96.

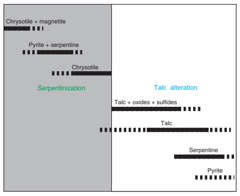

Serpentinization and Early Vein Formation

Serpentine veins, in their various incarnations (see **"Serpentine Veins,"** p. 15, in "Veins in Harzburgite and Dunite," above; Fig. **F38**), are common throughout the alteration history of Hole 1268A. The crosscutting relationships of various populations of veins outlined above yield the following relative sequence of veining. A first generation of serpentine veins was synchronous with the serpentinization of the harzburgites and dunites. These serpentine-magnetite veins are present chiefly in serpentinized dunite (90–105 mbsf). Later generations of pyrite ± serpentine veins followed by fibrous chrysotile veinlets within the serpentinites are part of the early background serpentine alteration. The presence of magnetite in veins as well as the occurrence of reduced iron and nickel sulfides (relict pyrrhotite/pentlandite and possible partial replacement by heazlewoodite) in a moderately altered orthopyroxenite (Sample 209-1268A-18R-4, 88–91 cm) suggest fairly reducing conditions during early serpentinization and veining (Fig. **F42A**). Phases indicating even lower oxygen fugacities, found in peridotites from Hess Deep and the Kane Fracture Zone (MARK) area (Alt and Shanks, 1998, 2003), were not identified in the course of our shipboard studies.

F42. Phase diagram for the Fe-Ni-S-O system, p. 97.

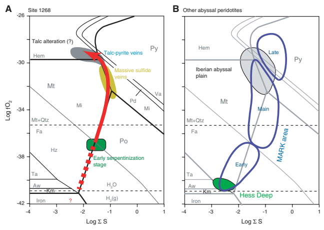

Talc Alteration and Main Stage of Vein Formation

The occurrence of massive pyrite veins with variable hematite modal percentages represents the most easily recognizable aspect of the main stage of alteration and veining. The coexistence of pyrite, magnetite, hematite, and trace millerite requires very specific oxygen and sulfur fugacities, provided that temperature and pressure can be estimated (Fig. **F42A**). This effectively pinpoints the emplacement of the massive sulfide veins at the position indicated on Figure **F42A.** When compared to other mid-ocean-ridge serpentinites, these conditions are unusual in that hematite is not developed in MARK and Hess Deep serpentinites (Alt and Shanks, 1998, 2003) (Fig. **F42B**).

Late-Stage Alteration and Vein Formation

The conditions recorded in veins that postdate emplacement of the massive sulfide veins (see above) also differ from the late-stage alteration conditions observed in other abyssal peridotites. In previous studies (Alt and Shanks, 1998, 2003), pyrite veins characterize late-stage alteration and hematite is absent (Fig. F42B). In the late-stage oxide sulfide–bearing veins in Hole 1268A, hematite is a major vein constituent, indicating more oxidizing conditions (and/or lower H_2S activities) during late-stage circulation than at Hess Deep and MARK.

Talc-pyrite veins crosscut the fine anastomosing sulfide-hematite veins in several locations throughout Hole 1268A (see above), and where this occurs sulfide is mobilized and appears more concentrated in the talc-dominated veins. This suggests that hematite formation may have occurred during the talc alteration stage. It is conceivable that increasing modal percentages of hematite in the late-stage talc-pyrite-hematite veins are associated with decreasing H_2S(aq) and H_2(aq) activities of the interacting hydrothermal solution. Such a trend can be expected in long-lived hydrothermal systems where the reducing capacity of the rock is exhausted by reduction of seawater sulfate (e.g., Seyfried and Ding, 1995). This scenario is consistent with the observation that the peridotites in Hole 1268A underwent multiple episodes of intense and pervasive alteration.

The last stage of veining in the Hess Deep and the MARK areas is the formation of aragonite veins under ambient conditions at or near the seafloor (e.g., Bluzstajn and Hart, 1996). Aragonite veins were not identified in core from Hole 1268A, suggesting that present-day veining and seawater ingress may be minimal—or that exposure at the seafloor was recent.

Silica Metasomatism of Serpentinites

In contrast to serpentinized ultramafic rocks from the Hess Deep and MARK areas (Früh-Green et al., 1996; Dilek et al., 1997b), which contain noticeable amounts of early talc and tremolite (after orthopyroxene) and brucite (after olivine), serpentinized peridotites in Hole 1268A do not contain these assemblages, except in one highly serpentinized orthopyroxenite. In other, more common localities, it is thought that early talc forms after orthopyroxene and is replaced by lizardite either during retrograde serpentinization (Wicks, 1984) or due to a combination of increased H_2O activity and decreased silica activity of the fluid (Frost, 1985). Hydrothermal experiments (at 400°C and 500 bar) confirm that fluids are talc-saturated as long as fresh pyroxene is left in the serpentinizing peridotite (Allen and Seyfried, 2003). Similarly, brucite is believed to be a product of incipient serpentinization which, due to reaction with aqueous SiO_2 released by the breakdown of orthopyroxene to lizardite, forms lizardite and magnetite (e.g., Toft et al., 1990). There is no relict talc, tremolite, or brucite in the rocks from Hole 1268A, suggesting that serpentinization reached an advanced stage at which only serpentine and magnetite were present. The high proportion of magnetite in the dunite-rich unit between 90 and 105 mbsf (cf. Fig. F92) is consistent with this scenario. The molar (Mg + Fe)/Si ratios of completely serpentinized rocks from Hole 1268A are close to 1.5 (cf. "Geochemistry," p. 33; Table T5), which is higher than the likely (Mg + Fe)/Si ratio of the protolith (i.e., [Mg + Fe]/Si = 1.8 for a harzburgite with 20% orthopyroxene). The comparatively low magnetic susceptibilities in the harzburgites and dunites from the upper 90 m in Hole 1268A may indicate destruction of magnetite during subsequent alteration that did not affect the dunite-rich section between 90 and 105 mbsf of Unit III. The (Mg + Fe)/Si ratios decrease from 1.62 ± 0.05 (1σ; $N = 4$) in the strongly magnetized harzburgites/dunites of Unit III to 1.41 ± 0.06 (1σ; $N = 11$) in the serpentinites in the upper 90 mbsf to 0.79 ± 0.06 (1σ;

N = 5) in the talc-altered serpentinites, suggesting increasing extent of relative Si gains or Mg + Fe losses.

Another indication of the advanced degree of serpentinization in Hole 1268A is the general scarcity of pseudomorphic mesh textures and the common development of transitional hourglass and ribbon textures (O'Hanley, 1996). Furthermore, interlocking textures, indicating recrystallization of mesh-textured serpentine, are common and serrate chrysotile veins formed at the expense of early lizardite.

The most unusual aspect of the hydrothermal alteration at Site 1268 is the widespread replacement of serpentine by talc. In previously drilled and dredged sections of upper mantle (Dilek et al., 1997b; Früh-Green et al., 1996; Bideau et al., 1991), gabbros are Ca metasomatized, whereas at Site 1268, serpentinites are Si metasomatized. Furthermore, zeolite facies alteration and veining, common in metagabbros from Hess Deep and MARK areas, is absent in core from Hole 1268A. Hence, we infer that the relative timing of deformation, magmatism, and hydrothermal alteration at Site 1268 is different from otherwise similar, previously investigated settings.

Instead of Ca metasomatism of gabbro, the serpentinites at Site 1268 reveal replacement of serpentine by talc. Serpentine has a molar (Mg + Fe)/Si = 1.5, whereas that of talc is 0.75. Talc alteration may hence be a result of Si metasomatism. One possible reaction between serpentine and fluid to form talc is

$$\underset{\text{serpentine}}{Mg_3Si_2O_5(OH)_4} + 2SiO_2(aq) \rightarrow \underset{\text{talc}}{Mg_3Si_4O_{10}(OH)_2} + H_2O,$$

which proceeds to the right if the silica activity of the fluid is increased and/or if the water activity is lowered. In some cases, the formation of talc-magnesite rocks after serpentinite have been a consequence of lowering the water activity of the fluid by adding CO_2 (e.g., Peabody and Einaudi, 1992). However, we did not observe magnesite (or other carbonates) in detectable amounts and conclude that carbonatization cannot account for the abundant development of talc after serpentine. It is hence more likely that an increase in silica activity is responsible for the conversion of serpentine to talc.

The close spatial association of talc alteration and gabbro intrusions suggests that gabbro emplacement and talc alteration are intimately linked. Gabbro intrusion and dike formation in serpentinite could revive hydrothermal circulation by providing a heat source and creating permeability. However, hydrothermal circulation long after gabbro emplacement could also transport SiO_2 from gabbro into host peridotite. Theoretical geochemical models suggest that at 350°C and 500 bar mafic rock–seawater reactions form hydrothermal fluids much higher in silica and lower in pH than hydrothermal fluids produced by reaction of seawater with ultramafic rocks (Wetzel and Schock, 2000).

Hydrothermal reaction between gabbro and seawater under greenschist facies conditions transformed pyroxene and plagioclase in the gabbros to chlorite, amphibole, and talc, releasing silica and acidity and causing Si metasomatism and talc formation in the serpentinites. The activity coefficient for aqueous SiO_2 is strongly pH dependent and becomes larger as the pH decreases. Silica activity and pH are hence strongly coupled, in particular at near-neutral conditions (Johnson et al., 1992).

Ca metasomatism takes place when gabbros and ultramafic rocks undergo the same metamorphic history (e.g., Schandl et al., 1989). Ca-rich fluids generated during serpentinization metasomatize the gabbros replacing pyroxene and plagioclase by clinopyroxene, tremolite, clinozoisite, prehnite, and hydrogrossular (e.g., O'Hanley et al., 1992). The lack of rodingitization—even in small gabbroic veins—may suggest that the gabbros intruded after serpentinization was largely completed and the Ca of the peridotites had already been leached out. Experimental studies show that Ca is lost most rapidly in the early stages of high-temperature serpentinization when the reactions rates of pyroxenes are fast (Allen and Seyfried, 2003). However, other considerations (see **"Cross-cutting Relationships and Deformation Paths,"** p. 28, in "Structural Geology") suggest that many or most of the gabbroic intrusions formed while the peridotite wallrocks were still quite hot (>500°C).

STRUCTURAL GEOLOGY

We present the results of a detailed structural analysis of the core recovered from Site 1268. Four categories of observations were recorded in spreadsheet format including magmatic structures, crystal-plastic deformation, cataclastic/brittle deformation, and alteration veins (see the **"Supplementary Material"** contents list). These were supplemented by microstructural observations in more than 60 thin sections. Details of the structural classification scheme for each feature are given in the **"Structural Geology,"** p. 9, in the "Explanatory Notes" chapter. We first present and discuss the observations for each category separately and then discuss the temporal and spatial relationships between them. Finally, we conclude with an initial interpretation of the structural evolution of the core in the context of the tectonic setting of Hole 1268A.

The lithologic stratigraphy of Hole 1268A is complex, consisting of a long section of highly altered peridotite, an intrusion breccia with locally intense crystal-plastic and brittle deformation, and two massive gabbro units with an intervening enclave of peridotite. The entire section has been altered to talc- and sperpentine-rich assemblages, with most primary features in the peridotite and breccia units preserved only as pseudomorphs. This complicates textural and structural interpretation, but many features are well preserved, making clear interpretation of their origin possible.

Crystal-Plastic Deformation

Structures preserved in the Hole 1268A cores indicate that crystal-plastic deformation occurred over a range of subsolidus conditions including high-temperature ductile flow and late, localized, high-temperature mylonitic deformation contemporaneous with gabbro intrusions in the shallow mantle section.

Gabbro and peridotite fabrics were logged using the semiquantitative deformation intensity scale that was used during Legs 118, 147, 153, 176, and 179 (see Table **T4,** p. 62, in the "Explanatory Notes" chapter). The orientation of these fabrics was measured in the core reference frame. In a few cases we were able to determine a shear sense. The variation in the intensity of crystal-plastic deformation with depth is shown in Figure **F43.** This figure represents a running downhole 20-piece average of the intensities measured on individual pieces of core. Although individual pieces vary in length, the plot will differ little from one based on average intensities for uniform length increments of the core. This is because the plot includes all 1074 pieces logged, with an

F43. Downhole intensity/orientation of crystal-plastic deformation, p. 98.

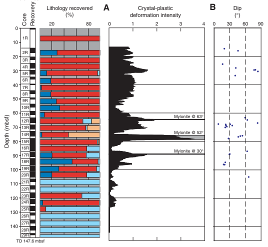

average length of only 6.6 ± 8.8 cm (1σ). The uppermost interval of the hole is not represented, as the first core is believed to be rubble rather than true basement. We also stopped averaging within 10 pieces of the top of Core 209-1268A-2R and within 10 pieces of the bottom of Core 29R.

High-Temperature, Low-Strain Fabrics

The most pristine and "least deformed" high-temperature mantle textures were locally observed in sections of harzburgite with no significant crystal-plastic foliation. These are protogranular textures characterized by relatively coarse granular olivine and orthopyroxene. Orthopyroxene has smooth curved grain boundaries, commonly interstitial to the olivine matrix (Fig. **F44**). Protogranular textures show little sign of internal high-temperature strain and are assigned a deformation intensity grade of 0 on our scale. In the core, these textures are present in areas with little or no foliation (e.g., Fig. **F44A, F44B**). Minor crystal-plastic deformation is observed in the form of very weak foliations (Fig. **F45**), infrequent kink bands in olivine (Fig. **F44G**), and rare slight bending of pyroxene cleavage. Evidence of extensive dynamic recrystallization is absent, and we interpret these textures as having formed during high-temperature, low-strain mantle deformation (e.g., Mercier and Nicolas, 1975).

The Hole 1268A harzburgites also exhibit a previously undescribed variant on protogranular texture that we term protointergranular texture (Fig. **F46**). This texture is defined on the basis of pyroxene morphology. Orthopyroxene has a very ragged intergranular or even subophitic appearance (Fig. **F44C**) and generally a smaller grain size than is normal in mantle peridotites. Whereas abyssal peridotites generally have orthopyroxene grains 3–4 mm in size (Dick, 1989), the Hole 1268A protointergranular harzburgites typically have average orthopyroxene grain sizes of <2 mm. A large proportion of the protointergranular textured harzburgites appear undeformed. This texture may have developed late in the emplacement history of the peridotite as a result of pyroxene dissolution by migrating melts. This conclusion is also suggested by common large vermiform spinel intergrown with single small orthopyroxene pseudomorphs in the protointergranular harzburgites (Fig. **F44D**). Chromian spinel probably forms during incongruent dissolution of pyroxene (e.g., Dickey et al., 1971; Dickey, 1976; Dick, 1977). These high-temperature, low-strain textures are preserved locally in the core (e.g., Sections 209-1268A-3R-1 and 3R-2) between higher-strain regions. We grade 45% of the harzburgites at 0 or 0.5 (transitional from protogranular to weak porphyroclastic) on our intensity scale (Fig. **F47**).

High-Temperature, Moderate-Strain Fabrics

The development of higher-strain zones at high temperatures is manifested in Hole 1268A by high-temperature porphyroclastic harzburgite. Of the harzburgites, ~55% have weak porphyroclastic (deformation intensity grade = 1) to foliated porphyroclastic (grade = 2) deformation textures (Fig. **F47**). This texture is generally characterized by rounded porphyroclasts of pyroxene in a matrix of recrystallized olivine. Pyroxene grains are commonly stretched, with aspect ratios varying between ~1:1 and 4:1. A weak to moderate penetrative foliation can be present over long intervals. In lower-temperature examples, kinked and strained pyroxene and olivine are abundant.

F44. Protogranular and protointergranular textures, p. 99.

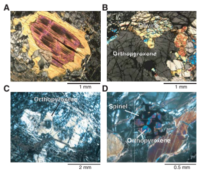

F45. Weakly foliated protogranular harzburgite, p. 101.

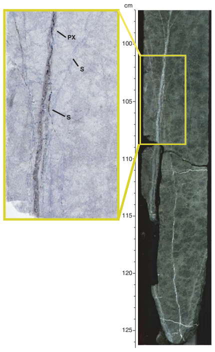

F46. Protointergranular texture in harzburgite, p. 102.

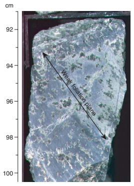

F47. Crystal-plastic deformation proportions, p. 103.

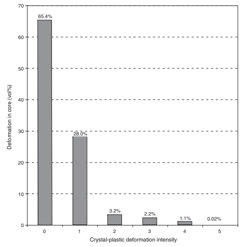

An important characteristic of the orthopyroxene pseudomorphs in the Hole 1268A porphyroclastic harzburgites is the abundance of relatively large neoblasts with polygonal grain boundaries that formed by recrystallization of porphyroclasts (Fig. F44E). This texture is not unusual in either abyssal or ophiolitic peridotites with weak to foliated porphyroclastic texture. More commonly, however, pyroxene neoblasts are finer grained and lack a well-developed polygonal texture. The coarser texture is associated with high-temperature recrystallization of orthopyroxene, often at temperatures >1000°C (e.g., Kelemen and Dick, 1995). The lower-temperature form of porphyroclastic texture is not common in the Hole 1268A harzburgites.

Porphyroclastic-textured higher-strain zones occur throughout the core, with strain varying downhole over tens of centimeters to meters (Fig. F43). Examples of coarse porphyroclastic harzburgites with varying intensities of foliation are found in Sections 209-1268A-19R-2 (Pieces 2–6, 14, 15) and 15R-1 to 15R-4. Downhole variability in the aspect ratios of orthopyroxene indicates variable strain on scales of centimeters to meters, an observation also recorded in peridotite cores from Site 920 in the Kane Fracture Zone (MARK) area (Shipboard Scientific Party, 1995). In the MARK region, however, the average overall extent of deformation appears higher. The succession of textures from protogranular to foliated porphyroclastic is well represented in virtually all mantle sections in ophiolites and is believed to represent solid-state flow and emplacement to the base of the crust.

High-Temperature, High-Strain Fabrics

Mylonites crosscut both the peridotites and the gabbro intrusives. The localized mylonitic deformation is superimposed on the earlier protogranular and porphyroclastic textures of the peridotites and clearly represents a later event as illustrated in Figure F48. Although the textures are only preserved in pseudomorphs, they are similar to those previously described in fresh abyssal peridotites (Jaroslow et al., 1996). Characteristic features include ribbon-textured olivine representing extreme stretching of grains, alternate enclaves of very fine and fine-grained olivine defining well-developed foliations, extreme grain size reduction, and porphyroclasts with either extreme ratios of length:width or near-perfect round or oval outlines. In the extreme, grain size reduction eliminates macroscopic foliation in the rocks. At these extents of deformation, no elements of protogranular texture are preserved.

F48. Changing foliation orientation/intensity in mylonitic shear zone, p. 104.

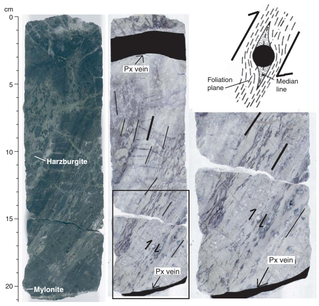

The late mylonitic deformation occurred prior to alteration, probably shortly after gabbro intrusion, based on several observations:

1. The viscosity and yield strength of serpentinized (or talcose) peridotite are quite low (Escartin et al., 1997a, 1997b), and yet gabbro and peridotite are deformed together in the mylonites. If peridotites had been serpentinized prior to deformation, we infer that deformation would have been localized within the peridotite, with boudinage of gabbro in a deforming serpentinite matrix, as commonly seen in rodingitized gabbros in sheared serpentinite belts.
2. The gabbros are medium to coarse grained, suggesting that they were not chilled by intrusion into cold, hydrated serpentinite.
3. Whereas the mylonitic textures are entirely pseudomorphed, the preservation of rolled pyroxene augen and evident grain size re-

duction in the matrix resembles high-temperature peridotite mylonites formed from 500° to 850°C (Jaroslow et al., 1996). For example, pseudomorphs of characteristic recrystallized olivine enclosed in a fine-grained matrix were recognized in Sample 209-1268A-12R-1 (Piece 14, 125–127 cm).

Several shear sense indicators in the major mylonite zone in Cores 209-1268A-14R and 15R indicate a reverse shear sense (reverse shear sense is also recorded by two shear zones in Hole 735B, though there are others with a normal shear sense [Shipboard Scientific Party, 1999]):

1. Figure **F48** shows a mylonite cutting weakly porphyroclastic harzburgite, with the mylonite foliation curving upward away from the central plane of the shear zone. The steep upward curvature indicates a reverse sense of shear (Ramsay and Huber, 1987).
2. A pressure shadow tail developed around a porphyroclast provides a second sense of shear. The tail is curved and narrow and is rotated with the porphyroclast. The median line of the tail crosses the main trend of the foliation. In this case, the shear strain is probably high and the recrystallization rates are lower than the rotation rates, again indicating a reverse sense of shear (Passchier and Simpson, 1986).
3. Similarly, a porphyroclast with dynamically recrystallized pressure shadow tails is shown in Figure **F49.** The median line of the tail does not cross the main foliation in the shear zone, showing that the rotation rate of the tails was higher than that of the porphyroclast itself, indicating a reverse shear sense (Passchier and Simpson, 1986).
4. Another example of reverse shear sense is seen in a pseudomorphed pyroxene in thin section, where a long, curved, narrow tail and rotated porphyroclast are well developed (Fig. **F50**).

F49. Serpentinized peridotite mylonite, p. 105.

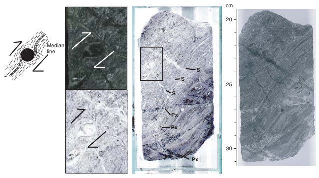

F50. Clinopyroxene porphyroclast and mylonite pressure shadow, p. 106.

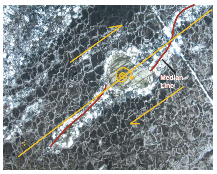

Intensity and Orientation of Crystal-Plastic Fabric

Early, well-developed crystal-plastic foliations are limited in the Hole 1268A cores. Only 30 measurements were made, the majority representing high-temperature, moderate-strain porphyroclastic foliations in the harzburgites. The remainder of the foliations were developed during the late high-temperature, high-strain mylonitic deformation event. Foliation dips are plotted in Figure **F43.** In general there are no systematic variations in the dip of the crystal-plastic foliation with depth.

Spatial Distribution of Crystal-Plastic Deformation

Narrow protomylonite zones (grade = 3) occur in small 0.5-cm shear zones at 14.6 and 53.3 mbsf within single pieces of harzburgite and dunite. There is also a 1-cm mylonite zone in gabbro-veined harzburgite from 88.7 to 89.2 mbsf. Mylonites occur in a 5-cm zone in harzburgite in Section 209-1268A-9R-1 (Piece 9) (49.4 mbsf), in a 40-cm zone in gabbro-veined harzburgite (64.4–64.8 mbsf), and in harzburgite-gabbro breccia (75.9–79.0 mbsf). Only a few fragments of ultramylonite (grade = 5) were found in the core in the 75.9- to 79.0-mbsf shear zone. At higher deformation grades (3–5), the transition from undeformed or weakly deformed rock to mylonite is usually quite sharp (e.g., Fig. **F48**), whereas the transition from lower-grade porphyroclastic deformation to mylonite is more transitional.

Both visual core description and thin section observations show that crystal-plastic deformation is not evenly distributed in Hole 1268A (Table T4). Overall, gabbros are the least deformed, with well-preserved igneous textures. They have an average crystal-plastic deformation intensity grade = 0.2. Gabbros drilled below 101 mbsf (from Core 209-1268A-20R downhole) have an average intensity grade = 0, whereas those higher in the hole have an average intensity = 0.4. The lower gabbros are not entirely undeformed, with occasional kinks in pyroxene grains, and recrystallization and polygonalization of plagioclase near the top of the lower gabbro units in Core 209-1268A-21R indicate very weak crystal-plastic deformation near the contact with the overlying peridotites (Fig. F44F). Harzburgite has an average deformation intensity = 0.9. This grade largely reflects background high-temperature deformation; therefore, the harzburgite probably underwent little penetrative deformation following intrusion of the gabbros. Dunite also appears to have a low average deformation intensity, although this may be due to the lack of deformation indicators preserved after alteration.

T4. Average crystal-plastic intensities, p. 158.

The harzburgite-gabbro intrusion breccias and the heavily gabbro-veined peridotites in Cores 209-1268A-15R to 20R are the most deformed rocks in Hole 1268A. These have an average deformation intensity = 1.3, and their location coincides with the three major mylonite zones in the hole (Fig. F43). This high-intensity deformation is not penetrative and is localized within the intrusion breccias, providing a sequence of textural relationships from undeformed to mylonitized intrusion breccia (Fig. F51A, F51B, F51C). The contrasts in competency created by the mixture of gabbroic rocks and peridotite in the intrusion breccia and heavily veined gabbros would provide a natural place for strain localization and failure to occur.

F51. Intrusion breccias showing increasing deformation, p. 107.

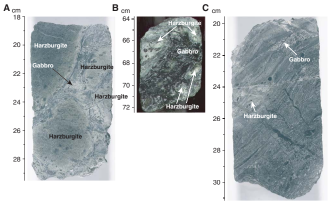

Taking into consideration the background high-temperature recrystallization, the Hole 1268A harzburgites and the intruding gabbros show only modest crystal-plastic deformation, compared to the more extensive deformation in the upper 500 m of Hole 735B drilled in the Atlantis Bank oceanic core complex. There, although perhaps as much as 100–200 m of the footwall was removed by erosion, 14% of the gabbros have undergone more than weak deformation (grade = >1), whereas only 6.5% of the Hole 1268A cores have undergone more than weak deformation (Fig. F47).

Brittle Deformation

Anastomosing Serpentine Foliation

Much of the serpentinized peridotite recovered from Site 1268 displays a weak to moderately strong, dominantly planar fabric defined by anastomosing arrays of serpentine veins. A similar foliation was described in serpentinite core from Ocean Drilling Program (ODP) Site 920 (Shipboard Scientific Party, 1995). Serpentine and magnetite veins that define the foliation are commonly deflected around pyroxene porphyroclasts (Fig. F52), which causes anastomosing waves in the foliation. The amplitude of these waves appears to be a function of the pyroxene porphyroclast grain size and the degree to which veins deflect around porphyroclasts. In some locations, veins penetrate pyroxene porphyroclasts and define a more planar, less anastomosing foliation. Serpentine fibers forming veins are commonly aligned perpendicular to

F52. Anastomosing serpentinization foliation, p. 108.

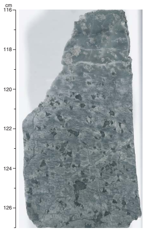

vein walls, suggesting growth during dilational opening of fractures. This suggests that the foliation is not a result of shear deformation (Fig. F53). In several samples, serpentine fibers in veins are aligned oblique to vein walls, suggesting that fractures opened by a combination of dilational and shear movement. This texture, however, does not appear to represent a large degree of shear strain accommodation. The serpentine foliation in much of the Site 1268 core is obscured and overprinted by pervasive talc alteration. Static replacement of serpentine minerals with very fine grained talc diminishes the fabric intensity, leaving only a faint trace of the original texture.

The orientation of anastomosing serpentinization foliation viewed in hand sample generally parallels that of preexisting crystal-plastic fabric. This relation was also observed in serpentinite from Site 920 (Shipboard Scientific Party, 1995). Veins defining serpentine foliation are generally aligned parallel to the long axis of pyroxene porphyroclasts. In most instances, serpentine foliation in Site 1268 core dips <40° (Fig. F54), with the highest population of dips between 20° and 30°. Serpentinization foliation is dominantly shallow dipping (<30°) at depths above 40 mbsf (Fig. F55). No serpentine foliation was present between 40 and 60 mbsf. Serpentine foliation measured at depths below 60 mbsf is more variable and generally steeper than that measured at shallow depths in the hole.

Depth intervals with the highest-intensity serpentinization foliation are located near, but not directly correlated with, intervals with highest crystal-plastic deformation intensity. Maxima in the intensity of serpentinization foliation generally appear on the shoulders of crystal-plastic deformation intensity maxima (Fig. F56). Observations of serpentine textures at Site 920 indicated a direct correlation between the intensity of crystal-plastic deformation fabric and the strength of anastomosing serpentinization foliation (Shipboard Scientific Party, 1995). This may not be the case in Site 1268 serpentinites. Depth intervals with the highest-intensity crystal-plastic deformation in Figure F56 correspond to intervals of peridotite mylonite deformed under granulite-grade conditions that do not display anastomosing serpentinization foliation. Serpentinite with the highest observed foliation strength occurs over intervals of moderate-intensity crystal-plastic deformation. Another factor that may contribute to the lack of complete correlation between serpentine foliation strength and crystal-plastic intensity is pervasive talc alteration. The crystal-plastic deformation intensity in many talc-altered peridotite samples may be estimated from the shape and alignment of pyroxene porphyroclasts that are pseudomorphed by the alteration, whereas serpentine foliation is partially to completely obscured.

Fault Gouge Zones

Hole 1268A core contains three intervals of nonfoliated gouge/breccia that likely formed in fault zones with significant shear displacement (Fig. F57). These include an 11-cm interval in Section 209-1268A-11R-2 (Piece 8), a 23-cm interval in Section 12R-1 (Piece 15), and a 9-cm interval in Section 15R-1 (Piece 21). All three gouges are matrix-supported breccias containing clasts of serpentinized and talc-altered peridotite. The matrix of the gouges is composed dominantly of serpentine and/or talc with variable amounts of disseminated sulfides. Clasts are subrounded to angular serpentinized and talc-altered peridotites that range in size from 0.3 to 3 cm with outsize clasts as large as 15 cm. The gouges in Cores 209-1268A-11R and 12R are noncohesive, and the gouge in

F53. Ribbon texture serpentine defining anastomosing foliation, p. 109.

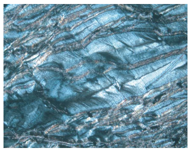

F54. Dips of anastomosing serpentine foliation, p. 110.

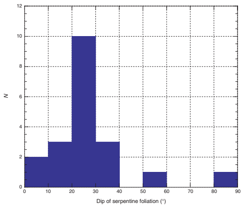

F55. Downhole dip of anastomosing serpentine foliation, p. 111.

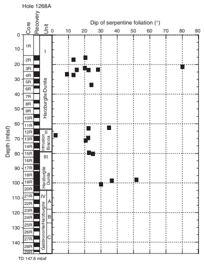

F56. Downhole serpentine foliation/crystal-plastic deformation, p. 112.

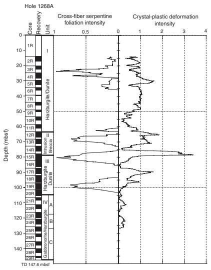

F57. Fault gouge, p. 113.

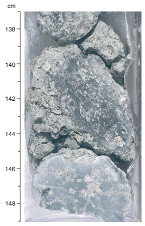

Core 15R contains zones of noncohesive and partially cohesive material. The gouge intervals in Core 209-1268A-12R occur at the lower boundary of an interval of peridotite mylonite deformed at granulite-grade conditions. The gouge in Core 209-1268A-15R is present at the lower boundary of an interval of mylonitized intrusion breccia. These gouge intervals represent the highest degree of brittle deformation at Site 1268.

Cataclastic Shear Zones

The peridotite section in Site 1268 core is cut by cataclastic shear zones that comprise densely spaced anastomosing fractures bounding small (<0.3 cm) phacoids of undeformed serpentinite (Fig. **F58**). The matrix of cataclastic breccias is composed dominantly of talc and/or serpentine with fibers parallel to the shear zone orientation. Discrete fractures in cataclasite zones are filled with fibrous serpentine and/or magnetite. Cataclastic shear zones are <3 cm wide, where visible in large core pieces, or comprise the bulk of small pebbles recovered from the core barrel. Crosscutting relations and mineralization patterns suggest that cataclastic shear zones formed during or shortly after the main phase of serpentinization. Three narrow cataclasite zones in Section 209-1268A-6R-1 (Fig. **F58**) were more resistant to pervasive talc alteration than surrounding dunite. Only eight cataclastic shear zones appear in core pieces large enough to measure orientation. Of these, there are no statistical trends in dip magnitude (Fig. **F59**), nor is there any relation between dip and curated depth (Fig. **F60**).

Small Faults and Shear Fractures

Discrete shear fractures and small-offset faults ranging 0.1–0.3 cm in thickness are present throughout much of Units I, II, and III of Hole 1268A, for example (Fig. **F61**). Crosscutting relations indicate these are the last structural features formed at this location. Where microfaults cut distinct marker horizons, the offset is generally <1 cm. In several sections of core, groups of microfaults with the same sense of motion are aligned parallel to one another to create a composite structure with greater total shear offset. Talc veins containing fibers parallel to the direction of fracture opening typically fill fractures and microfaults. In faults with >0.5-cm offset, talc veins commonly contain slickenfibers that may indicate the direction of fault slip and sense of shear. Slickenfibers indicate that normal, reverse, strike-slip, and oblique-slip motion all occurred within these structures. Measurement of the orientation of 37 such fractures was possible in Hole 1268A cores. A histogram of fracture dips (Fig. **F62**) shows that the dips of the shear fractures and small faults are highly variable with no dominant preferred orientation. A plot of dip vs. depth (Fig. **F63**) shows that shear fractures at depths above 40 mbsf all dip <40°. Shear fractures measured at depths below 60 mbsf have slightly higher and more variable dips than the fractures at shallow depths.

Brittle Deformation of Gabbro

Coarse-grained gabbro in the lower portion of Hole 1268A (Unit IV) contains several zones of minor to moderate cataclastic fracturing and incipient brecciation. These occur over intervals ranging from 1 to >50 cm thick and generally decrease in intensity and frequency downsec-

F58. Serpentinized dunite band and cataclastic shear zones, p. 114.

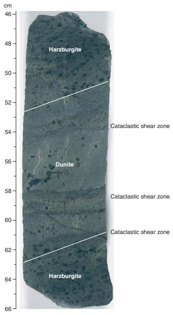

F59. Dip range of cataclastic shear zones, p. 115.

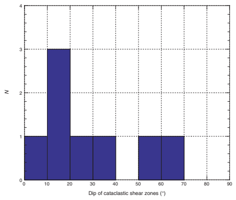

F60. Dips of cataclastic shear zones with depth, p. 116.

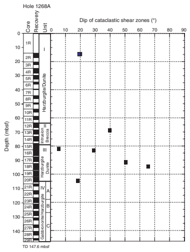

F61. Fibrous serpentine-filled fault cutting serpentine-sulfide veins, p. 117.

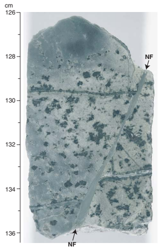

F62. Dip range of small faults and shear fractures, p. 118.

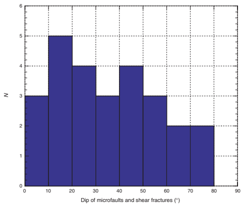

tion. The lowest-intensity brittle gabbro shear zones are composed of networks of fine fractures with small shear offset (<0.1 cm) cutting plagioclase and deflecting around pyroxenes in the gabbro. Higher-intensity brittle shearing of gabbro results in coalescing fractures that reduce plagioclase grain size but do not affect pyroxene porphyroclasts (Fig. **F64**). Unlike cataclastic shear fractures in the peridotites, fractures and breccias in Unit IV gabbros do not have any preferred orientation or create breccias with visible foliation. The relative timing of gabbro brittle deformation vs. brittle strain of overlying peridotite is not constrained by crosscutting relations in Site 1268 core.

Alteration Veins

Veins in the harzburgites and dunites range in morphology from planar and continuous to thin, irregular, discontinuous veinlets. Five distinct types of veins were measured: massive sulfide veins, talc pyrite veins, massive talc veins, serpentine veins, and chlorite veins. The relative timing of the events corresponding to these veins is complicated, and there are at least two generations of serpentine and sulfide veins. However, the observed crosscutting relationships are consistent with the following simplified sequence of events: (1) magmatic veins, (2) serpentine veins and associated serpentinization of the peridotites, (3) massive sulfide mineralization, (4) talc alteration and massive talc veins, and (5) late sulfide and serpentine veins. Evidence that the pervasive serpentinization postdates the magmatic vein event is indicated by the magmatic veins themselves, which characteristically show pale green serpentine-filled tension cracks perpendicular to their length (Figs. **F65, F66**). These cracks are a consequence of volume expansion of the host ultramafic rock relative to the magmatic vein during serpentinization and thus suggest that the magmatic veins were present within the ultramafics before serpentinization. Figure **F65** also shows that these features predate the late serpentine veining events. A detailed discussion of the mineralogy of the alteration veins can be found in **"Metamorphic Veins,"** p. 13, in "Metamorphic Petrology." We measured the intensity and orientation of veins using the intensity scale outlined in **"Fabric Intensities,"** p. 11, in "Structural Geology" in the "Explanatory Notes" chapter. The intensity of these planar features is a measure of their average frequency in a 10-cm interval.

The total intensity of alteration veining varies considerably throughout the cored interval, as shown in Figure **F67.** The intensity is uniformly greater in the peridotite units (0–105 and 117–126 mbsf) than in the gabbro units (105–117 and 126 mbsf to the bottom of the hole) and is greatest in the intrusion breccia interval (63–78 mbsf). There are two other maxima in vein intensities in the ultramafic rocks. The lower maxima occurs at the contact of the Unit III harzburgites and dunites with the Unit IV gabbros (90–100 mbsf). The increase in vein intensity at the latter can be related to the intense magmatic veining and diking within Unit III. The upper maxima occurs in the upper part of the cored interval (37–48 mbsf) and corresponds to a zone of relatively high crystal-plastic deformation intensity.

Figure **F68** shows plots of the downhole intensity for each of the five different types of veins. These plots show that sulfide veins are most concentrated in the upper 80 m of the hole and high intensities of serpentine veining occur at 48, 73, and 98 mbsf. The approximate inverse correlation of talc veins and serpentine veins is partly a consequence of the alteration of serpentine to talc in some of the peridotites.

F63. Dips of small faults and shear fractures with depth, p. 119.

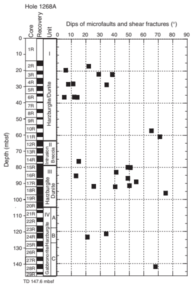

F64. Gabbro cataclasite, p. 120.

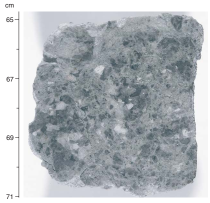

F65. Magmatic vein with serpentine-filled tension gashes, p. 121.

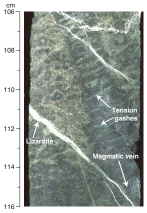

F66. Gabbroic vein with serpentine-filled tension gashes, p. 122.

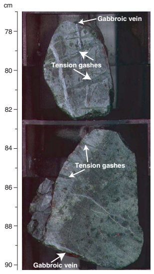

F67. Downhole metamorphic and magmatic vein intensity, p. 123.

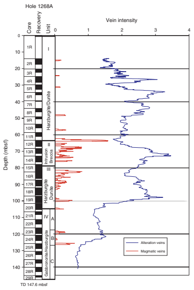

The variation of dip with depth for each of the major vein types is shown in Figure F69. A total of 125 measurements were made from all the veins that could be measured within the core reference frame. The veins exhibit a wide range of dips, showing concentrations at ~30°, 60°, and 90°. The plots for the individual vein types show that the massive sulfide and massive talc veins have similar dips, with concentrations at ~30° and 60°, whereas the serpentine veins have concentrations at ~90° and 20°–50°. The steeply dipping serpentine veins correspond to the last phase of brittle lizardite veining, which is prominent in the harzburgite dunite Unit III (Fig. F70). This steeply dipping population is significant because steeply dipping veins should be undersampled by a vertical borehole.

Crosscutting Relationships and Deformation Paths

Below, we try to assemble the pertinent crosscutting relationships in terms of time and temperature starting with the oldest features. Although the features are discussed in sequence, the structural and magmatic events they represent should be viewed as a continuum.

Dunite and Harzburgite Banding

Bands of dunite (Fig. F58) and bands with varying modal pyroxene content (Fig. F71) are parallel to the crystal-plastic foliation in the harzburgite sections. This banding is commonly subtle and is not pervasive throughout the core. Although there are a few bands with preserved contacts, several zones of dunite were recovered without preserved contact relations (see "Site 1268 Visual Core Descriptions"). Dunite banding is similar to transposed banding subparallel to tectonic foliations in ophiolite ultramafic massifs. This probably represents source heterogeneity or banding created during melting and melt transport processes. As such, the banding is the oldest recognizable structure in the harzburgites. Where contacts are observed, their parallelism with foliation suggests complete transposition into the mantle flow direction.

Early Magmatic Vein Series

There are abundant pyroxenite and gabbroic dikes or veins throughout all ultramafic sections of the core. There is a particularly high concentration of these features in the central part of the cored section. Commonly, serpentinite and talc veins follow the pyroxenite and gabbro dikes or veins and mimic their trend, creating severely altered regions in the core. Magmatic dikes or veins in Hole 1268A tend to be irregular, thickening and tapering on a small scale. Most are thin (<20 cm thick) and discontinuous on the scale of the core. The pyroxenite and gabbroic dikes or veins can be planar tabular to curviplanar sheetlike forms to highly irregular.

The pyroxenite and gabbroic veins or dikes probably represent the traces of melts that migrated along small fractures or localized porous channels. They are composed of coarse crystals and show no evidence of chilled margins. These veins vary from pyroxenite (clinopyroxenites or websterites) to gabbroic or composite veins with pyroxenitic margins and gabbroic cores. (We emphasize that these mineral compositions are inferred from alteration minerals and pseudomorphic textures.)

F68. Variation in vein intensity with depth, p. 124.

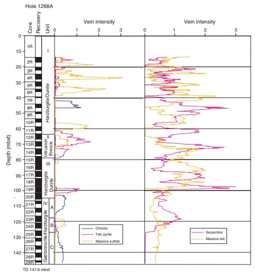

F69. Dips of alteration veins, p. 125.

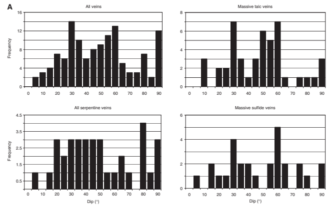

F70. Harzburgite cut by late lizardite veins, p. 127.

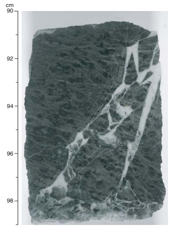

F71. Dunite banding and modal pyroxene in harzburgites, p. 128.

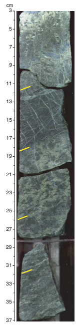

In general, these high-temperature magmatic veins or dikes are postkinematic (or undeformed) with respect to the ductile deformation events that formed foliation and banding in the harzburgite-dunite country rock. Examples of these postkinematic magmatic veins are shown in Figures **F72, F73,** and **F45.** Figure **F72** contains a pyroxenite vein obliquely cutting the crystal-plastic foliation in a porphyroclastic harzburgite; Figure **F73** shows two similar pyroxenite veins cutting the crystal-plastic foliation in porphyroclastic harzburgite, in turn cut by several serpentine-talc veins; and Figure **F45** shows longitudinal magmatic veins cutting protogranular textured harzburgite. Similar veins in the MARK area of the Mid-Atlantic Ridge were observed during Leg 153 (Shipboard Scientific Party, 1995).

F72. Porphyroclastic texture in harzburgite, p. 129.

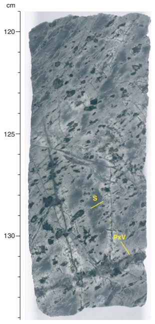

Late-Stage, High-Temperature Mylonitic Deformation

Late stage, high-strain, high-temperature deformation in localized mylonite zones is best developed in Sections 209-1268A-12R-1, 12R-2, 14R-2, 14R-3, 15R-1, and 17R-1. An example of mylonite crosscutting porphyroclastic harzburgite can be seen in Figure **F48.** The foliated mylonites contain selvages of an early pyroxenite that has been completely transposed into the foliation plane, unlike other pyroxenite and gabbroic dikes and veins. A second generation of pyroxenites crosscuts the mylonites (Figs. **F48, F49**). They are undeformed, indicating they are postkinematic with respect to high-temperature crystal-plastic deformation in each mylonite zone. The narrow pyroxenite veins are coarse grained and without chilled margins, which indicates that the mylonitic wallrock was still at a high temperature during magmatic intrusion.

F73. Pyroxenite veins cutting deformed harzburgites, p. 130.

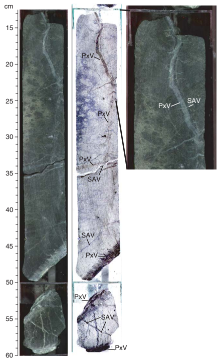

Most mylonites occur in the section containing the intrusion breccias (Fig. **F43**). Intrusion breccias showing only varying degrees of local subsolidus deformation lie above the major mylonite zone at the bottom of Core 209-1286A-14R and the top of Core 15R and continue below it down to the last major mylonite zone in Core 17R. In the underlying harzburgites, which continue down into Core 209-1268A-20R, there is little evidence of late deformation and there are only a few gabbro veins.

Continued Magmatic Veining and Larger Gabbroic Intrusions

Several lines of evidence suggest that igneous intrusive events occurred over a range of temperatures as the host peridotites cooled. For example, the postkinematic pyroxenite veins cutting the mylonites represent a younger generation than their deformed counterparts. The base of the hole is characterized by a thick section of gabbroic rocks (Unit IV) that is first encountered at the base of Unit III. Although the contact between the harzburgite and gabbro is mostly not preserved, in Section 209-1268A-20R-3 the boundary region of the core preserves a fine-grained gabbro (Piece 8) between serpentinized harzburgite (Piece 7) and coarse-grained gabbro (Piece 9). This could represent a remnant of the chilled margin of the gabbro. Coarse-grained gabbro, however, dominates Unit IV and crosscuts porphyroclastic harzburgite at the upper gabbro contact. Another contact zone is preserved in Section 209-1268A-25R-1 between Pieces 4 and 5.

The massive gabbros in Unit IV retain some of their primary phases, although they are heavily talc altered. Plagioclase contains igneous growth twins with blunt ends that are nontapering in most samples.

Pyroxene appears largely undeformed with only a few kinked grains seen in thin section. The sharp crosscutting contact at the top of Subunit IVA and the lack of internal deformation suggest that the larger gabbros postdate the high-temperature, low-strain crystal-plastic deformation in the peridotites or that peridotites were weaker than the gabbroic rocks during that deformation event. Since these gabbros are neither cut by nor crosscut zones with mylonitic deformation, the timing of their intrusion cannot be established with respect to the mylonitic deformation.

Relative Timing of Hydration, Crystal-Plastic Deformation, and Intrusion

As noted previously, the mantle and gabbroic sections sampled in Hole 1268A are pervasively altered under greenschist facies conditions (see **"Hydrothermal Alteration,"** p. 11, in "Metamorphic Petrology"). The deformation of the mantle section started to localize along mylonite zones under high-temperature crystal-plastic conditions (probably >900°C), perhaps synchronous with igneous intrusion. However, there is no involvement of low- to moderate-temperature alteration phases in the crystal-plastic deformation, and thus we infer that by the time alteration took place the crystal-plastic deformation of primary mantle phases had ceased and peridotites were brittle. Greenschist facies alteration phases commonly pseudomorph plastically deformed mantle phases and undeformed igneous phases in gabbroic rocks, indicating a static metamorphic overprint as documented in **"Metamorphic Petrology,"** p. 10.

The gabbroic rocks that intrude peridotite do not preserve high-temperature hydrous magmatic phases that would be expected if the intrusions stoped and incorporated material that was previously hydrated. Figures **F65** and **F66** show magmatic veins of pyroxenite and gabbro containing tapering cracks or tension gashes that become wider in the center of the vein and decrease in width in both directions into the surrounding olivine-rich harzburgite. This suggests that the volume expansion of the peridotites during serpentinization caused dilation in a direction parallel to the pyroxenite vein. Gabbroic veins show similar relationships throughout the core, suggesting that hydration took place after the intrusion events, consistent with the lack of chilled margins, the coarse-grained nature of the pyroxenites and gabbroic veins, and the lack of amphibolite facies metamorphism.

Brittle Deformation, Hydration, and Alteration

Strain localization in the peridotites became more intense as they passed through the brittle–ductile transition, as indicated by the presence of cataclastic shear zones, fault gouges, alteration veins, and fractures throughout the core. The first generation of brittle structures is associated with the anastomosing serpentine foliation, which is subparallel to the crystal-plastic foliation (see **"Brittle Deformation,"** p. 24). Although most serpentinization is associated with dilation crack-seal features, cataclastic shear zone and fault zones lined with serpentine slickenfibers are locally present throughout the core. These appear to be somewhat late in the deformation history. Two significant gouge zones likely represent some of the youngest structural features that formed a long shallow-level cataclastic fault zone.

Orientation of Structures

We measured a total of 75 orientations: 52 magmatic veins, 15 lithologic contacts (resulting from modal pyroxene variation from dunite to harzburgite), 2 spinel foliation planes, and 5 gabbro magmatic fabrics. There was generally no discernible magmatic fabric in the gabbros; where the measurements were taken, the fabric strength was mild and a contribution from deformation was likely. Out of the 75 measurements, 54 were on pieces with paleomagnetic declination determinations. The downhole distribution of these 75 features and corresponding dip angles are shown in Figure **F74.**

In order to plot the azimuthal distribution of magmatic features, the orientation of the individual pieces of the core were corrected to a common orientation using paleomagnetic measurements (see **"Structures in Peridotite and Gabbroic Intrusions,"** p. 8, in "Mantle Upwelling, Melt Transport, and Igneous Crustal Accretion" in the "Leg 209 Summary" chapter). The resulting data set is shown in a plot of poles to the planes in Figure **F75.** The data are identified according to quality of the paleomagnetic data, but there are no obvious inconsistencies between the higher- and lower-quality paleomagnetic data.

All data were plotted in Figure **F75B,** keyed according to nature of the magmatic feature. Also plotted in Figure **F75B** are spinel foliations measured from 8-cm^3 cubes (Fig. **F76** shows an example). A total of 20 cubes were taken from harzburgites and dunites of oriented pieces of core throughout Hole 1268A, but the harzburgites were spinel poor, so not enough spinel grains were visible to determine the foliation. The data set for lithologic contacts and spinel foliations (Fig. **F75B**), all presumably predating the magmatic veins, is relatively sparse. The average dip of magmatic veins is 59°; the average dip of lithologic contacts is 49°.

Shown in Figure **F77** are poles to crystal-plastic foliations reoriented to a common reference frame (see **"Structures in Peridotite and Gabbroic Intrusions,"** p. 8, in "Mantle Upwelling, Melt Transport, and Igneous Crustal Accretion" in the "Leg 209 Summary" chapter). This plot clearly differentiates the early high-temperature, moderate-strain porphyroclastic foliations from those produced by the lower-temperature, higher-strain localized mylonitic events. Although there are several outliers, the high-temperature porphyroclastic harzburgite foliations cluster around a pole giving an apparent strike of ~N30°E and apparent dip of 25°E in the common reference frame. Two of the four outliers lie within Core 209-1268A-4R, which also includes one foliation lying within the main cluster. The clustered porphyroclastic foliations range 8°–56° in dip. Paleomagnetic inclinations suggest a late block rotation of ~60° for the mantle peridotites at Site 1268, assuming a rotation axis striking ~20°N, parallel to the trend of the Mid-Atlantic Ridge immediately east of Site 1268 (see **"Site 1268,"** p. 15, in "Site Summaries" in the "Leg 209 Summary" chapter). Removing this rotation would bring the dominant porphyroclastic foliation plane to near vertical, subparallel to the present-day ridge orientation.

The orientations of 22 cataclasite zones, shear fracture systems, and small faults were reoriented to a common reference frame using paleomagnetic declination measurements. This analysis assumes that the time-averaged magnetic pole for this location is true north and that the hole is vertical. Results of this analysis are shown in Figure **F78,** a lower hemisphere stereo plot of poles to fractures and shear zones. A moderately strong preferred orientation exists in the rotated measurements.

F74. Downhole distribution/dip of magmatic veins and contacts, p. 131.

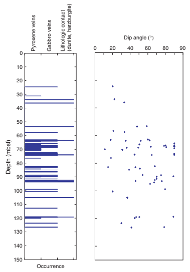

F75. Poles to planes for foliation, veins, contacts, and gabbro fabrics, p. 132.

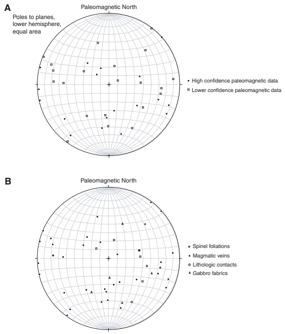

F76. Spinel foliation, p. 133.

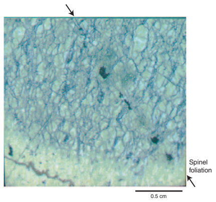

F77. Poles to crystal-plastic foliation, p. 134.

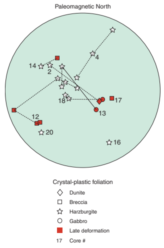

F78. Poles to cataclastic shear zones and small faults, p. 135.

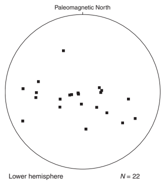

Shear zones and fractures preferentially strike north–north-northeast in the common reference frame, with dip directions varying from east to west.

The alteration veins also exhibit a variety of azimuths downhole. Figure **F79** shows the orientations of the veins restored to a common reference frame. Unfortunately, only 50% of the data set could be reoriented in this way because of the limited number of suitable paleomagnetic measurements. It should be emphasized that there is error associated with these final orientations, due to (1) the difficulty in measuring two precise orientations on the half rounds of core, (2) the uncertainties associated with the magnetic measurements, and (3) possible tectonic rotations of the recovered rocks. However, the existence of a distinct trend of poles to the brittle structures (Fig. **F78**) after reorientation implies that these errors are relatively small. This result suggests that the weak alignment of poles to the late serpentine veins and the talc pyrite veins is correct and, hence, that these veins have a preferred orientation. The scatter of the poles to the earlier massive talc and massive sulfide veins reveals that these veins formed an isotropic vein network.

F79. Poles to planes for alteration vein orientations, p. 136.

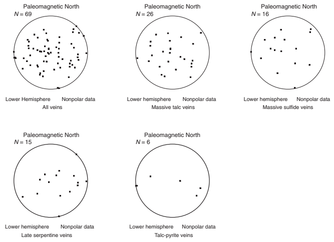

Summary

Hole 1268A provides a glimpse into a mantle section that is tectonically exposed on the seafloor. The region is unusual because extensive peridotite exposures on the western flank of the rift valley are matched by another peridotite massif on the eastern side of the rift valley. Serpentinized harzburgites and dunites, intruded by pyroxenites and gabbroic rocks, form the section cored.

Hole 1268A has a significant range of both high-temperature crystal-plastic structures and crosscutting magmatic features that formed in a retrograde metamorphic environment. These record deformation during ascent of mantle peridotites to the surface from ductile and crystal-plastic conditions, through the brittle-ductile transition, and finally into moderate- to low-temperature brittle cataclastic and fracture regimes, accompanied by intense low-temperature hydrous alteration.

The earliest deformation in the harzburgites resulted in transposition of dunite bands into a foliation plane defined by the preferred dimensional orientation of elongate orthopyroxene in porphyroclastic and weakly foliated protogranular and protointergranular textured harzburgites. At high temperatures, coarse protogranular and "protointergranular" textures formed under low deviatoric stresses, whereas the porphyroclastic textures formed under more moderate deviatoric stress conditions. High-temperature banding in the peridotites may have been near vertical to the ridge axis and was subsequently rotated about 60° along a ridge-parallel, horizontal axis after cooling of intrusive gabbros below ~570°C. Finally, the last stages of crystal-plastic deformation led to formation of localized mylonites under high deviatoric stress conditions.

Pyroxenitic and gabbroic magmatic veins increase in density in the central part of the core in the region of mylonite formation. They are dominantly postkinematic in low- to moderate-strain regions of the harzburgite section but are pre-, syn-, and postkinematic with respect to the mylonite deformation.

Magmatic intrusion probably took place prior to significant hydration of the peridotites. Large gabbro bodies and early magmatic veins in low-strain regions of the mantle without significant crystal-plastic deformation appear to have been carried to the surface along localized shear and fault zones.

Hydration of the peridotites is associated with the formation of brittle dilational and shear features, eventually allowing nearly complete alteration of the harzburgite-dunite sections. These produced a complex series of anastomosing serpentine fabrics parallel to the crystal-plastic fabric and an array of crosscutting veins.

Late cataclastic deformation and alteration in the Hole 1268A cores is localized, varying considerably downhole. Like the late mylonitization, cataclastic deformation may have followed zones of intense crystal-plastic deformation.

The reverse shear sense found in the principal mylonite zone could result from (1) local strains caused by intrusion of gabbroic rocks or (2) normal-sense mylonites that later underwent tectonic rotations. Counterclockwise rotations of up to 60° for the mantle sections have been tentatively inferred from data on magnetic azimuth and inclination of Hole 1268A gabbroic rocks (see **"Site 1268,"** p. 15, in "Site Summaries" in the "Leg 209 Summary" chapter).

GEOCHEMISTRY

We performed chemical analyses on 16 harzburgites, 4 dunites, and 7 gabbros, selected by the shipboard scientific party, using inductively coupled plasma–atomic emission spectrometry (ICP-AES) for determining major and trace element concentrations and gas chromatography for H_2O, CO_2, and sulfur. These 27 samples are representative of the highly altered material recovered from Hole 1268A (see **"Igneous and Mantle Petrology,"** p. 3, and **"Metamorphic Petrology,"** p. 10). The results for the major and trace elements are reported on a volatile-free basis for both ultramafic and mafic rocks (Table **T5**). In order to determine the optimum analysis conditions for elements at low concentration in ultramafic rocks (Ti, Al, K, Na, Sr, V, Cu, Co, Ni, Cr, Sc, Y, and Zr), the first six samples were analyzed at three different dilutions (4000-, 2000-, and 1000-fold). Although detection limits and precision for elements present in low abundance should have been improved at lower dilution factors, instrument performance and stability degraded significantly. This compromised our ability to efficiently perform high-quality shipboard measurements at the higher analyte concentrations present in the 1000-fold and 2000-fold dilutions. Maximum analytical efficiency was achieved by using shorter elemental menus for each run, operating at 4000-fold dilution, and running major and trace elements as separate analytical routines.

Peridotites

Bulk-rock analyses of peridotites from Site 1268 show that their compositions were significantly modified by hydrothermal alteration, leading to the addition of variable amounts of volatile constituents. The ultramafic rocks with predominant serpentine alteration, based on the visual core descriptions and XRD results (see **"Metamorphic Petrology,"** p. 10), display the highest loss on ignition ([LOI] = 11.8–13.1 wt%). The five ultramafic samples showing evidence for a further stage of alteration to talc display significantly lower LOI values (4.7–6.3 wt%). LOI is correlated with water content in the peridotites, with H_2O contents of 12.6–15.2 wt% where serpentine is predominant and 4.3–

7.1 wt% where talc is predominant. LOI slightly underestimates the total volatile content because of the conversion of FeO to Fe_2O_3 during heating of the sample powders to ~1000°C (see **"Geochemistry,"** p. 14, in the "Explanatory Notes" chapter).

Talc-altered rocks have CO_2 of <0.04–0.11 wt%, whereas the serpentine-altered rocks show a CO_2 range of 0.05–0.20 wt%. In the peridotites that have not been altered to talc, elevated CO_2 tends to occur in samples with elevated H_2O, leading to a positive correlation between CO_2 and H_2O. The overall scatter, however, precludes making any conclusions about the origin of CO_2 variations in these rocks. Sulfur contents in the peridotites range 1,100–16,000 ppm (Table T5). Based on our initial results, there does not seem to be a systematic covariation between sulfur and other elements.

T5. Major and trace element composition, p. 159.

Bulk rock compositions primarily reflect the proportions of minerals present. Pervasively serpentinized peridotites are composed of SiO_2 (44–50 wt%), MgO (40–45 wt%), and Fe_2O_3 (6.7–9.5 wt%). These values correspond to the compositions of serpentinites from Leg 153 Hole 920B (Dilek et al., 1997a). The Site 1268 peridotites that are altered to talc are significantly enriched in SiO_2 (60–66 wt%) and depleted in MgO (30–32 wt%) and Fe_2O_3 (3.7–8.2 wt%) relative to serpentinized peridotites at Site 1268. The composition of these five rocks approaches talc end-member compositions in SiO_2, Fe_2O_3, MgO, and H_2O (Fig. F80). Site 1268 peridotites are characterized by high and variable Mg# (molar Mg/[Mg + Fe]) (89%–94%). Although some of Site 1268 peridotites have Mg#s close to those of tectonically emplaced peridotites and abyssal peridotites (Fig. F81), others with high Mg# probably reflect depletions in iron relative to magnesium during alteration (see **"Hydrothermal Alteration,"** p. 11, in "Metamorphic Petrology" for more details about hydrothermal alteration mineralogy). Notably, all the peridotites are strongly depleted in CaO (relative to Al_2O_3), suggesting that serpentinization at Site 1268 removed almost all of the calcium that was originally present in the peridotite protolith.

F80. Fe_2O_3 MgO, and H_2O vs. SiO_2 in peridotites, p. 137.

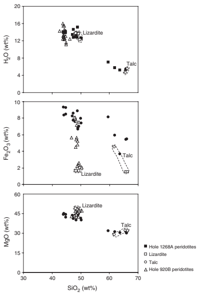

F81. FeO vs. MgO whole-rock concentrations of peridotites, p. 138.

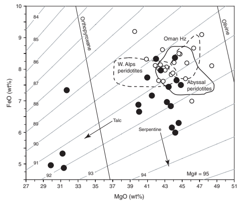

F82. Zr, Sc, and V vs. Al_2O_3 in peridotites, p. 139.

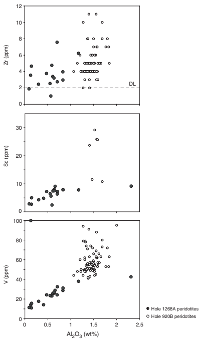

Site 1268 peridotites are depleted in trace elements that are considered to be mobile during alteration, such as Sr (<5 ppm) relative to peridotites from Leg 109 Site 670 and Leg 153 Site 920. Like calcium, these elements appear to have been leached from the peridotites during alteration. The Site 1268 peridotites are highly depleted in TiO_2 (<0.01 wt%), Y (<2 ppm), and Zr (<2–8 ppm) and, to a lesser extent, V (11–38 ppm) and Sc (<4–9 ppm) compared to other Mid-Atlantic Ridge peridotites. They display high values in Cr (1920–3850 ppm) and Ni (2200–3500 ppm). All these elements are considered to be relatively immobile during alteration (e.g., Hébert et al., 1990). Therefore, they can be used as indicators of protolith composition, although it should be noted that the talc-altered ultramafic samples have the lowest Cr (830–1100 ppm) and Ni (1750–2200 ppm) concentrations, probably indicating that leaching of some of these "immobile" elements occurs during talc alteration. V, Sc, and Cr variations and, to a lesser extent, Zr, Ti, and Y variations correlate with Al_2O_3 contents (Fig. F82). Zr, V, Sc, Ti, and Y behave as moderately incompatible elements (preferentially partitioning into the liquid during partial melting) whereas Cr and Ni behave as compatible elements. Al_2O_3 is mainly concentrated in pyroxenes and may be used as an indicator of the protolith pyroxene content. The trace element composition of Site 1268 peridotites suggests that the protolith was composed of depleted, highly refractory peridotite, except for Sample 209-1268A-13R-1, 33–37 cm. This sample has higher TiO_2 (0.22

wt%), Y (9 ppm), and Zr (50 ppm) concentrations, suggesting that this peridotite protolith had a higher pyroxene fraction and was less depleted than other peridotites from Hole 1268A, although the visual core and thin section descriptions do not show evidence of former lithologic variations in the altered peridotites at this location.

Mafic Rocks

We analyzed seven gabbro samples from Site 1268. Sample 209-1268A-16R-4, 9–13 cm, is a gabbro from Unit III (see **"Lithology and Stratigraphy,"** p. 4, in "Igneous and Mantle Petrology"), where gabbro is subordinate (9%) to harzburgite and dunite. Six additional samples were analyzed from Unit IV (104.4–147.6 mbsf), where gabbro and gabbronorite are dominant. In this latter group, the four lowermost samples are variably textured gabbronorites, one from Subunit IVA above an ultramafic portion of the core in Subunit IVB and the three others from Subunit IVC.

With the exception of two gabbros from the upper part of Unit IV (Samples 209-1286A-21R-1, 31–35 cm, and 21R-2, 21–24 cm), the analyzed gabbroic rocks from Site 1268 are relatively uniform in major and trace element contents of SiO_2 (49.9–51.4 wt%), MgO (10.5–12.7 wt%), and CaO (8–13 wt%) (Fig. **F83**). In contrast, the two upper gabbros from Unit IV have higher MgO concentrations (20.8–22.3 wt%) and Al_2O_3 contents (19–23 wt%) but lower CaO (~2 wt%). In addition, they have high water contents (11.13–13.10 wt%) and LOI values (8.80–9.30 wt%) compared to other Site 1268 gabbros. These high values are associated with their high degree of alteration, as revealed by visual core and thin section description (see **"Metamorphic Petrology,"** p. 10). Sample 209-1268A-16R-4, 9–13 cm, from Unit III appears less altered, yet it has also high water content (4.31 wt%) and LOI (3.89 wt%). H_2O in Unit IV gabbronorite reaches the lowest concentrations observed at Site 1268 (2.8–4.1 wt%). CO_2 in the gabbro shows limited variability (0.07–0.11 wt%), and there is no covariation with H_2O content. Sulfur in the gabbroic rocks from this section is below the limit of detection (~400 ppm).

F83. Cr, MgO, and LOI vs. SiO_2 in gabbroic rocks, p. 140.

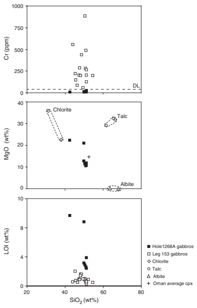

The variation in major element geochemistry can be related to the alteration observed within the gabbros of Site 1268. The two uppermost samples of Unit IV (Samples 209-1268A-21R-1, 31–35 cm, and 21R-2, 21–24 cm) have undergone alteration of plagioclase and clinopyroxene, producing significant amounts of chlorite and leading to relative increases in MgO and H_2O and a decrease CaO. Significantly, the possible removal of calcium from the gabbros during serpentinization suggests that the calcium from the ultramafic rocks is not being redistributed within the system but is almost completely removed. The remaining gabbro samples from both Units III and IV appear to be significantly less altered (see **"Metamorphic Petrology,"** p. 10), even though they have higher LOI values than the variety of gabbros recovered during Leg 153 (Fig. **F83**).

The trace element geochemistry of the Site 1268 gabbros shows that, like the peridotites, the gabbros are depleted in mobile elements such as Sr (~120 ppm). The two gabbros from the top of Unit IV that have undergone plagioclase alteration contain lower Sr (50–65 ppm) compared to all but one of the Leg 153 gabbros (100–400 ppm) (Agar et al., 1997). As discussed previously, the immobile trace elements such as Ni and Cr may still yield information about the original protolith (e.g., Hébert et al., 1990). When compared to gabbros from Leg 153, the Site 1268 gabbros are depleted in Cr (less than the detection limit) and other immobile compatible elements, illustrating that the original gabbro protolith was probably more evolved than the comparable compilation of gabbros recovered during Leg 153.

Discussion

The compositional variations in major element, trace element, and volatile contents of the Site 1268 peridotites are controlled by the style of alteration. Where visual and XRD evidence (see **"Metamorphic Petrology,"** p. 10; Table **T2**) points to serpentine as the dominant alteration phase, the serpentinized harzburgites and dunites approach the composition of a pure serpentine end-member (Fig. **F80**). Similarly, where such evidence points to the dominant presence of talc, the serpentinized harzburgites and dunites approach the composition of pure talc. In comparison to other localities where significant serpentinite has been recovered, such as Sites 670 and 920, the alteration in Hole 1268A peridotites is even more extensive. At Site 1268, all the geochemical evidence, as well as evidence from the visual core and thin section descriptions of the petrology groups (see the **"Supplementary Material"** contents list), points to a marked silica metasomatism at this locality. This style of alteration appears to be characterized by strong open-system behavior for key elements, leading to a notable loss of Ca and perhaps also Sr.

Although it is possible that rodingitization and sequestering of Ca occurred below the depth sampled at the bottom of Hole 1268A, it seems more likely that alteration led to nearly complete removal of Ca by hydrothermal fluids that were ultimately vented into the deep ocean. This is consistent with the observation that areas actively undergoing serpentinization, such as the Rainbow and Logatchev hydrothermal systems on the Mid-Atlantic Ridge, discharge hydrothermal vent fluids having the highest Ca/Cl ratios observed along the global mid-ocean-ridge system (Charlou et al., 2002; Douville et al., 2002).

Some of the gabbroic rocks at Site 1268 are also highly altered, especially the two rocks analyzed from the top of Unit IV. These two rocks may show significant Ca loss, together with possible Mg uptake, and one of them (Sample 209-1268A-21R-1, 21–24 cm) shows significant depletion in SiO_2 (down to 42.6 wt%), consistent with metasomatic alteration to chlorite. At deeper levels in the section, the extent of alteration in the gabbroic rocks is significantly lower and the rocks appear to have retained much of their original chemical composition.

The Fe_2O_3 and H_2O concentrations measured on individual samples were compared with magnetic susceptibility determined by multisensor track (MST) (see **"Magnetic Susceptibility,"** p. 37, in "Physical Properties") for the same depth level at Site 1268 (Fig. **F84**). As expected for their Fe_2O_3 concentrations of 6–8.5 wt%, the gabbroic rocks show uniformly low magnetic susceptibilities (between 32×10^{-5} and 50×10^{-5} SI) and there is no correlation with Fe_2O_3. However, there is a scattered positive correlation between Fe_2O_3 concentration and magnetic susceptibility in the peridotites. This trend is largely related to the style of alteration. The peridotites with the lowest Fe_2O_3 and H_2O contents, indicative of their pervasive alteration to talc, have the lowest magnetic susceptibilities. Some of the serpentinized ultramafic rocks with high Fe_2O_3 and H_2O have high magnetic susceptibilities. However, within this high-H_2O group, samples with the highest H_2O contents have in-

F84. Fe_2O_3 and H_2O rocks vs. magnetic susceptibility, p. 141.

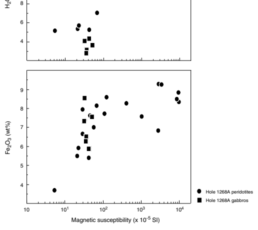

termediate Fe_2O_3 and lower magnetic susceptibilities, so a 1:1 correlation between magnetic susceptibility and any simple combination of chemical indicators appears to be absent.

The chemical composition of the Site 1268 peridotites has been almost entirely modified by pervasive alteration. Previous studies of altered peridotites from Sites 670 and 920 along the Mid-Atlantic Ridge revealed that the original protolith can potentially be characterized through bulk-rock chemistry, when elements that are relatively immobile during alteration are evaluated. The trace element composition of Site 1268 ultramafic rocks suggests that the protolith was composed of depleted and highly refractory peridotites. The low chromium contents of gabbros suggest that the original protolith was depleted in chromium and was therefore more evolved than the gabbros recovered during Leg 153.

PHYSICAL PROPERTIES

The physical properties of the peridotites and gabbros cored in Hole 1268A were characterized through a series of measurements on whole-core sections, split-core pieces, and discrete samples as described in **"Physical Properties,"** p. 18, in the "Explanatory Notes" chapter. We measured natural gamma ray (NGR) activity and magnetic susceptibility on the MST and thermal conductivity, compressional wave velocity, density, and porosity. The rock names reported in data tables correspond to the primary lithologies assigned by the igneous core description group. Most of the peridotites are highly serpentinized, and some have been pervasively altered to talc. The gabbros recovered from this site are also highly altered. The data are summarized as a function of depth in Figure **F85.**

Natural Gamma Radiation

All cores recovered during Leg 209 were measured using the NGR logger on the MST at intervals of 10 cm and a time period of 30 s. Results are output in counts per second. A few intervals in Hole 1268A appear to display natural radioactivity significantly higher than the background radiation (Fig. **F86**). The two highest peaks in the NGR data record range 15–25 cps (corrected) and are related to highly altered serpentinite and pyroxenite vein intervals in Sections 209-1268A-5R-2 and 16R-1 (Fig. **F86**).

Magnetic Susceptibility

Magnetic susceptibility is particularly sensitive to the presence of magnetite and can be used to identify iron-rich zones in the rock, such as oxide-rich gabbros and magnetite-rich serpentinized peridotites. Magnetic susceptibility values were acquired on the MST at 2.5-cm intervals for all recovered cores. High–magnetic susceptibility intervals (Fig. **F87**) correspond to serpentinized magnetite-rich, relatively massive altered harzburgites and dunites. Except for these few intervals, the magnetic susceptibility of peridotites in Hole 1268A cores is at least two orders of magnitude lower on average than that of peridotite cores recovered during previous Legs 147 and 153 (Fig. **F88**).

F85. Physical properties of peridotites and gabbros, p. 142.

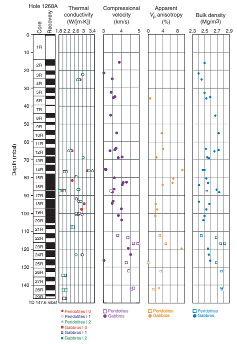

F86. NGR, p. 143.

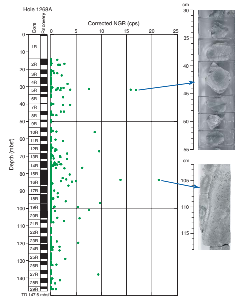

F87. MST magnetic susceptibility, p. 144.

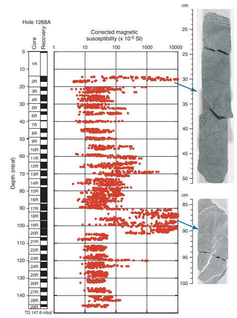

F88. Peridotite MST magnetic susceptibility, p. 145.

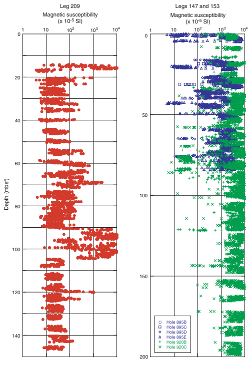

Thermal Conductivity

Thermal conductivity measurements were made at irregularly spaced intervals (Fig. **F85**). The data are summarized in Table **T6.** Thermal conductivity is a tensor property, and most known single-crystal thermal diffusivities are anisotropic (e.g., Kobayashi, 1974; Tommasi et al., 2002). We tried to evaluate the anisotropy of thermal conductivity in the measured peridotites and gabbros as described in **"Thermal Conductivity,"** p. 19, in "Physical Properties" in the "Explanatory Notes" chapter. The average thermal conductivity is 2.84 W/(m·K) in serpentinized peridotites and 2.13 W/(m·K) in gabbros. The apparent measured anisotropy ranges 0.8%–12.0%. High apparent anisotropy is found in both serpentinized peridotites and gabbros. Because of their complex structural pattern, combining one or several networks of cracks and veins and possible preferred mineral orientations, it is not easy to infer the cause of the measured anisotropy from the shipboard observations. In several samples, the thermal anisotropy is lower when the needle is aligned subparallel to the foliation (i.e., in the plane across the foliation).

T6. Thermal conductivity, p. 161.

Thermal conductivity data are shown in Figure **F89** with the measured thermal conductivities of gabbros and peridotites recovered from other ODP sites (Robinson, Von Herzen, et al., 1989; Cannat, Karson, Miller, et al., 1995; Gillis, Mével, Allan, et al., 1993; Dick, Natland, Miller, et al., 1999). The thermal conductivities of the altered peridotites from Hole 1268A range 2.30–3.51 W/(m·K) and are similar to the properties of peridotites from ODP Legs 147 and 153. Thermal conductivities in the altered gabbros from Hole 1268A range 1.84–2.52 W/(m·K). This range of values is considerably smaller than the range of thermal conductivities exhibited by the gabbros recovered from ODP sites on Atlantis Bank (Robinson, Von Herzen, et al., 1989; Dick, Natland, Miller, et al., 1999), Hess Deep (Gillis, Mével, Allan, et al., 1993), and the MARK area (Cannat, Karson, Miller, et al., 1995). Whether this reflects the different type of alteration of the gabbros from Hole 1268A, or that our data set is small, is unknown.

F89. Thermal conductivity, p. 146.

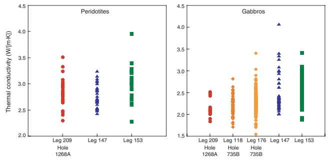

Porosity, Density, and Seismic Velocity

As noted above, we measured *P*-wave velocity, wet bulk density, and porosity on selected samples, as described in **"*P*-Wave Velocity,"** p. 20, and **"Porosity and Density,"** p. 20, in "Physical Properties" in the "Explanatory Notes" chapter. For unknown reasons, the penta-pycnometer was unable to measure the volume of some of the minicores of highly serpentinized peridotite. Therefore, some porosities and densities were estimated from 1- to 2-cm^3 chips trimmed from minicores sampled for paleomagnetic measurements. A possible explanation for this problem is that some helium is trapped in the very low permeability claylike structure of serpentine and/or talc. As a result, the pycnometer seems to be unable to equilibrate the helium pressure in the cell for sample volumes as large as the minicores (~10 cm^3). Interestingly, this problem has not been reported for previous measurements on serpentinized peridotites (Gillis, Mével, Allan, et al., 1993; Cannat, Karson, Miller, et al., 1995); it might be related to the specific type of alteration in this core. All the minicores measured in the pycnometer were samples that were logged by the metamorphic alteration shipboard description team as containing little or no talc. We encountered no problem measuring the volumes of the gabbro minicore samples.

Results are presented in Figure F85 and Tables T7 and T8. For most minicore samples, the volume was measured in the helium pycnometer, using either chips or minicores when possible (gabbros and a few peridotites), giving a direct estimate of grain density. The bulk volume of all minicores was also computed from length and diameter measurements using a caliper, giving a direct estimate of bulk density. The two methods give comparable results for bulk density, within error, but there is some difference between the grain density results. Except for one sample (Sample 209-1268A-24R-2, 90–92 cm), all grain densities derived from volumes measured in the pycnometer are higher than those calculated from the bulk volume. For the six minicores measured in the pycnometer, the difference is low (0.03–0.12 Mg/m^3). The difference is higher (0.14–0.17 Mg/m^3) for those samples for which we used chips for the pycnometer volume measurements. The grain densities estimated from dry masses and pycnometer volume measurements are probably overestimated, possibly a result of the small volume of the chips (2 cm^3 on average) and/or of the difficulties encountered in using the pycnometer to measure the volumes of highly serpentinized peridotites (see above).

T7. Minicore sample results, p. 162.

T8. Saturated “cube” sample results, p. 163.

In both altered gabbros and serpentinized peridotites, the calculated porosities are more than two times higher when using the pycnometer technique than determined using the bulk volume technique. Unlike bulk density, this difference is apparently not related to the volume of the samples or to the rock type. Therefore, it is difficult to infer the real porosities of these rocks and these estimates should be taken with extreme caution.

Aside from the minicores and cubes in which we measured velocity and density, we also determined the grain density of some powders prepared for ICP-AES analyses by measuring their dry mass and volume. The very fine grained powders were prepared as described in **“Sample Preparation,”** p. 14, in “ICP-AES Analyses of Major and Trace Elements” in “Geochemistry” in the “Explanatory Notes” chapter. The grain densities range 2.78–4.01 Mg/m^3. These densities are difficult to reconcile with the ICP-AES and XRD analyses that indicate the samples are composed of ~99% talc and/or lizardite with little or no magnetite. All densities measured this way appear to be unreasonably high in view of the composition of the samples.

We tested the procedure by using silicon carbide powders of known density (3.21 Mg/m^3) and different grain sizes (120 grit/110 µm and 600 grit/15 µm). The density measured on the coarse-grained sample agrees with the nominal density within error, whereas the density measured on the fine-grained sample is always too high (~0.1 Mg/m^3 higher than the nominal density for ~16 g of powder). This overestimation of the density seems to result from an underestimation of fine-grained powder volumes by the helium pycnometer. The reasons for this effect are unknown but are likely related to the properties of very fine grained powders.

We measured *P*-wave velocity and wet bulk density of ~8-cm^3 cube samples (Fig. F85; Table T8) and minicores that were also used for paleomagnetic measurements (Fig. F85; Table T7). Velocity was measured in three directions in each of the cube samples (Table T8) in the conventional x-, y-, z- core reference frame (see Fig. F7, p. 49, in the “Explanatory Notes” chapter; i.e., normal to the core axis and to the cut face [V_x], normal to the core axis and parallel to the cut face [V_y], and parallel to the core axis [V_z]). *P*-wave anisotropy ranges 0.0%–9.2% (mean = 3.8%).

The relationship between bulk density and *P*-wave velocity is summarized in Figure **F90.** The properties of the serpentinized peridotites are similar to the measured densities and velocities of serpentinites from the MARK area (Cannat, Karson, Miller, et al., 1995), but the gabbros from Hole 1268A have lower velocities and densities than similar rocks recovered during Leg 153. This is likely because the Hole 1268A gabbros are affected by strong hydrothermal alteration. Oceanic gabbros typically have velocities, measured at bench pressure, of >5 km/s and densities >2.5 Mg/m³. In the altered gabbros from Hole 1268A, densities range 2.44–2.82 Mg/m³ and velocities range from 3.4 to just over 4.9 km/s.

F90. Wet bulk density vs. *P*-wave velocity, p. 147.

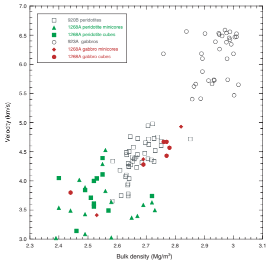

Although they were measured at bench pressure, the *P*-wave velocities in serpentinites and altered gabbros recovered from Hole 1268A have interesting implications for interpreting the seismic structure of the crust in the vicinity of the 15°20′N Fracture Zone, where serpentinites are widely exposed at the seafloor. Two unpublished seismic profiles from 16°N and 15°37′N (J. Collins and R. Detrick, pers. comm., 1998) are shown in Figure **F91.** Several other profiles are included in this figure; one is a seismic profile through "typical" oceanic crust at 9°N on the East Pacific Rise (Vera et al., 1990). Also shown are velocity-depth profiles calculated from the average *P*-wave velocities measured in oceanic gabbros from ODP Holes 735B, 894G, and 923A over a range of effective pressures appropriate to the oceanic crust (Iturrino et al., 1991, 1996; Miller and Christensen, 1997) and a set of profiles showing the variation of velocity with depth in partially serpentinized ultramafic rocks as a function of serpentinization. The latter profiles were estimated from the measured properties of ultramafic rocks reported by Christensen (1966) and Miller and Christensen (1997).

F91. *P*-wave velocity in gabbros and peridotites, p. 148.

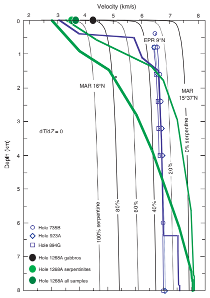

Of note is the fact that the East Pacific Rise 9°N profile is a close match to the gabbro profiles, indicating that "typical" seismic profiles are consistent with a lower crust composed of gabbroic rocks, whereas the seismic profiles from 16°N and 15°37′N do not match the gabbro profiles. Instead, these profiles show a gradual and continuous increase of velocity with depth, from ~3 km/s at the top of the crust to 8.0–8.1 km/s, velocities typical of the upper mantle at depths of 5 and 7.5 km.

Whereas the seismic profiles from 16°N and 15°37′N are not consistent with a lower crust composed of comparatively unaltered oceanic gabbros, they can be readily interpreted in terms of the measured seismic properties of partially serpentinized peridotites. At the top of the crust, the in situ seismic velocities are lower than the velocities in completely serpentinized rocks, suggesting that the uppermost 0.5–1.2 km of the crust contains large-scale fractures. This inference is consistent with both our experience of drilling at Site 1268 and with the character of the rocks, which have been heavily altered by hydrothermal circulation through a network of fractures. At comparatively shallow depths the seismic profiles reach the 100% serpentinization contour. Thereafter, the seismic profiles suggest a progressive decrease in proportion of cracks and/or the degree of serpentinization from 100% near the top of the section to fresh ultramafic rocks at depths of 5 and ~7.5 km, where the seismic profiles reach velocities characteristic of the upper mantle; the fact that both seismic profiles lie near the 0% serpentinization contour below the point where they reach ~8 km/s lends support to this interpretation. Variably altered gabbroic rocks, such as those recovered in Hole 1268A, could also form a substantial fraction of the crust, with their degree of alteration and/or their proportion relative to peridotite decreasing downhole.

The seismic properties of the rocks recovered from Hole 1268A are consistent with this interpretation. The average *P*-wave velocity in the 38 samples measured is 3.84 ± 0.08 km/s. The mean for the 30 serpentinites is 3.69 ± 0.07 km/s, and the mean for the 8 altered gabbros is 4.35 ± 0.16 km/s. These averages are shown in Figure F90, where we note that the average for the whole data set and the average for the serpentinites lie on or near the 100% serpentinization contour, whereas the mean for the gabbros is significantly higher. These observations have two important implications for the interpretation of the seismic profiles. One is that the seismic properties of the rocks recovered from Hole 1268A are arguably consistent with the seismic structure of the crust. The other is that the seismic velocities near the seafloor are consistent with a crust composed of serpentinized peridotite with a small proportion (up to 25%) of altered gabbros.

PALEOMAGNETISM

Continuous Measurements

Susceptibility

Susceptibility data from the whole cores provides important information on the content of iron-titanium oxides in the mafic and ultramafic rocks recovered from Site 1268. Magnetite has a volume susceptibility (κ) of ~3 SI (Heider et al., 1996), which is one to three orders of magnitude higher than other ferrimagnetic minerals likely to occur in gabbroic and ultramafic rocks (e.g., pyrrhotite, hematite, and ilmenite). Iron-bearing silicate minerals will also contribute to the susceptibility signal. This paramagnetic contribution is well approximated by the total iron content (1 wt% FeO corresponds to $\kappa \approx 6 \times 10^{-5}$ SI) (Collinson, 1983). Thus, whole-core susceptibilities higher than $\sim 50 \times 10^{-5}$ SI (corresponding to the highest measured FeO content of ~9 wt%) primarily reflect the concentration of magnetite and may be used as a semiquantitative estimate of its abundance.

Susceptibility was measured at 2.5-cm intervals with a Bartington MS2C sensor (coil diameter = 80 mm) on the MST (see "Magnetic Susceptibility," p. 37, in "Physical Properties"). Two possible complications in the interpretation of the susceptibility data should be mentioned. First, the susceptibility data from the MST ($\times 10^{-5}$ SI) represent the volume susceptibility for a whole core with a diameter of 6.6 cm. The diameter of cores from Site 1268 is invariably smaller (typically ~5.5–6.0 cm), and thus the true susceptibility will be underestimated by as much as 40%. In addition, readings from the Bartington sensor of >0.1 SI are clipped, so that the most significant digit of the susceptibility value is not recorded. Because this clipping effect has been noted for some core pieces, care should be taken when interpreting the width of individual high-susceptibility zones as well as in the calculation of average susceptibility or magnetite content.

Despite these complications, the susceptibility data from Site 1268 (Fig. F92) reveal large variations in magnetite content that are correlated to lithology and type/degree of alteration. Gabbroic rocks and peridotites that have experienced talc alteration typically have susceptibilities $<100 \times 10^{-5}$ SI, indicating that only trace amounts of magnetite

F92. Long-core magnetic measurements, p. 149.

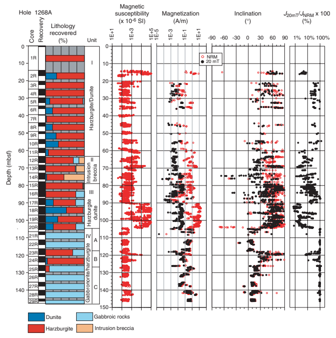

(~0.1%–0.2%) are present in addition to the contribution from paramagnetic silicates. In contrast, serpentinized peridotites from the top of lithologic Unit I and the lower part of lithologic Unit III (see **"Lithology and Stratigraphy,"** p. 4, "Igneous and Mantle Petrology") have susceptibility values near and occasionally above 0.1 SI. These values reflect magnetite concentrations of ~3%.

Remanent Magnetization

The natural remanent magnetization (NRM) intensity of archive halves spans four orders of magnitude (Fig. **F92**) (0.001–10 A/m). The general pattern of NRM intensity shows a clear positive correlation with the whole-core magnetic susceptibility. Gabbroic rocks from the lower one-third of Hole 1268A (115 mbsf to the bottom of the hole) have NRM intensities in the range of 0.01–1.0 A/m. The overlying peridotite sequence (90–104 mbsf) has a distinct NRM signature, with intensities of up to 15 A/m. Some peridotites with lower susceptibility values, presumably reflecting talc alteration, have NRM intensities similar to those of the gabbros. The inclinations of the NRM also show a similar covariance with rock type. Gabbros have distinct shallow inclinations (typically 10°–20°), whereas peridotites have very steep positive inclinations prior to demagnetization. This difference is most readily attributed to a downward-directed drilling-induced magnetization that overprinted the remanence to a variable degree as a function of the magnetic stability of the different rocks. This substantial drilling overprint precludes obtaining any reliable estimate of the in situ magnetization intensity of most of the peridotites.

All archive halves were subjected to stepwise alternating-field (AF) demagnetization in an effort to isolate the characteristic remanence (ChRM) direction. Demagnetization was typically carried out up to 80 mT, the maximum field available for long-core measurements. A treatment of 20–30 mT removes much of the low-stability (presumably drilling related) overprint in the peridotites. However, this low-stability component usually represents more than half, and commonly >90%, of the remanence (Fig. **F92**). For example, dunites from lithologic Unit III have ~1% remanence remaining at 20 mT and ~0.1% after treatment at 60 mT. In contrast, the remanence of the gabbros was very stable, with >50% of NRM remaining after 80-mT demagnetization.

The overall effectiveness of AF cleaning in recovering the ChRM direction for the archive halves can be evaluated in Figure **F92,** where remanent inclinations are plotted at the NRM and the 20-mT demagnetization steps. Gabbros (primarily in lithologic Subunits IVA and IVC; see **"Lithology and Stratigraphy,"** p. 4, in "Igneous and Mantle Petrology") show only minor directional changes as a result of their high magnetic stability and cluster at shallow positive inclinations (10°–20°). Peridotites show more scattered inclinations as a result of the varying degrees of the low-stability overprint. The ratio of the remanence remaining at 20 mT to the original NRM intensity ($[J_{20\mathrm{mT}}/J_{\mathrm{NRM}}] \times 100$) provides a measure of the likely significance of the remanence direction at the highest field steps. Directions representing less than ~10% of the initial remanence should be interpreted with caution. For samples with $J_{20\mathrm{mT}}/J_{\mathrm{NRM}} > 10\%$ (solid circles in right panel of Fig. **F92**), the inclination after 20-mT treatment is highly variable (–70° to +90°) but includes some values closer to the expected time-averaged normal polarity direction (000°/28°) at the site (e.g., lithologic Unit II and base of Unit I). This suggests that a geologically significant direction may have been isolated for these samples. In other intervals, particularly in the lower portion of Unit III, inclinations remain steep throughout demagnetization and the remanence apparently consists almost entirely of a drilling-induced magnetization. AF demagnetization of discrete samples was typically more successful in isolating a ChRM direction. This difference in demagnetization behavior as well as some other complicating factors in interpreting the archive-half data are discussed below.

The characteristic inclinations in the gabbros are significantly different from the expected inclinations of the geocentric axial dipole at this latitude (28°). With the exception of three pieces (Sections 209-1268A-22R-2 [Piece 5], 27R-2 [Piece 14], and 28R-1 [Piece 10]), all gabbroic samples yield shallow positive inclinations suggestive of normal polarity. The three pieces noted above were reexamined and their remanence directions remeasured. All three pieces preserved red markings on the piece bottom and only one (Section 209-1268A-28R-1 [Piece 10]) was found to have been measured in an inverted position. The remaining two pieces apparently were archived and measured in the proper orientation.

Discrete Sample Measurements

Stepwise AF (45 samples) and thermal (5 samples) demagnetization of discrete samples (Table T9) was carried out in order to provide accurate directional information for tectonic restoration and core orientation purposes. Figure F93 illustrates the characteristic demagnetization behavior of gabbros and peridotites. The majority of peridotites exhibit a low-stability (drilling) component of variable amplitude. In contrast to observations on long-core measurements, AF demagnetization at relatively low fields (<15 mT and often lower) (e.g., Fig. F93A, F93B) was sufficient to remove this low-stability component. A small number of peridotites have no appreciable low-stability overprint (e.g., Fig. F93C). The gabbroic samples yielded stable single-component trends with no signal of drilling overprint (Fig. F93D, F93E).

T9. Discrete sample data, p. 164.

F93. Demagnetization of discrete samples, p. 150.

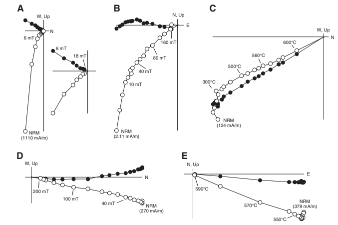

The median destructive field (MDF; the AF treatment necessary to reduce the remanence to 50% of its initial value) provides an estimate of the stability of the remanence. Because many samples have multiple remanence components, the remanence decay (and MDF) is calculated from the sum of the vector differences between successive treatment steps. Gabbroic samples have uniformly high MDF values (78–97 mT) (Fig. F94A). Peridotite samples have a broad range of MDF values. Nearly half have MDF values <5 mT. Much higher values (up to 140 mT) are apparently associated with higher degrees of talc alteration. Four of the five samples with MDF > 70 mT have a talc alteration index of 1.5 or 2.0 (see **"Metamorphic Petrology,"** p. 10), although there is a considerable range of MDF values at a given talc alteration level.

F94. MDF and NRM unblocking temperatures, p. 151.

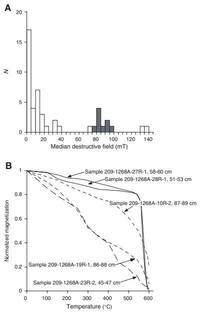

Thermal treatment in both types of rock yields directional results that agree with AF data. Maximum unblocking temperatures range between 570° and 590°C, typical of magnetite (possibly maghemite). Two gabbroic samples have discrete high unblocking temperatures (Fig. F94B). Together with the high stability to AF, these data suggest that the remanence in the gabbros is carried by very fine (submicron) magnetite. Peridotite samples exhibit either distributed unblocking temperatures, consistent with the presence of a range of magnetic grain sizes, or discrete unblocking temperature spectra similar to the gabbroic samples. This latter type of behavior appears to be related to higher degrees of talc alteration.

Results from the discrete samples corroborate the difference in inclination between gabbroic and ultramafic rocks at Site 1268. All but two samples yielded reliable results, as shown in Table **T9.** Using the method of McFadden and Reid (1982) for azimuthally unoriented cores, the average inclination for the gabbroic samples is 15° (+7°/–8° asymmetric 95% confidence limits; κ = 39.4; N = 11). The average inclination for the serpentinized peridotite samples (40° +5°/–9°; κ = 12.4; N = 38) is significantly steeper.

Anisotropy of Magnetic Susceptibility

The anisotropy of magnetic susceptibility was measured on all minicore samples with the Kappabridge KLY-2 using the standard 15-position measuring scheme (Table **T10**). The degree of anisotropy (P, where P = maximum/minimum eigenvalue of the susceptibility tensor) ranges 1.02–1.40. The higher degrees of anisotropy correspond to samples of peridotites with a lower talc alteration index. In these cases the magnetic fabric has a marked foliation. Samples subject to talc alteration have low degrees of anisotropy, similar to those of the gabbros. However, this may simply reflect the combined effect of the low bulk susceptibility of the talc-altered samples and the higher level of noise of these measurements compared to shore-based laboratory environments.

T10. Anisotropy of magnetic susceptibility, p. 165.

Comparison of Discrete Sample and Whole-Core Directions

Although comparison of the archive-half and discrete sample data shows general agreement, some significant discrepancies were observed. We regard the discrete sample demagnetization data as more accurate for the following reasons:

1. With the exception of five samples that were measured using the Molspin spinner magnetometer, all of the discrete samples were measured in three positions such that each component of the remanence was measured by all three superconducting quantum interference device (SQUID) sensors. This procedure ameliorates any systematic bias from the discrete sample holder in the 2G magnetometer.
2. Each sample was subjected to double demagnetization (in the DTech D-2000 AF demagnetizer) at fields >30 mT to average any bias field in the demagnetizing coil.
3. The off-line demagnetizer allowed more complete demagnetization to maximum fields of 200 mT. More than 90% of the discrete samples have demagnetization trajectories that trend to the origin, suggesting that these procedures were effective.

Long-core continuous AF demagnetization revealed some features, such as demagnetization trends not directed toward the origin or steep inclinations at high demagnetization AF fields, that were not common in off-line AF treatment of discrete samples. In a few cases, extreme directional changes at a centimeter scale led to apparent polarity reversals and multicomponent remanence. For example, Section 209-1268A-21R-1 (Piece 1) showed directional changes from shallow, northerly directions at the top of the piece to nearly antipodal directions at the base of the piece (Fig. **F95A**). Because adjacent pieces might influence the mag-

F95. Apparent reversal transition due to remanent intensity, p. 152.

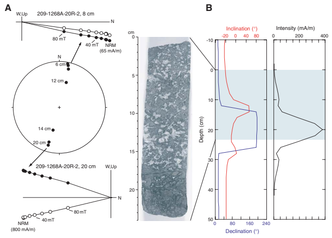

netic data, this piece was remeasured alone and header and trailer data were also recorded. The same trends in direction are seen as in the routine archive-half measurements, indicating that there was little influence from the adjacent core pieces. A transition from north to south is observed at 12 cm, with an associated increase in inclination (Fig. **F95A**). However, a nearly identical transition from south to north is observed at 29 cm, where no core material is present. These directional changes may be attributed to the order of magnitude higher magnetization of the pyroxene-rich lower 6 cm of the piece. The response functions of the x- and y-SQUID sensors have negative sidelobes that are ~15% of the peak response. When the high-magnetization material lies within these sidelobes of the response function, spurious directional and intensity data are produced. This effect is most serious when the magnetization varies by an order of magnitude over few centimeters, but all the archive-half directional data will be affected to varying degrees by intensity changes. The effects of neighboring pieces with different magnetization directions have been linked to the presence of spurious multicomponent magnetizations in the archive-half data. Finally, measurement of half cores rather than whole cores is expected to introduce a further bias into the continuous measurements (Parker and Gee, 2002).

Given the potential complications with the archive-half data, we do not necessarily expect close agreement between the continuous and discrete data. Nonetheless, careful piece-by-piece examination of the archive-half data in many cases is very similar to the discrete sample measurements (Tables **T9, T11**). Because half cores were demagnetized at five to eight different peak fields, vector endpoint diagrams could be used to assess the quality of the data. Principal component directions were calculated for the centers of apparently homogeneously magnetized core pieces. Directions were calculated only for pieces where the low-stability drilling overprint was absent (talc-altered samples or gabbros) or could be mostly removed. The resulting principal components typically represent 10%–30% of the NRM for ultramafic samples and 50%–100% for talc-altered samples or gabbros (Table **T11**). These data may be combined with the discrete sample directions to give orientations for ~150 pieces.

T11. Piece orientations, p. 166.

Discussion

The paleomagnetic directions estimated from discrete samples indicate significant differences between the inclination of the gabbroic and peridotite samples. Whereas the latter could be consistent with the time-averaged geomagnetic field (expected inclination = 28°), the remanent inclination in the gabbros is significantly shallower (15°). One possible explanation is that the gabbroic rocks do not average secular variation and therefore do not necessarily have an inclination corresponding to that expected from a geocentric axial dipole. However, the range of inclinations (6°–36°) is larger than would be expected solely from orientation errors, suggesting that the remanence directions from the gabbros likely represent some degree of time averaging.

Evaluating whether a particular paleomagnetic data set has adequately averaged secular variation is a key element for subsequent tectonic interpretation of the mean remanence directions. This assessment involves comparing the dispersion of the paleomagnetic directions with the expected dispersion at the site from models of paleosecular variation (e.g., Butler, 1992). For this analysis to be valid, each paleomagnetic direction should represent an independent sampling of the field;

various criteria have been used to identify such independent estimates (e.g., baked sediments between lava flows and grouping adjacent stratigraphic samples with statistically indistinguishable directions). For the gabbro samples from Site 1268, the number of independent samples of the field is uncertain. Comparison of the within-site dispersion at Site 1268 with that recorded by the ~1500-m gabbroic section from Hole 735B (Shipboard Scientific Party, 1999), which might reasonably be expected to have recorded a substantial duration of secular variation, provides a qualitative indication of the possible time averaging at Site 1268. For Hole 735B the observed directional dispersion parameter (κ = 59; N = 339; each sample is assumed to be an independent sampling of the field) is 1.6 times the dispersion expected for the site (κ = 37). For this analysis, we have used the paleosecular variation model of McFadden et al. (1991) and calculated the expected dispersion as the average of the dispersions assuming either virtual geomagnetic poles or site directions are Fisher distributed (Cox, 1970). For the gabbros from Site 1268, the observed dispersion parameter is 39.4 and the expected value is 25, yielding an identical ratio (1.6) as that for Hole 735B. This analysis does not prove that secular variation has been adequately averaged at Site 1268 (both sites have less dispersion, i.e., higher κ values, than predicted) but does show that the amount of dispersion is comparable to a larger gabbroic section that could be composed of many intrusions (Dick et al., 2000).

If it is assumed that the geomagnetic secular variation has been adequately averaged upon cooling of the gabbros, this suggests that the rocks were tilted after cooling. Restoration of the rocks to their pretilt position has, however, no unique solution. Unless other independent information on core orientation is available, the indeterminate azimuth of cores precludes an estimation of the strike of the rotation axis along which tilting was produced. Because block rotations might reasonably be expected to occur about approximately ridge-parallel rotation axes, the angle between the rotation axis and the paleomagnetic reference direction (360°/28°) will be small (~30°). The amount of block rotation required to untilt the observed paleomagnetic vector to the reference value, therefore, will strongly vary depending on the trend and plunge of the rotation axis (see **“Orientation of Structures,”** p. 31, in “Structural Geology”).

The mean inclination observed in the peridotites (40° +5°/–9°) is statistically distinct from the expected dipole inclination at the site. However, the steeper mean inclination may in part reflect the effect of the drilling component that partially overlaps the characteristic remanence. Indeed, the most talc-altered ultramafic samples (talc index = 2) (see **“Metamorphic Petrology,”** p. 10) have smaller drilling overprints and a mean inclination (36° +12°/–14°; N = 9) that is statistically indistinguishable from the dipole value at the 95% confidence level. Although the number of samples is small, the higher magnetic stability and smaller drilling overprint in these talc-altered peridotites suggests that they may provide a more accurate estimate of the characteristic magnetization. The mean inclination of the talc-altered peridotites does not require rotation since the magnetization of the peridotites was acquired, which in these rocks is most likely related to hydrothermal alteration and serpentinization. The remanence of the gabbros might reflect tectonic rotations at temperatures below the dominant unblocking temperature of 550°–580°C. Thus, if the alteration responsible for the remanence of the ultramafics postdates this rotation event, the alteration process must have taken place later than the intrusion of the gabbros and at a lower temperature.

MICROBIOLOGY

Solid Sample

Sample 209-1268A-2R-1 (Piece 7B, 38–47 cm)

At Site 1268 one rock interval (Sample 209-1268A-2R-1 [Piece 7B, 38–47 cm]) was collected to characterize the microbial community inhabiting this environment. The sample is a dunite that has been serpentinized and subsequently altered to talc along talc-oxide-sulfide veins.

The outer surface was quickly flamed with a propane torch, which is a simple and fast sterilization method to minimize drilling-induced and handling contamination of the outer sample surface. The speed of the sterilization technique helped minimize the time (~20 min) the rock sample was exposed to oxygen. After sterilization, enrichment cultures, samples for deoxyribonucleic acid (DNA) analysis, total organic carbon analysis, and scanning electron microscope studies were prepared as described in **"Igneous Rocks,"** p. 24, in "Microbiology" in the "Explanatory Notes" chapter.

Two methods were used to examine the type and extent of contamination caused by drill fluids that penetrated the interior of the rock sample used for microbial studies, perfluorocarbon tracer (PFT) and fluorescent microspheres. Both methods were deployed and analyzed as described in **"Contamination Tests,"** p. 26, in "Microbiology" in the "Explanatory Notes" chapter. The results of the perfluorocarbon tracer analyses confirm the delivery of PFT to the cores. Samples taken from the interior show the presence of PFT but at levels one to two orders of magnitude less than on the exterior of cores. The amount of PFT reported for the interior pieces is at or slightly above values reported for blanks analyzed at other sites during Leg 209 (Table T12; Fig. F96). The rock sample was rinsed in nanopure water, and the collected water was filtered and examined under a fluorescence microscope. An interior piece of the sample and a thin section were both examined under a fluorescence microscope to detect microsphere penetration. The fluorescent microsphere results showed that the microspheres reached the exterior of Piece 7B but did not penetrate to the interior of the core (Table T13).

T12. PFT contamination, p. 168.

F96. PFT standard and samples, p. 153.

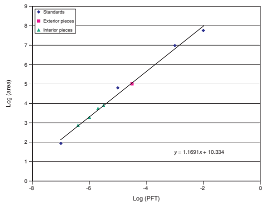

Seawater and Water Samples and Atmospheric Data

Aliquots of surface and bottom water samples were collected and prepared for DNA analysis and direct counts (Table T14) as described in **"Seawater and Water Samples,"** p. 26, in "Microbiology" in the "Explanatory Notes" chapter.

Table T15 is a summary of atmospheric and surface water data for the period of 22–28 May 2003. Data were obtained in order to investigate the relationship of atmospheric microbial transport and nutrient loading of the water column to atmospheric dust impacting the sample sites. For surface water direct count data, 1 mL of water was stained as described in **"Microbiology,"** p. 24, in the "Explanatory Notes" chapter. One milliliter of funnel rinse water was used as a control. Salinity,

T13. Fluorescent microspheres contamination, p. 169.

T14. Bacteria and viruses in a bottom water sample, p. 170.

T15. Surface water and atmospheric microbiology results, p. 171.

temperature, and pH values for all surface water values varied; salinity ranged 36.0–36.5 psu, temperature 25.5–25.8°C, and pH 7.95–7.96. Surface water samples were collected between 1302 and 1356 hr. Air samples were collected for culture-based studies between 0630 and 0800 hr. Air sample volumes were 112–135 L per sample (two samples were taken). Microbial growth (colony forming units) was for the total volume at 48 and 96 hr of incubation (Table **T15**). Air temperatures, humidity, wind speed, and wind direction ranged 25.1°–27.3°C, 68.1%–81.8%, 5.1–8.2 m/s, and 82°–113°, respectively. Samples for shore-based analysis of bacterial community DNA and bacteria and viral direct counts were collected daily and stored according to protocol.

DOWNHOLE MEASUREMENTS

Temperature Measurements

On 23 May, the WSTP was lowered to a depth of ~3016 mbrf, or 2 m above seafloor, for a 38-min station before drilling operations began in Hole 1268A (Fig. **F97A**). A temperature-time-series of ocean bottom water and a water sample were obtained for microbiology studies (see **"Seawater and Water Samples and Atmospheric Data,"** p. 47, in "Microbiology"). The temperature-time series shows a gradual increase for ~8 min before the water-sampling valve opened, followed by a 2-min period with no sampling of temperature data, one stationary temperature reading, another 2-min interval with no temperature readings while the water-sampling valve was closing, and a 9-min period before the tool began its ascent to the rig floor (Fig. **F97B**).

F97. WSTP temperature results, p. 154.

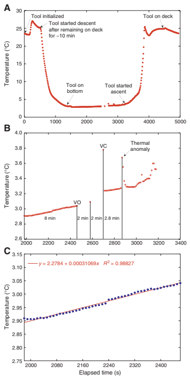

The ocean bottom water temperature increased from 2.91° to 3.04°C, or a rate of ~0.0003°C/s over the 8-min time interval before the water-sampling valve was opened (Fig. **F97C**). These temperatures are consistently higher than 2.81°C, which was recorded with the concentration/temperature/depth probe between 3012 and 3019 mbsl by the Shinkai 6500 submersible during Dive 427 in the same area in 1998 (P. Kelemen, pers. comm., 2003). Either tool drift or a steady warming of the bottom water may have caused this increase in temperature. The highest temperature was recorded after the water-sampling valve closed and the tool resumed recording temperatures (Fig. **F97B**). Bench tests during Leg 209 showed a temperature increase after the valve was closed. Hence, this anomalous point is probably related to heating due to the added voltage needed to close the valve. The high value was 3.78°C, or 0.69°C higher than the previous temperature reading. A temperature anomaly was also recorded during a 2.8-min period after the valve closed, when values increased from 3.28° to 3.68°C (Fig. **F97B**). This anomaly may have been caused by (1) tool malfunction, (2) frictional heating caused by inadvertent contact with the seafloor or the drill pipe because of heave conditions, or (3) slightly warmer fluids emanating from the seafloor.

REFERENCES

Agar, S.M., Casey, J.F., and Kempton, P.D., 1997. Textural, geochemical, and isotopic variations in gabbroic shear zones from the MARK area. *In* Karson, J.A., Cannat, M., Miller, D.J., and Elthon, D. (Eds.), *Proc. ODP, Sci. Results,* 153: College Station, TX (Ocean Drilling Program), 99–121.

Allen, D.E., and Seyfried, W.E., Jr., 2003. Compositional controls on vent fluids from ultramafic-hosted hydrothermal systems at mid-ocean ridges: an experimental study at 400°C, 500 bars. *Geochim. Cosmochim. Acta,* 67:1531–1542.

Alt, J.C., and Shanks, W.C., III, 1998. Sulfur in serpentinized oceanic peridotites: serpentinization processes and microbial sulfate reduction. *J. Geophys. Res., [Solid Earth],* 103:9917–9929.

————, III., 2003. Serpentinization of abyssal peridotites from the MARK area, Mid-Atlantic Ridge: sulfur geochemistry and reaction modeling. *Geochim. Cosmochim. Acta,* 67:641–653.

Bideau, D., Hebert, R., Hekinian, R., and Cannat, M., 1991. Metamorphism of deep-seated rocks from the Garrett ultrafast transform (East Pacific Rise near 13°25′S). *J. Geophys. Res.,* 96:10079–10099.

Blusztajn, J., and Hart, S.R., 1996. Sr and O isotopic ratios of aragonite veins from Site 895. *In* Mével, C., Gillis, K.M., Allan, J.F., and Meyer, P.S. (Eds.), *Proc. ODP, Sci. Results,* 147: College Station, TX (Ocean Drilling Program), 311–313.

Bodinier, J.-L., 1988. Geochemistry and petrogenesis of the Lanzo peridotite body, Western Alps., *Tectonophysics,* 149:67–88.

Butler, R.F., 1992. *Paleomagnetism: Magnetic Domains to Geologic Terranes:* Boston (Blackwell).

Cannat, M., Karson, J.A., Miller, D.J., et al., 1995. *Proc. ODP, Init. Repts.,* 153: College Station, TX (Ocean Drilling Program).

Casey, J.F., 1997. Comparison of major- and trace-element geochemistry of abyssal peridotites and mafic plutonic rocks with basalts from the MARK region of the Mid-Atlantic Ridge. *In* Karson, J.A., Cannat, M., Miller, D.J., and Elthon, D. (Eds.), *Proc. ODP, Sci. Results,* 153: College Station, TX (Ocean Drilling Program), 181–241.

Charlou, J.-L., Donval, J.-P., Fouquet, Y., Jean-Baptiste, P., and Holm, N., 2002. Geochemistry of high H_2 and CH_4 vent fluids issuing from ultramafic rocks at the Rainbow hydrothermal field (36°14′N, MAR). *Chem. Geol.,* 19:345–359.

Christensen, N.I., 1966. Elasticity of ultrabasic rocks. *J. Geophys. Res.,* 71:5921–5931.

Collinson, D.W., 1983. *Methods in Rock Magnetism and Palaeomagnetism: Techniques and Instrumentation:* London (Chapman and Hall).

Cox, A., 1970. Latitude dependence of the angular dispersion of the geomagnetic field. *Geophys. J. R. Astron. Soc.,* 20:253–269.

Deer, W.A., Howie, R.A., and Zussman, J., 1992. *An Introduction to the Rock-Forming Minerals* (2nd ed.): Harlow, United Kingdom (Longman Scientific Technical).

Dick, H.J.B., 1977. Partial melting in the Josephine peridotite, I. The effect of mineral composition and its consequence for geobarometry and geothermometry. *Am. J. Sci.,* 277:801–832.

————, 1989. Abyssal peridotites, very slow spreading ridges and ocean ridge magmatism. *In* Saunders, A.D., and Norry, M.J. (Eds.), *Magmatism in the Ocean Basins.* Spec. Publ.—Geol. Soc. London, 42:71–105.

Dick, H.J.B., Natland, J.H., Alt, J.C., Bach, W., Bideau, D., Gee, J.S., Haggas, S., Hertogen, J.G.H., Hirth, G., Holm, P.M., Ildefonse, B., Iturrino, G.J., John, B.E., Kelley, D.S., Kikawa, E., Kingdon, A., LeRoux, P.J., Maeda, J., Meyer, P.S., Miller, D.J., Naslund, H.R., Niu, Y.-L., Robinson, P.T., Snow, J., Stephen, R.A., Trimby, P.W., Worm, H.-U., and Yoshinobu, A., 2000. A long in situ section of the lower ocean crust: results of ODP Leg 176 drilling at the Southwest Indian Ridge. *Earth Planet. Sci. Lett.,* 179:31–51.

Dick, H.J.B., Natland, J.H., Miller, D.J., et al., 1999. *Proc. ODP, Init. Repts.,*176 [CD-ROM]. Available from: Ocean Drilling Program, Texas A&M University, College Station, TX 77845-9547, U.S.A.

Dickey, J.S., Jr., 1976. A hypothesis of origin for podiform chromite deposits. *Geochim. Cosmochim. Acta,* 39:1061–1074.

Dickey, J.S., Jr., Yoder, H.S., Jr., and Schairer, J.F., 1971. Incongruent melting of chromian diopside and the origin of podiform chromite deposits. *Geol. Soc. Am., Abstr.,* 3:543–544.

Dilek, Y., Coulton, A., and Hurst, S.D., 1997a. Serpentinization and hydrothermal veining in peridotites at Site 920 in the MARK area. *In* Karson, J.A., Cannat, M., Miller, D.J., and Elthon, D. (Eds.), *Proc. ODP, Sci. Results,* 153: College Station, TX (Ocean Drilling Program), 35–59.

Dilek, Y., Kempton, P.D., Thy, P., Hurst, S.D., Whitney, D., and Kelley, D.S., 1997b. Structure and petrology of hydrothermal veins in gabbroic rocks from Sites 921 to 924, MARK area (Leg 153): alteration history of slow-spread lower oceanic crust. *In* Karson, J.A., Cannat, M., Miller, D.J., and Elthon, D. (Eds.), *Proc. ODP, Sci. Results,* 153: College Station, TX (Ocean Drilling Program), 155–178.

Douville, E., Charlou, J.L., Oelkers, E.H., Bienvenu, P., Jove-Colon, C.F., Donval, J.P., Fouquet, Y., Prieur, D., and Appriou, P., 2002. The Rainbow vent fluids (36°14′N, MAR): the influence of ultramafic rocks and phase separation on trace metal content in Mid-Atlantic Ridge hydrothermal fluids. *Chem. Geol.,* 184:37–48.

Escartin, J., Hirth, G., and Evans, B., 1997a. Effects of serpentinization on the lithospheric strength and the style of normal faulting at slow-spreading ridges. *Earth Planet. Sci. Lett.,* 151:181–189.

————, 1997b. Nondilatant brittle deformation of serpentinites: implications for Mohr-Coulomb theory and the strength of faults. *J. Geophys. Res.,* 102:2897–2913.

Frost, B.R., 1985. On the stability of sulfides, oxides, and native metals in serpentine. *J. Petrol.,* 26:31–63.

Früh-Green, G.L., Plas, A., and Dell' Angelo, L.N., 1996. Mineralogic and stable isotope record of polyphase alteration of upper crustal gabbros of the East Pacific Rise (Hess Deep, Site 984). *In* Mével, C., Gillis, K.M., Allan, J.F., and Meyer, P.S. (Eds.), *Proc. ODP, Sci. Results,* 147: College Station, TX (Ocean Drilling Program), 235–254.

Gillis, K., Mével, C., Allan, J., et al., 1993. *Proc. ODP, Init. Repts.,* 147: College Station, TX (Ocean Drilling Program).

Godard, M., Jousselin, D., and Bodinier, J.-L., 2000. Relationships between geochemistry and structure beneath a paleo-spreading centre: a study of the mantle section in the Oman ophiolite. *Earth Planet. Sci. Lett.,* 180:133–148.

Hébert, R., Adamson, A.C., and Komor, S.C., 1990. Metamorphic petrology of ODP Leg 109, Hole 670A serpentinized peridotites: serpentinization processes at a slow spreading ridge environment. *In* Detrick, R., Honnorez, J., Bryan, W.B., Juteau, T., et al., *Proc. ODP, Sci. Results,* 106/109: College Station, TX (Ocean Drilling Program), 103–115.

Heider, F., Zitzelberger, A., and Fabian, K., 1996. Magnetic susceptibility and remanent coercive force in grown magnetite crystals from 0.1 µm to 6 mm. *Phys. Earth Planet. Inter.,* 93:239–256.

Iturrino, G.J., Christensen, N.I., Kirby, S., and Salisbury, M.H., 1991. Seismic velocities and elastic properties of oceanic gabbroic rocks from Hole 735B. *In* Von Herzen, R.P., Robinson, P.T., et al., *Proc. ODP, Sci. Results,* 118: College Station, TX (Ocean Drilling Program), 227–244.

Iturrino, G.J., Miller, D.J., and Christensen, N.I., 1996. Velocity behavior of lower crustal and upper mantle rocks from a fast-spreading ridge at Hess Deep. *In* Mével, C., Gillis, K.M., Allan, J.F., and Meyer, P.S. (Eds.), *Proc. ODP, Sci. Results,* 147: College Station, TX (Ocean Drilling Program), 417–440.

Jaroslow, G.E., Hirth, G., and Dick, H.J.B., 1996. Abyssal peridotite mylonites: implications for grain-size sensitive flow and strain localization in the oceanic lithosphere. *Tectonophysics,* 256:17–37.

Johnson, J.W., Oelkers, E.H., and Helgeson, H.C., 1992. SUPCRT92: a software package for calculating the standard molal thermodynamic properties of minerals, gases, aqueous species, and reactions from 1 to 5000 bar and 0 to 1000°C. *Comput. Geosci.,* 18:899–947.

Kelemen, P.B., and Dick, H.J.B., 1995. Focused melt flow and localized deformation in the upper mantle: juxtaposition of replacive dunite and ductile shear zones in the Josephine peridotite, SW Oregon. *J. Geophys. Res.,* 100:423–438.

Kobayashi, Y., 1974. Anisotropy of thermal diffusity in olivine, pyroxene and dunite. *J. Phys. Earth,* 22:35–373.

Lachize, M., 1993. La chambre magmatique fossile d'Haymiliyah (massif de Haylayn, ophiolite de Semail: un cas de précipitation de sulfures magmatiques dans la couche 3 de la lithosphère océanique [Thèse de Doctorat]. Université de Bretagne Occidentale.

McFadden, P.L., Merrill, R.T., McElhinny, M.W., and Lee, S., 1991. Reversals of the Earth's magnetic field and temporal variations of the dynamo families. *J. Geophys. Res.,* 96:3923–3933.

McFadden, P.L., and Reid, A.B., 1982. Analysis of paleomagnetic inclination data. *Geophys. J. R. Astron. Soc.,* 69:307–319.

Mercier, J.-C.C., and Nicolas, A., 1975. Textures and fabrics of upper mantle peridotites as illustrated by xenoliths from basalts. *J. Petrol.,* 16:454–496.

Miller, D.J., and Christensen, N.I., 1997. Seismic velocities of lower crustal and upper mantle rocks from the slow-spreading Mid-Atlantic Ridge, south of the Kane Transform Zone (MARK). *In* Karson, J.A., Cannat, M., Miller, D.J., and Elthon, D. (Eds.), *Proc. ODP, Sci. Results,* 153: College Station, TX (Ocean Drilling Program), 437–454.

O'Hanley, D.S., 1992. Solution to the volume problem in serpentinization. *Geology,* 20:705–708.

————, 1996. Serpentinites: records of tectonic and petrological history. *Oxford Monogr. Geol. Geophys.,* Vol. 34.

Parker, R.L., and Gee, J.S., 2002. Calibration of the pass-through magnetometer—II. Application. *Geophys. J. Int.,* 150:140–152.

Parkinson, I.J., and Pearce, J.A., 1998. Peridotites from the Izu-Bonin-Mariana forearc (ODP Leg 125); Evidence for partial melting and melt-mantle interactions in a supra-subduction zone setting. *J. Petrol.,* 39:1577–1618.

Passchier, C.W., and Simpson, C., 1986. Porphyroclast systems as kinematic indicators. *J. Struct. Geol.,* 8:831–843.

Peabody, C.E., and Einaudi, M.T., 1992. Origin of petroleum and mercury in the Culver-Baer cinnabar deposit, Mayacmas District, California. *Econ. Geol.,* 87:1078–1103.

Rampone, E., Hofmann, A.W., Piccardo, G.B., Vannucci, R., Bottazzi, P., and Ottolini, L., 1996. Trace element and isotope geochemistry of depleted peridotites from an N-MORB type ophiolite (Internal Liguride, N. Italy). *Contrib. Mineral. Petrol.,* 123:61–76.

Ramsay, J.G., and Ghram, R.H., 1970. Strain variation in shear belts. *Canadian. J. Earth Sci.,* 7:786–813.

Ramsay, J.G., and Huber, M.I., 1987. *The Techniques of Modern Structural Geology* (Vol. 2): *Folds and Fractures:* New York (Academic Press).

Robinson, P.T., Von Herzen, R., et al., 1989. *Proc. ODP, Init. Repts.,* 118: College Station, TX (Ocean Drilling Program).

Schandl, E.S., O'Hanley, D.S., and Wicks, F.J., 1989. Rodingites in serpentinized ultramafic rocks of the Abitibi greenstone belt, Ontario. *Can. Mineral,* 27:579–591.

Seyfried, W.E., Jr., and Ding, K., 1995. Phase equilibria in subseafloor hydrothermal systems: a review of the role of redox, temperature, pH and dissolved Cl on the chemistry of hot spring fluids on mid-ocean ridges. *In* Humphris, S.E., Zierenberg, R.A., Mullineaux, L.S., and Thomson, R.E. (Eds.), *Seafloor Hydrothermal Systems: Physical, Chemical, Biological, and Geological Interactions.* Geophys. Monogr., 91:248–272.

Shipboard Scientific Party, 1995. Site 920. *In* Cannat, M., Karson, J.A., Miller, D.J., et al., *Proc. ODP, Init. Repts.,* 153: College Station, TX (Ocean Drilling Program), 45–119.

————, 1999. Site 735. *In* Dick, H.J.B., Natland, J.H., Miller, D.J., et al., *Proc. ODP, Init. Repts.,* 176, 1–314 [CD-ROM]. Available from: Ocean Drilling Program, Texas A&M University, College Station, TX 77845-9547, U.S.A.

Snow, J.E., and Dick, H.J.B., 1995. Pervasive magnesium loss by marine weathering of peridotite. *Geochim. Cosmochim. Acta,* 59:4219–4235.

Toft, P.B., Arkani-Hamed, J., and Haggerty, S.E., 1990. The effects of serpentinization on density and magnetic susceptibility: a petrophysical model. *Phys. Earth Planet. Inter.,* 65:137–157.

Tommasi, A., Gibert, B., Seipold, U., and Mainprice, D., 2002. Anisotropy of thermal diffusivity in the upper mantle. *Nature,* 411:783–786.

Vera, E.E., Mutter, J.C., Buhl, P., Orcutt, J.A., Harding, A.J., Kappus, M.E., Detrick, R.S., and Brocher, T.M., 1990. The structure of 0- to 0.2-m.y.-old oceanic crust at 9°N on the East Pacific Rise from expanded spread profiles. *J. Geophys. Res.,* 95:15529–15556.

Wetzel, L.R., and Shock, E.L., 2000. Distinguishing ultramafic- from basalt-hosted submarine hydrothermal systems by comparing calculated vent fluid compositions. *J. Geophys. Res., [Solid Earth],* 105:8319–8340.

Wicks, F.J., 1984. Deformation histories as recorded by serpentinites: I. Deformation prior to serpentinization, and II. Deformation during and after serpentinization. *Can. Mineral.,* 22:185–203.

Figure F1. **A.** Bathymetric map showing location of Hole 1268A. (Continued on next two pages.)

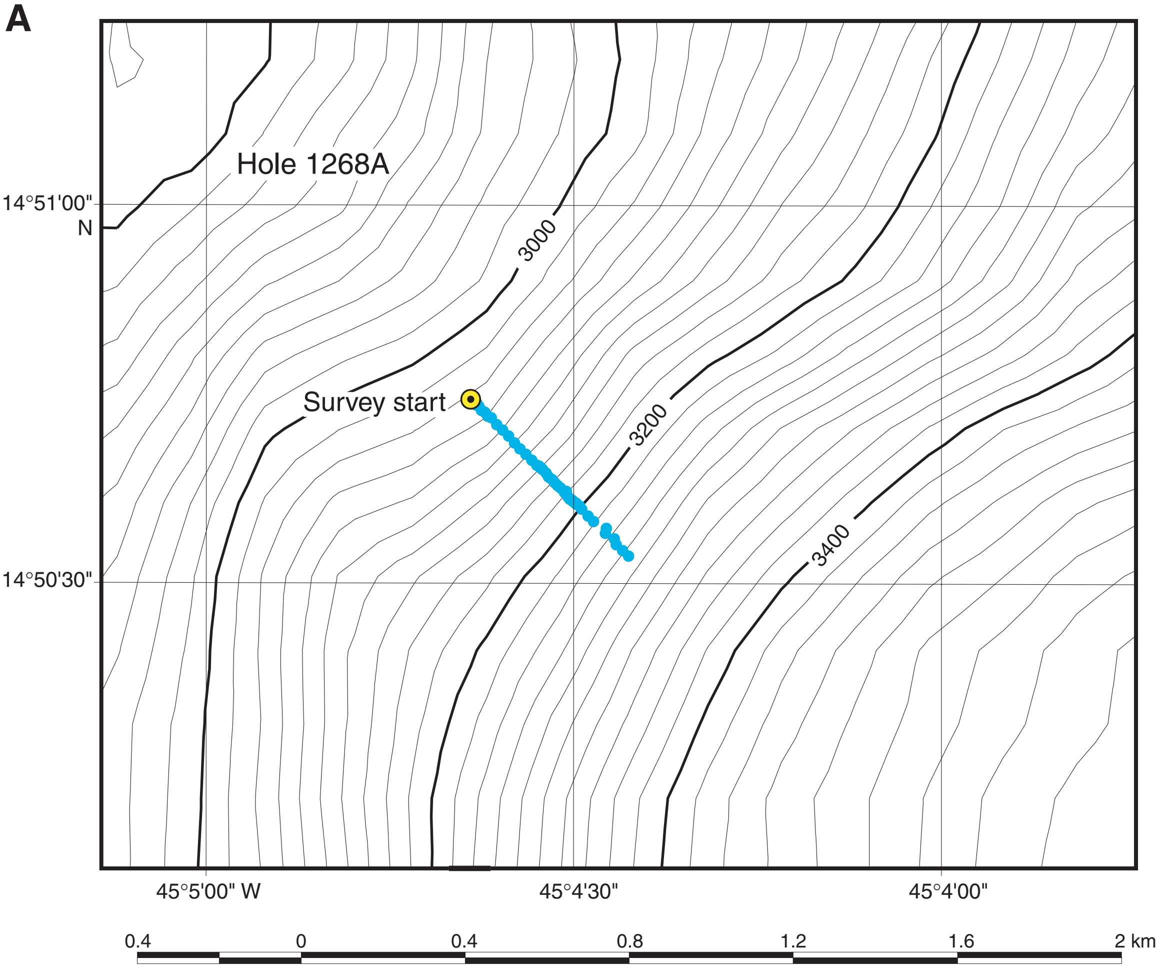

Figure F1 (continued). B. Location map with track of *Shinkai* 6500 Dive 427 and location of samples from that dive as well as Hole 1268A.

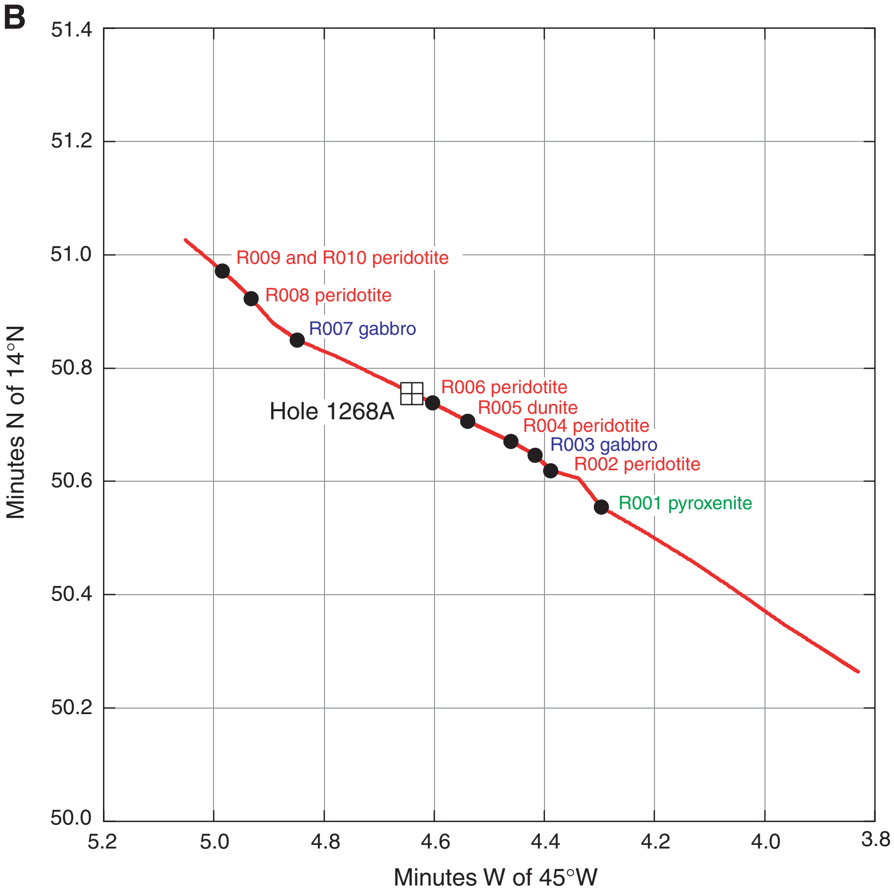

Figure F1 (continued). C. Bathymetric section of the area around Hole 1268A, based on depth and locations from *Shinkai* 6500 Dive 427, projected along 303° with no vertical exaggeration.

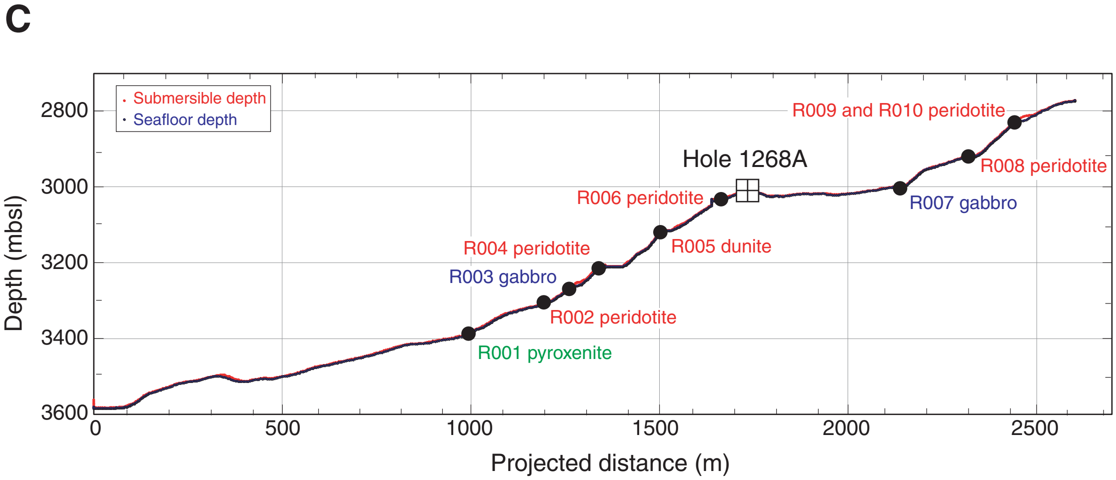

Figure F2. Comparison of data from the precision depth recorder (PDF) in the underway geophysics laboratory on board *JOIDES Resolution, Shinkai* 6500 Dive 427, projected along 315° with no vertical exaggeration, and depth information from video and sonar on the VIT frame during the camera survey on 22 May 2003. DP = dynamic positioning.

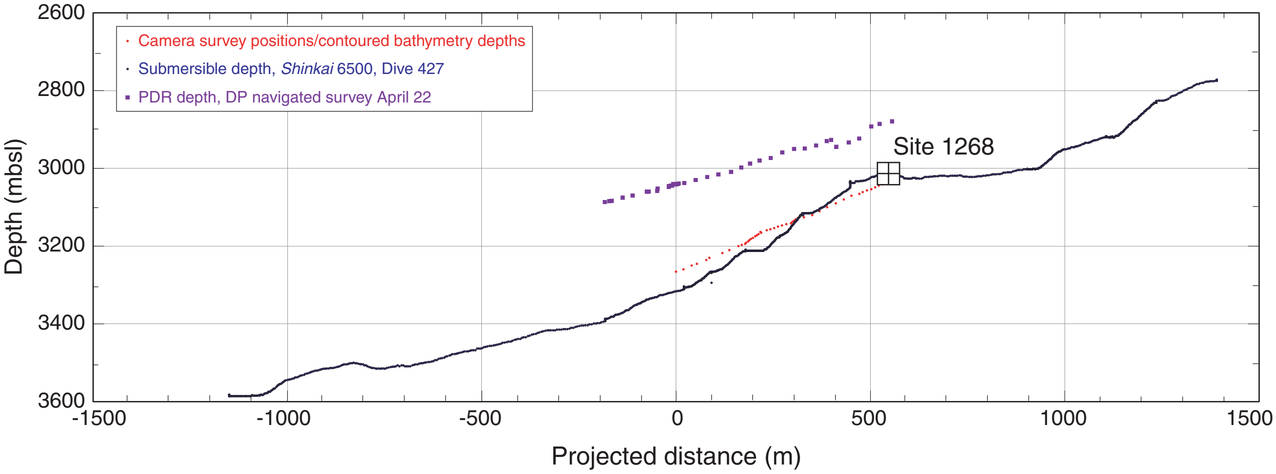

Figure F3. Hole 1268A lithology and stratigraphy, shown as percentages for each section (middle column) and as individual observations (right column). The lithologies are grouped as dunites (rocks with ≥90% olivine), harzburgites (includes all ultramafic rocks exclusive of dunites but the bulk are harzburgites in the strict sense), gabbroic rocks (includes gabbronorites, microgabbros, and gabbroic rocks of undeterminable mineralogy), and intrusion breccias (mixtures of highly altered, probably originally gabbroic material and ultramafic host—these are often so altered that evaluating the original compositions and proportions of the two components is not possible). TD = total depth.

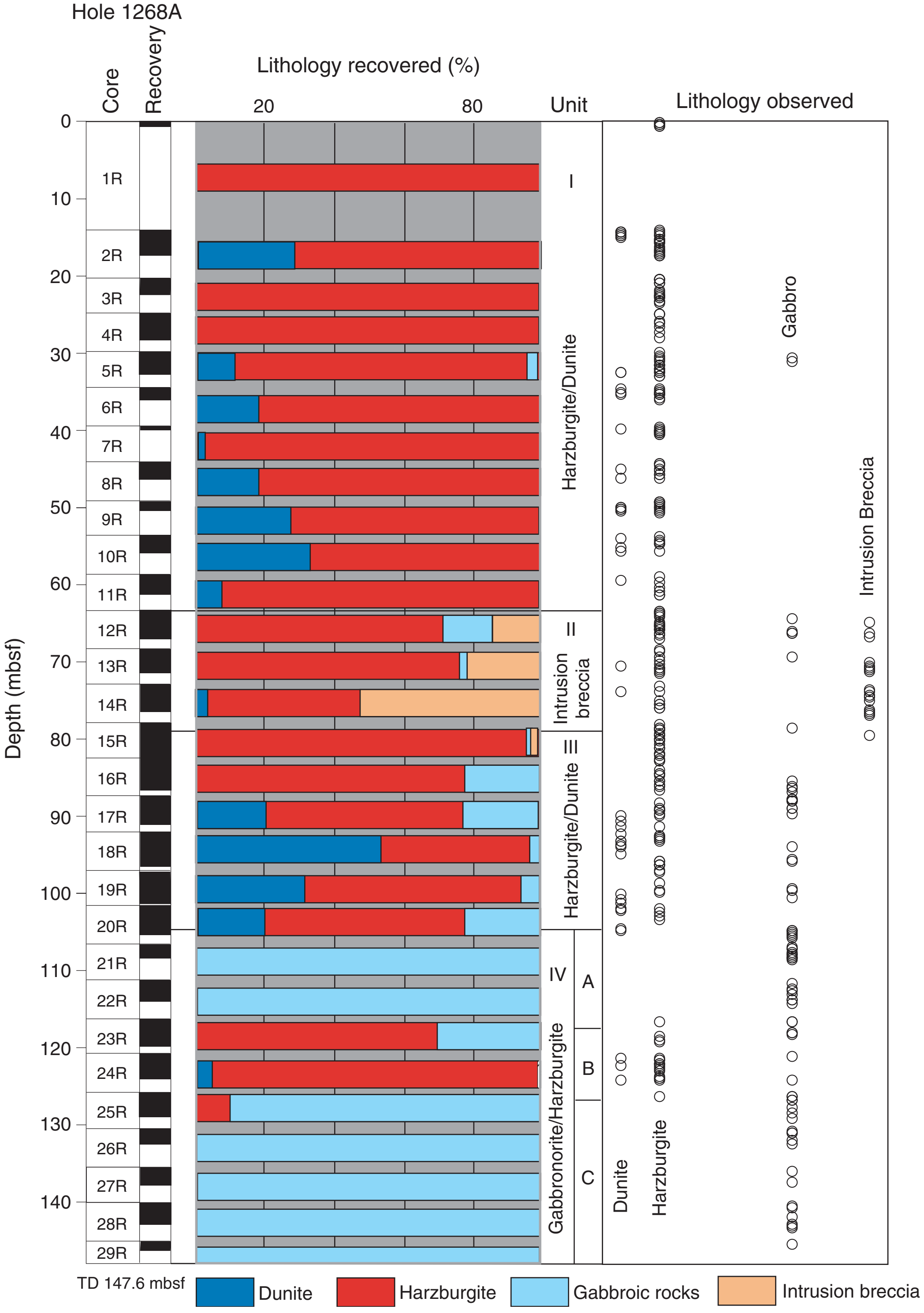

Figure F4. Close-up photographs showing Unit II contacts. At both the upper and lower contacts a mylonitized zone containing both gabbroic and ultramafic material immediately overlies a low-temperature fault breccia. **A.** Upper contact (interval 209-1268A-12R-1, 125–136 cm). **B.** Upper contact (interval 209-1268A-12R-1, 137–149 cm). **C.** Lower contact (interval 209-1268A-15R-1, 8–18.5 cm). **D.** Lower contact (interval 209-1268A-15R-1, 134–143 cm).

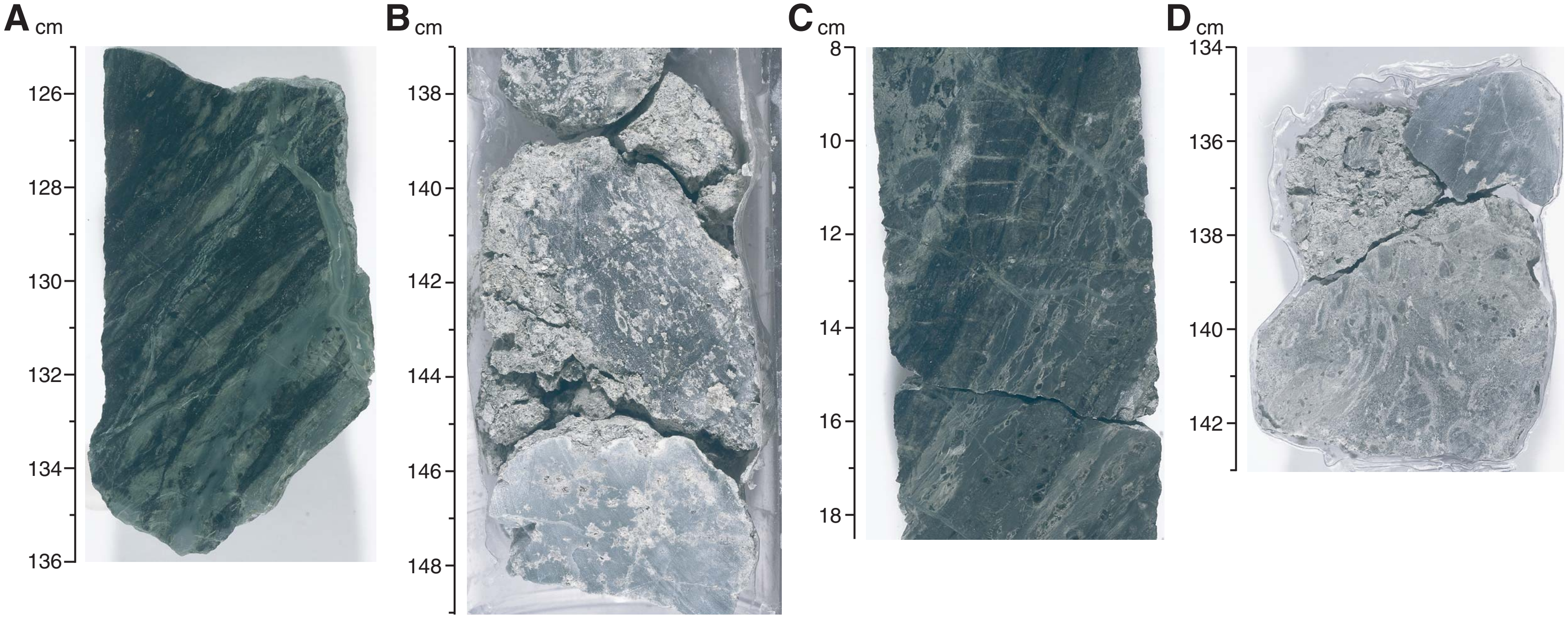

Figure F5. Close-up photograph of lower contact of Unit III showing growth of pyroxene crystals along a contact with dunite (interval 209-1268A-20R-2, 133–138 cm).

Figure F6. Photomicrographs showing altered orthopyroxene. **A, B.** Porphyroclast with deformation in the right part (contact with serpentinized olivine) (Sample 209-1268A-4R-1, 12–15 cm) (plane-polarized light: blue + light gray filters; field of view = 5.5 mm); (A) image 1268A_012; (B) image 1268A_013. **C, D.** Anhedral to interstitial orthopyroxene in serpentinized olivine matrix. Note that the orthopyroxene has been converted to bastite (Sample 209-1268A-4R-1, 124–127 cm) (field of view = 5.5 mm); (C) plane-polarized light: blue filter; image 1268A_008; (D) cross-polarized light: blue filter; image 1268A_009. (Continued on next page.)

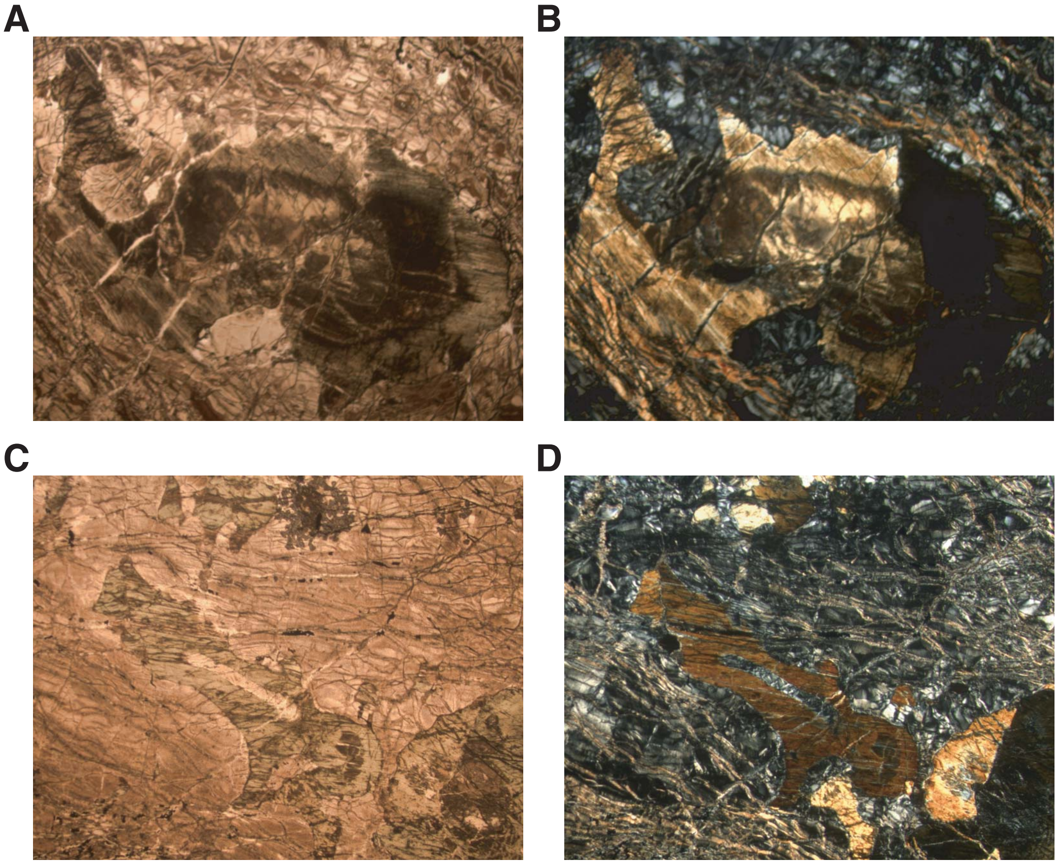

Figure F6 (continued). E. Orthopyroxene transformed to pleochroic serpentine cut and locally replaced along cleavage planes by massive nonpseudomorphic talc. A talc vein also cuts chrysotile veins associated with background alteration (Sample 209-1268A-12R-3, 71–75 cm) (cross-polarized light: blue + light gray filters; field of view = 2.75 mm; image 1268A_019). **F.** Interstitial grains of orthopyroxene in a serpentinized olivine matrix (Sample 209-1268A-5R-2, 58–61 cm) (plane-polarized light: blue filter; field of view = 5.5 mm; image 1268A_010).

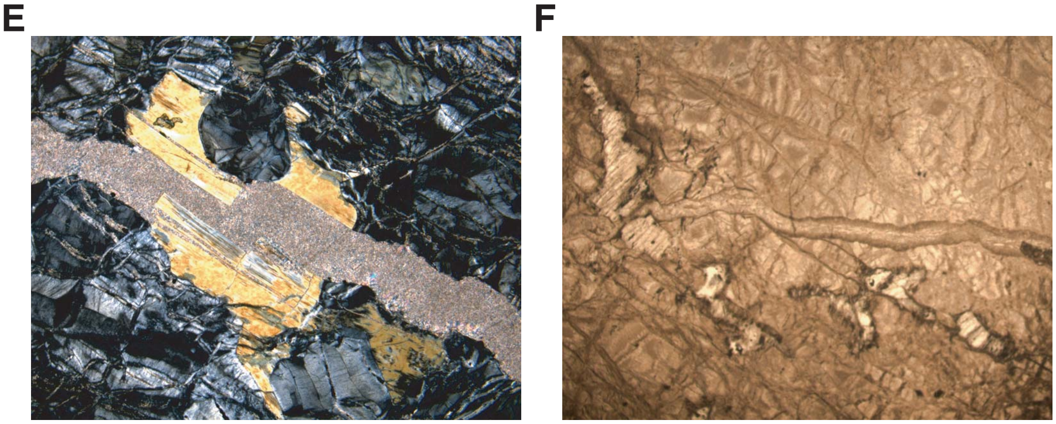

Figure F7. Photomicrograph showing texture characterized by anhedral to interstitial (altered) orthopyroxene crystals in a serpentinized olivine matrix (Sample 209-1268A-12R-3, 71–74 cm) (plane-polarized light: blue + light gray filters; field of view = 5.5 mm; image 1268A_017).

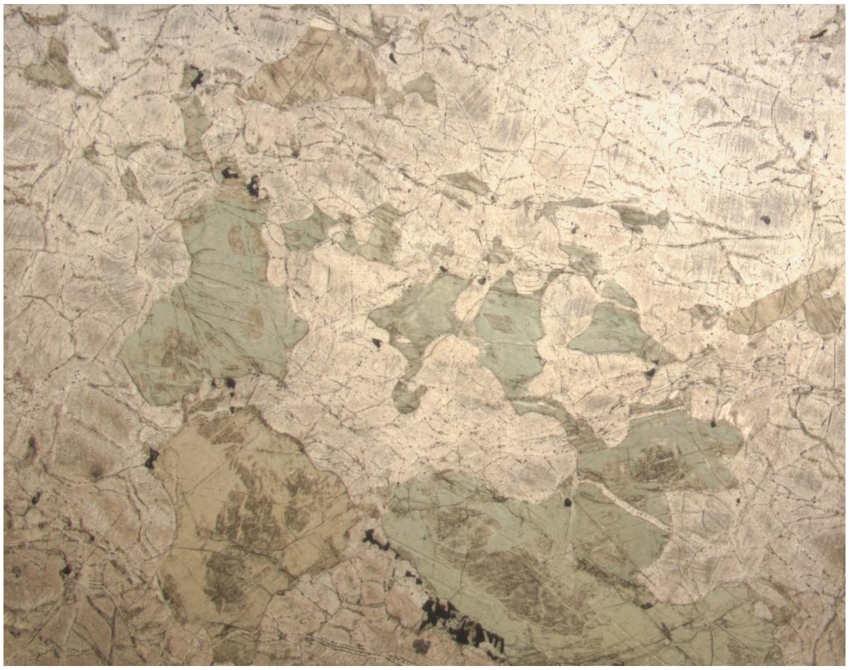

Figure F8. Photomicrograph showing orthopyroxene porphyroclast recrystallized into subgrains (Sample 209-1268A-3R-2, 109–113 cm) (cross-polarized light: blue filter; field of view = 5.5 mm; image 1268A_003).

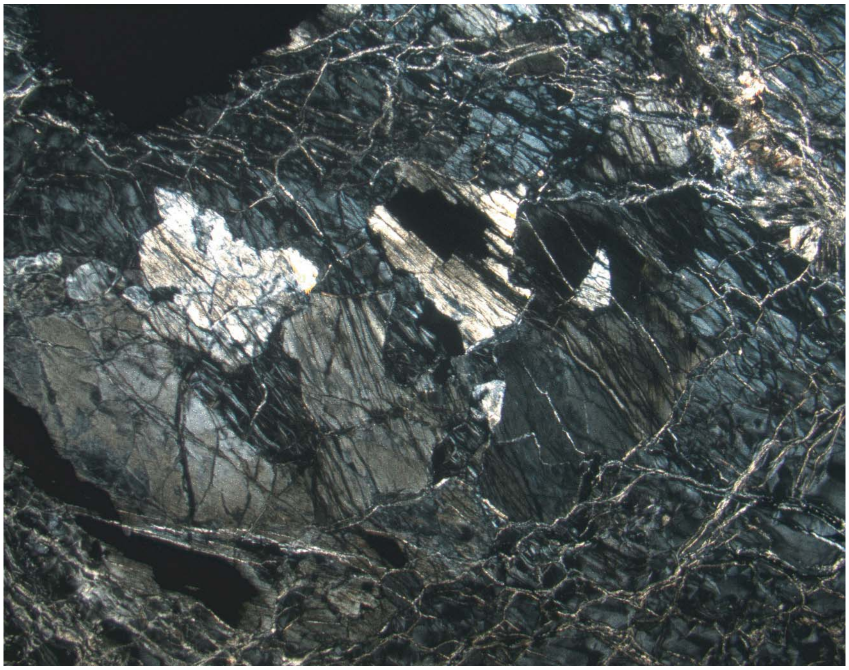

Figure F9. Photomicrographs showing protogranular to porphyroclastic textures in harzburgite (Sample 209-1268A-3R-3, 6–9 cm). **A.** Recrystallized orthopyroxene porphyroclast with olivine; small clinopyroxene at orthopyroxene grain boundary in the lower right corner (cross-polarized light: blue filter; field of view = 5.5 mm; image 1268A_006). **B.** Protogranular texture with primary olivine and orthopyroxene. The orthopyroxene is partly recrystallized at the lower end and olivine is sometimes included in orthopyroxene (cross-polarized light: blue filter; field of view = 5.5 mm; image 1268A_007). **C.** Protogranular texture with the orthopyroxene at extinction (cross-polarized light: blue filter; field of view = 2.75 mm; image 1268A_014). **D.** Kink bands in olivine that preserve evidence of deformation of the rock (cross-polarized light: blue + light gray filters; field of view = 2.75 mm; image 1268A_015).

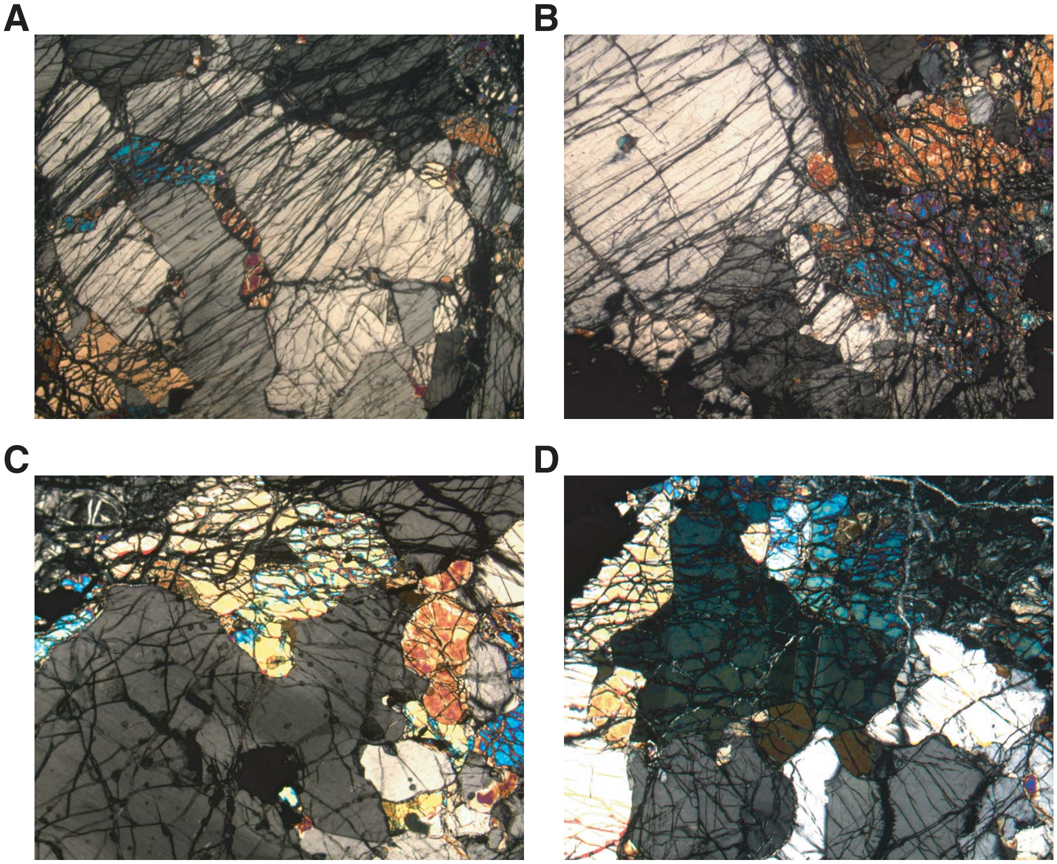

Figure F10. Photomicrograph showing spinel and clinopyroxene near recrystallized orthopyroxene (Sample 209-1268A-3R-2 [Piece 20A, 109–113 cm]) (plane-polarized light: blue filter; field of view = 0.70 mm; image 1268A_001).

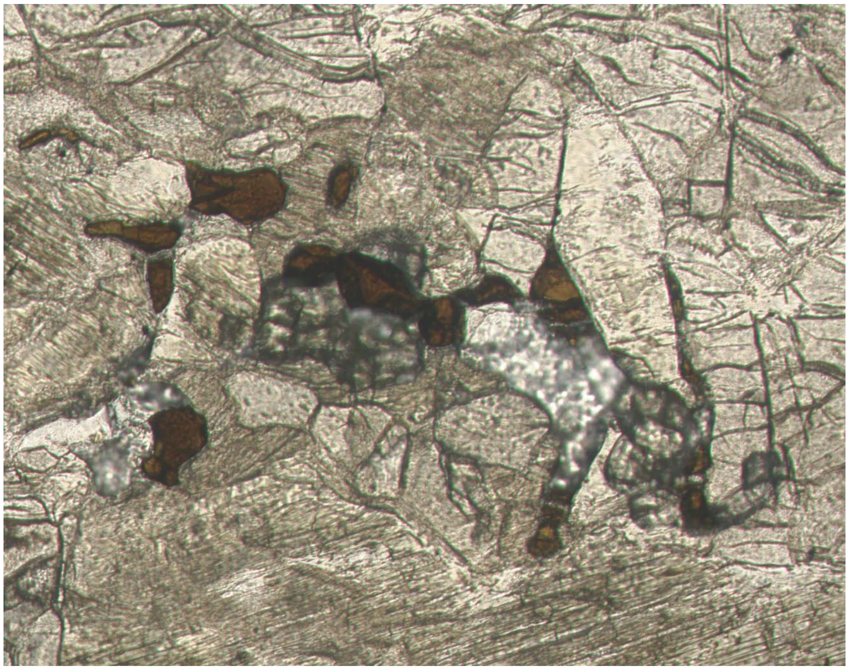

Figure F11. Photomicrographs showing altered clinopyroxene crystals (Sample 209-1268A-19R-1 [Piece 2A, 16–18 cm]) (cross-polarized light: blue + light gray filters; field of view = 1.4 mm). **A.** Altered pyroxene that could have been a clinopyroxene interstitial in a serpentinized olivine matrix (image 1268A_030). **B.** Altered pyroxene that could have been a clinopyroxene in a serpentinized olivine matrix (image 1268A_031).

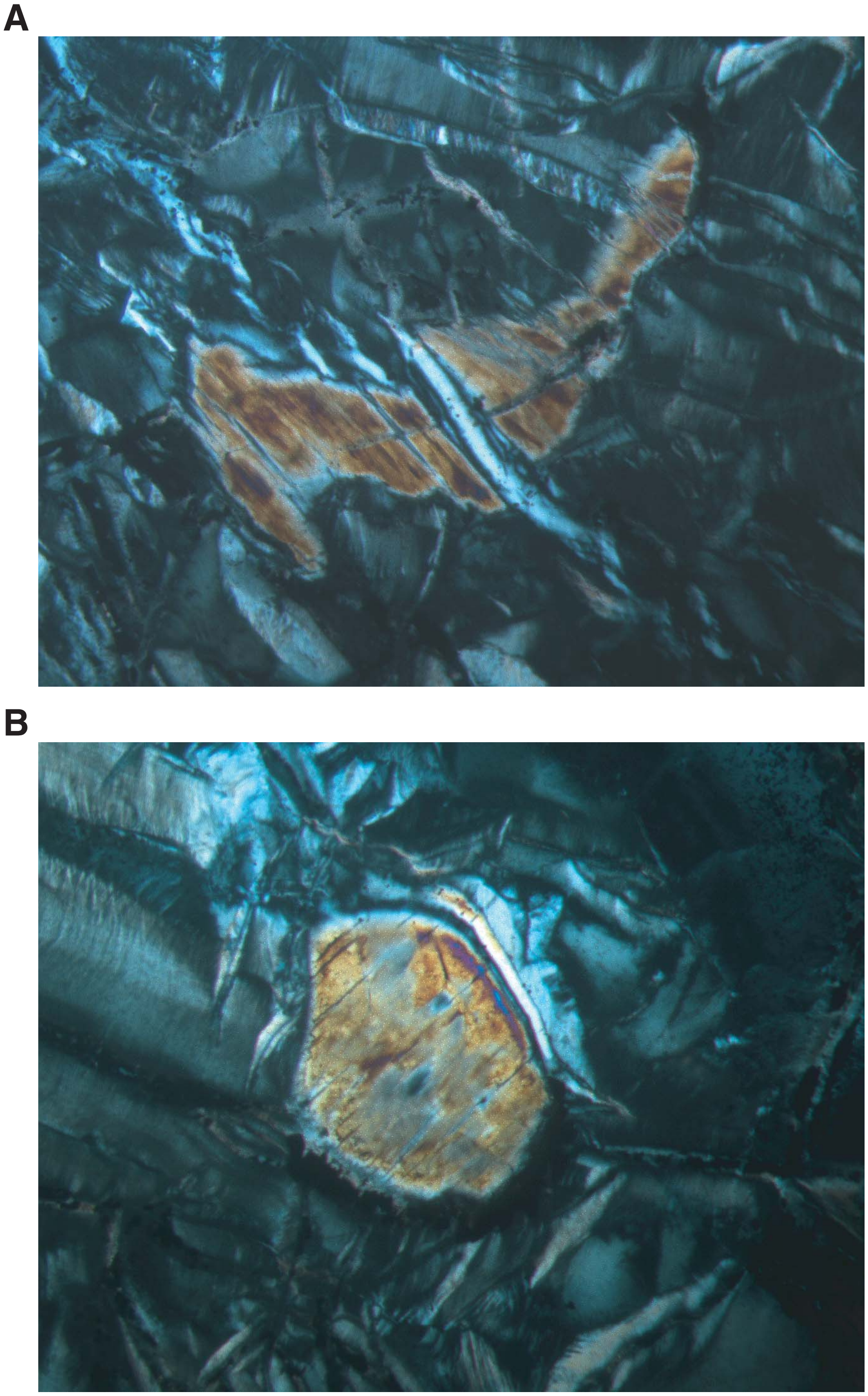

Figure F12. Photomicrographs showing orthopyroxene/spinel textural relations. **A, B.** Wormy spinel intergrowths(?) in a small orthopyroxene grain (Sample 209-1268A-19R-1 [Piece 2B, 51–53 cm]) (cross-polarized light: blue filter; field of view = 1.4 mm); (A) image 1268A_048; (B) image 1268A_049. **C.** The margins of this orthopyroxene grain have been recrystallized into orthopyroxene neoblasts and spinel (Sample 209-1268A-3R-2 [Piece 20A, 109–112 cm]) (plane-polarized light: blue filter; field of view = 0.7 mm; image 1268A_002).

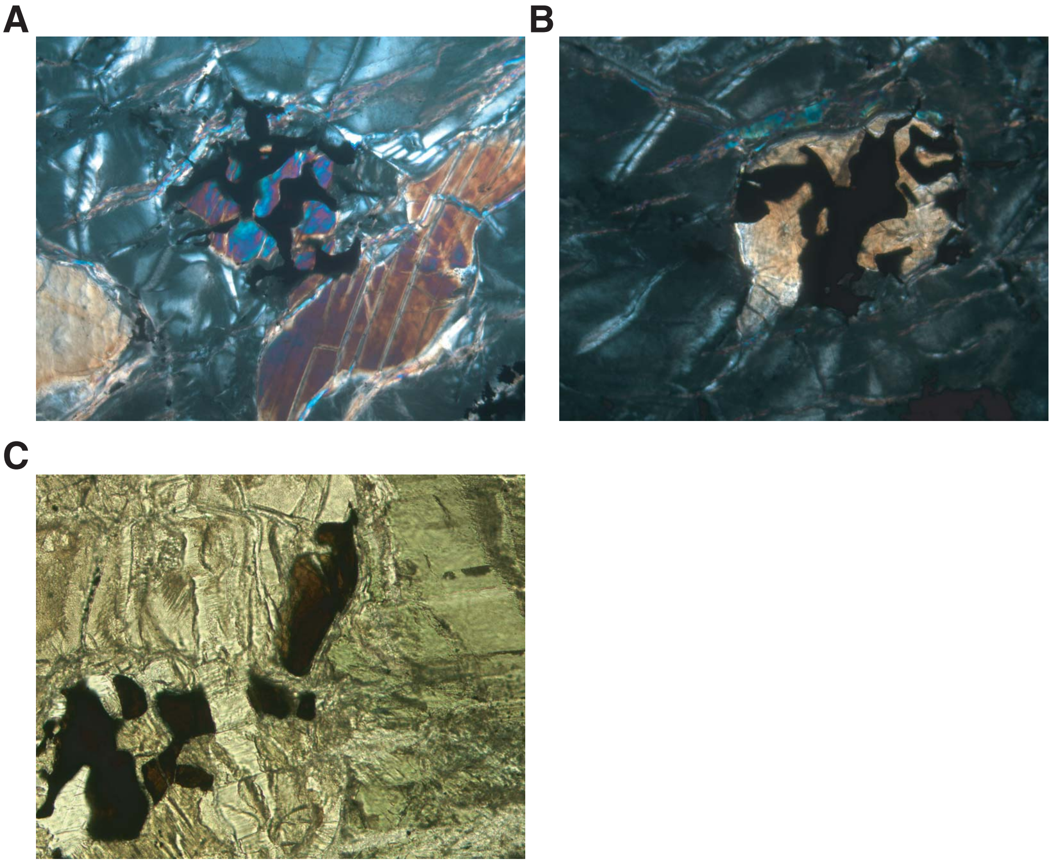

Figure F13. Histogram showing the proportion in the harzburgites and dunites of altered pyroxene of >1 mm size, interpreted to be former orthopyroxene. Proportions have been visually estimated in hand samples, checked in representative thin sections, and averaged in 5% intervals.

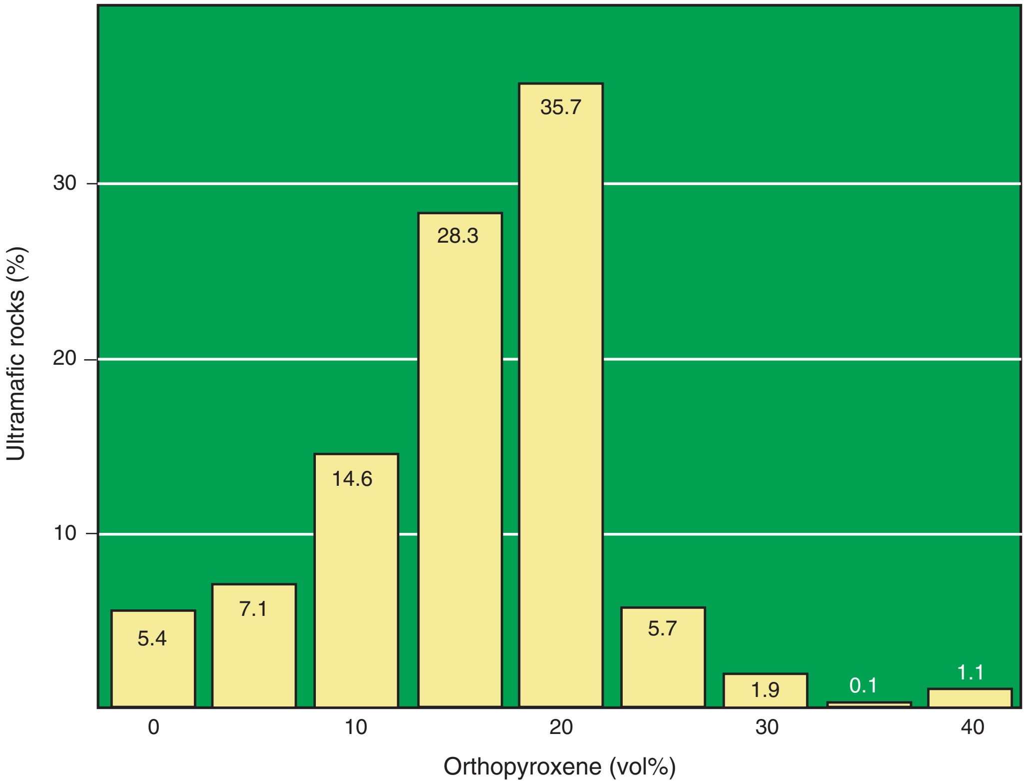

Figure F14. Photomicrographs showing textures in recrystallized orthopyroxene (Sample 209-1268A-18R-4 [Piece 11, 89–91 cm]) (cross-polarized light: blue filter). **A.** Two clinopyroxene grains are located at the lower boundary of the main orthopyroxene crystal and at the triple junction (to the right) (field of view = 1.4 mm; image 1268A_036). **B.** Two orthopyroxene crystals with curvilinear boundaries. One encloses a spinel grain (field of view = 1.4 mm; image 1268A_037). **C.** Orthopyroxene and olivine grains in orthopyroxenite (field of view = 5.5 mm; image 1268A_038).

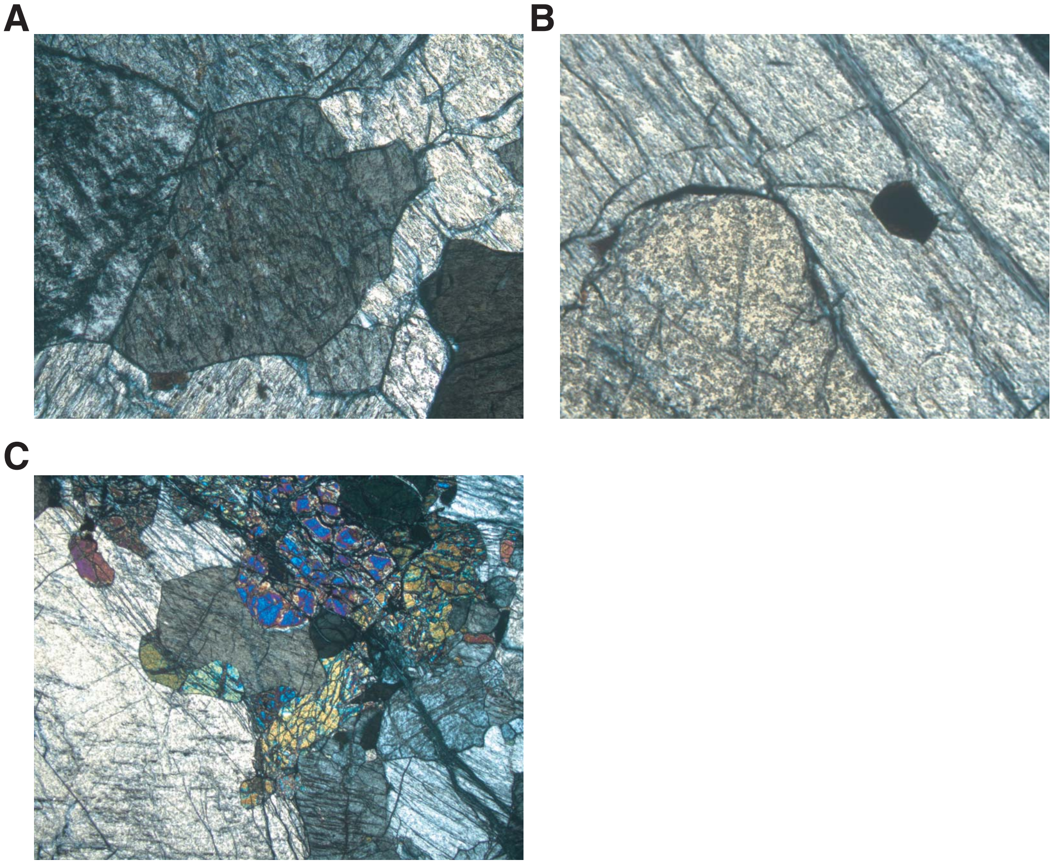

Figure F15. Close-up photograph of intrusion breccia typical of Unit II. Note that the bulk of the material between the clasts is either smaller ultramafic clasts or ground-up ultramafic material and the intrusive material, probably originally gabbroic, occurs as thin selvages at the margins of the larger clasts (interval 209-1268A-13R-2, 18–29 cm).

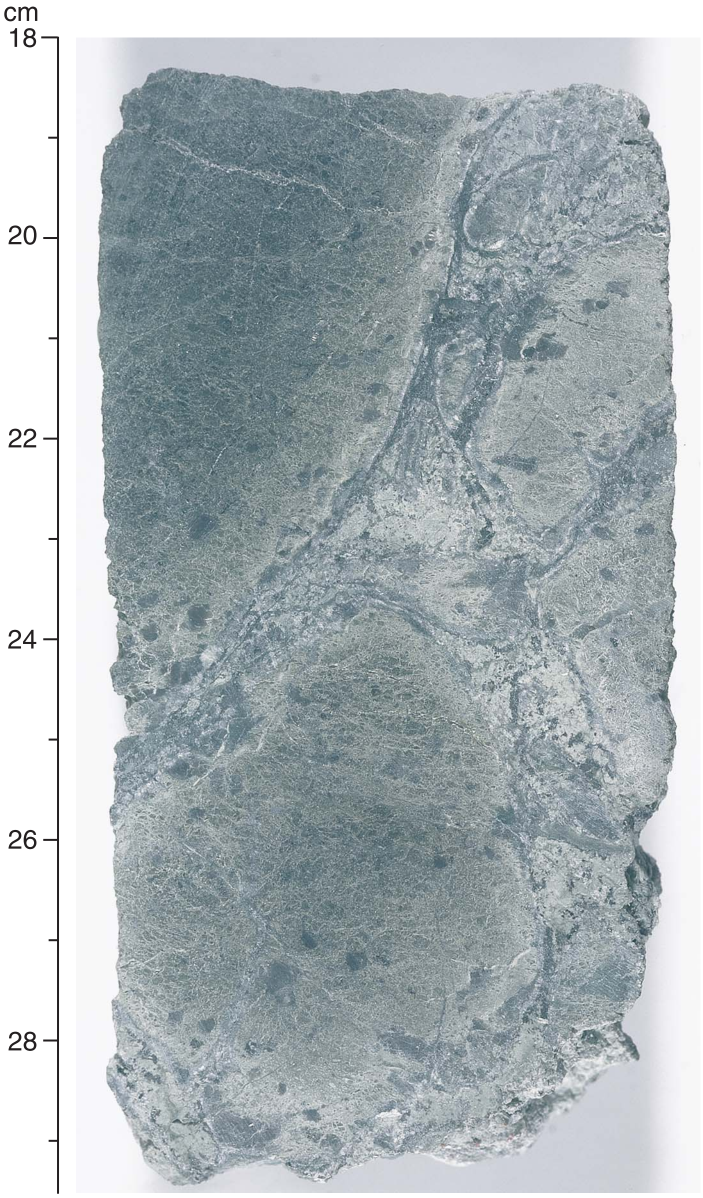

Figure F16. Close-up photograph of pegmatitic textured gabbro from near the upper contact of Unit IV (interval 209-1268A-21R-1, 10–21 cm).

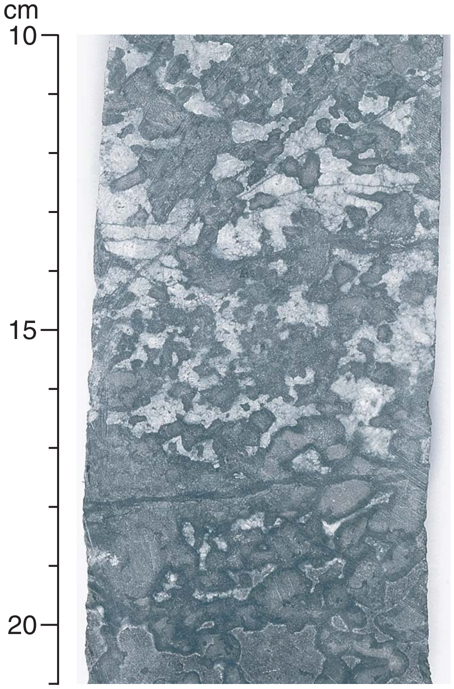

Figure F17. Stratigraphic distribution of the proportions in the harzburgites and dunites of altered pyroxene of >1 mm size, interpreted to be former orthopyroxene. The first column shows the locations of gabbroic intrusions. Lightest intervals had no recovery.

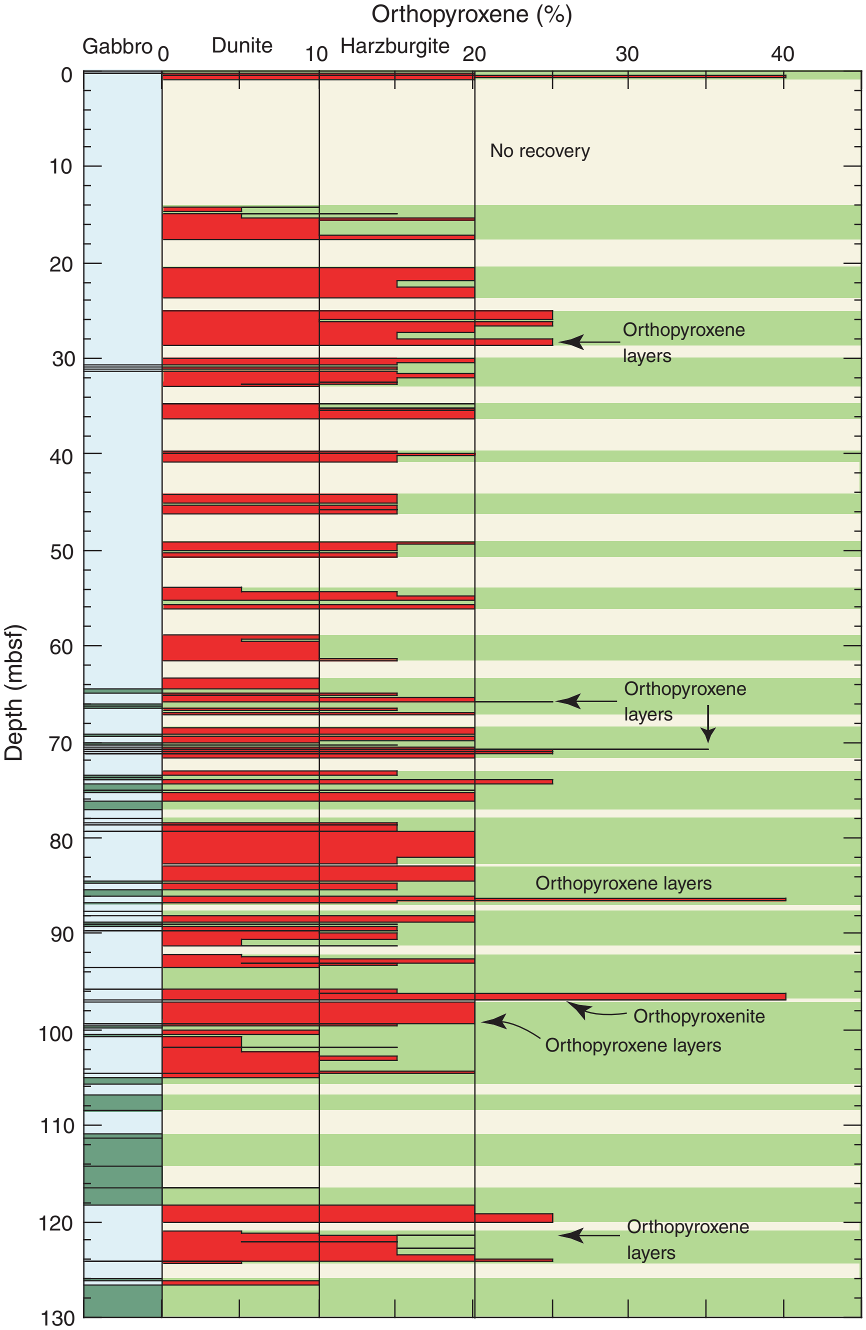

Figure F18. **A.** Photograph of hand specimen of a typical example of completely serpentinized harzburgite (interval 209-1268A-19R-1, 50–62 cm). **B.** XRD spectrum of sample from A shows that it consists almost entirely of serpentine and magnetite.

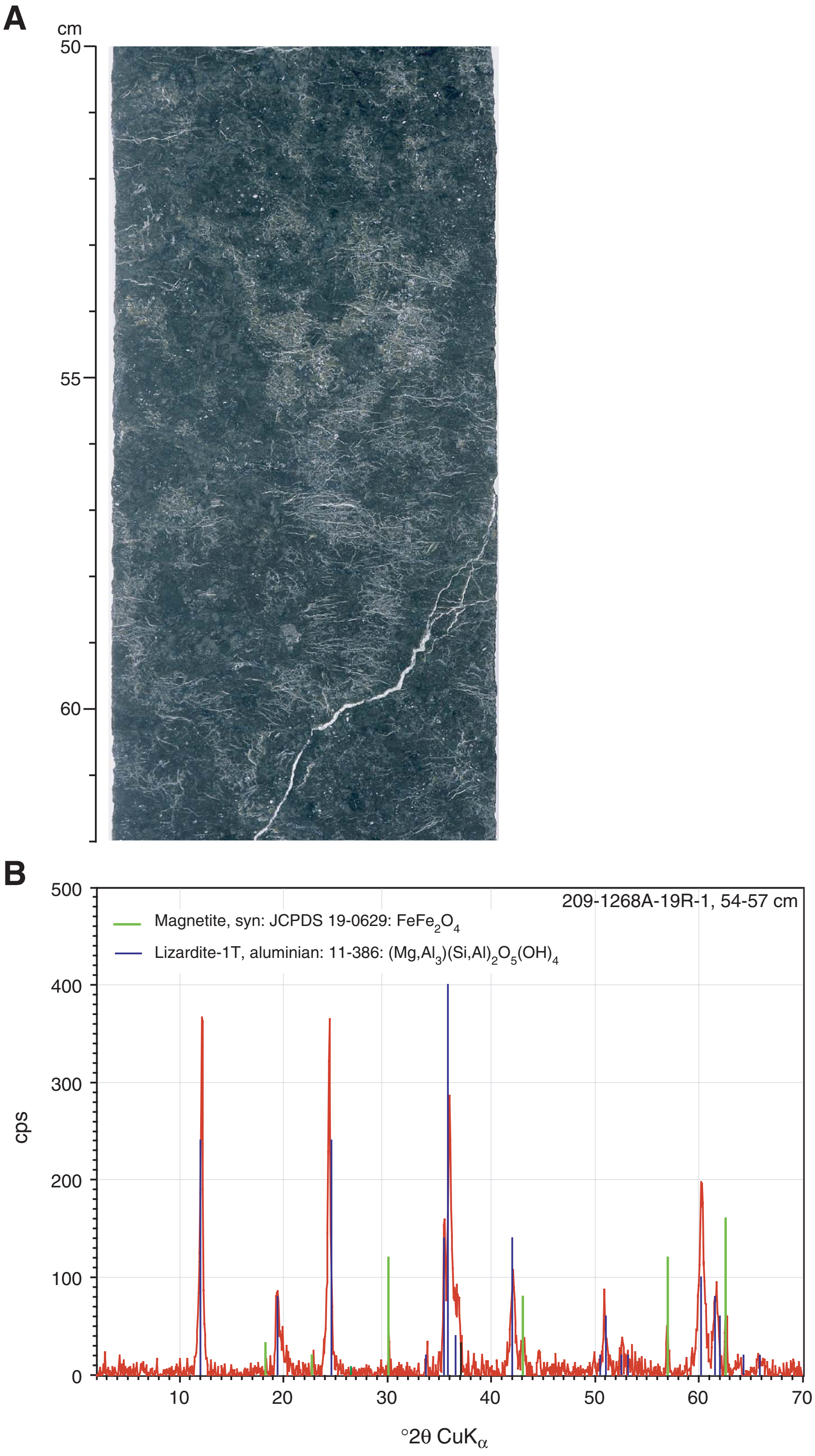

Figure F19. Photomicrograph of serpentinized harzburgite showing a typical hourglass texture with black, anastomosing serpentine + magnetite veins (north-northwest–south-southeast) cut by white chrysotile (cross fiber, length fast) + magnetite veins (Sample 209-1268A-18R-3, 5–7 cm) (cross-polarized light: blue + light gray filters; field of view = 1.4 mm; image 1268_033).

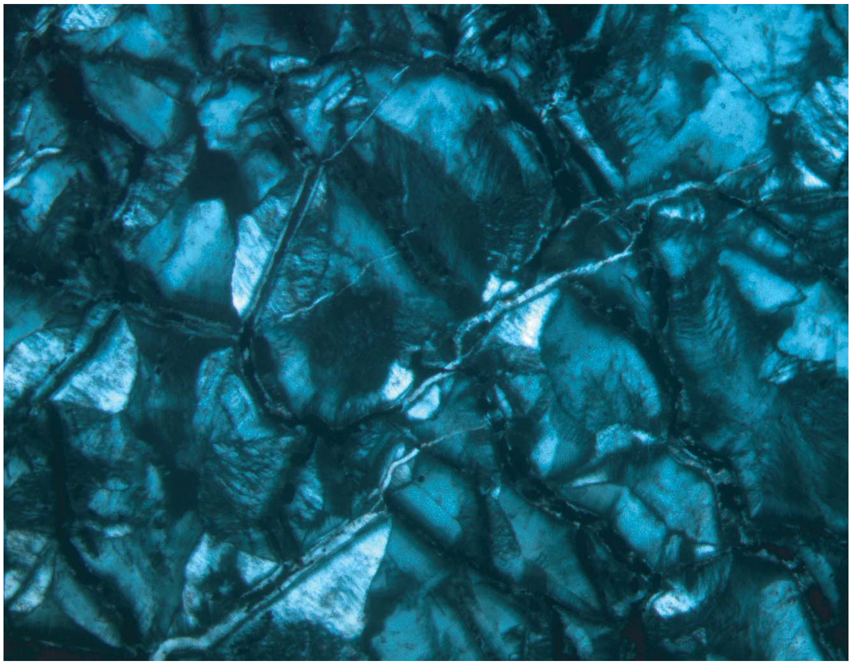

Figure F20. Photomicrograph showing interlocking texture in a serpentinized harzburgite with early chrysotile + magnetite veins (northwest–southeast) cut by later chrysotile veins (northeast–southwest) and talc + pyrite veins (northeast–southwest). Talc is present at bottom right of the image (Sample 209-1268A-15R-3, 135–137 cm) (cross-polarized light: blue + gray filters; field of view = 1.4 mm; image 1268A_055).

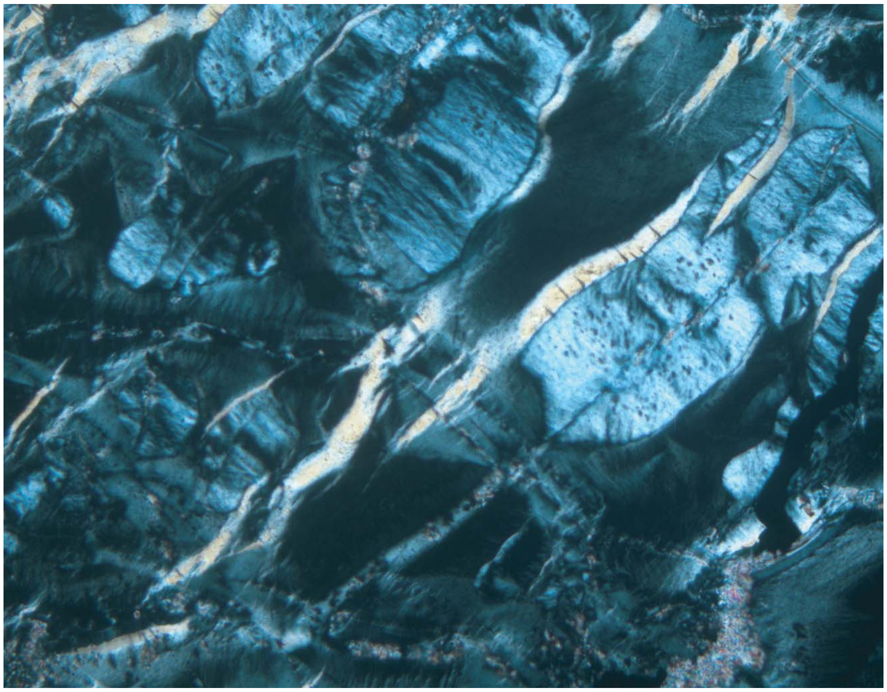

Figure F21. A. Photograph of a hand specimen of a typical example of completely talc-altered serpentinized harzburgite (interval 209-1268A-5R-2 [Piece 14, 55–64 cm]). **B.** XRD spectrum of sample in A shows that it consists almost entirely of talc.

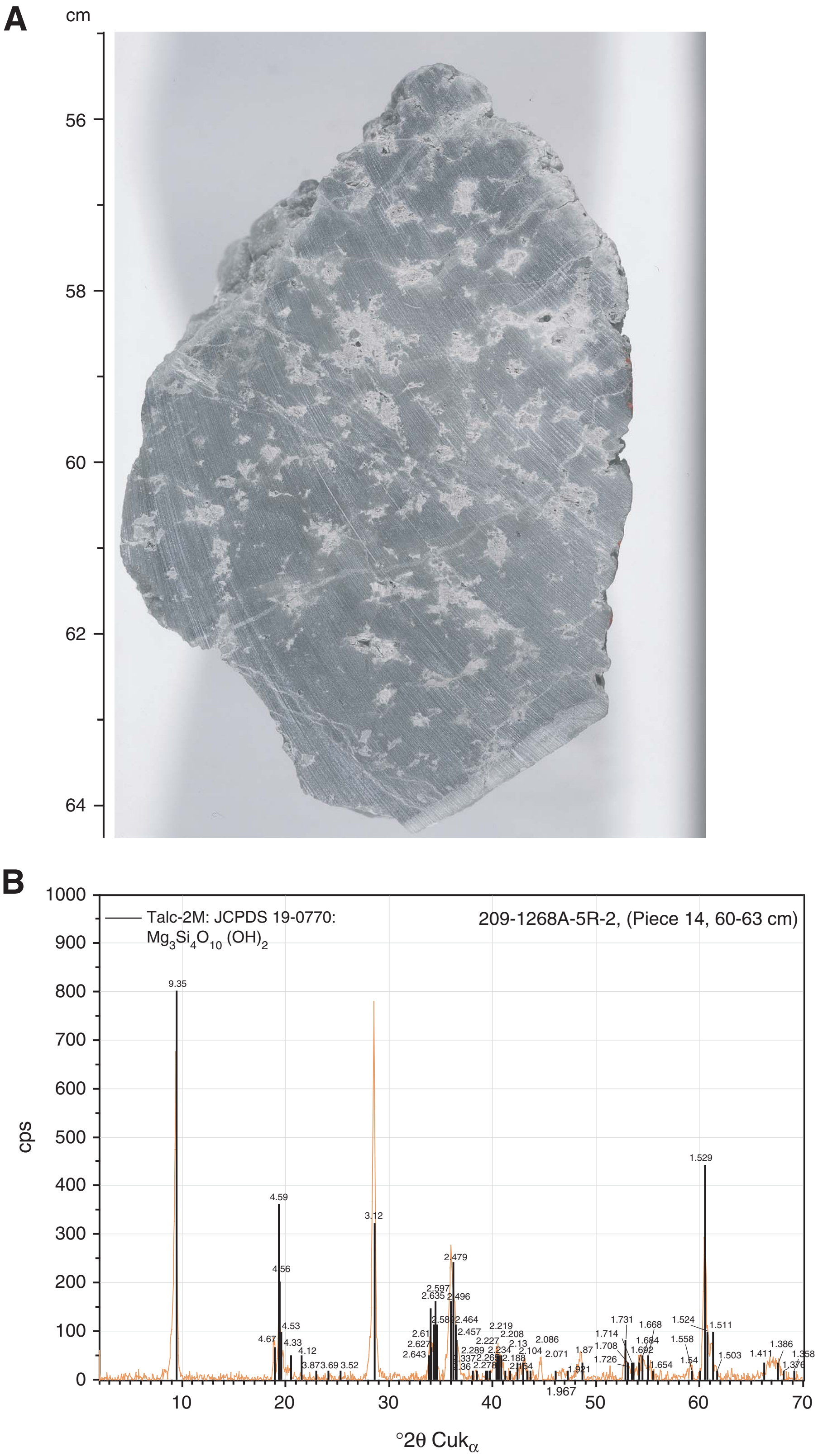

Figure F22. A. Photograph of partially talc altered serpentinite with remnants of serpentine pseudomorphs after orthopyroxene (interval 209-1268A-23R-2, 15–28 cm). Arrows indicate approximate position of thin section photographs. **B, C.** Photomicrographs of sample shown in A (Sample 209-1268A-23R-2, 18–21 cm) (cross-polarized light: blue filter; field of view = 2.75 mm). (B) Pervasive talc alteration has completely erased the matrix texture of the serpentinized harzburgite. A bastite pseudomorph after orthopyroxene (left) is partly replaced by veinlets of massive talc (image 1268A_40). (C) Talc replaces orthopyroxene (to the left of prominent spinel crystal in center of image) and former serpentine-chrysotile veins (left). Talc has completely erased the mesh texture of the serpentinized harzburgite (image 1268A_39).

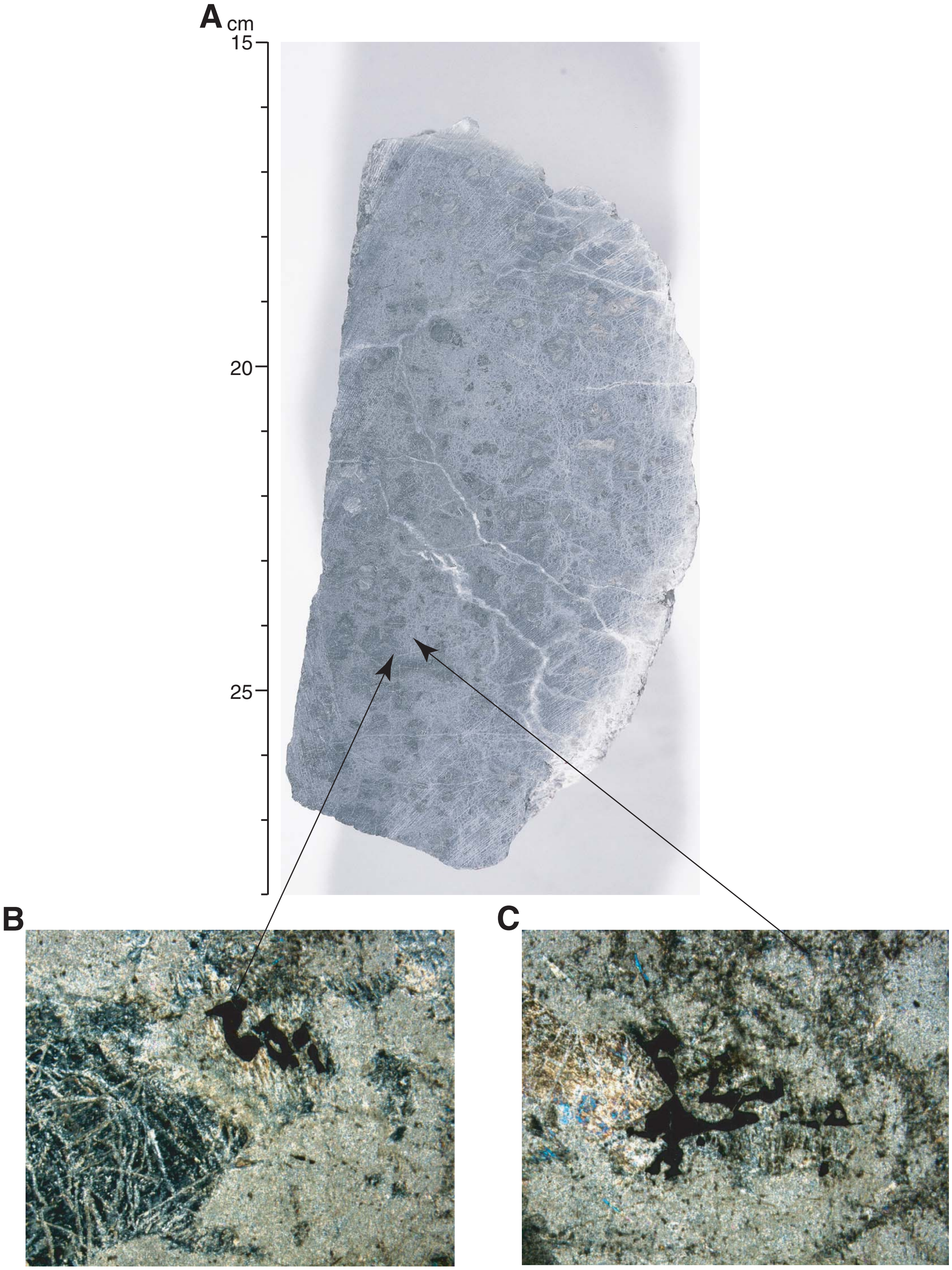

Figure F23. Photomicrograph showing the core of an orthopyroxene crystal pseudomorphed by talc and pyrite. The core is surrounded by a corona of pleochroic serpentine. Pseudomorphic talc and pleochroic serpentine are partly replaced by late, nonpseudomorphic talc (bottom) (Sample 209-1268A-13R-2, 3–6 cm) (crossed polarized light: blue filter; field of view = 2.75 mm; image 1268A_016).

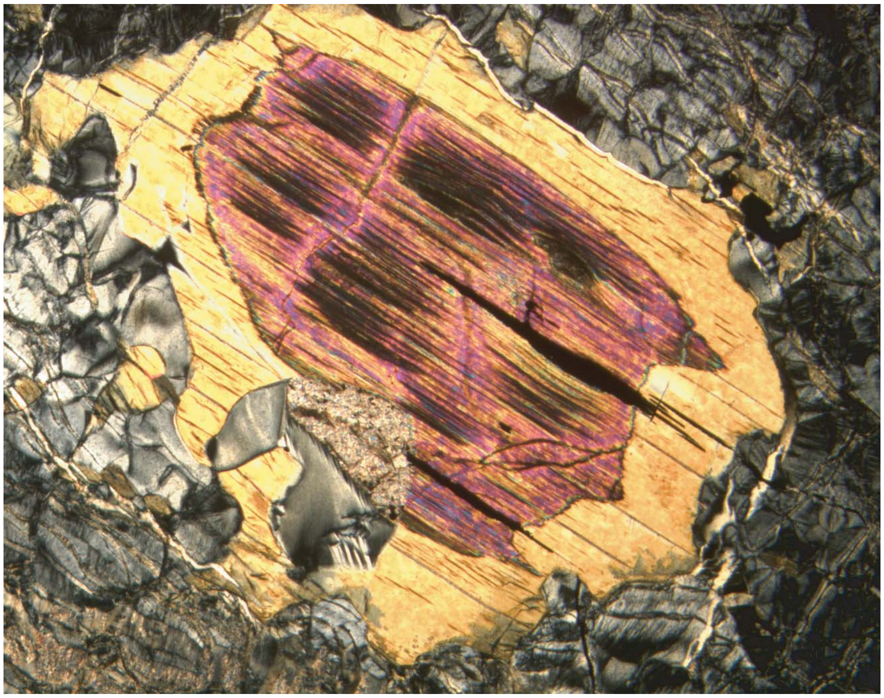

Figure F24. Photomicrograph showing ribbon-textured serpentine in the groundmass that is partly replaced by a swarm of talc + pyrite veinlets (Sample 209-1268A-4R-1, 124–127 cm) (cross-polarized light: blue filter; field of view = 1.4 mm; image 1268A_029).

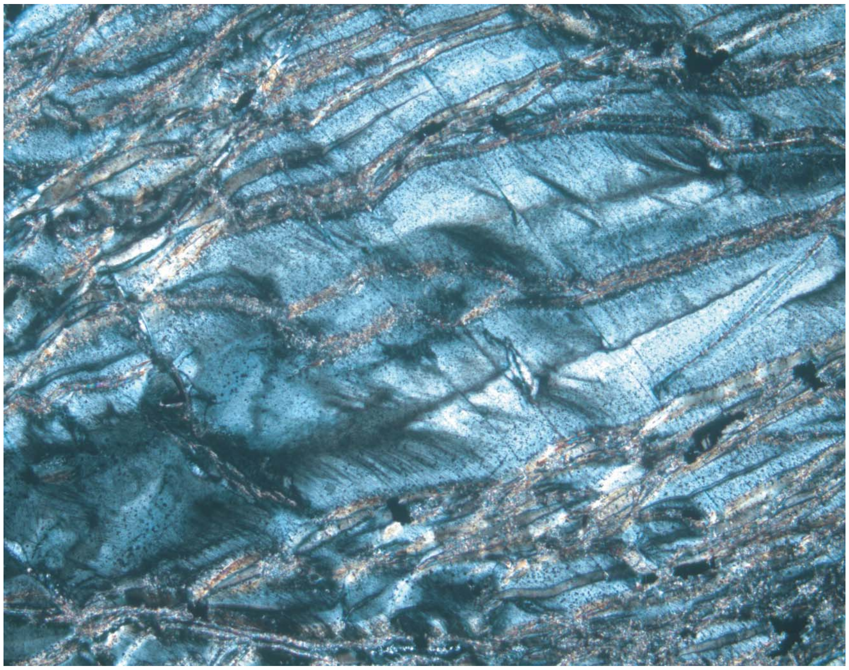

Figure F25. Photomicrograph showing a completely talc-altered rock in which the original (hourglass?) serpentinite microtexture is still preserved even though the serpentine has been completely replaced by talc (Sample 209-1268A-8R-1, 117–119 cm) (cross-polarized light: blue filter; field of view = 1.4 mm; image 1268A_051).

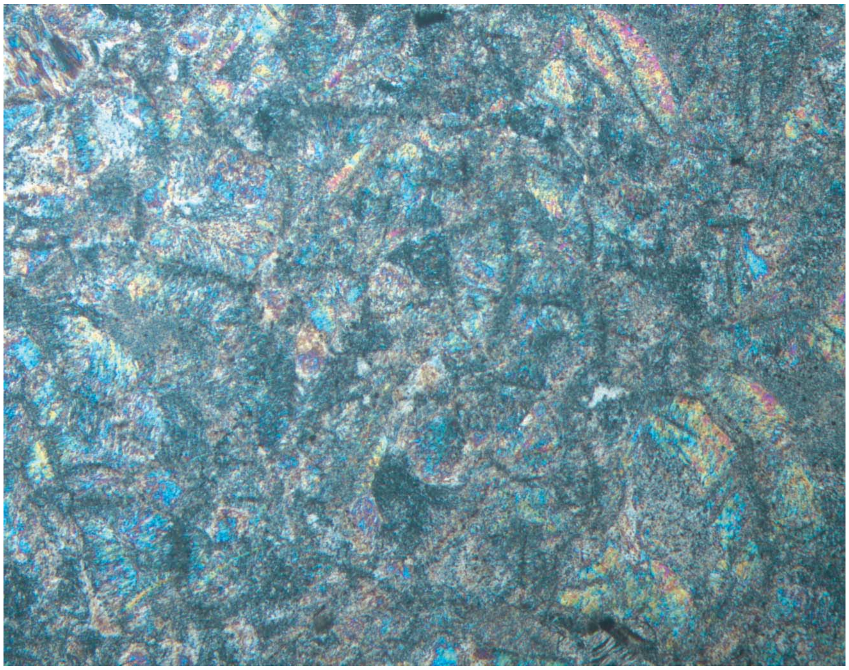

Figure F26. Photomicrograph showing a network of talc veins replacing serpentine and crosscutting chrysotile veins. Talc veins also replace the centers of serrate serpentine veins. This image demonstrates that talc alteration was initiated after serpentinization had reached an advanced stage, indicated by the presence of transitional to nonpseudomorphic textures of serpentine. Furthermore, the talc veins are crosscutting wispy chrysotile veins, which in turn crosscut even earlier chrysotile + magnetite veins. These relationships indicate that talc alteration occurred at a late stage during the metamorphic evolution of the rock (Sample 209-1268A-15R-3, 135–137 cm) (cross-polarized light: blue + gray filters; field of view = 1.4 mm; image 1268A_055).

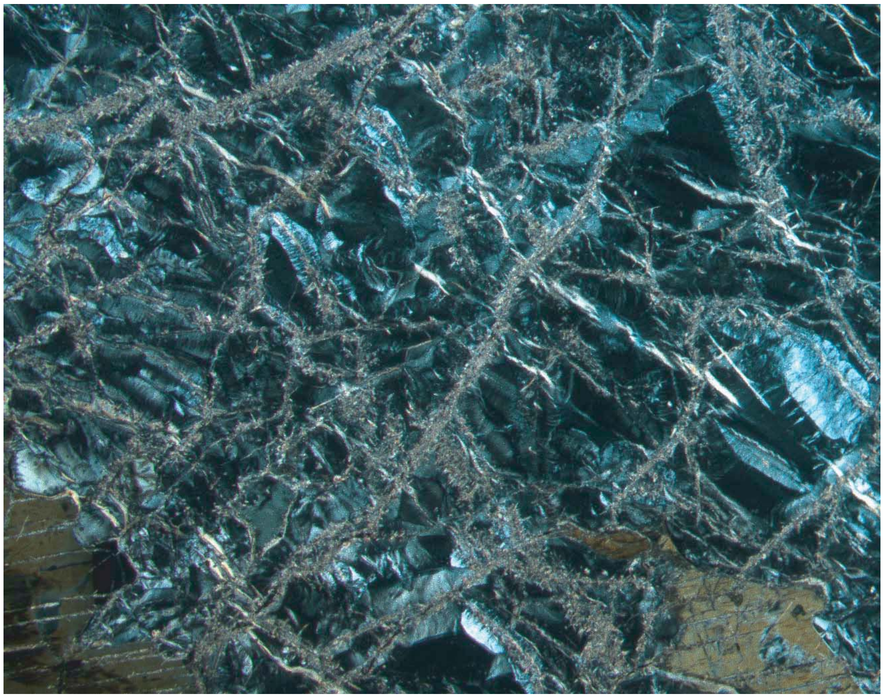

Figure F27. **A.** Photograph of hand specimen of completely serpentinized harzburgite with magmatic dikes (interval 209-1268A-13R-2, 0–8 cm). **B.** Photomicrograph of one of the magmatic dikes shown in A reveals a talc-amphibole-biotite assemblage. The amphibole (a) in the center of the image is separated from the biotite (b) by talc. The talc-amphibole-biotite vein has talc-rich halos that appear white in hand specimen (Sample 209-1268A-13R-2, 3–6 cm) (plane-polarized light: blue + light gray filters; field of view = 2.75 mm; image 1268A_022).

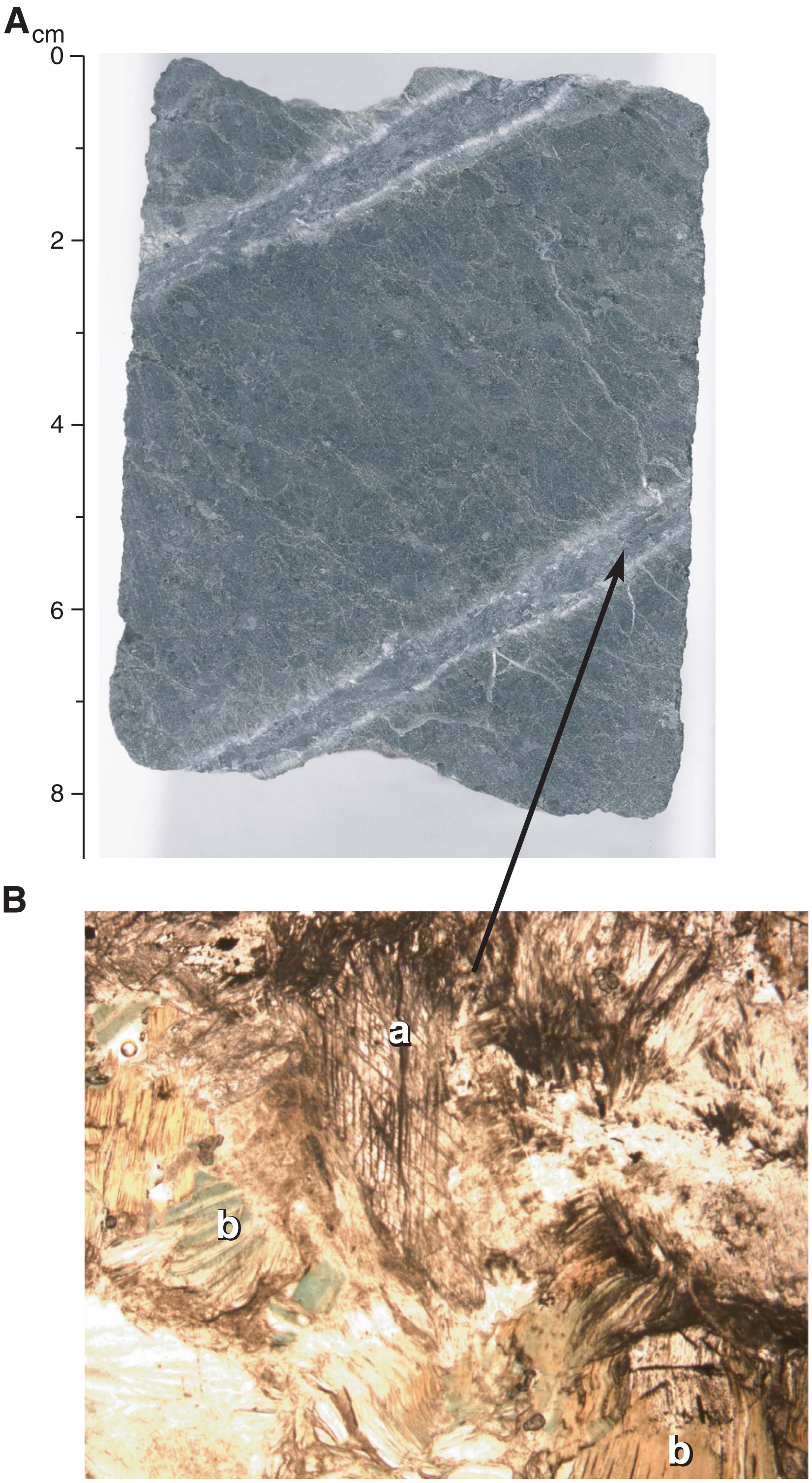

Figure F28. Close-up photograph of an example of intrusion breccias. Clasts of completely talc-altered harzburgite are hosted in a matrix consisting of completely talc-altered material interpreted as replacing fine-grained gabbro. Late, dark, talc-serpentine veins are present in the breccia matrix (interval 209-1268A-14R-1, 133–146 cm).

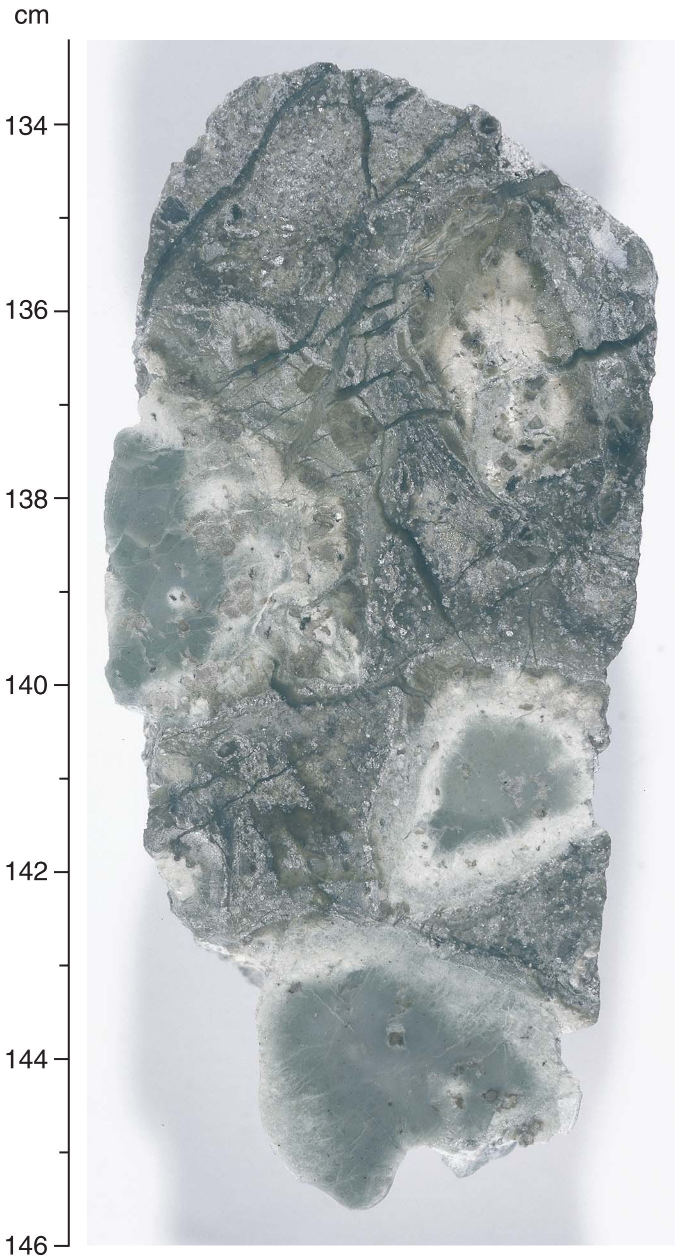

Figure F29. Close-up photograph showing a small intrusion of gabbro into serpentinized harzburgite. The gabbro is represented by the rubbly, talc-altered material in the center of this section. The margins of the serpentinized harzburgite are overprinted by talc alteration. This observation suggests that at least some of the observed talc alteration is related to the presence of gabbro (interval 209-1268A-16R-2, 43–96 cm).

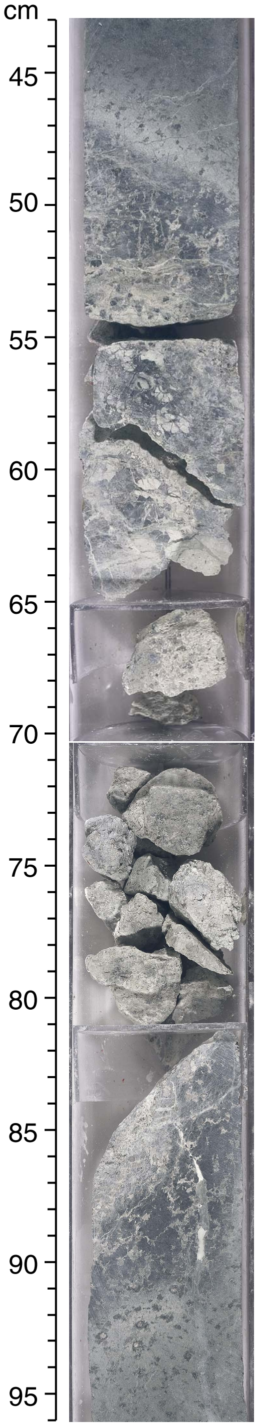

Figure F30. Close-up photograph depicting a moderately altered gabbro. Presumed orthopyroxene is completely altered to talc ± chlorite (brown), whereas clinopyroxene (gray) is partly altered to green amphibole and chlorite (interval 209-1268A-21R-1, 37–43 cm).

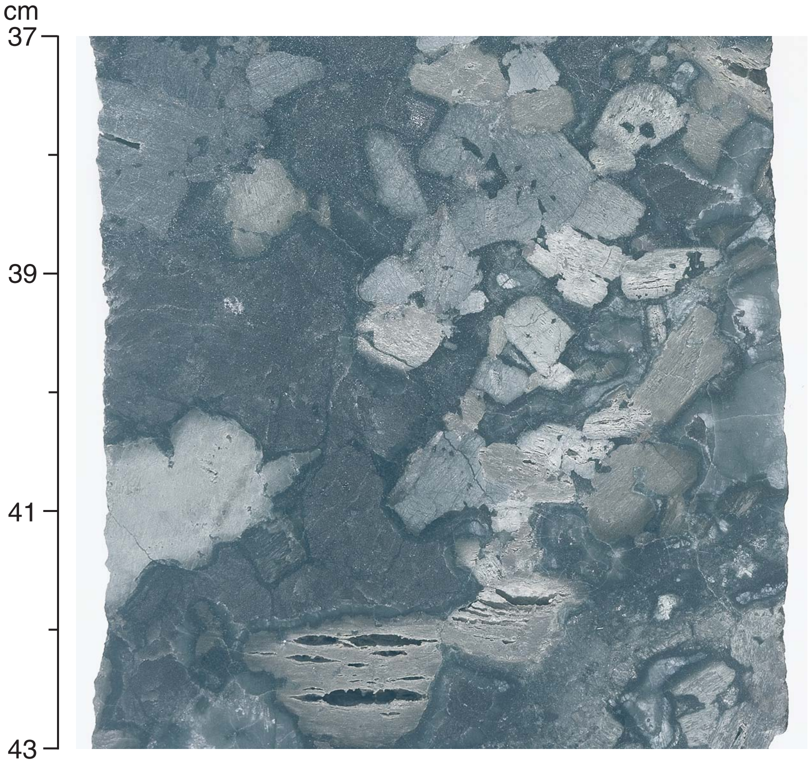

Figure F31. Photomicrograph showing the image of two pyroxenes in thin section of the gabbro in the lower portion of Hole 1268A. Brown, low-relief pyroxene on the left is completely pseudomorphed by talc and may have been orthopyroxene. Pale green, high-relief pyroxene on the right is largely fresh clinopyroxene. In between the two pyroxene crystals is plagioclase that reacted with the pyroxenes to form chlorite (green, surrounding the plagioclase) (Sample 209-1268A-28R-2, 26–28 cm) (plane-polarized light: blue + gray filters; field of view = 2.75 mm; image 1268A_043).

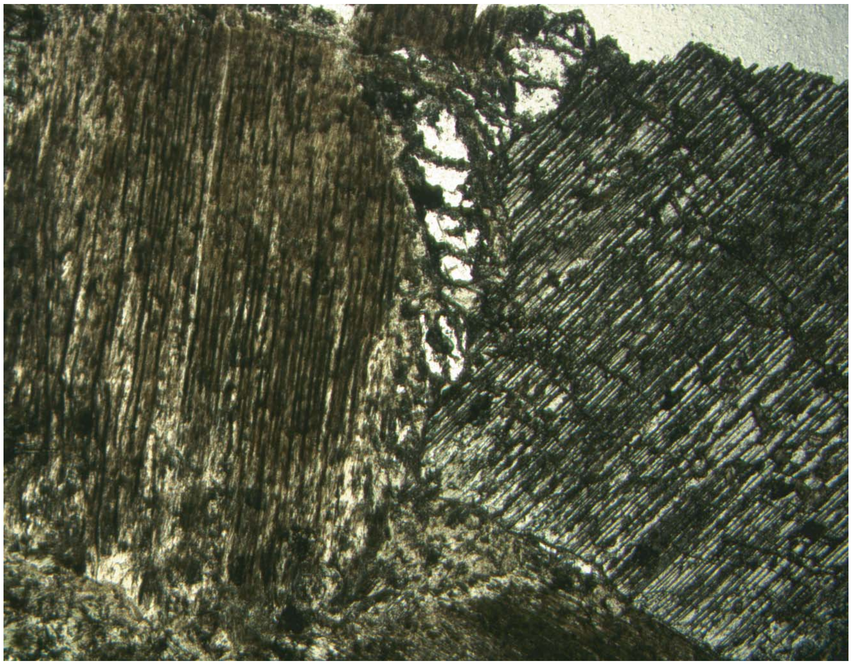

Figure F32. Close-up photograph of pronounced dark coronas created along the grain boundaries of plagioclase and pyroxene due to the formation of chlorite and amphibole (interval 209-1268A-20R-3, 42–53 cm).

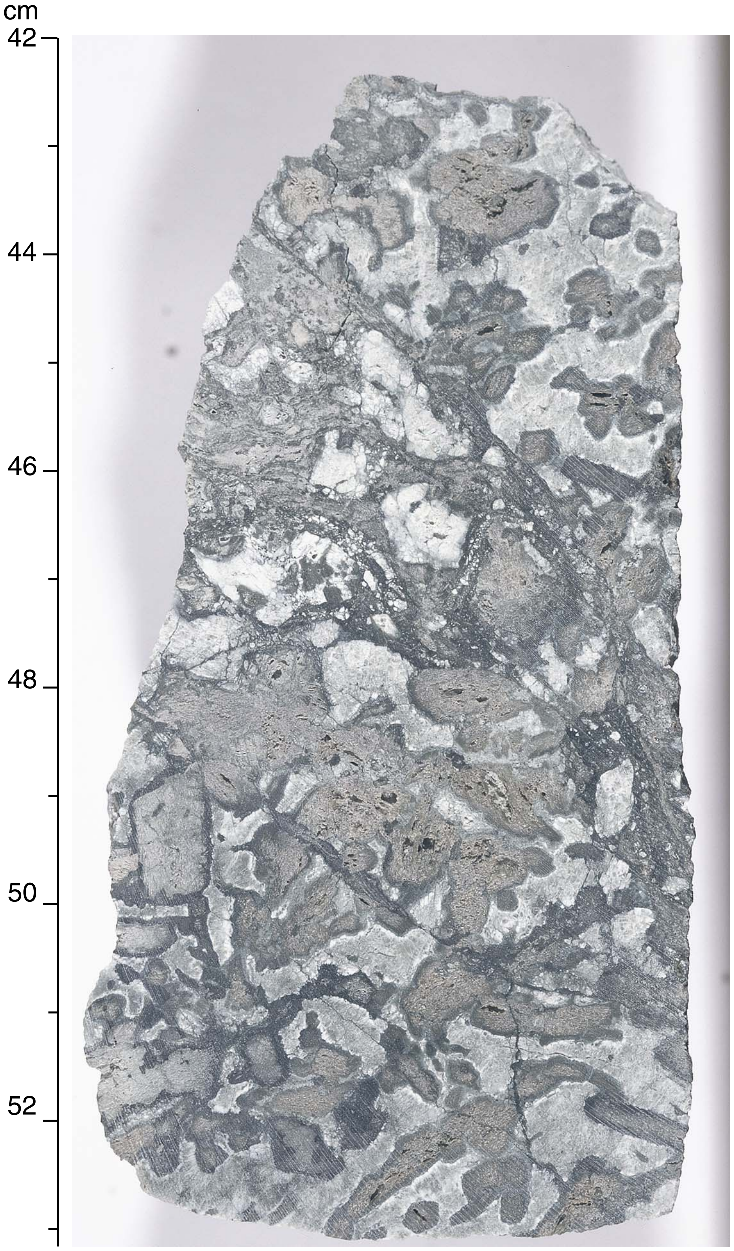

Figure F33. Photomicrograph showing green amphibole (acicular) and chlorite (fibrous, anomalous interference colors) formed on a triple junction between two plagioclase and a clinopyroxene grain in gabbronorite (Sample 209-1268A-27R-1, 64–66 cm) (crossed polarized light: blue filter; field of view = 1.4 mm; image 1268A_041).

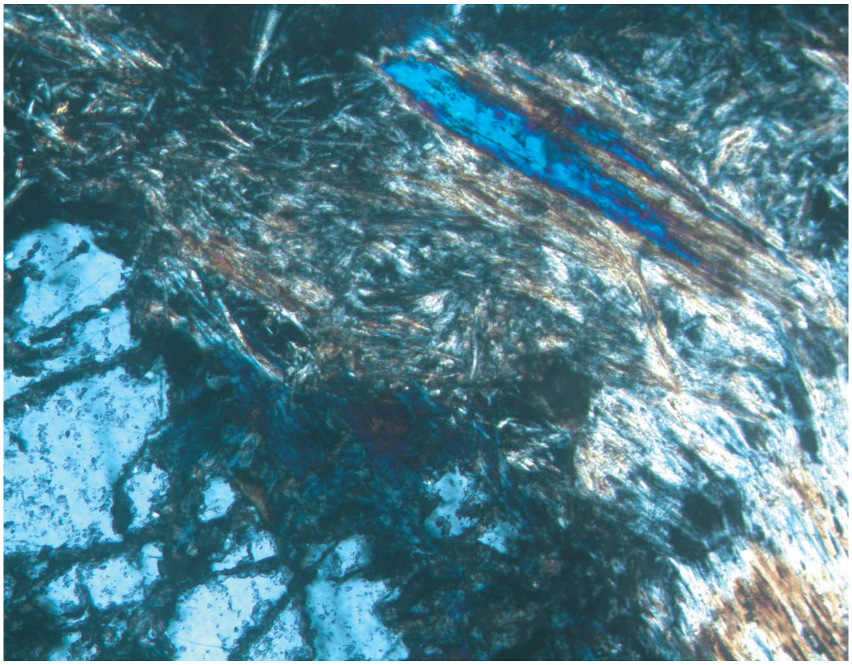

Figure F34. Photomicrograph showing plagioclase replaced by chlorite (chl) and quartz (qtz) in a completely altered gabbro (Sample 209-1268A-21R-1, 129–131 cm) (cross-polarized light: blue + gray filters; field of view = 2.75 mm; image 1268A_045).

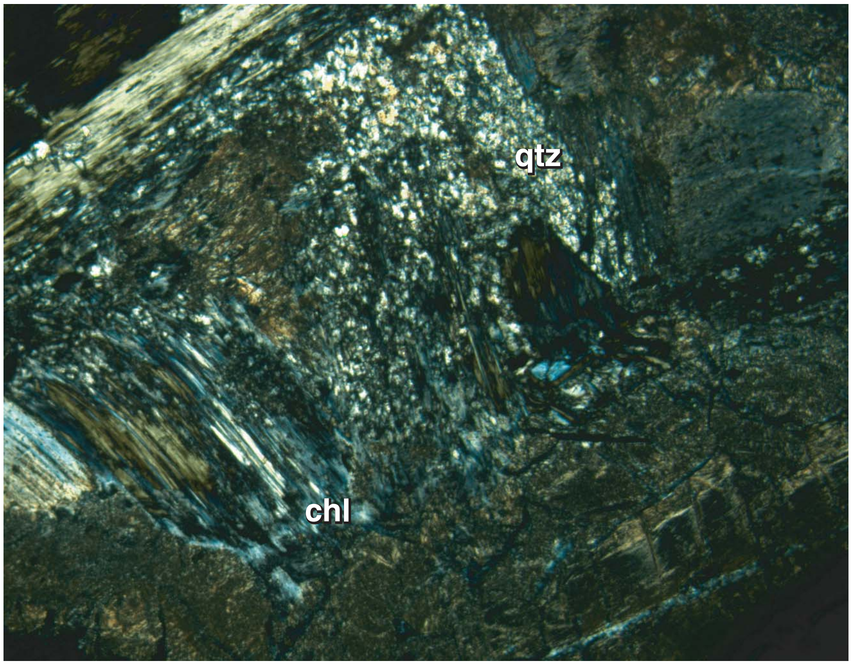

Figure F35. Variation of alteration intensity in Hole 1268A. The degree of alteration represents the volume percent replacement of primary minerals by secondary minerals. Horizontal lines mark lithologic boundaries. TD = total depth.

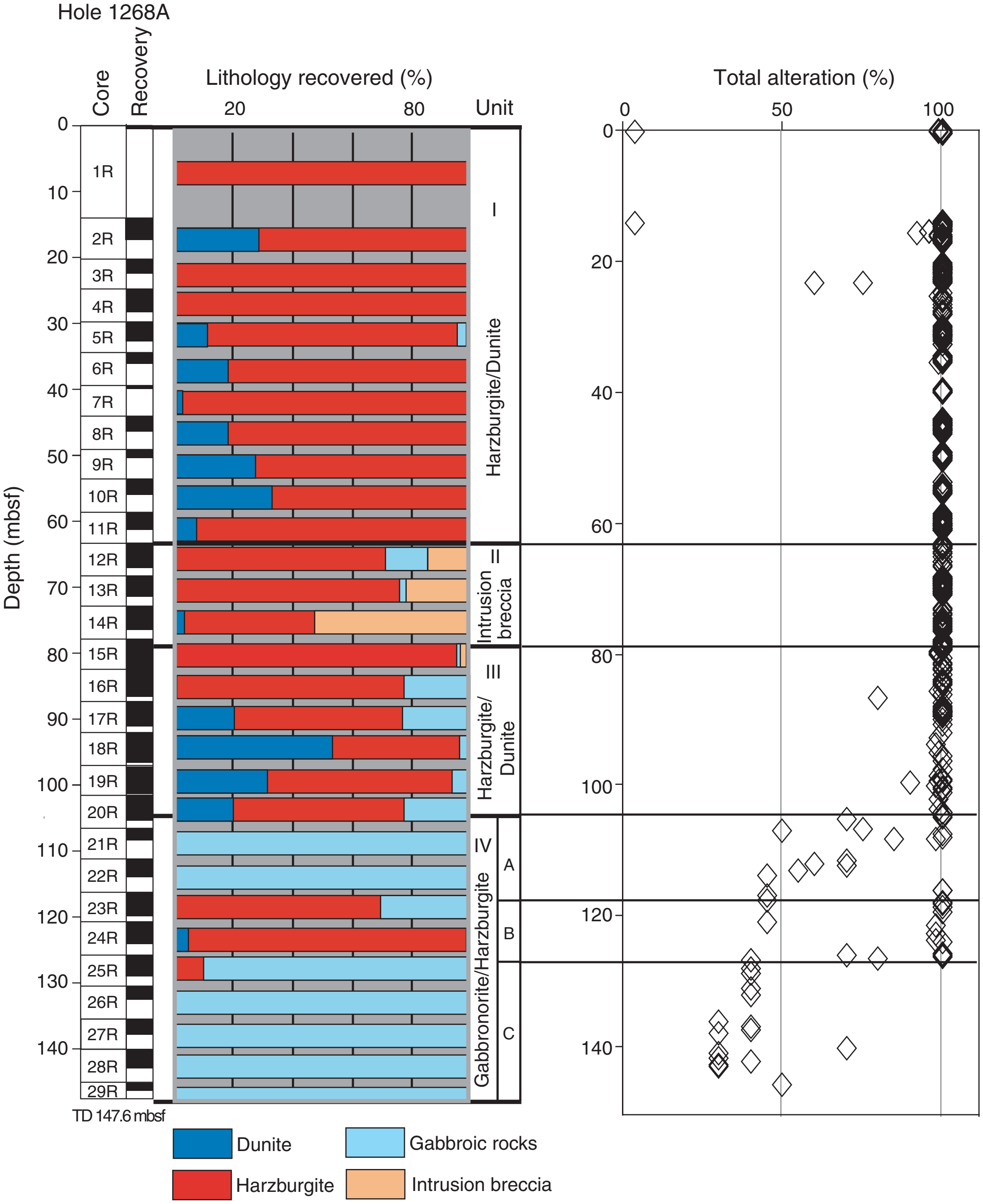

Figure F36. Downhole variability in the abundance of metamorphic veins. **A.** Abundance of veins with oxides, chlorite, and sulfides. **B.** Abundance of veins with talc and serpentine. Horizontal lines mark lithologic boundaries. TD = total depth.

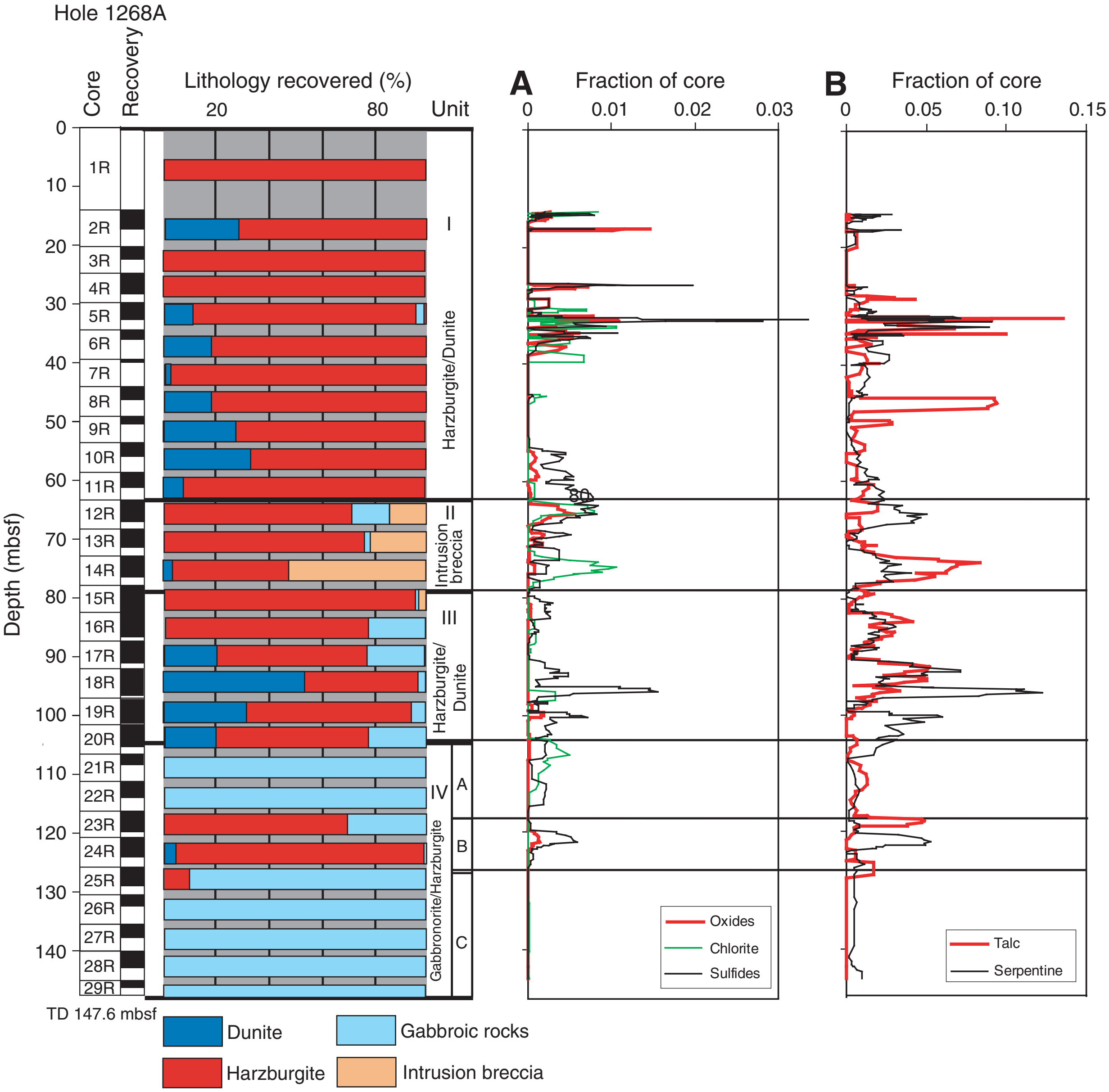

Figure F37. Volume percentage of minerals in veins in Hole 1268A (large pie chart in center) and the distribution of individual minerals (small pie charts) in the different vein populations distinguished in this work (see Table T3, p. 157).

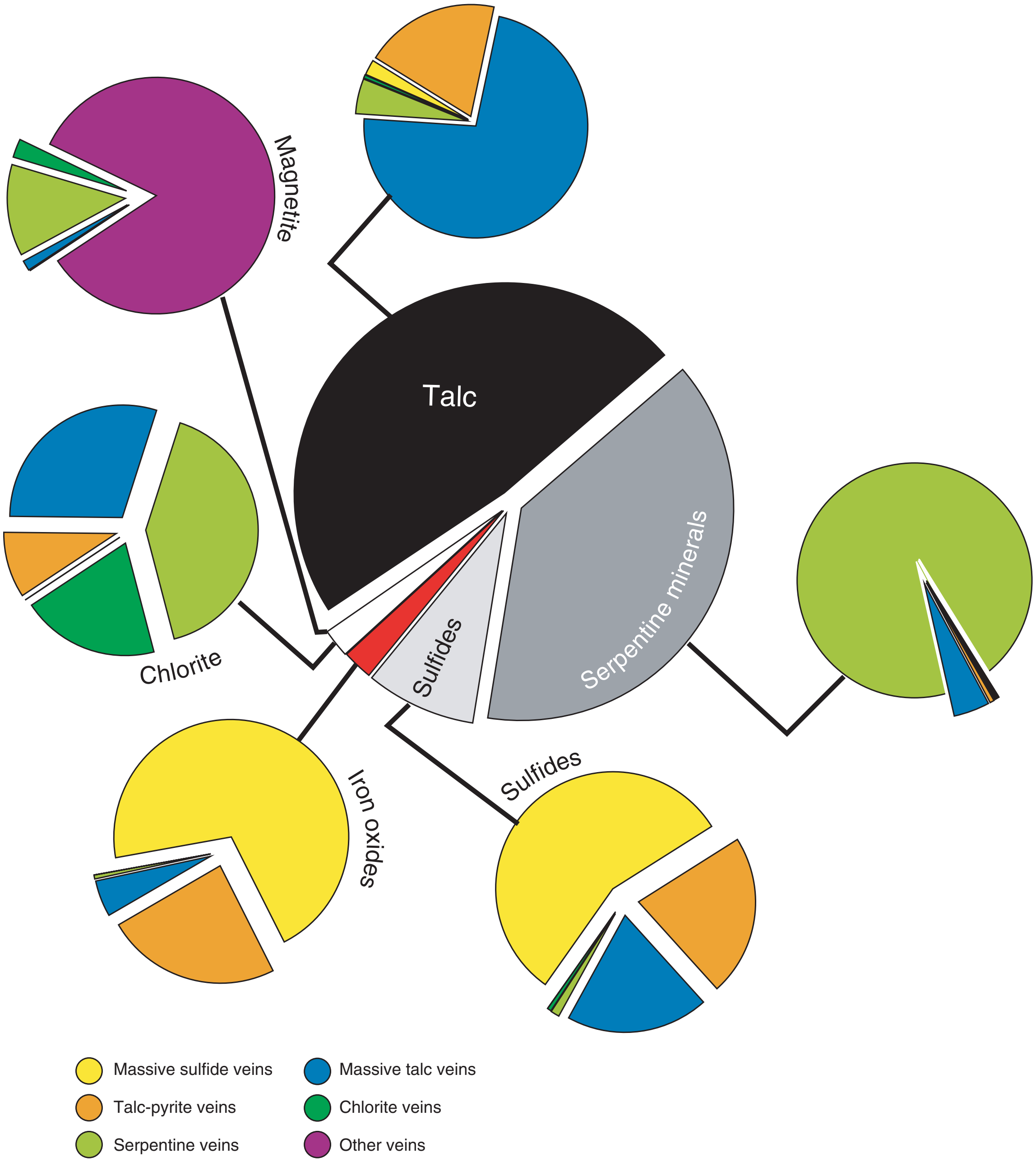

Figure F38. Histograms illustrating (**A**) vein texture, (**B**) vein shape, (**C**) vein structure, and (**D**) vein connectivity of different vein populations in Hole 1268A peridotites (see **"Metamorphic Petrology,"** p. 7, in the "Explanatory Notes" chapter for details on classification of veins). MSV = massive sulfide veins, TPV = talc-pyrite veins, MTV = massive talc veins, SPV = serpentine veins.

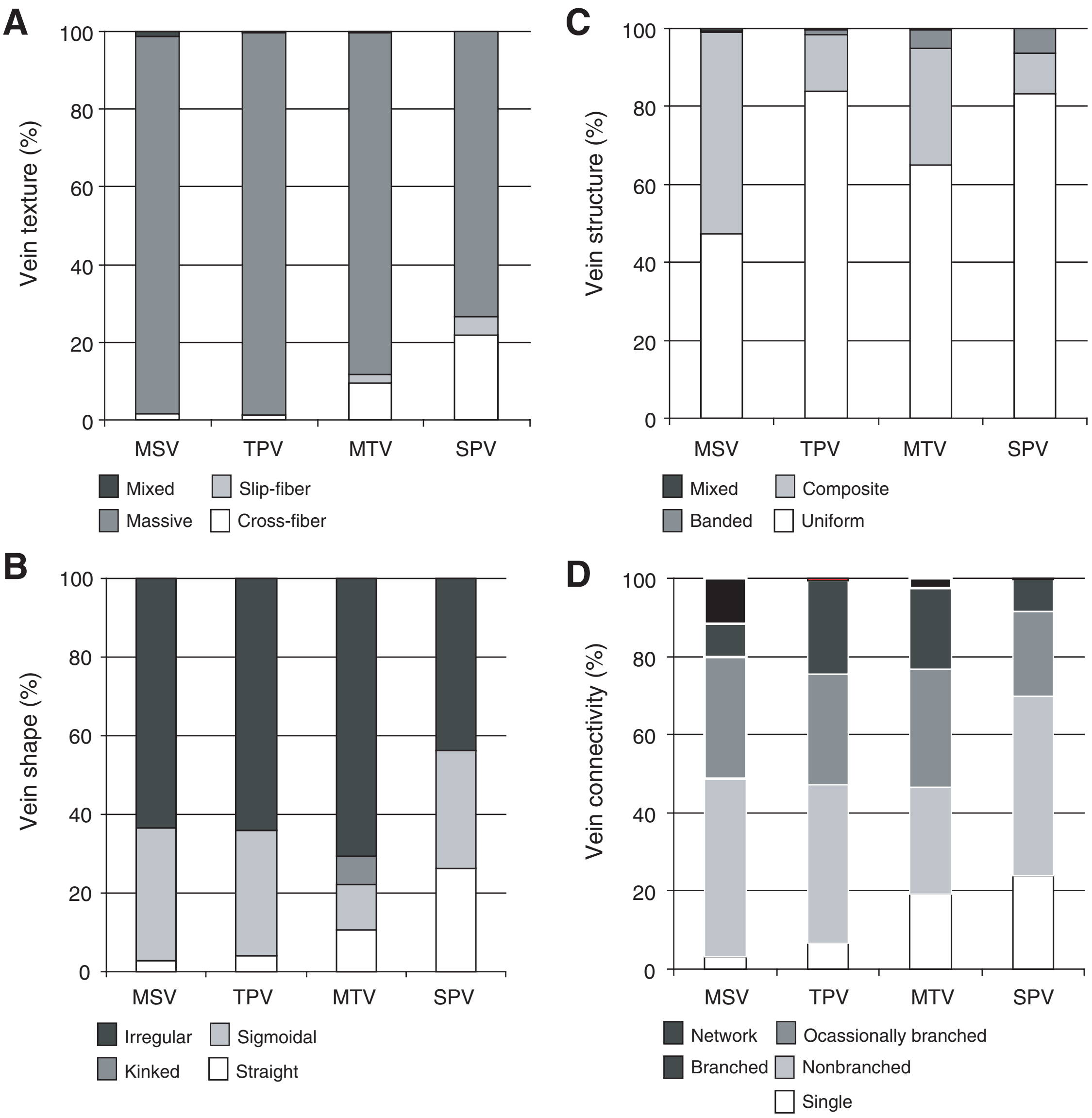

Figure F39. Photomicrographs illustrating crosscutting relationships between different generations of veins in Hole 1268A. **A.** Late pyrite-hematite vein cuts and transposes previous veins of chrysotile—now replaced by talc and bastite (Sample 209-1268A-13R-1, 68–71 cm) (cross-polarized light: blue + gray filters; field of view = 2.75 mm; image 1268_021). **B.** Bastite cut by a massive talc vein and locally replaced along cleavage by talc. The massive talc vein also crosscuts chrysotile veins—now pseudomorphed to talc and an earlier talc-pyrite vein (Sample 209-1268A-12R-3, 71–74 cm) (cross-polarized light: blue + light gray filters; field of view = 2.75 mm; image 1268A_019). **C, D.** Boundary between serpentine background alteration and overprinting talc alteration. An early chrysotile vein is replaced by late, nonpseudomorphic massive talc alteration, becoming a "ghost vein" in the area of talc alteration (to the lower right) (Sample 209-1268A-14R-3, 3–5 cm) (field of view = 2.75 mm); (C) cross-polarized light: blue filter; image 1268A_027; (D) plane-polarized light: blue + light gray filters; image 1268A_028.

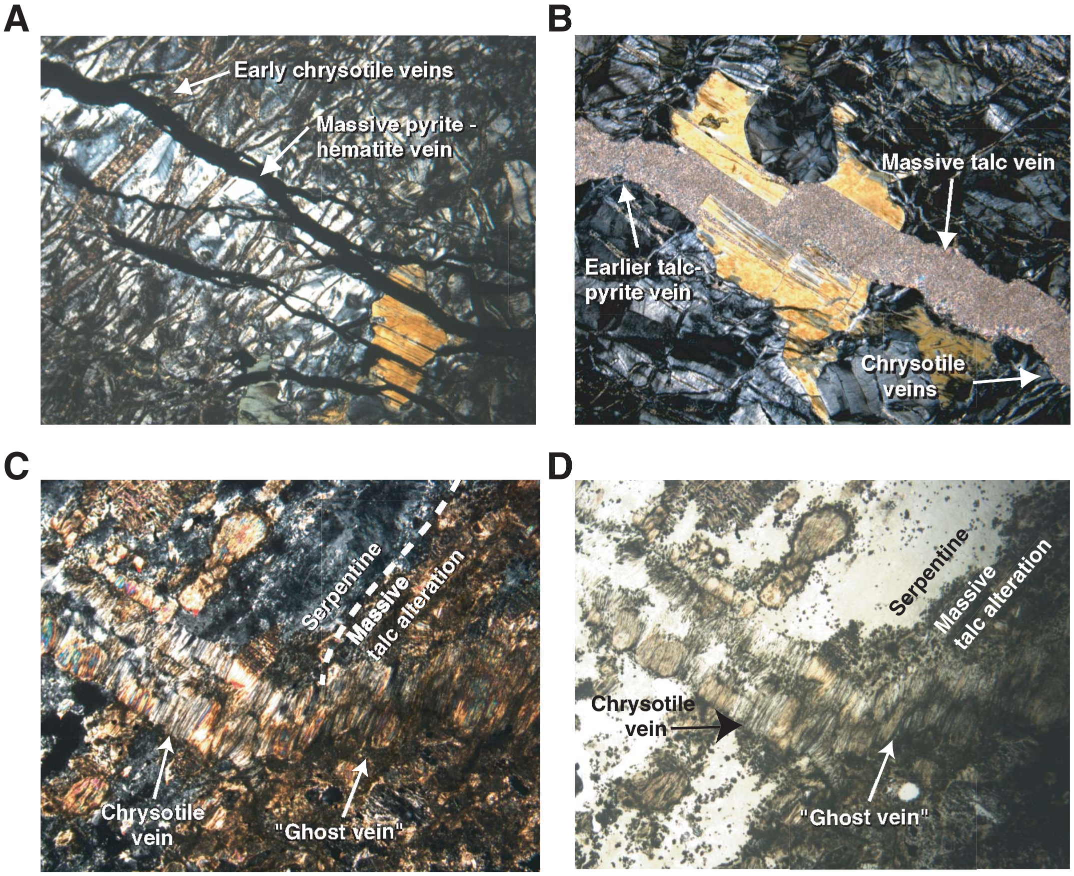

Figure F40. Close-up photographs of core sections illustrating crosscutting relationships between different generations of veins in Hole 1268A. **A.** Early pyrite-hematite vein network is crosscut by later talc-pyrite vein (interval 209-1268A-3R-2, 102–116 cm). **B.** Pyrite-hematite vein (arrowed) fading as it approaches a zone of talc alteration (interval 209-1268A-3R-2, 124.5–130 cm). **C.** Ghost pyrite-hematite veins fading in proximity to late talc alteration. A serpentine vein system is developed subparallel to the leading edge of the talc alteration front (interval 209-1268A-3R-2, 96–100 cm). **D.** Late massive talc vein crosscutting and offsetting earlier talc-pyrite veins. This relationship suggests that the emplacement of the massive talc vein was synchronous with normal faulting (interval 209-1268A-11R-1, 126–136 cm).

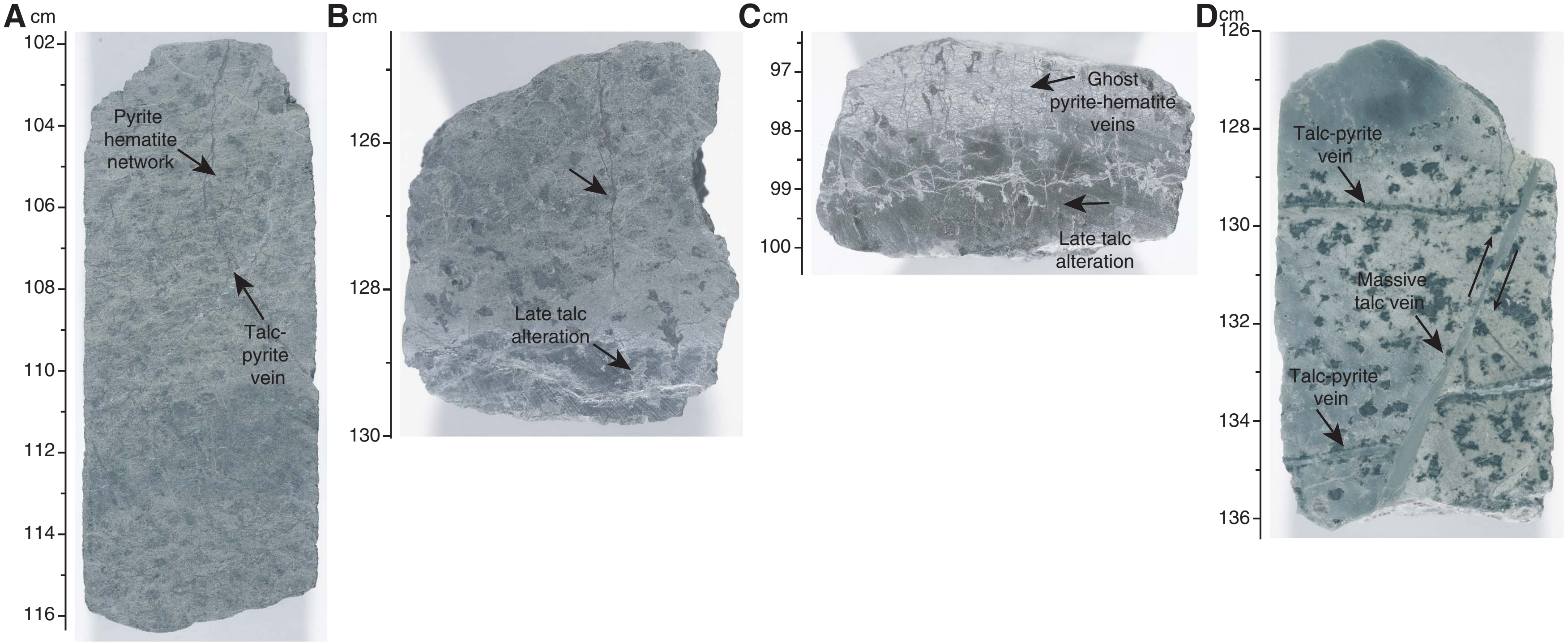

Figure F41. Relative timing of alteration and veining events affecting basement at Site 1268. See text for details.

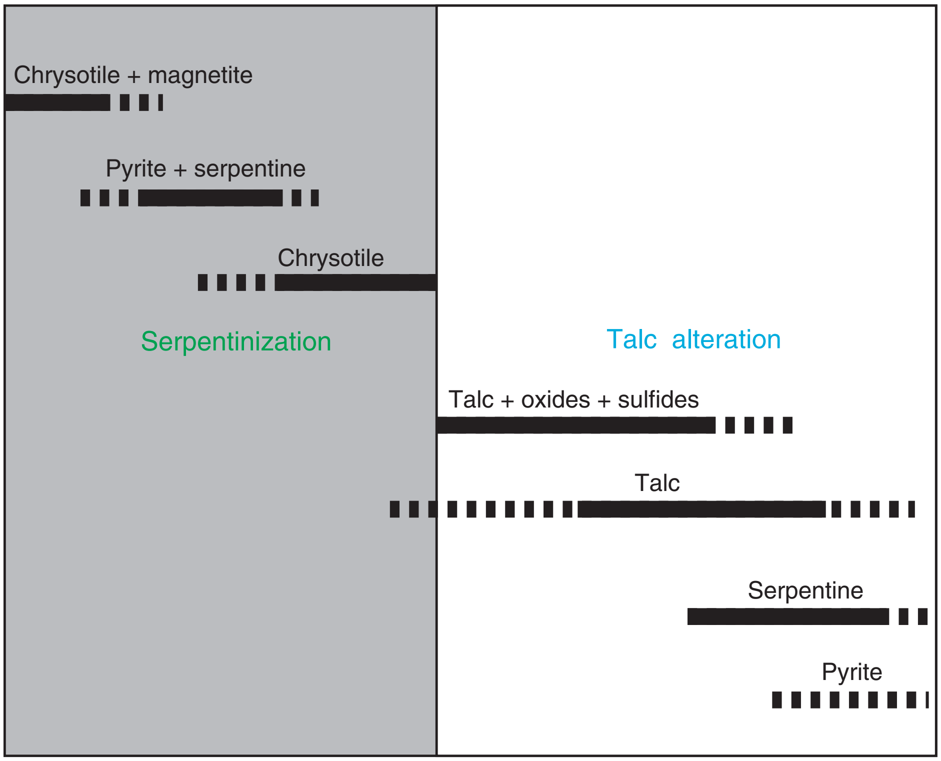

Figure F42. Phase diagram for the Fe-Ni-S-O system at 300°C and 2 kbar. Phase boundaries of Fe phases are marked by thick lines, those of Ni phases and Ni-Fe alloys are thin lines, and others are dashed lines. Fe phases: Hem = hematite (Fe_2O_3), Py = pyrite (FeS_2), Mt = magnetite (Fe_3O_4), Po = pyrrhotite ($Fe_{1-x}S$); Ni and Ni-Fe phases: Va = vaesite (NiS_2), Pd = polydymite (Ni_3S_4), Mi = millerite (NiS), Hz = heazlewoodite (Ni_3S_2), Ta = taenite (TagFeNi), Aw = awaruite (Ni_3Fe), Ka = kamacite (αFeNi). Oxide/sulfide phase boundaries are simplified after Frost (1985); others are calculated with SUPCRT92 (Johnson et al., 1992). **A.** Fields mark oxide-sulfide assemblages observed in Hole 1268A, red arrow = inferred evolution path. **B.** Fields mark oxide-sulfide assemblages observed in Hess Deep and the Kane Fracture Zone (MARK) areas (Alt and Shanks, 1998, 2003).

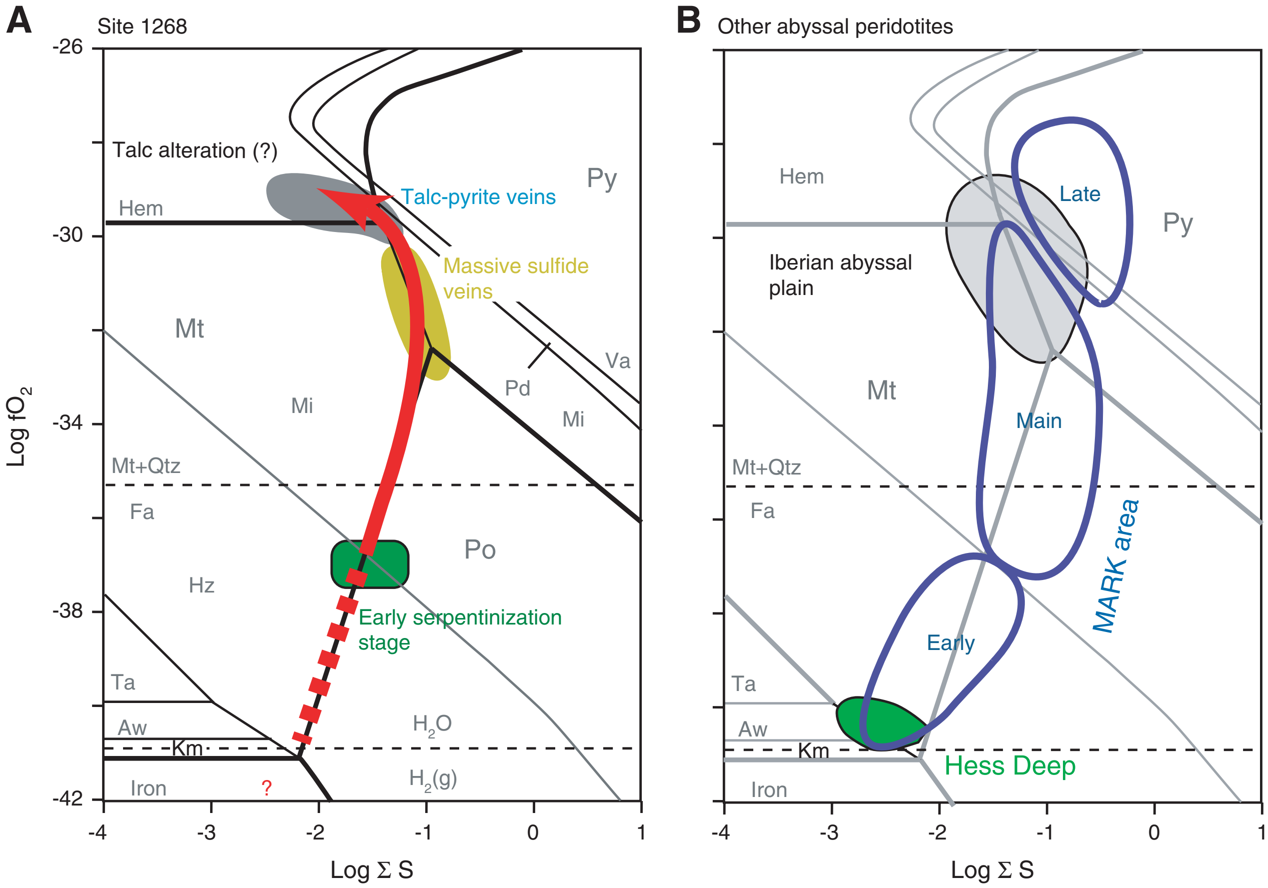

Figure F43. Variation in crystal-plastic deformation intensity and orientation of crystal-plastic foliation with depth. **A.** Plot of average deformation intensity vs. depth. The locations of major mylonite zones are also shown as gray bands. **B.** Plot of the dip of the crystal-plastic foliation in the core reference frame vs. depth. TD = total depth.

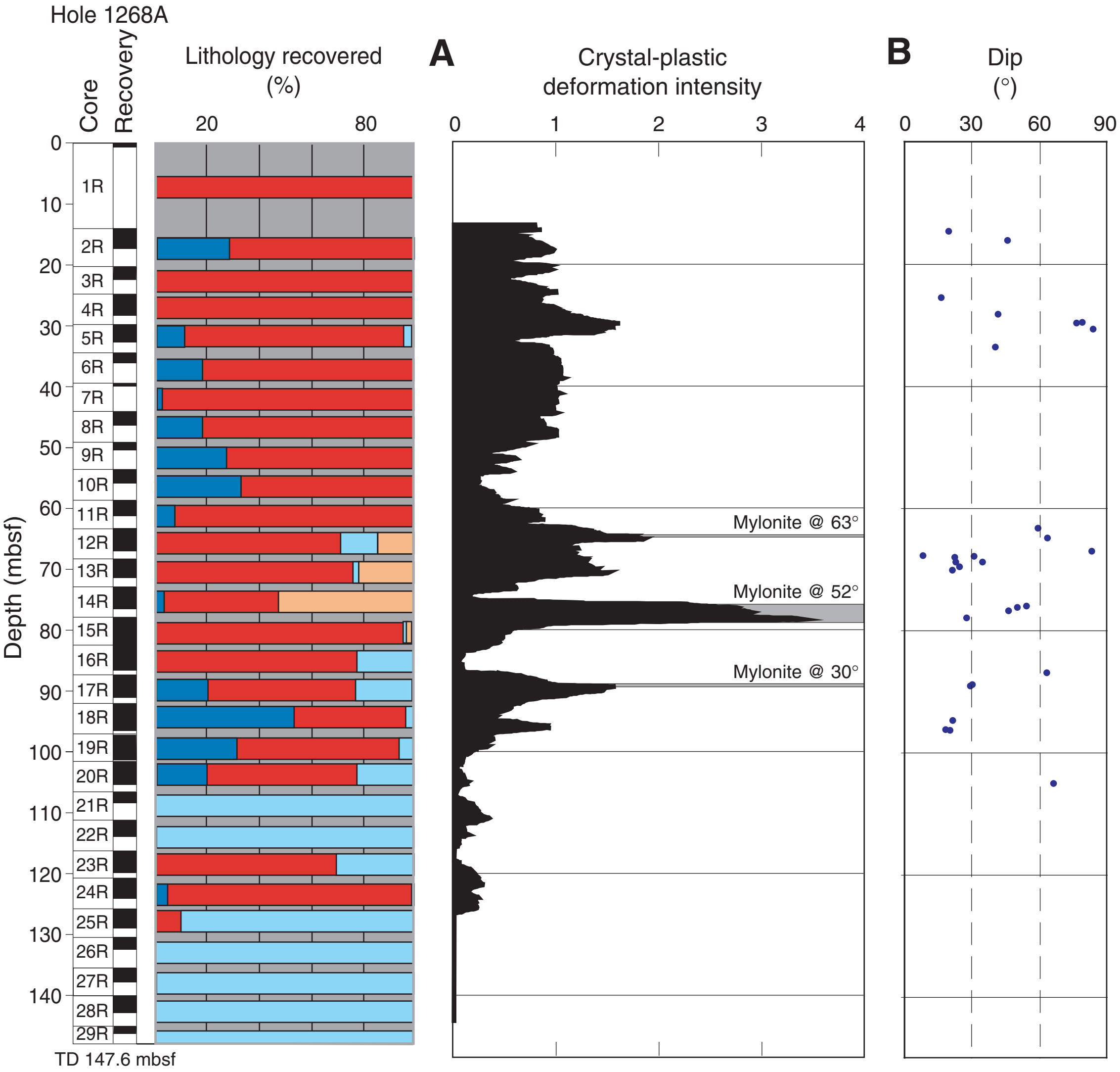

Figure F44. Photomicrographs showing protogranular and protointergranular textures. **A.** Protogranular serpentine bastite after orthopyroxene (Sample 209-1268A-13R-2, 3–6 cm) (cross-polarized light [XPL]: blue filter; field of view [FOV] = 2.75 mm; image 1268A_016). **B.** Protogranular texture showing interlocking orthopyroxene and olivine (Sample 209-1268A-3R-3, 6–9 cm) (XPL: blue + light gray filters; FOV = 2.75 mm; image 16268A_014). **C.** Protointergranular serpentine bastite after orthopyroxene showing the ragged, embayed, commonly intergranular appearance of orthopyroxene pseudomorphs that are characteristic of this texture (Sample 209-1268A-2R-2, 70–73 cm) (XPL: blue filter; FOV = 5.5 mm; image 1268A_046). **D.** Spinel clot intergrown with small serpentine bastite after orthopyroxene in a protointergranular harzburgite (Sample 209-1268A-19R-1, 51–53 cm) (XPL: blue filter; FOV = 1.4 mm; image 1268A_048). (Continued on next page.)

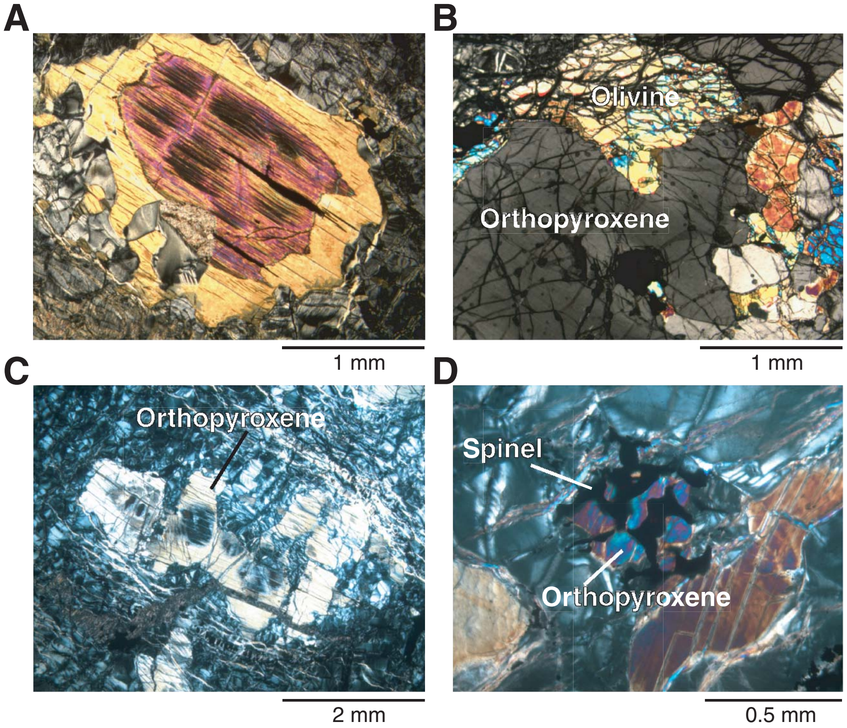

Figure F44 (continued). **E.** Strain-free serpentine bastites replacing large orthopyroxene neoblasts with a well-developed polygonal texture following high-temperature deformation of a primary orthopyroxene grain (Sample 209-1268A-17R-3, 66–68 cm) (XPL: blue filter; FOV = 1.4 mm; image 1268A_047). **F.** Recrystallized plagioclase in an otherwise little deformed gabbro showing polygonal texture. Locally there are slightly bent plagioclase grains with deformation twins (Sample 209-1268A-21R-1, 37–39 cm) (XPL: blue + gray filters; FOV = 5.5 mm; image 1268A_050). **G.** Olivine with kink bands showing protogranular texture. Note equigranular nature and large grain size in this textural type (Sample 209-1268A-4R-1, 124–127 cm) (XPL: blue filter; FOV = 1.4 cm; image 1268A_029).

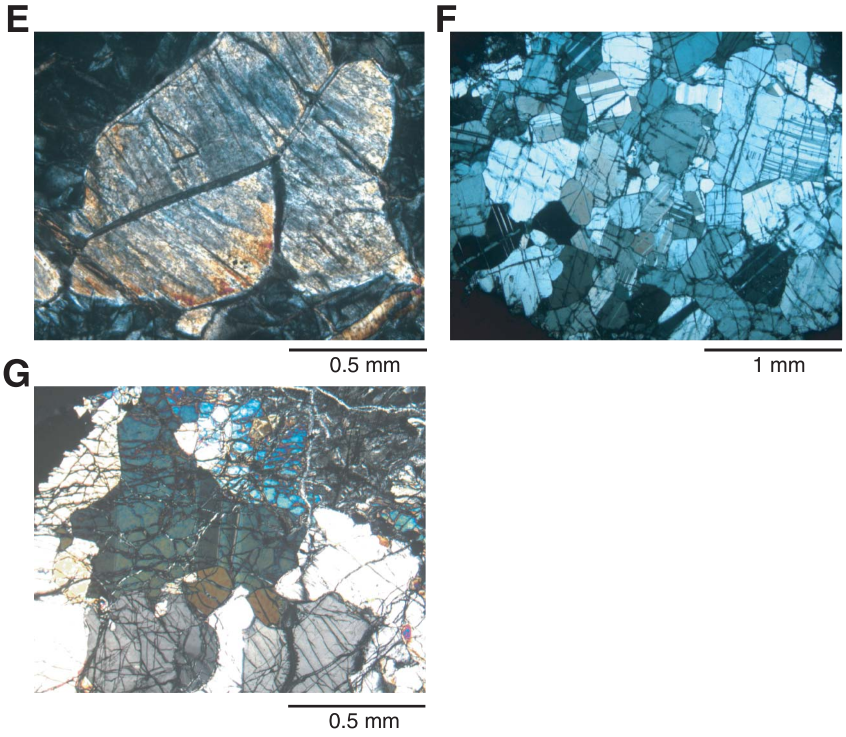

Figure F45. Photographs of a weakly foliated protogranular harzburgite with a subvertical pyroxenite vein on the left side of the core. An expanded negative view of the inset area outlined in the core is also shown for clarity. The subvertical pyroxenite vein cuts a weak, low-angle foliation in the harzburgite and is not affected by the crystal-plastic deformation. The negative image (inset) shows the pyroxenite vein (PX) cut by serpentine-talc veins (S). One of these alteration veins merges with the pyroxenite vein and then follows it, as is common in the magmatic veins. As a result, the magmatic veins are significantly altered (interval 209-1268A-15R-3, 97–126 cm).

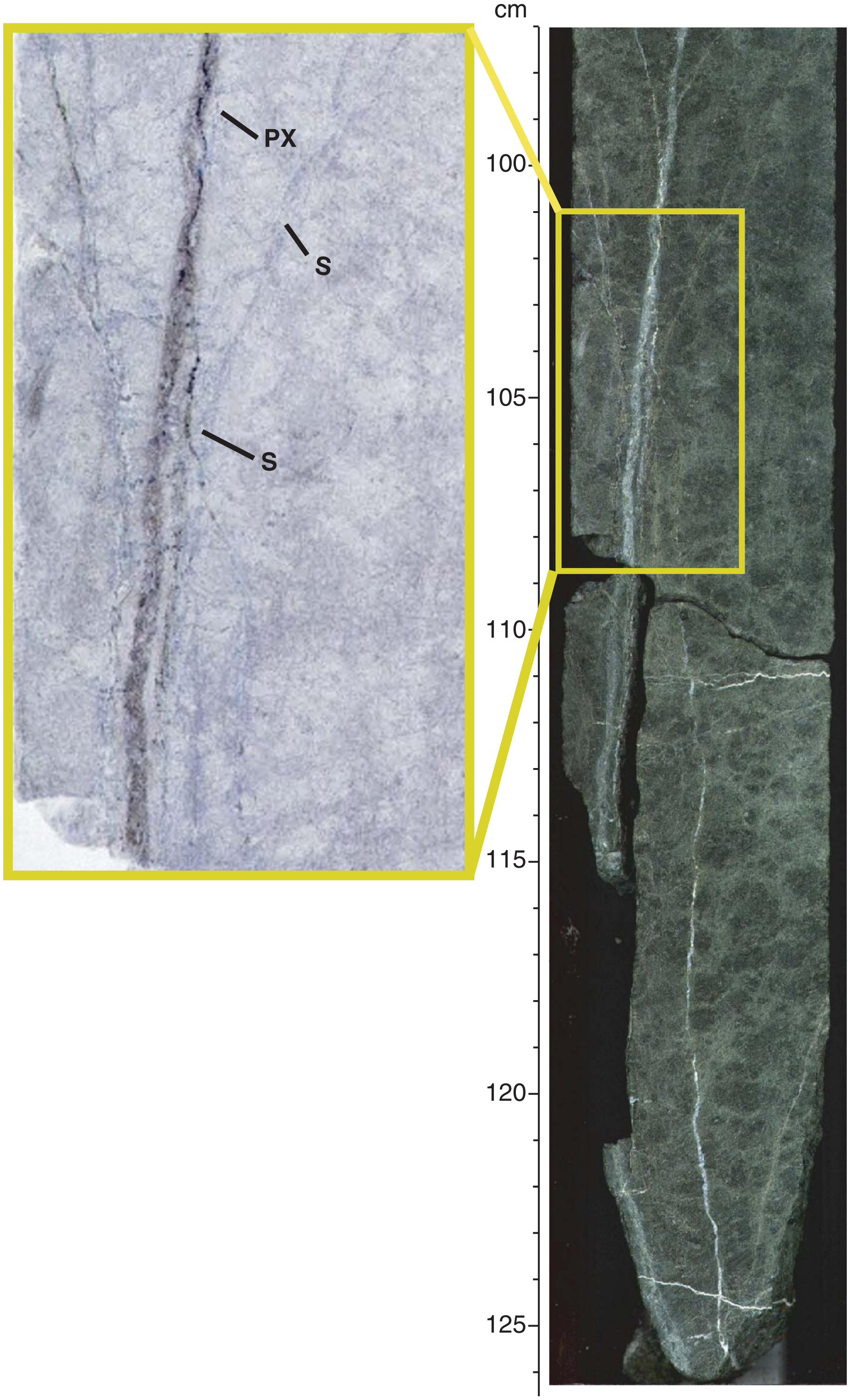

Figure F46. Close-up photograph of an example of protointergranular texture with ragged outlines of orthopyroxene, areas of sparse orthopyroxene within the harzburgite, and a weak crystal-plastic foliation (interval 209-1268A-4R-2, 91–100.5 cm).

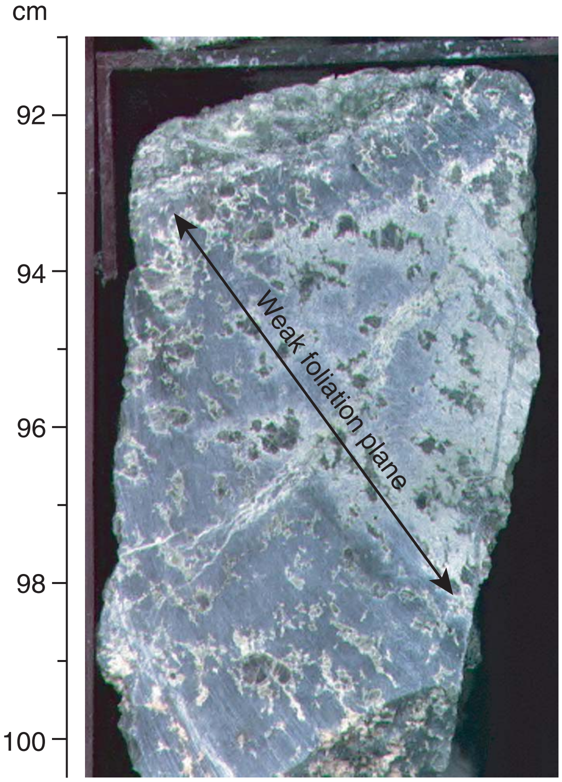

Figure F47. Histogram showing the proportions of the core exhibiting different crystal-plastic deformation intensities.

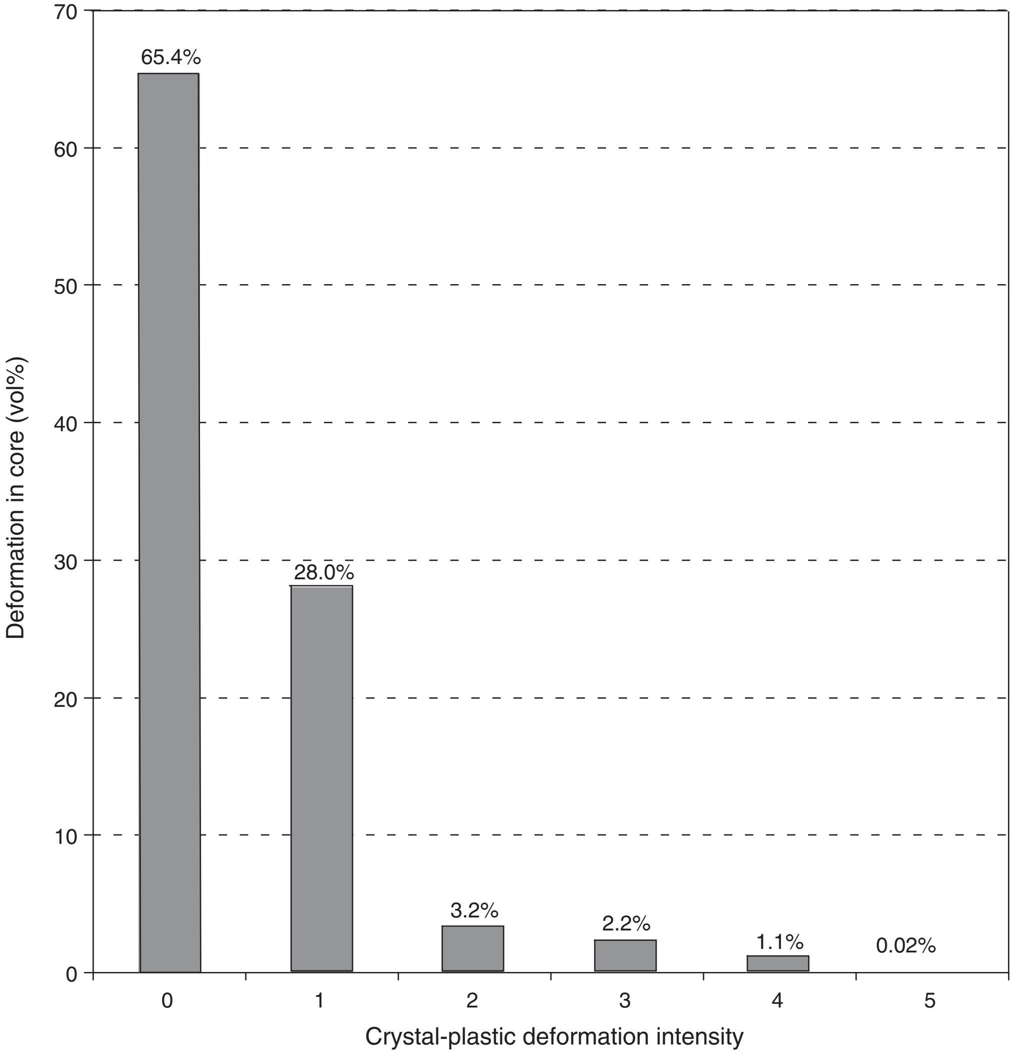

Figure F48. Close-up photographs of a ductile shear zone in which the foliation orientation and foliation intensity changes from the upper left (undeformed; grade = 0.5) to lower right (porphryroclastic mylonite; grade = 4). Both true color (dark) and negative (light) images are shown for clarity. Lines on negative images define the local orientation of the foliation, which tracks the finite strain ellipse as the high-strain mylonite is approached. The shear sense from this fanning orientation is reverse (Ramsay and Ghram, 1970). In addition, the inset is an enlargement of the negative image (right) that shows porphyroclasts with sigma-shaped pressure shadows. As shown in the inset, the pressure shadows also indicate a reverse sense of shear. The mylonite is cut by two coarse-grained, undeformed pyroxenite veins (Px) (interval 209-1268A-15R-1, 1–22 cm).

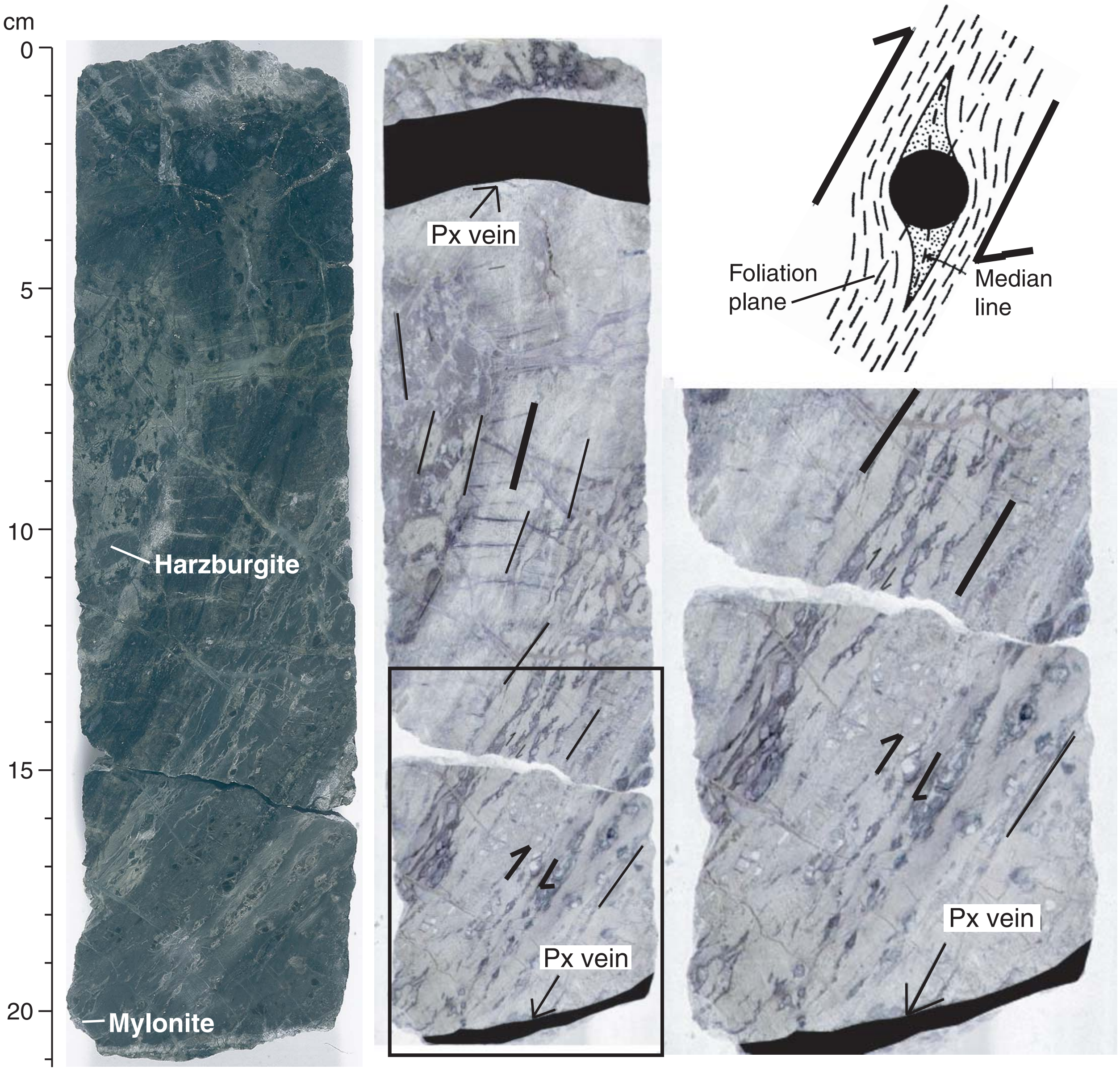

Figure F49. Close-up photographs showing a serpentinized mylonite zone (negative and positive images). A porphyroclast and pressure shadow tail of recrystallized (now altered) clinopyroxene was used to determine a reverse sense of shear (Passchier and Simpson, 1986). The mylonite is also cut by postkinematic pyroxenite (Px) veins and serpentinite veins (S) indicating continued magmatic activity after cessation of crystal-plastic deformation, later followed by serpentine alteration. As discussed in the text, this sample also contains pyroxenite that was pre- or synkinematic (interval 209-1268A-14R-3, 19–31 cm).

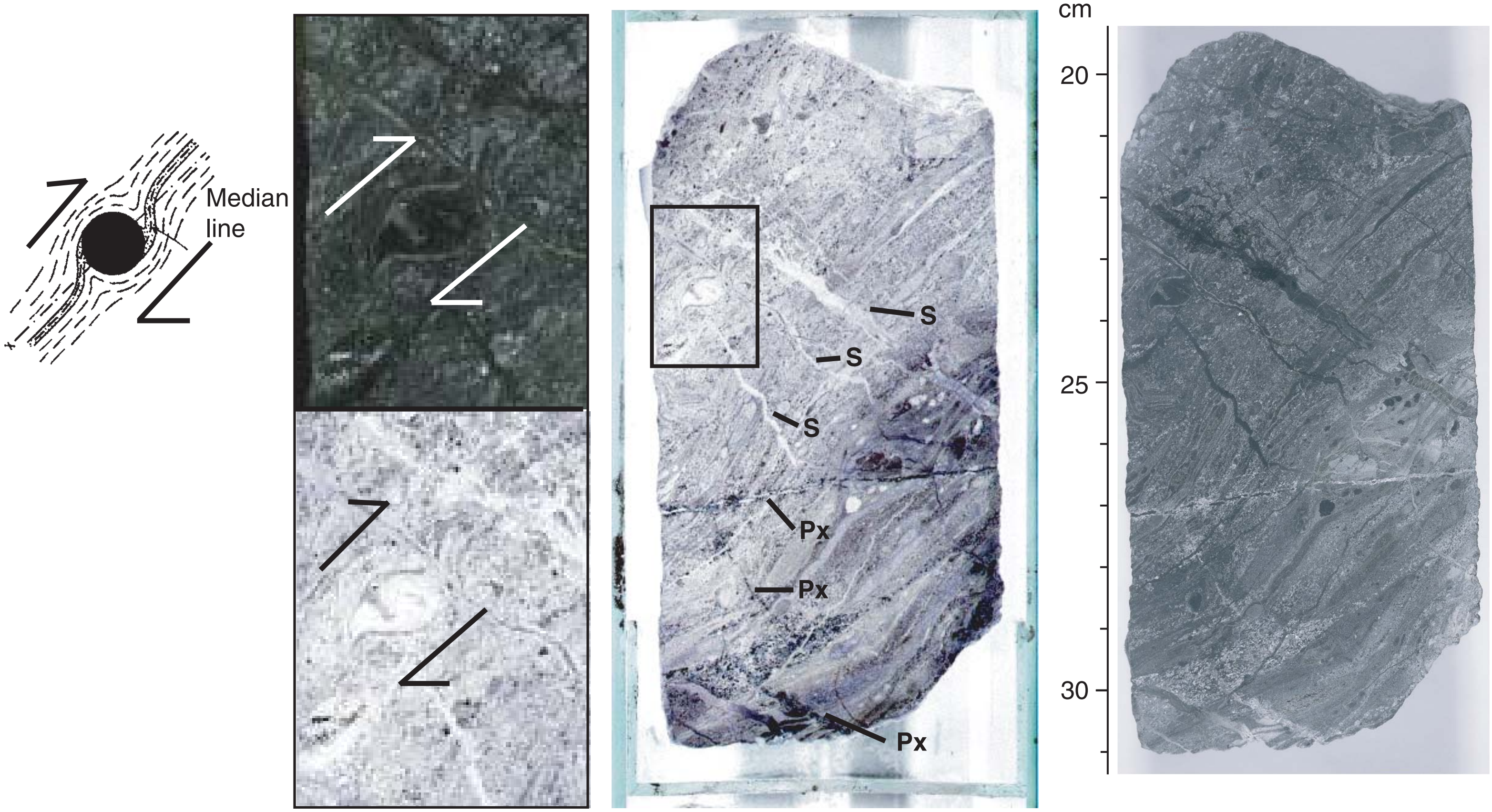

Figure F50. Photomicrograph showing a pseudomorphed clinopyroxene porphyroclast with a pressure shadow in mylonite. The image shows the median line of the pressure shadow crossing the foliation plane, the sense of rotation of the porphyroclast, and the inferred reverse sense of shear (Sample 209-1268A-14R-2, 130–133 cm) (cross-polarized light: blue + gray filters; field of view = 2.75 mm; image 1268A_057).

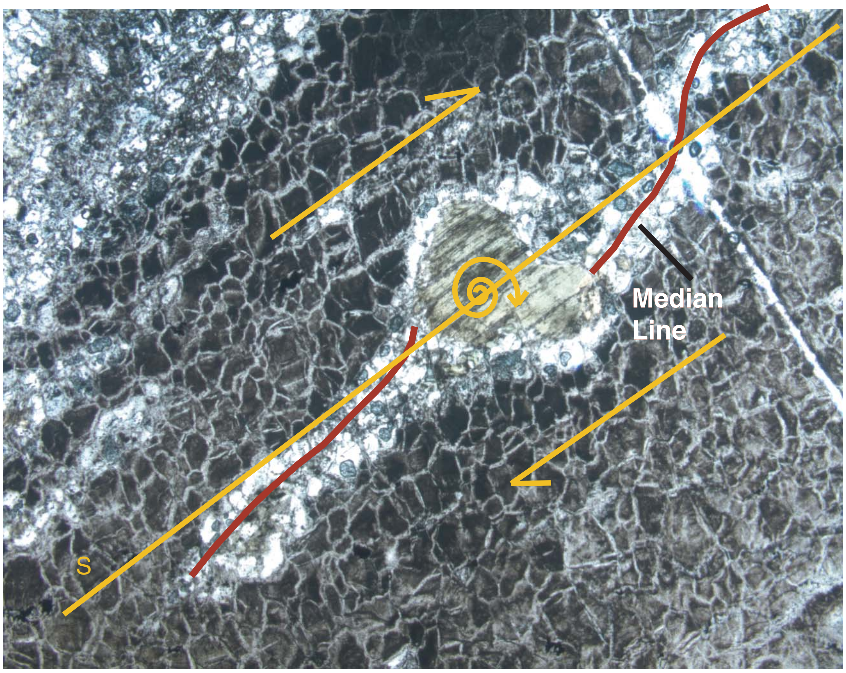

Figure F51. Close-up photographs of intrusion breccias from Hole 1268A showing progressive deformation. **A.** Undeformed breccia showing angular talc pseudomorphed clasts of harzburgite in pseudomorphed medium-grained gabbro with small rotated clasts of harzburgite (interval 209-1268A-13R-2 [Piece 4, 18–29 cm]). **B.** Moderately deformed pseudomorphed intrusion breccia (interval 209-1268A-13R-2 [Piece 10, 64–72 cm). **C.** Pseudomorphed ultramylonite to mylonite with recognizable enclaves of less deformed harzburgite and gabbro (interval 209-1268A-14R-3 [Piece 4, 20–31 cm]).

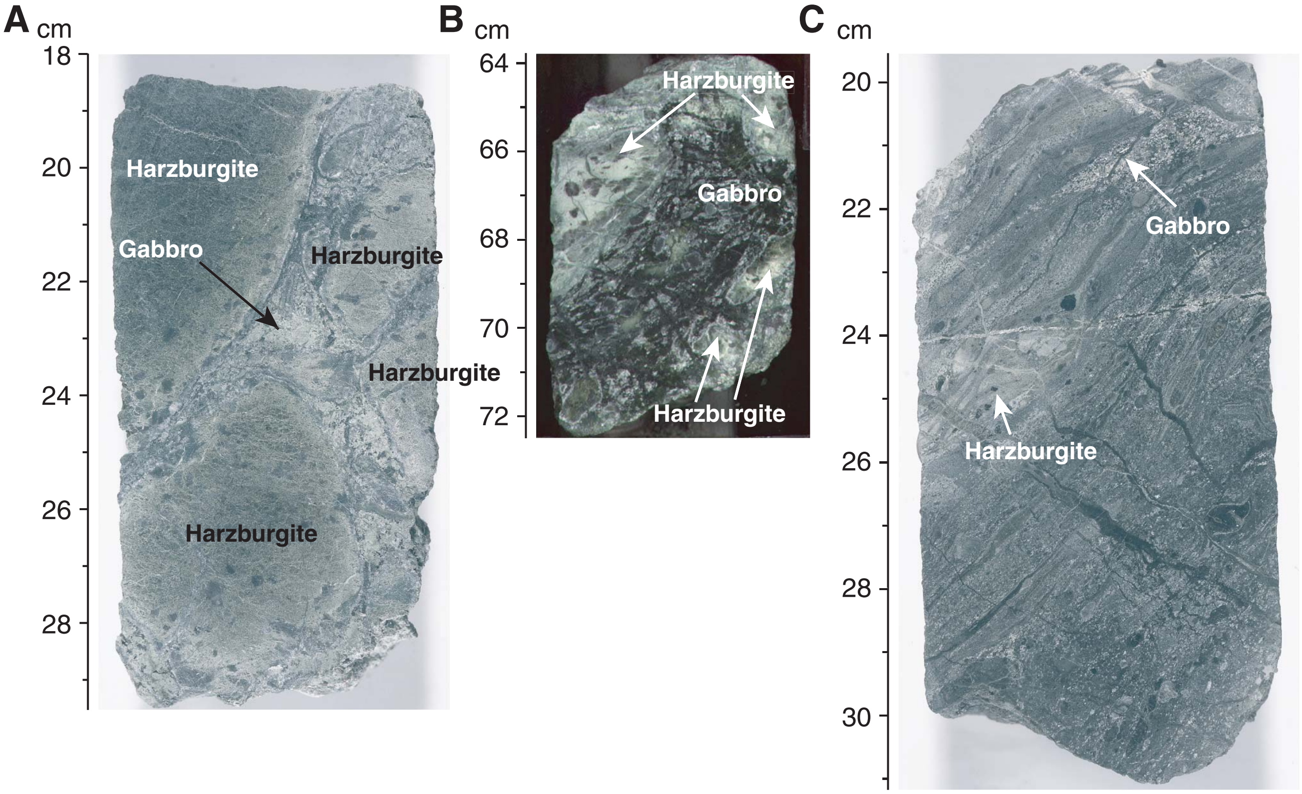

Figure F52. Close-up photograph shows typical moderately well developed anastomosing serpentinization foliation typical of peridotite in Unit I (interval 209-1268A-3R-1, 116–127 cm).

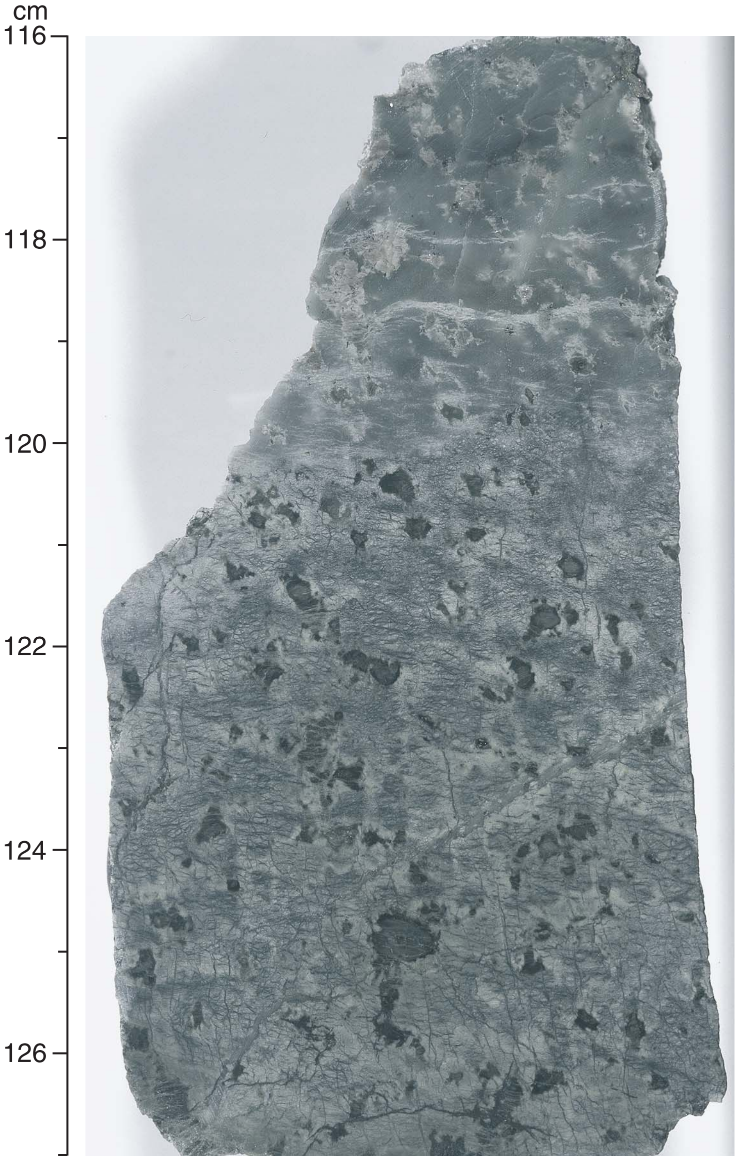

Figure F53. Photomicrograph showing well-developed ribbon texture serpentine that defines anastomosing foliation (Sample 209-1268A-4R-1, 124–127 cm) (cross-polarized light: blue filter; field of view = 1.4 mm; image 1268A_029).

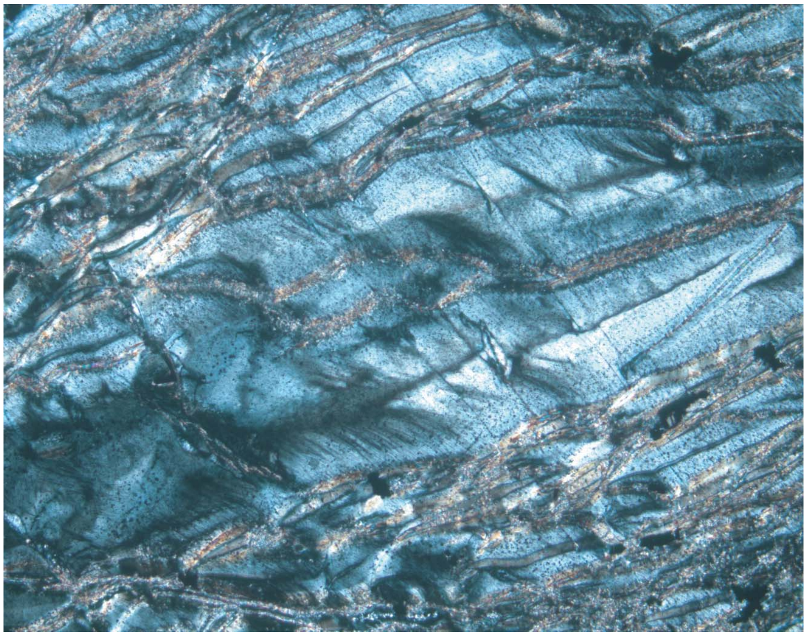

Figure F54. Histogram showing range of measured dips of anastomosing serpentine foliation at Site 1268.

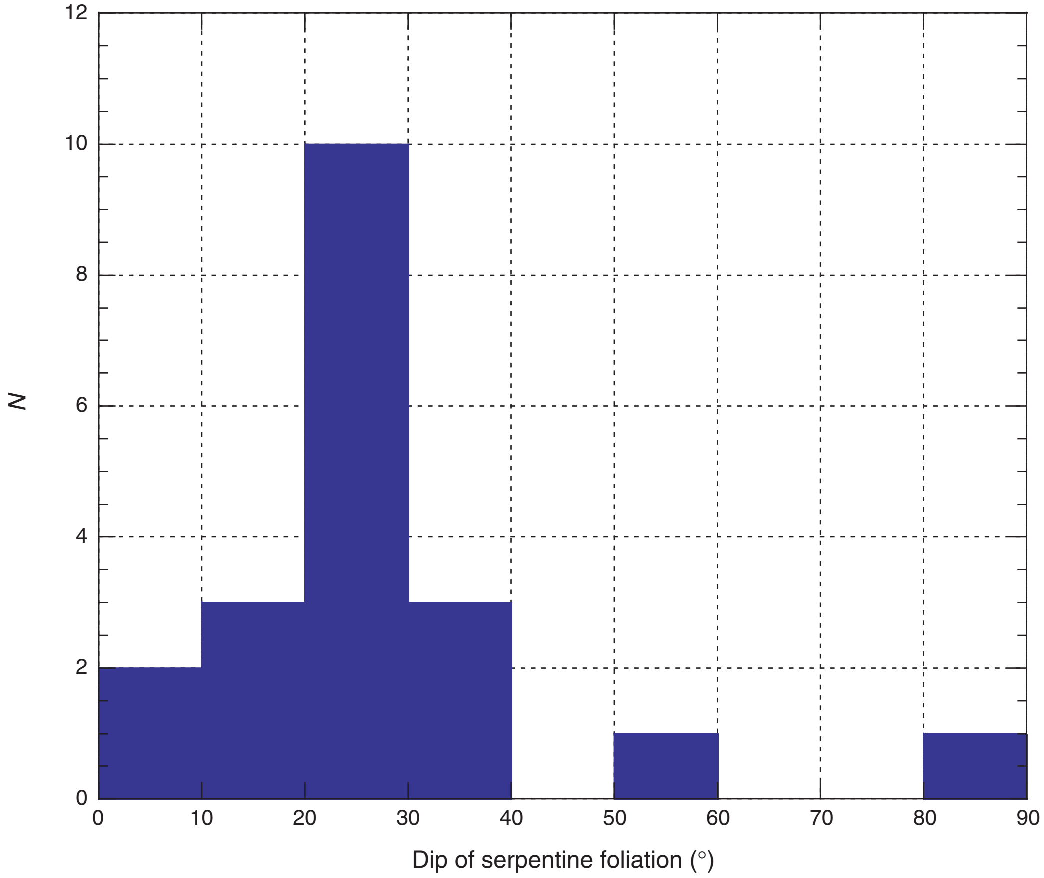

Figure F55. Diagram of dip measurements of anastomosing serpentine foliation over the cored depth range of Site 1268. TD = total depth.

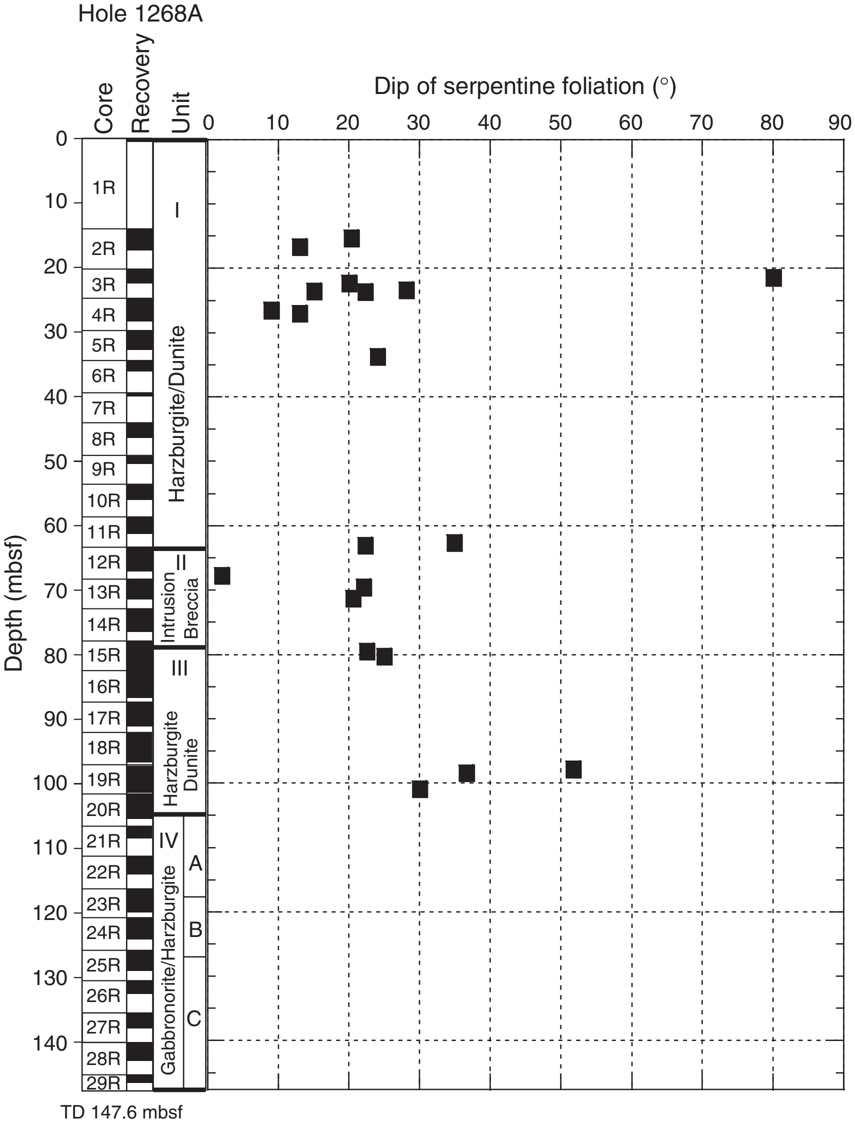

Figure F56. Depth vs. intensity plot of cross-fiber serpentine foliation and crystal-plastic deformation intensities. TD = total depth.

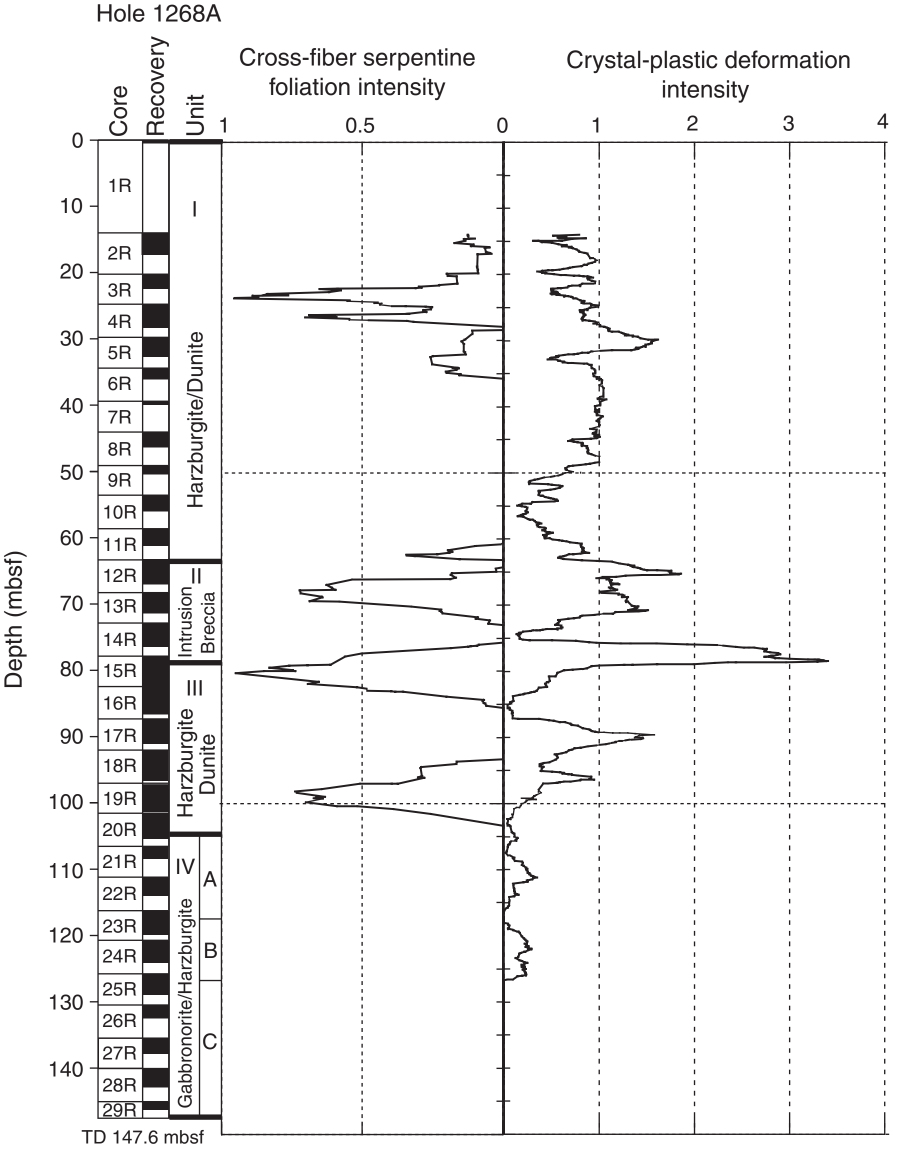

Figure F57. Close-up photograph of an example of one of three zones of fault gouge cored in Hole 1268A (interval 209-1268A-12R-1, 137–149 cm).

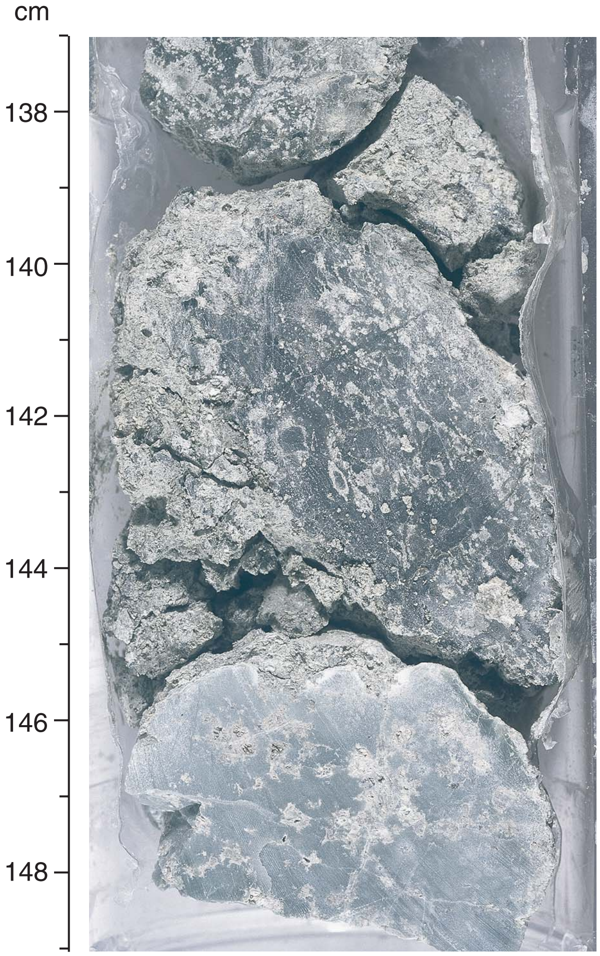

Figure F58. Close-up photograph showing orthopyroxene-bearing serpentinized dunite band sandwiched by harzburgite. The boundaries of the band are defined by the appearance of abundant pyroxene along contacts that are parallel or subparallel to the crystal-plastic foliation defined by the shape of the pyroxene within the harzburgite. Light gray areas in the dunite are talc altered, and buff brown bands are serpentine-altered fine-grained cataclastic regions (interval 209-1268A-6R-1, 46–66 cm).

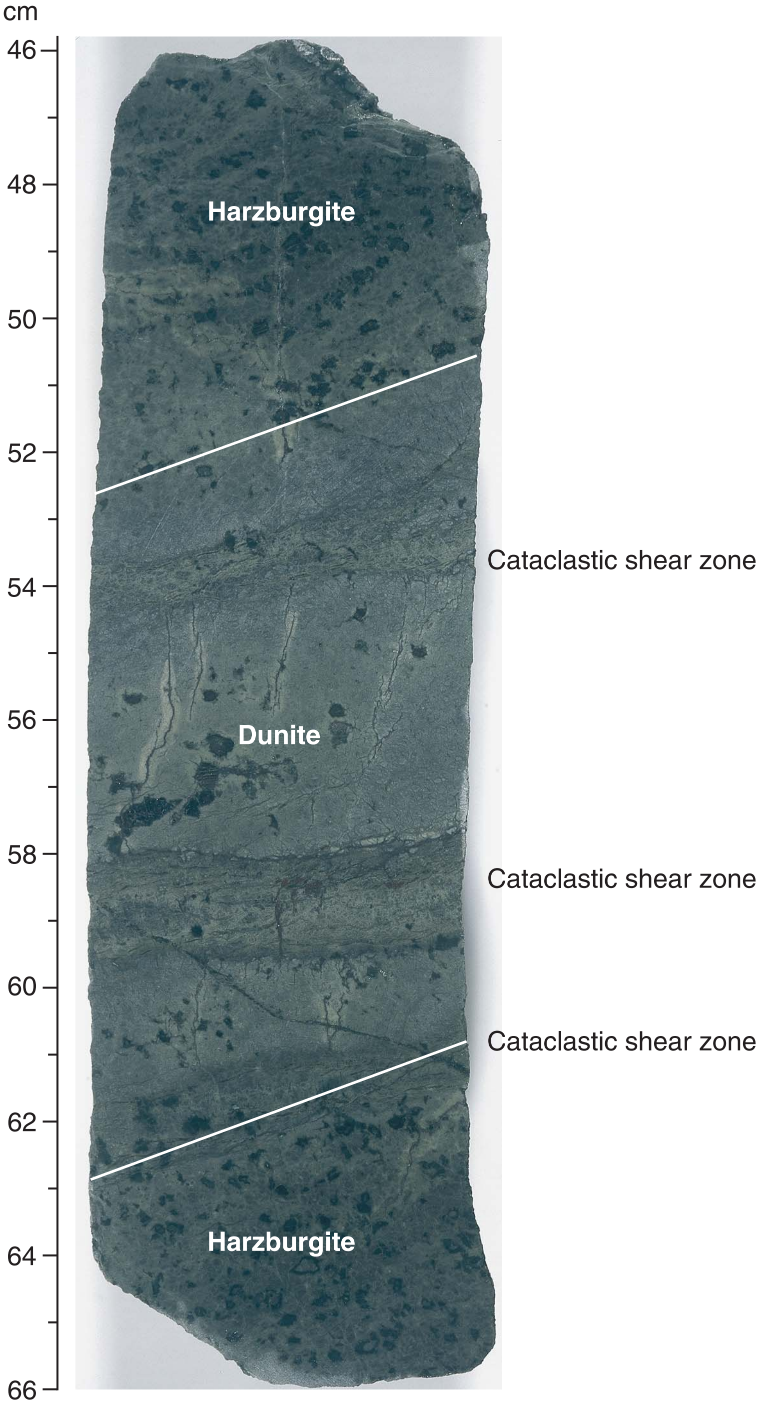

Figure F59. Histogram showing range of measured dips of cataclastic shear zones in Hole 1268A. *N* = number.

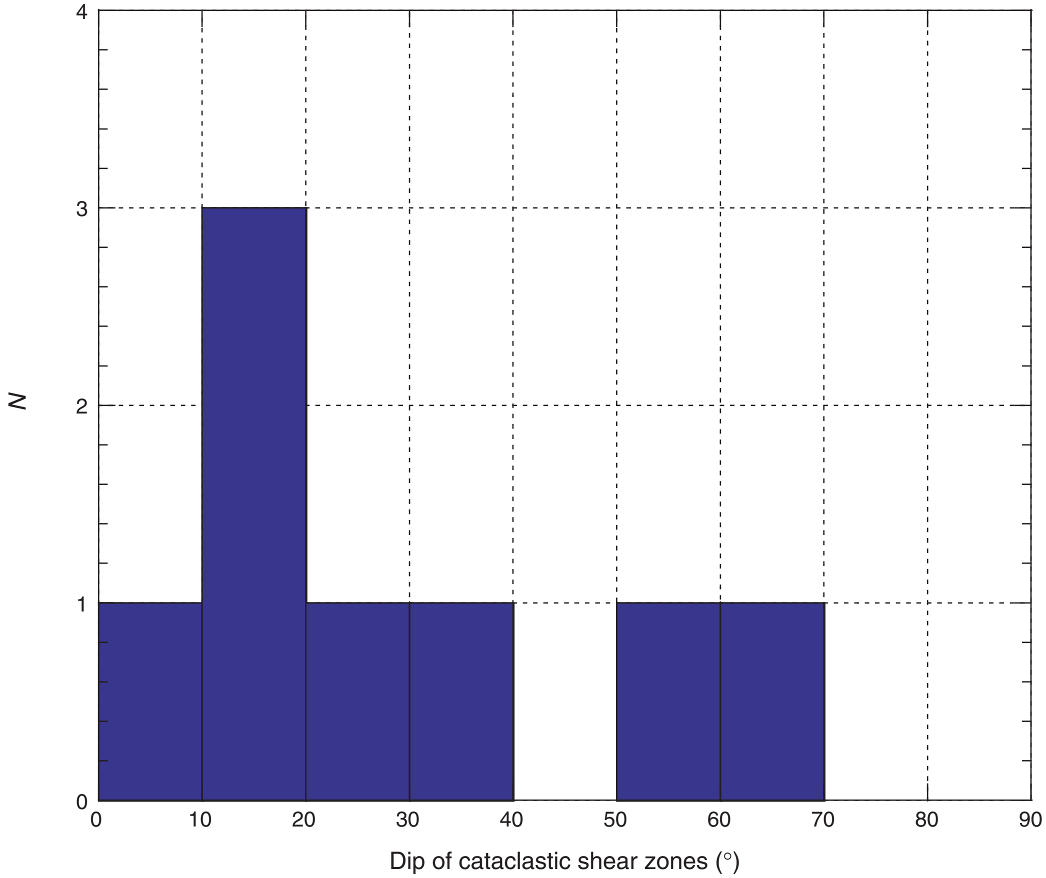

Figure F60. Variation of dips of cataclastic shear zones over the cored depth range of Hole 1268A. TD = total depth.

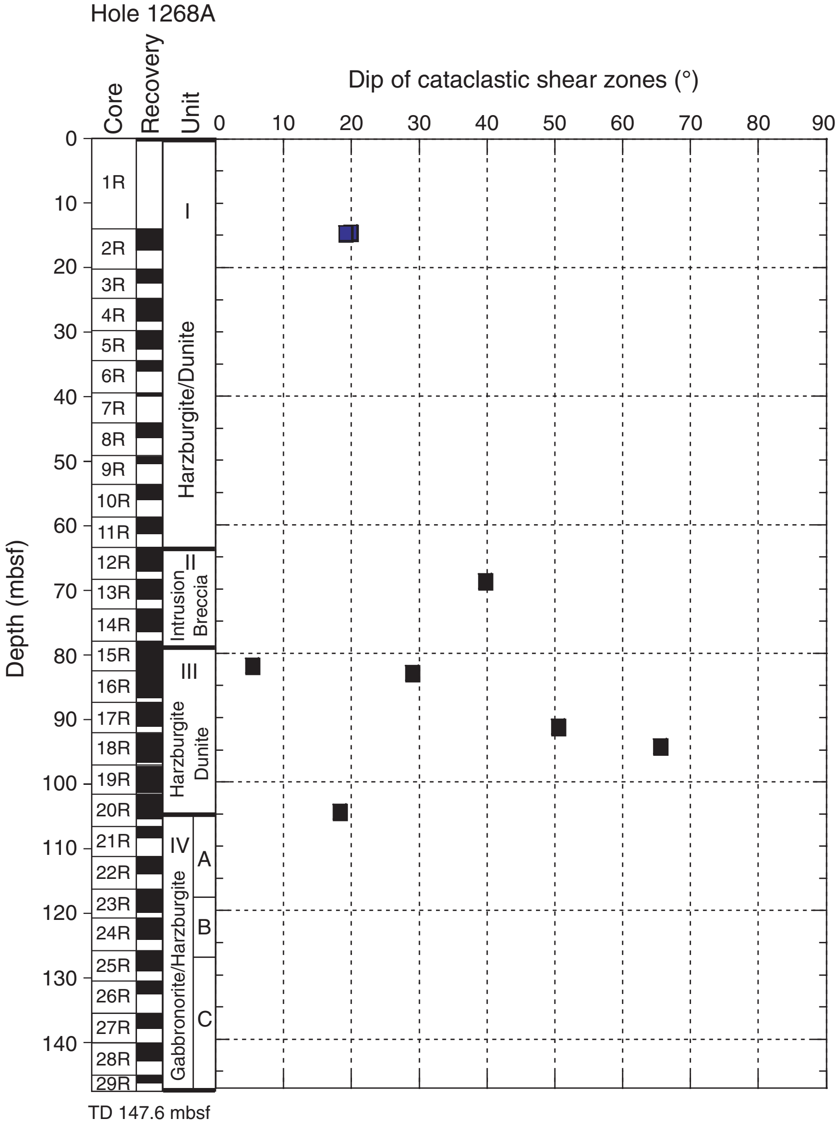

Figure F61. Close-up photograph of a small normal fault (NF) filled with fibrous serpentinite cutting serpentine-sulfide veins (interval 209-1268A-11R-1, 126–136 cm).

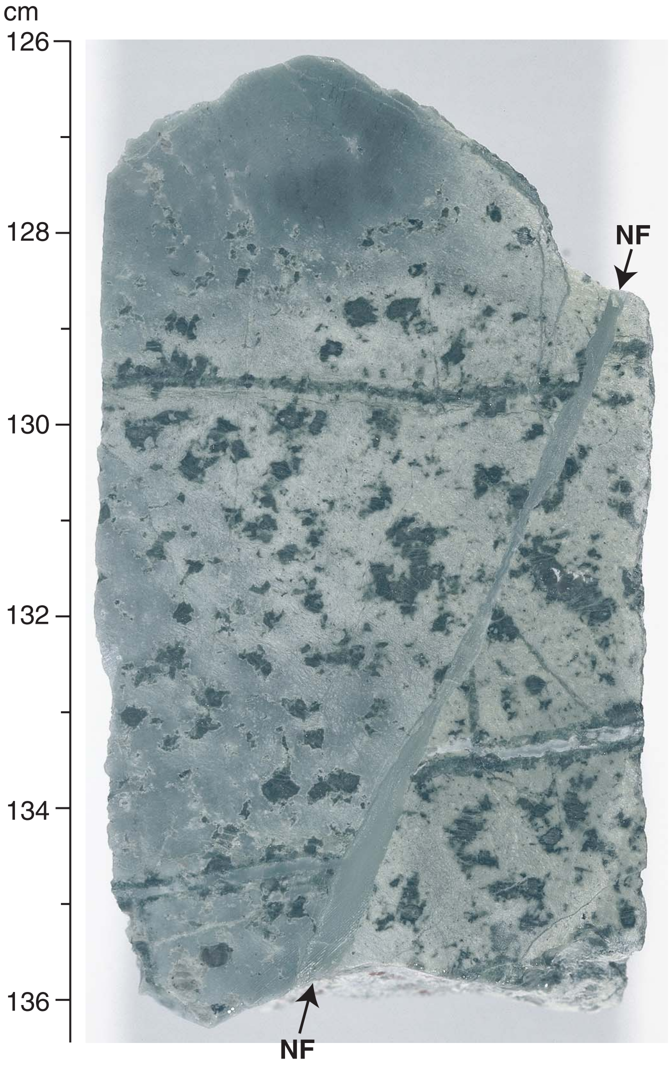

Figure F62. Histogram showing range of measured dips of small faults and shear fractures in Hole 1268A. *N* = number.

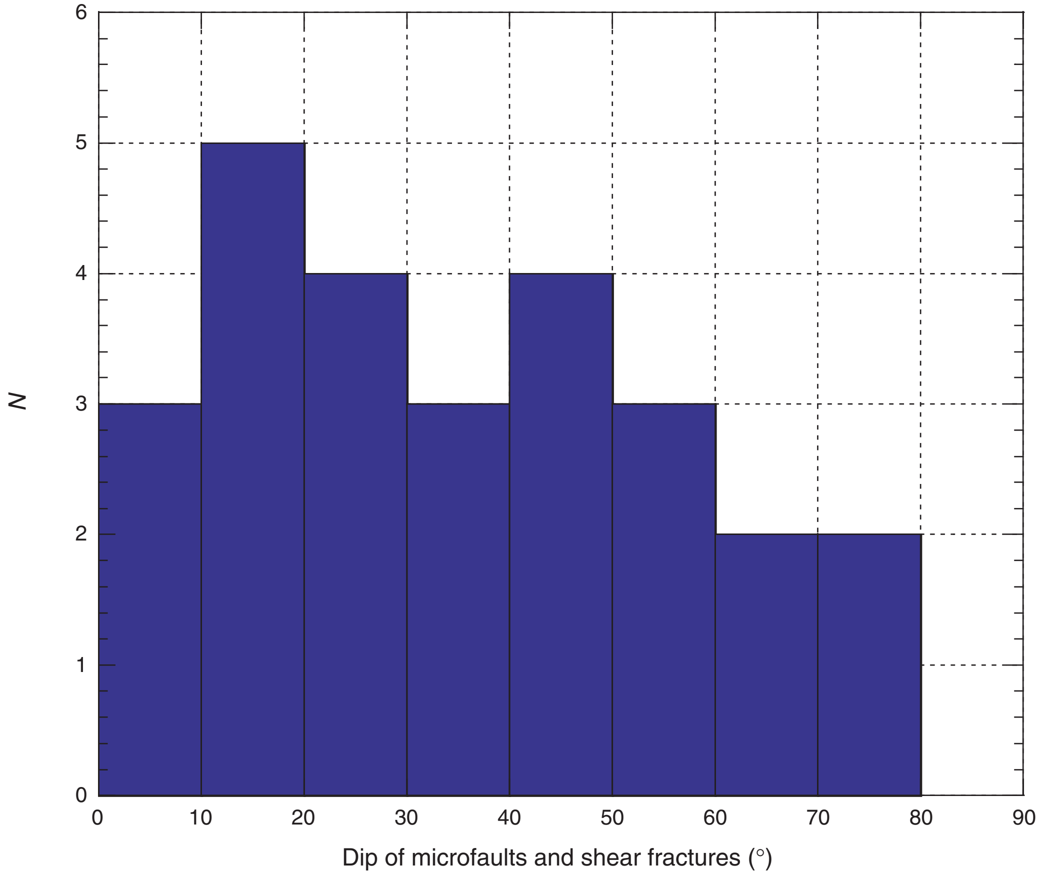

Figure F63. Diagram of dip measurements of small faults and shear fractures over the cored depth range of Hole 1268A. TD = total depth.

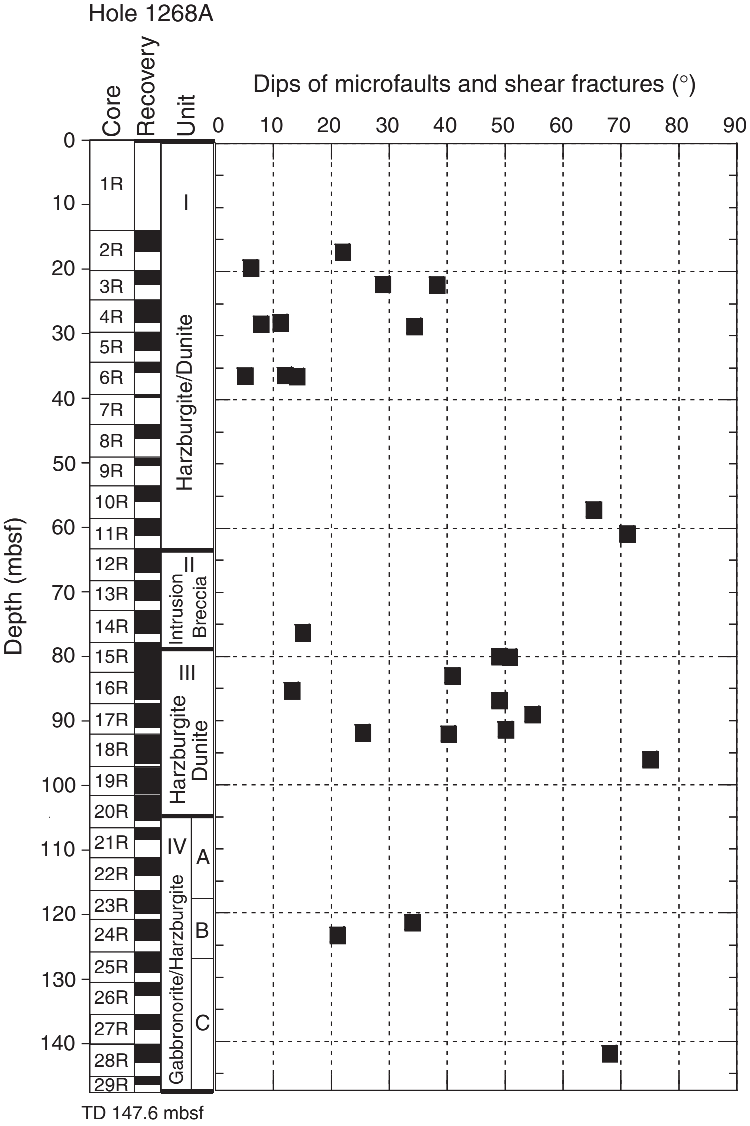

Figure F64. Close-up photograph of cataclastically deformed Unit IV gabbro (interval 209-1268A-25R-1, 65–71 cm).

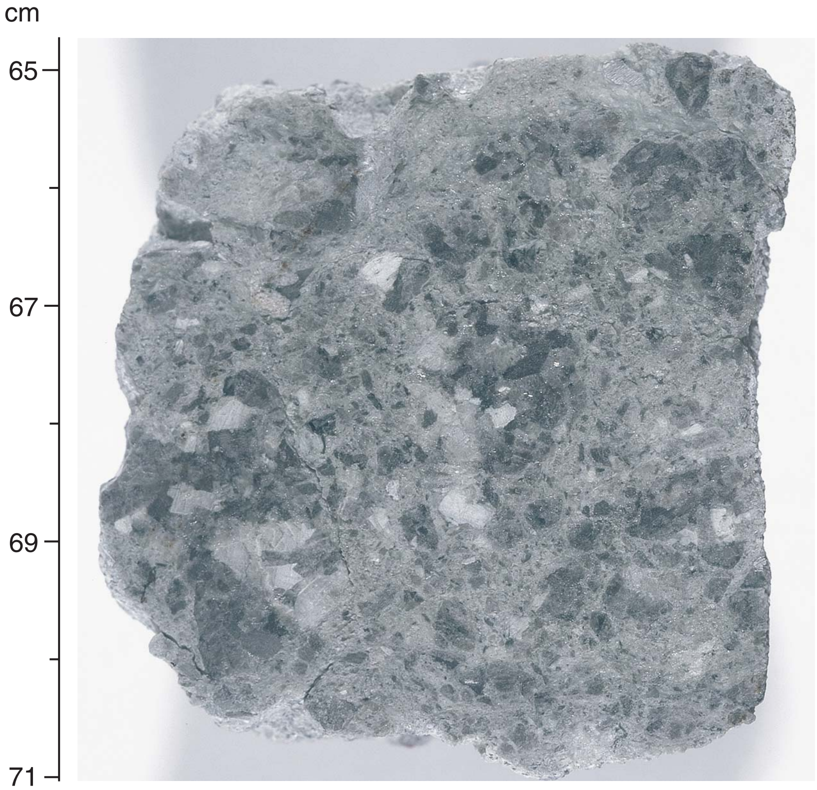

Figure F65. Close-up photograph of a magmatic vein with serpentine-filled tension gashes cut by later white lizardite veining (interval 209-1268A-19R-1 [Piece 4, 106–116 cm]).

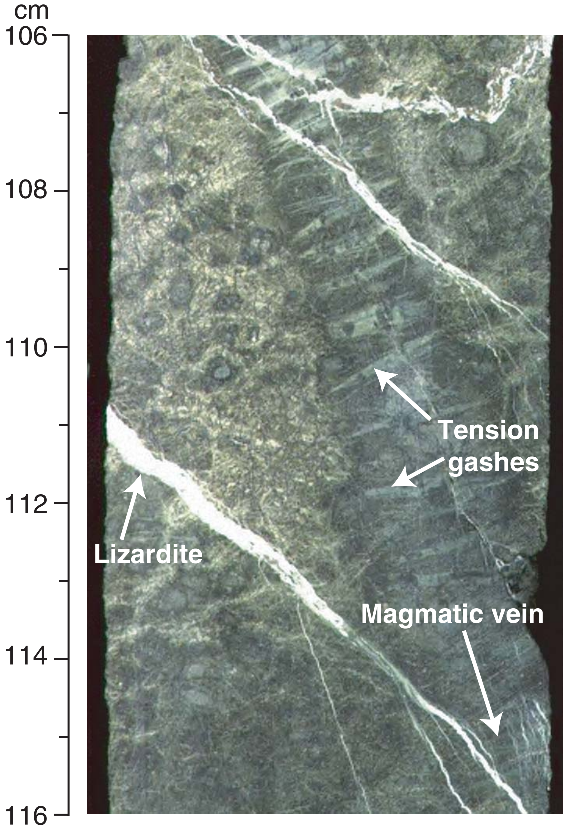

Figure F66. Close-up photograph of two pieces containing a gabbroic vein with serpentine-filled tension gashes (interval 209-1268A-6R-1, 77–90 cm).

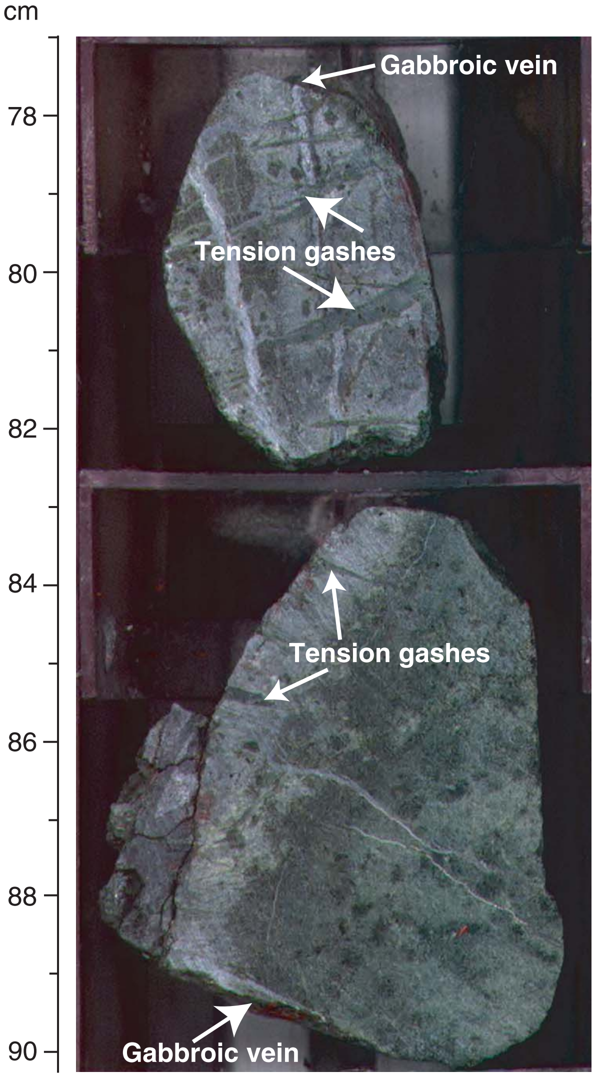

Figure F67. Variation of total alteration and magmatic vein intensity (running average over ~1 m) with depth. TD = total depth.

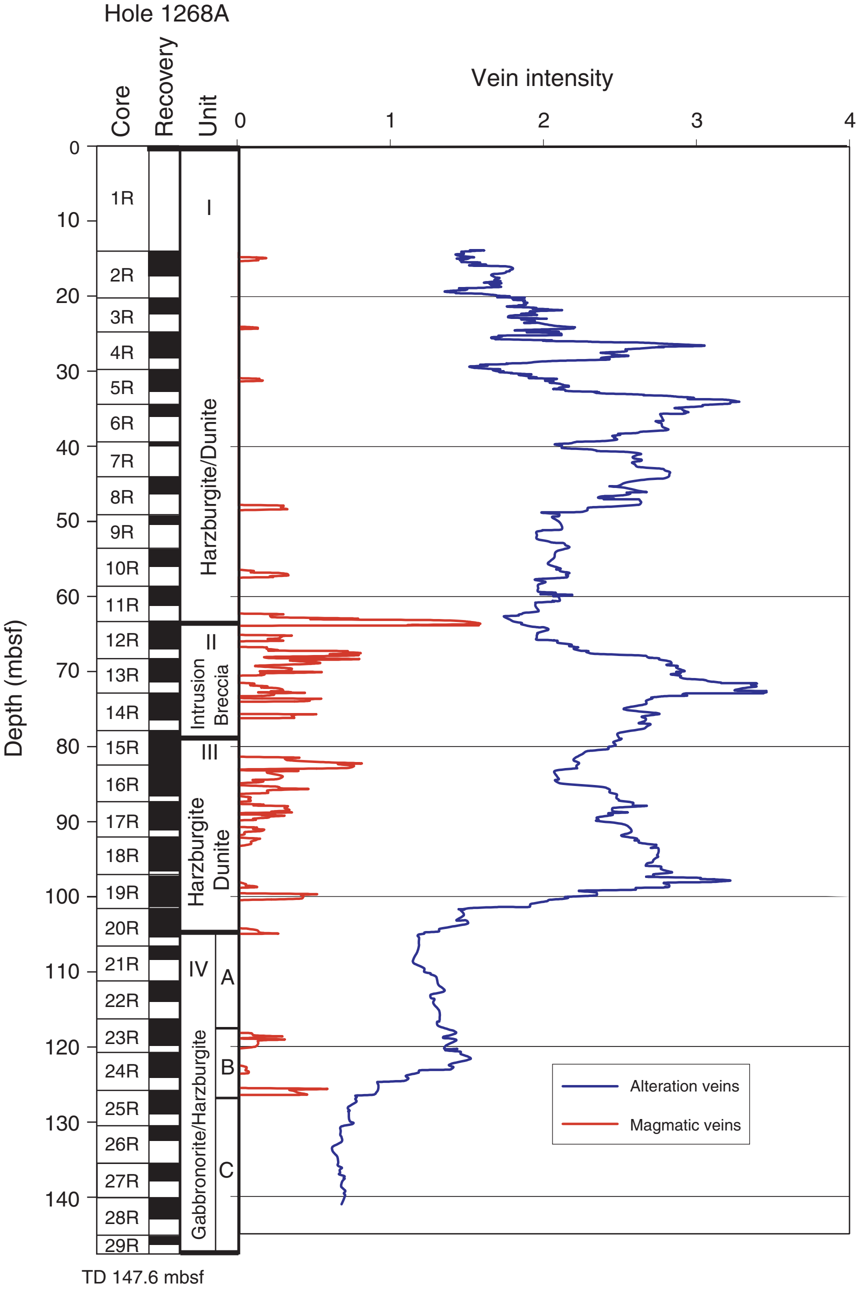

Figure F68. Variation of vein intensities for the five different alteration vein types with depth (running average over ~1 m).

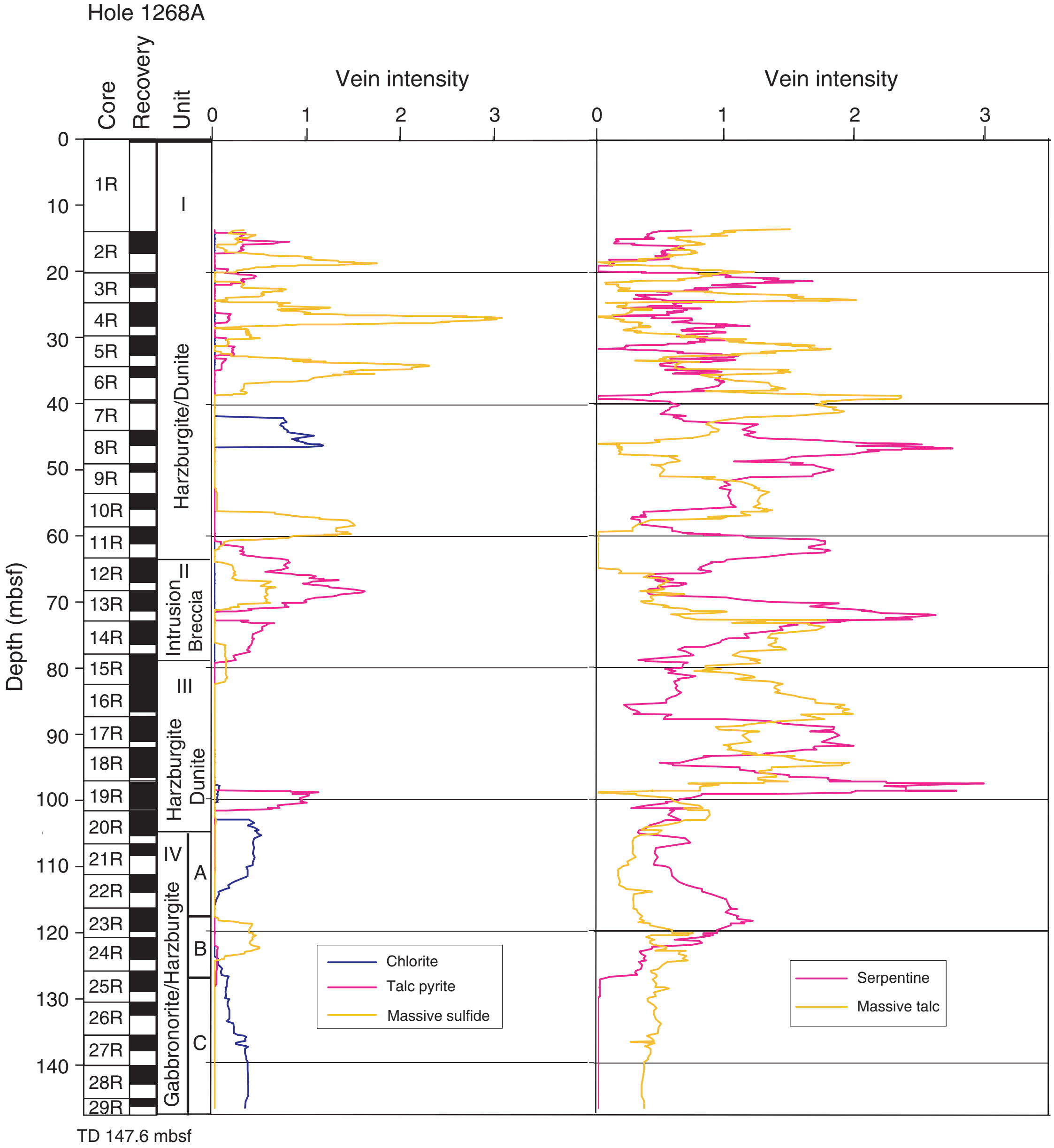

Figure F69. A. Histograms showing the measured dips of the alteration veins within the core reference frame. (Continued on next page.)

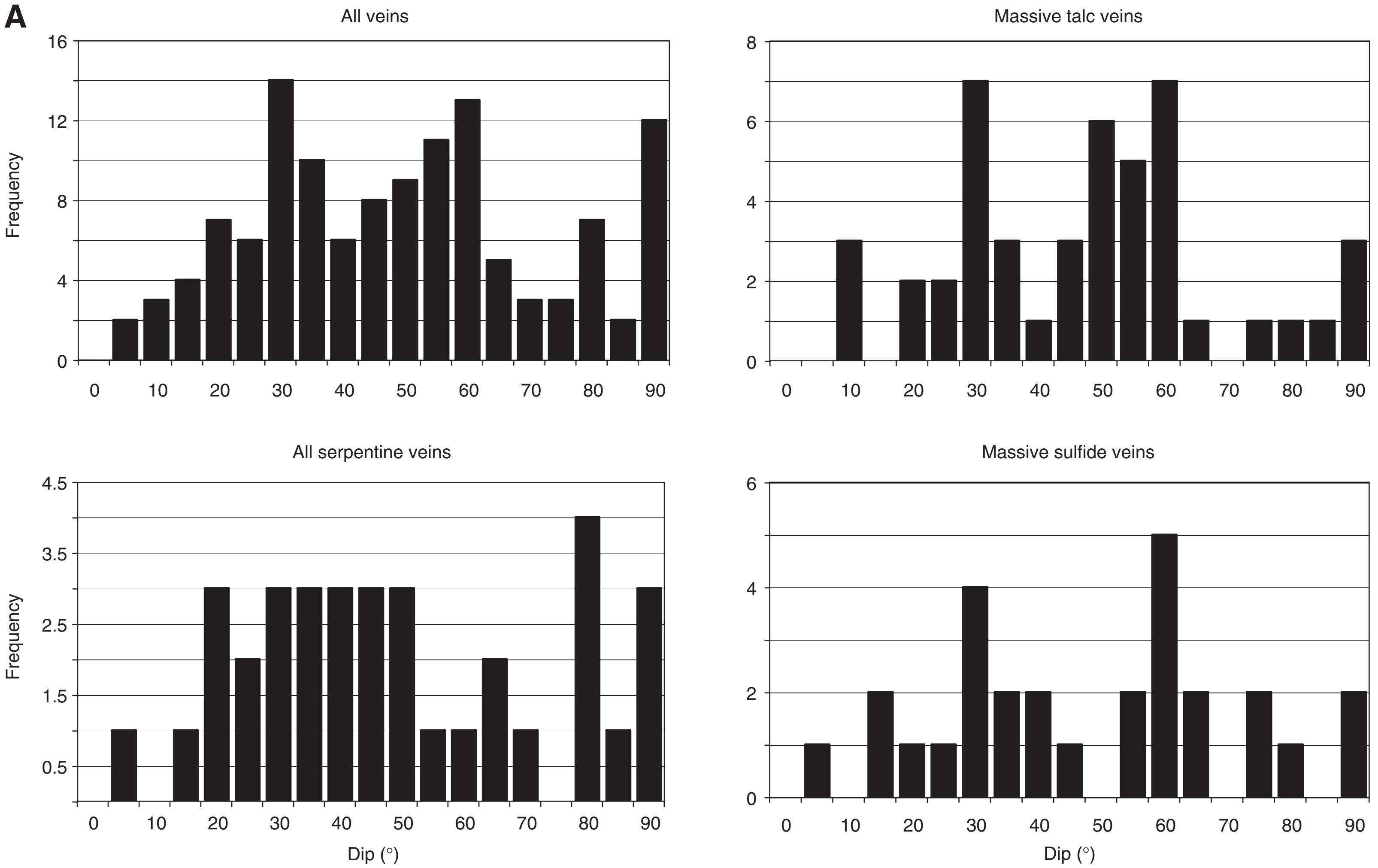

Figure F69 (continued). B. Plots of the dips of the veins in the core reference plane with depth.

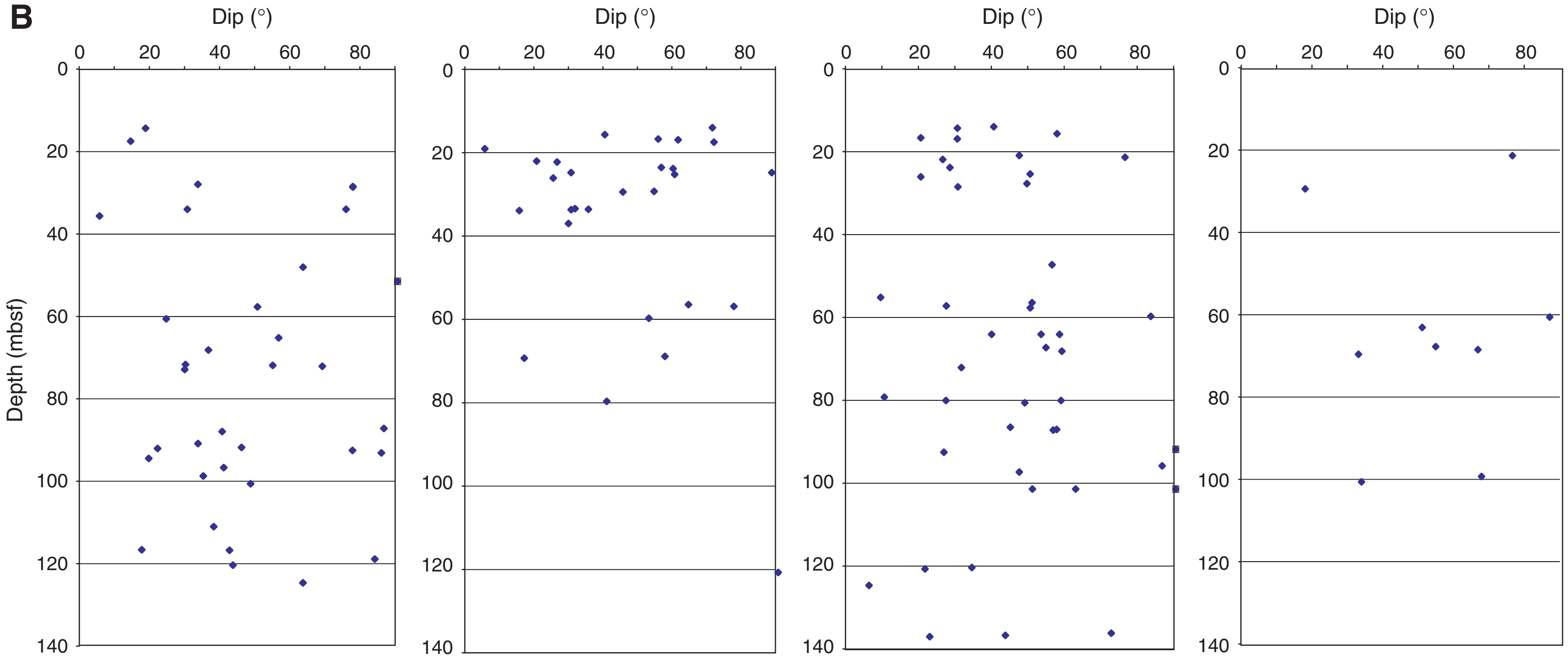

All serpentine veins

Massive sufide veins

Massive talc veins

Talc pyrite veins

Figure F70. Close-up photograph of harzburgite cut and brecciated by late brittle white lizardite veins (interval 209-1268A-23R-2, 90–99 cm).

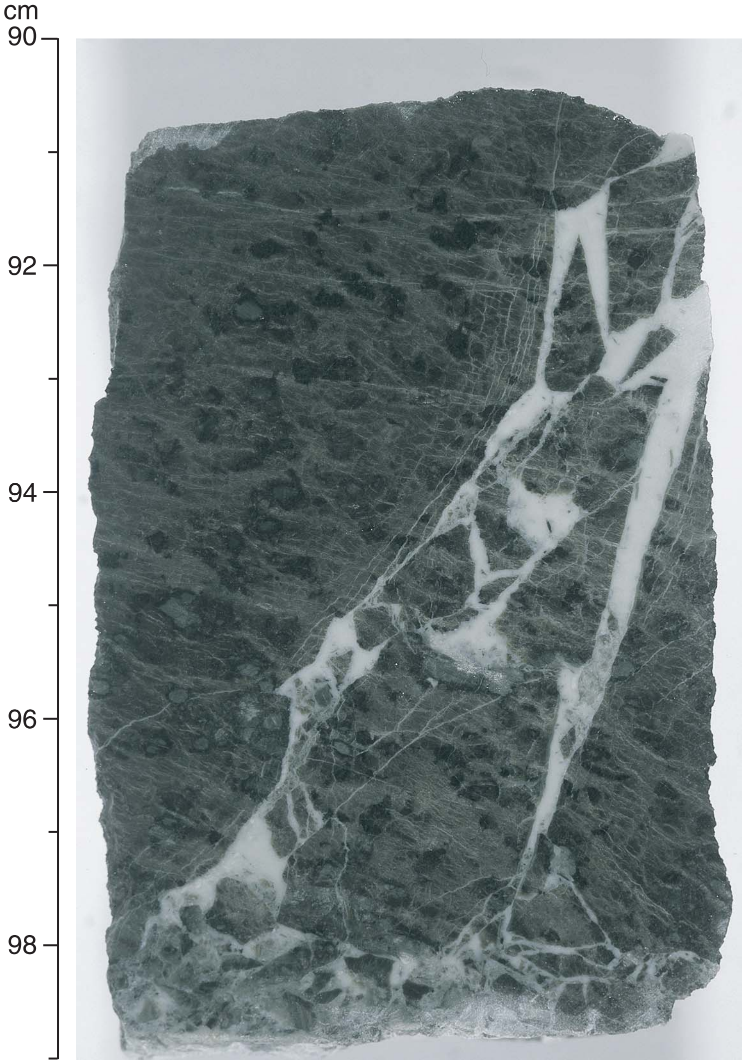

Figure F71. Close-up photograph showing banding from dunite to more subtle variations in the modal proportion of pyroxene in the harzburgites. Band boundaries and orientations are depicted by the yellow lines. Note that the band boundaries are parallel to the crystal-plastic fabric defined by the shape of pyroxene porphyroclasts (interval 209-1268A-18R-4, 3–37 cm).

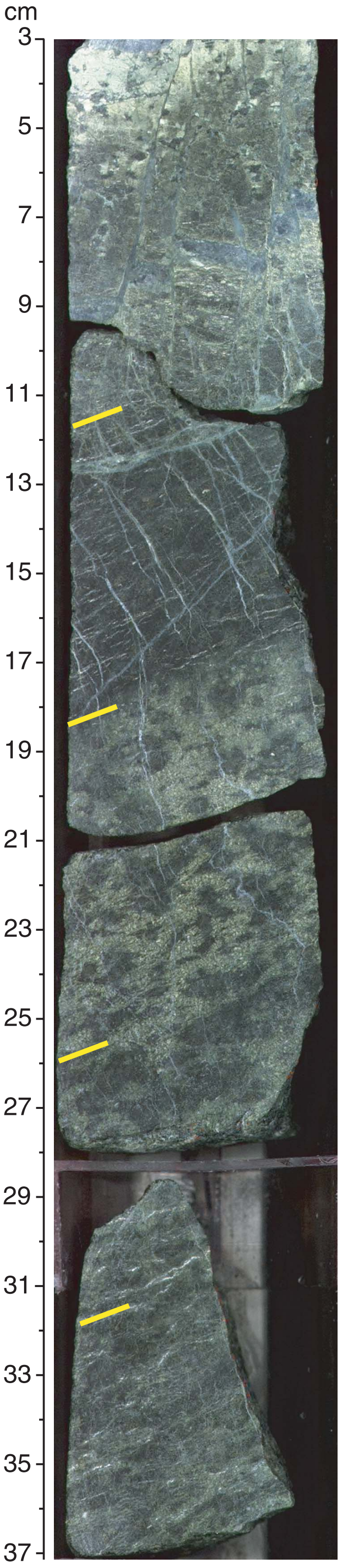

Figure F72. Close-up photograph of an example of a porphyroclastic texture in harzburgite with moderate crystal-plastic deformation defined by a foliation of the shape of altered orthopyroxene (dark reddish gray mineral) with aspect ratios of 3:1 to 4:1. The foliation plane is marked S and is inclined by ~40° in the cut face of the core. Dark gray steeply inclined veins are alteration veins. A postkinematic subhorizontal pyroxenite (PxV) is strongly oblique to the foliation, unlike dunite bands in the recovered core (interval 209-1268A-14R-2, 119–134 cm).

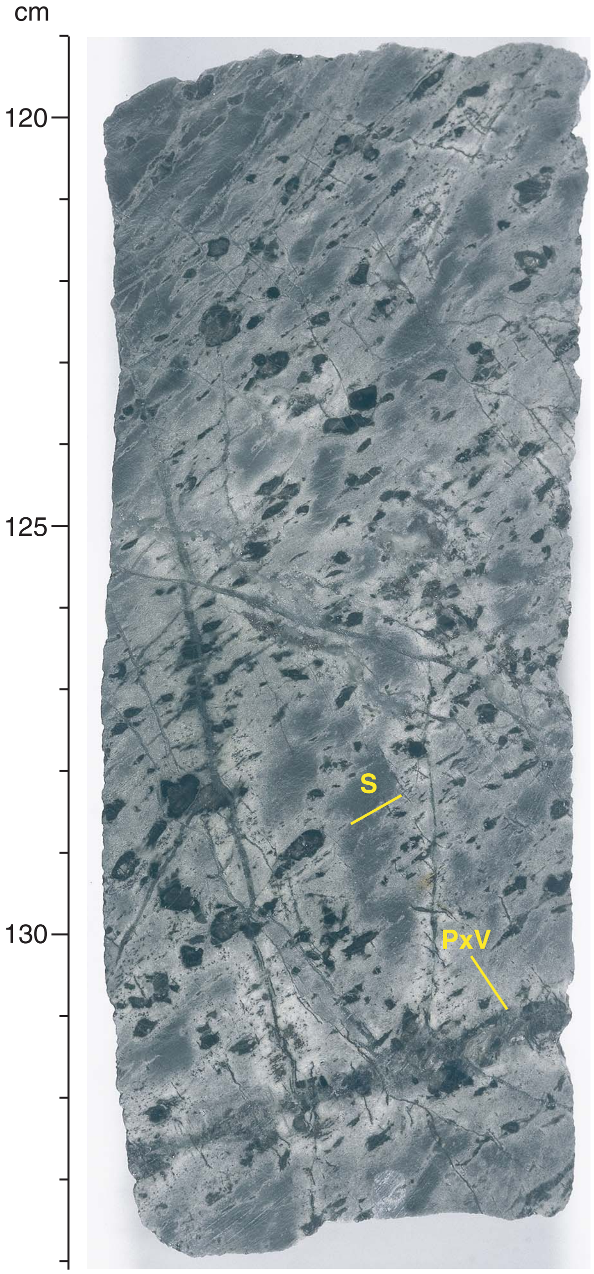

Figure F73. Close-up photographs showing examples of undeformed pyroxenite veins (PxV) that cut the crystal-plastic foliation in deformed harzburgites. True color image (dark) is matched by a negative image to highlight the pyroxenite veins. Serpentine-talc alteration veins (SAV) cut across the magmatic pyroxenite veins. An enlargement image of the top of the interval also shows a characteristic set of tapered tension gashes filled with serpentine that are orthogonal to the pyroxenite vein. This relationship may indicate that serpentinization of the surrounding olivine resulted in volumetric strains that progressively fractured the pyroxenite, which is more resistant to serpentinization. The serpentine-talc alteration veins are widest in the center of the pyroxenite and taper into the harzburgite (interval 209-1268A-16R-1, 13–60 cm).

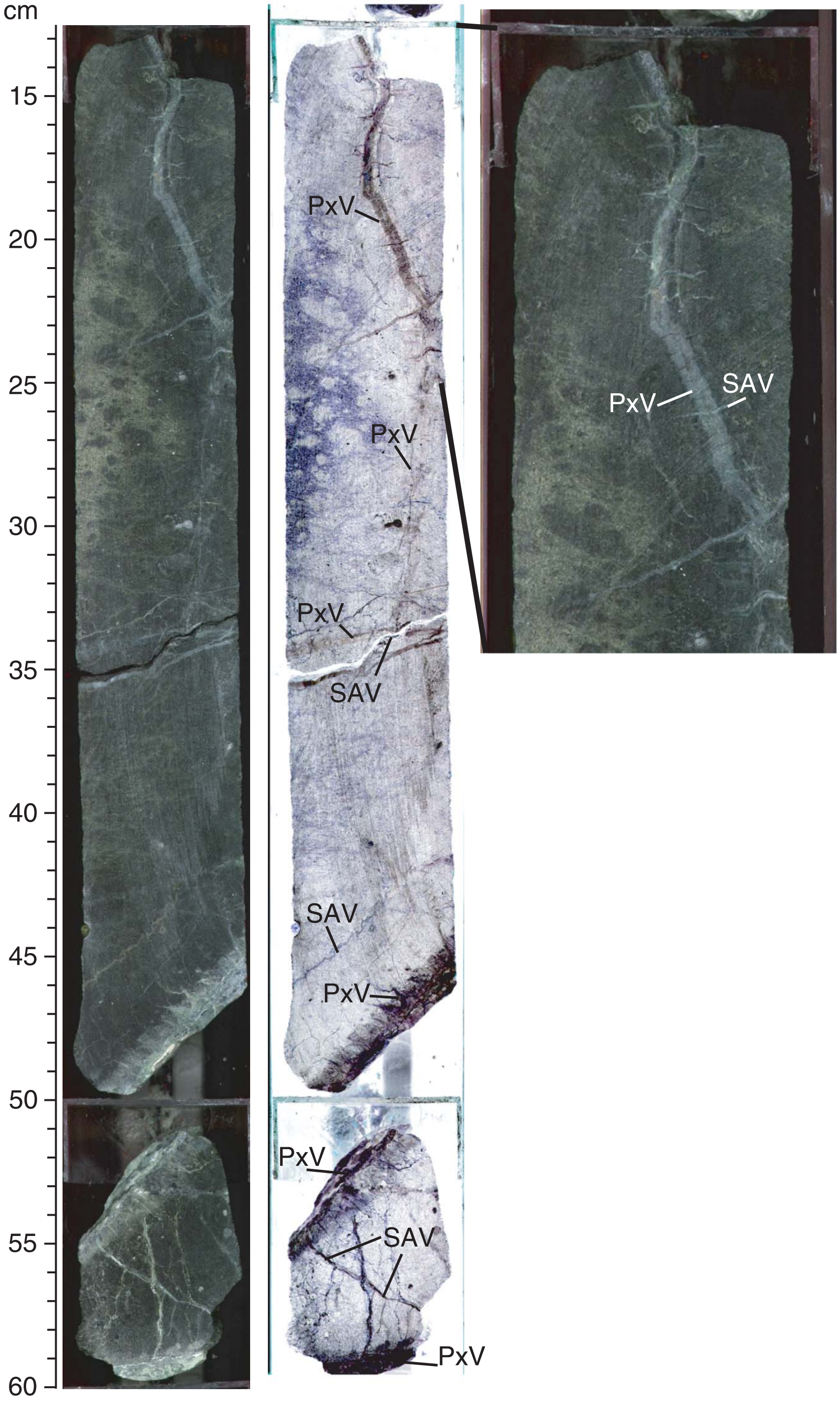

Figure F74. Distribution and dip of magmatic veins and contacts with depth below seafloor.

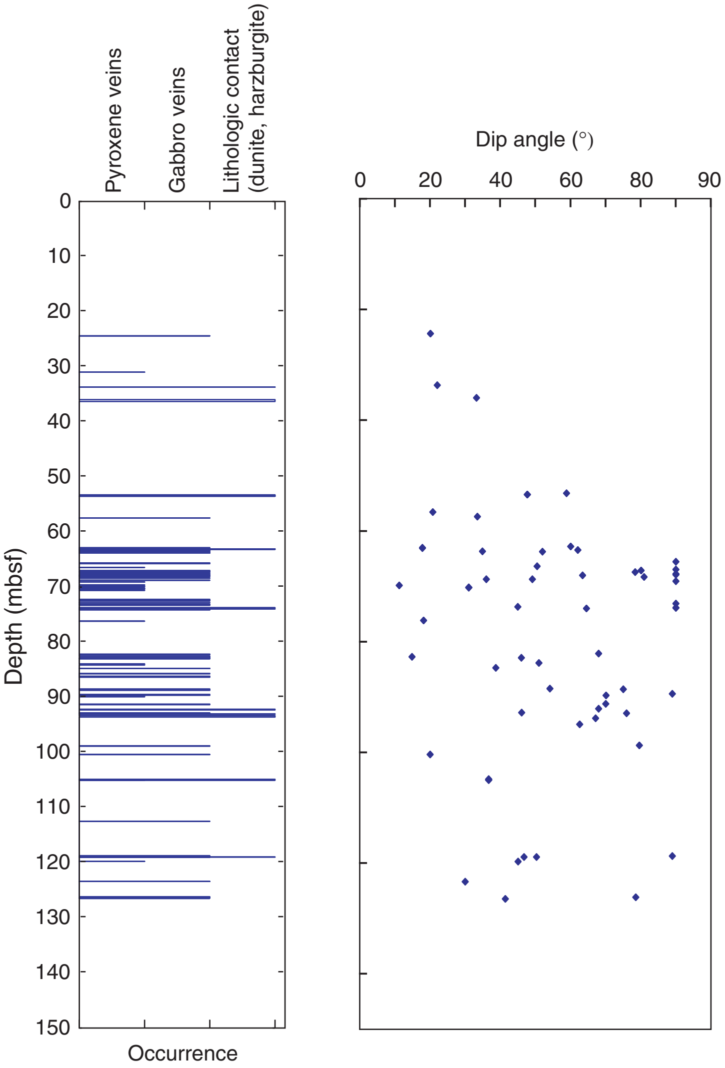

Figure F75. Poles to planes in lower hemisphere equal-area stereo plots showing the orientation of spinel foliation, magmatic veins, lithologic contacts, and gabbro fabrics. The azimuthal orientation of features in individual pieces of the core was corrected to a common reference frame using paleomagnetic azimuth data (see "Structures in Peridotite and Gabbroic Intrusions," p. 8, in "Mantle Upwelling, Melt Transport, and Igneous Crustal Accretion" in the "Leg 209 Summary" chapter). **A.** All data plotted and identified according to quality of the paleomagnetic measurements. No significant differences in the distribution of lower- and higher-quality data can be identified; all data are therefore plotted in B. **B.** Data set broken down by the type of feature measured. Assuming magnetic north is close to geographical north, magmatic veins and lithologic contacts form rough girdles rotated around a north–south axis. Magmatic veins tend to be more steeply dipping than lithologic contacts.

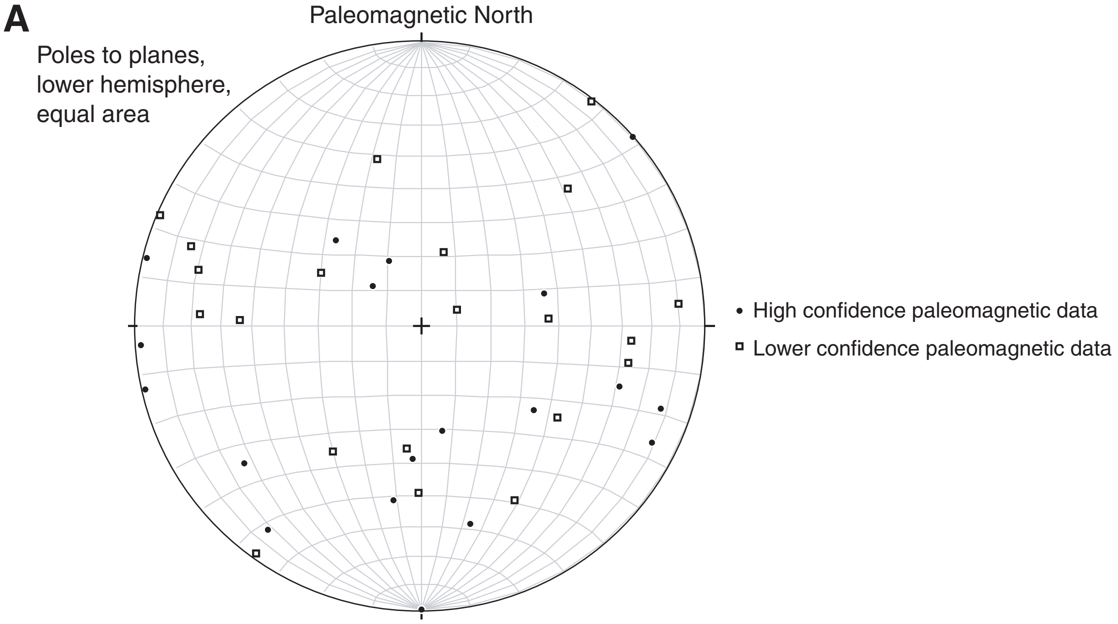

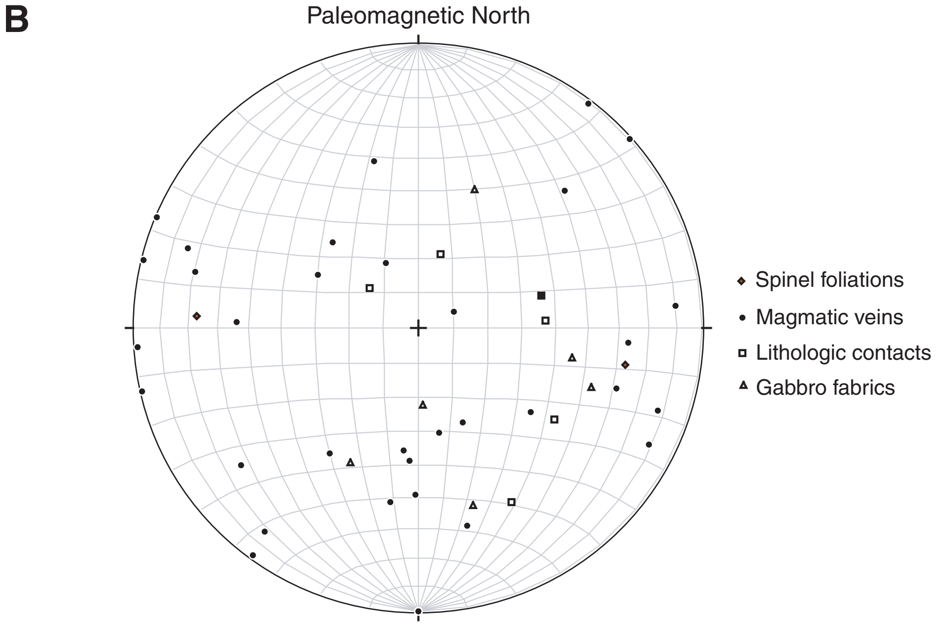

Figure F76. Close-up photograph of spinel foliation (interval 209-1268A-18R-3 [Piece 1B, 29–31 cm]).

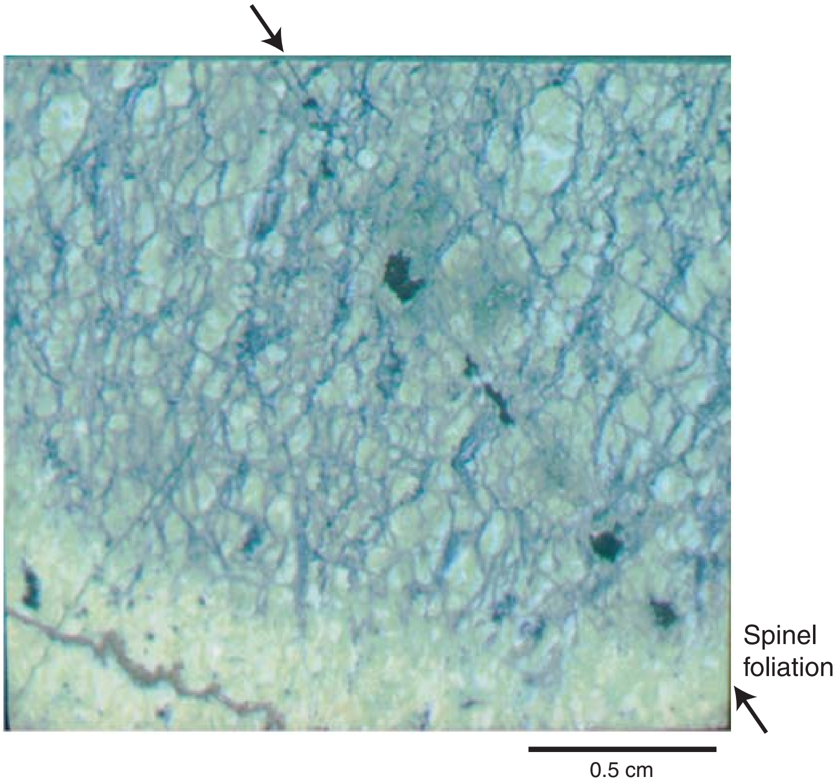

Figure F77. Lower hemisphere stereo plot of poles to crystal-plastic foliation. Dotted lines connect foliations measured within a single core, solid line connects measurements within a single piece.

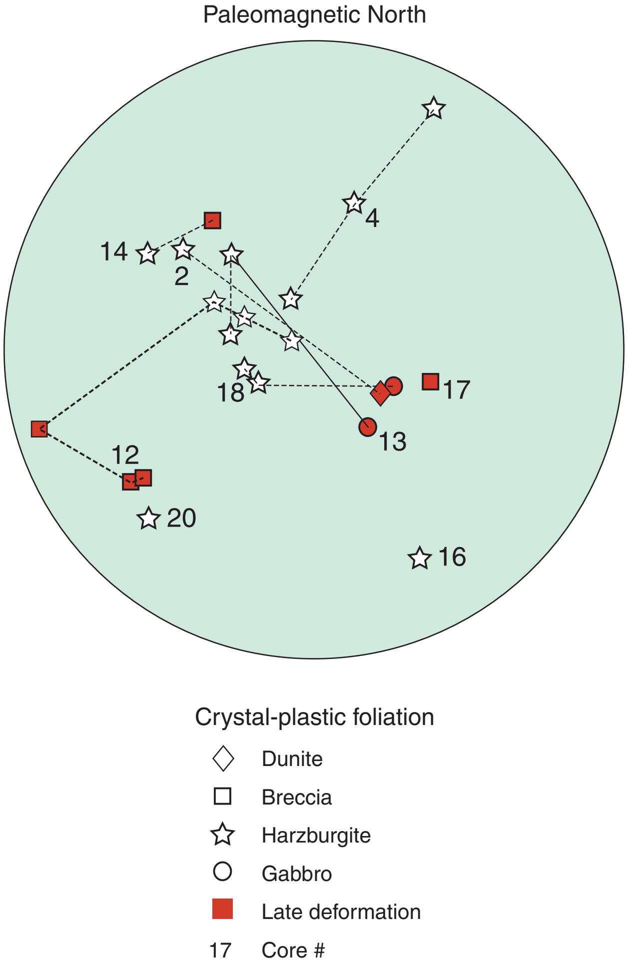

Figure F78. Lower hemisphere stereo plot of poles to cataclastic shear zones and small faults. Measurements have been rotated into a common reference frame using shipboard magnetic declination measurements.

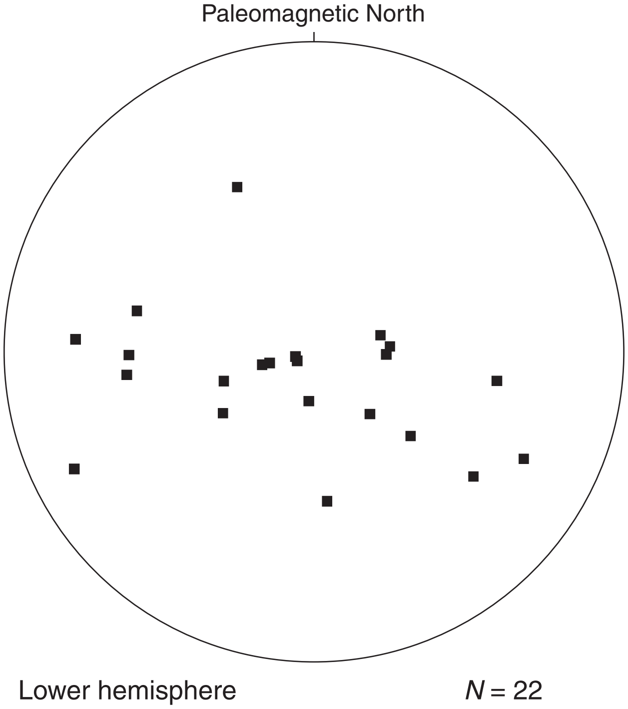

Figure F79. Poles to planes for alteration vein orientations in Hole 1268A. Measurements have been rotated into a common reference frame using shipboard magnetic declination measurements.

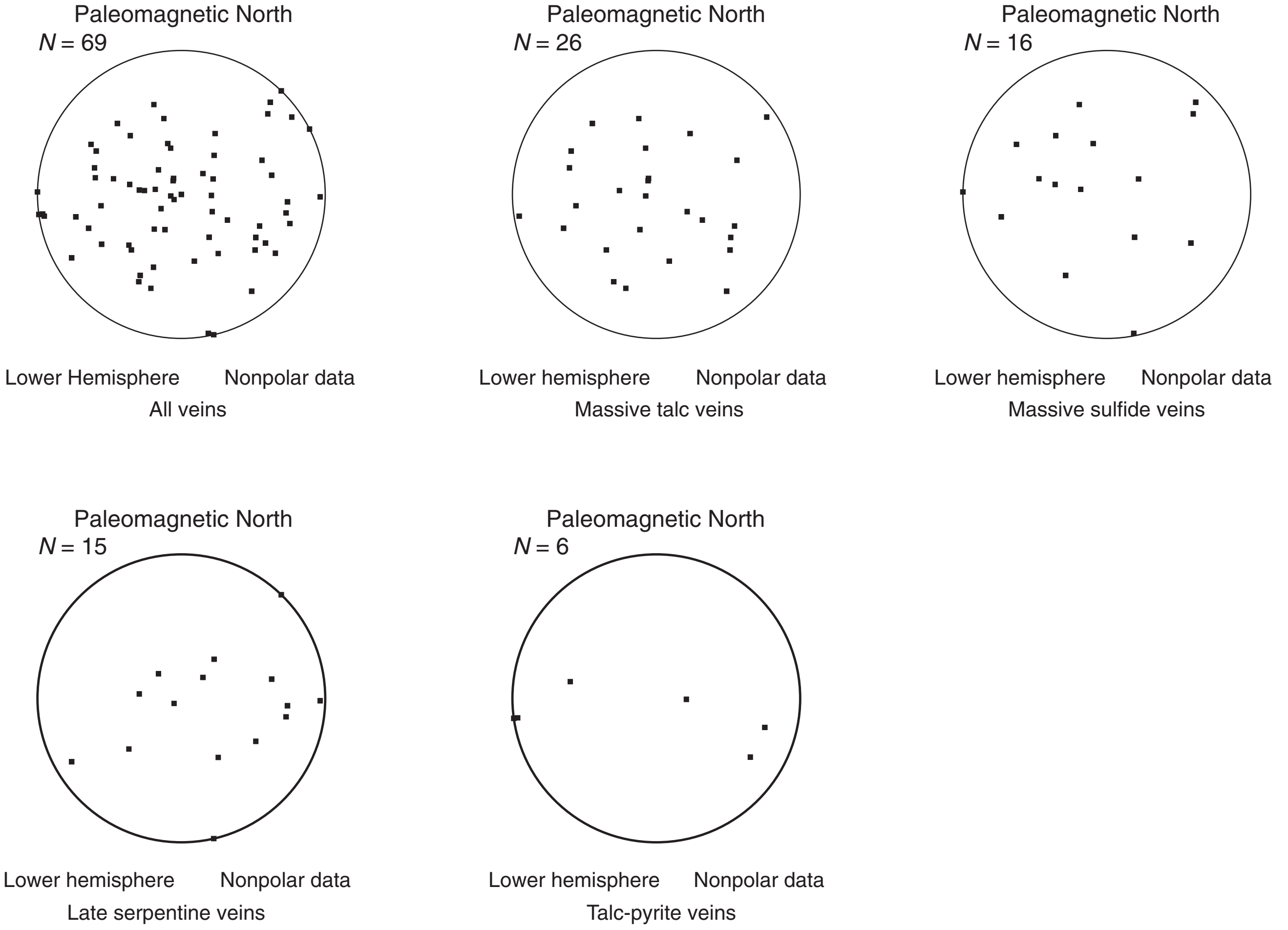

Figure F80. Fe_2O_3 MgO, and H_2O vs. SiO_2 in peridotites from Site 1268. Also shown for comparison are end-member compositions for lizardite, talc, and tremolite (Deer et al., 1992) and Site 920 serpentinites (Cannat, Karson, Miller, et al., 1995; Dilek et al., 1997a).

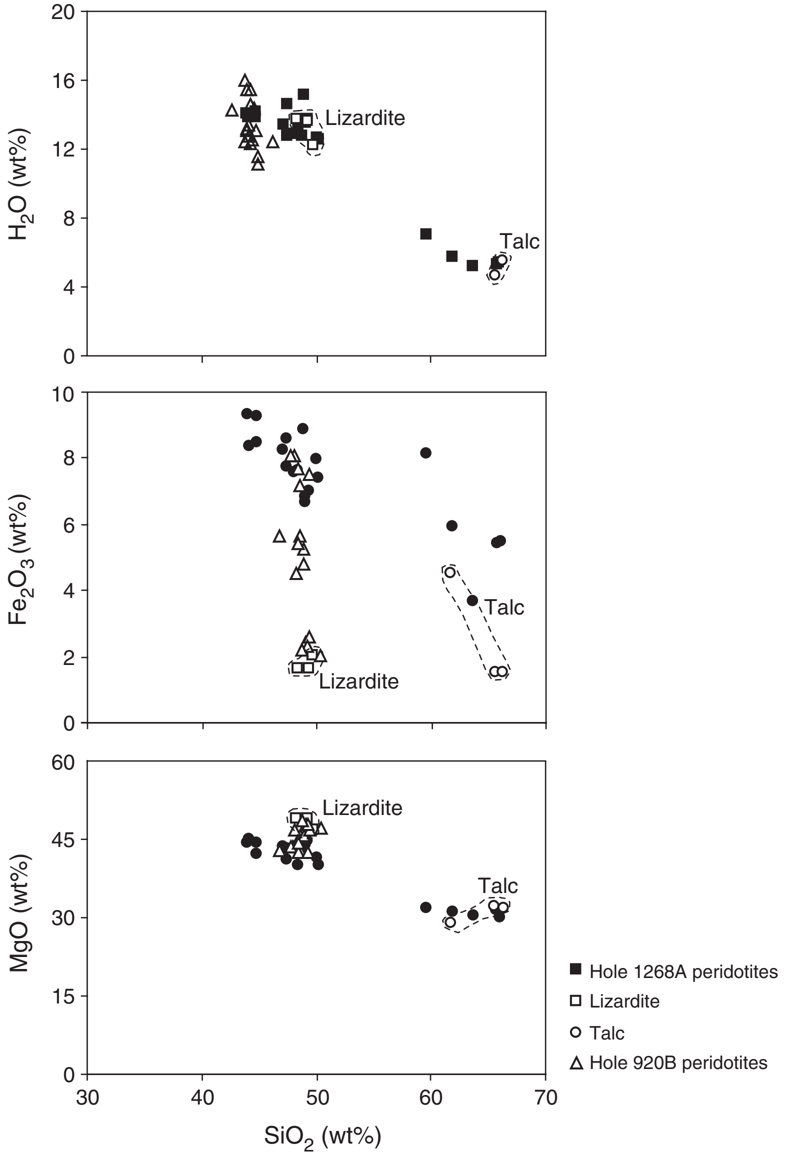

Figure F81. FeO vs. MgO whole-rock concentrations of Site 1268 peridotites (solid circles). Published data are also shown for comparison (open circles): Mid-Atlantic Ridge peridotites from Leg 109, Site 670, and Leg 153, Site 920. Abyssal peridotites = Southwest Indian Ridge (Snow and Dick, 1995) and Izu-Bonin-Mariana forearc (Parkinson and Pearce, 1998); W. Alps peridotites = western Alps orogenic lherzolites and ophiolites (Bodinier, 1988; Rampone et al., 1996), Oman Hz = Oman ophiolite harzburgites (Godard et al., 2000). Whole-rock compositions are presented on a volatile-free basis. The solid black lines show the variation of olivine composition constrained by FeO + MgO = 66.67 mol% and that of orthopyroxene constrained by FeO + MgO = 50 mol%. Fine gray lines show constant Mg# values (Mg# = 100 × molar Mg/[Mg + Fe_{total}]). Fe_{total} = total Fe as FeO.

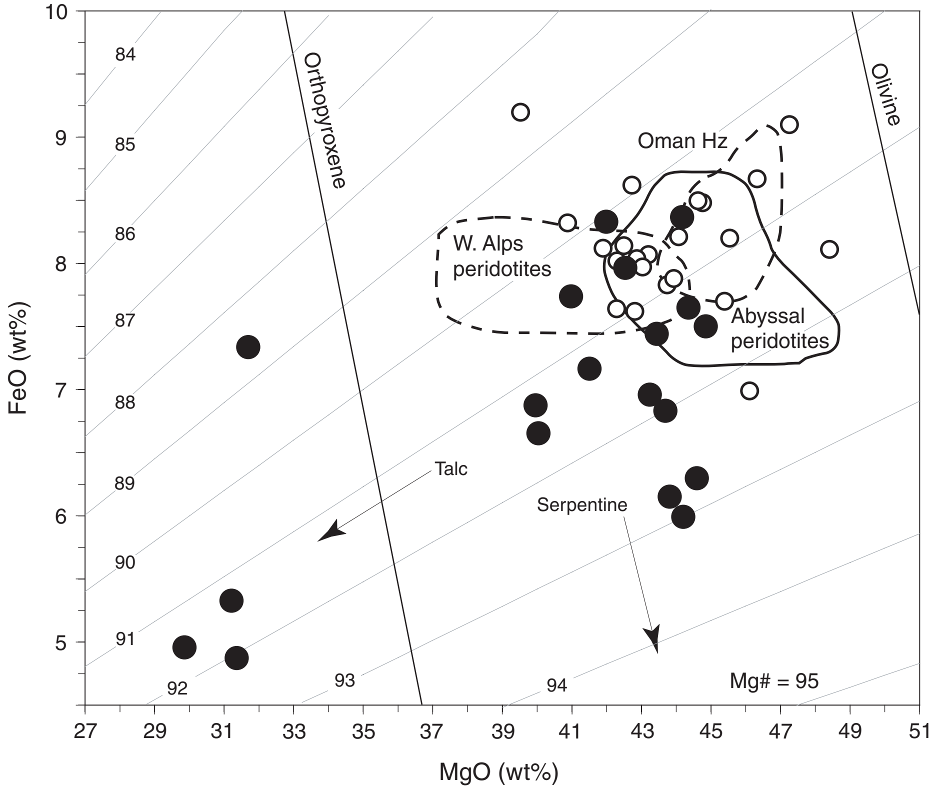

Figure F82. Zr, Sc, and V vs. Al_2O_3 in peridotites from Site 1268. Published data on Leg 153, Site 920 peridotites (Casey, 1997) are shown for comparison. Dashed line shows detection limit (DL) for Zr.

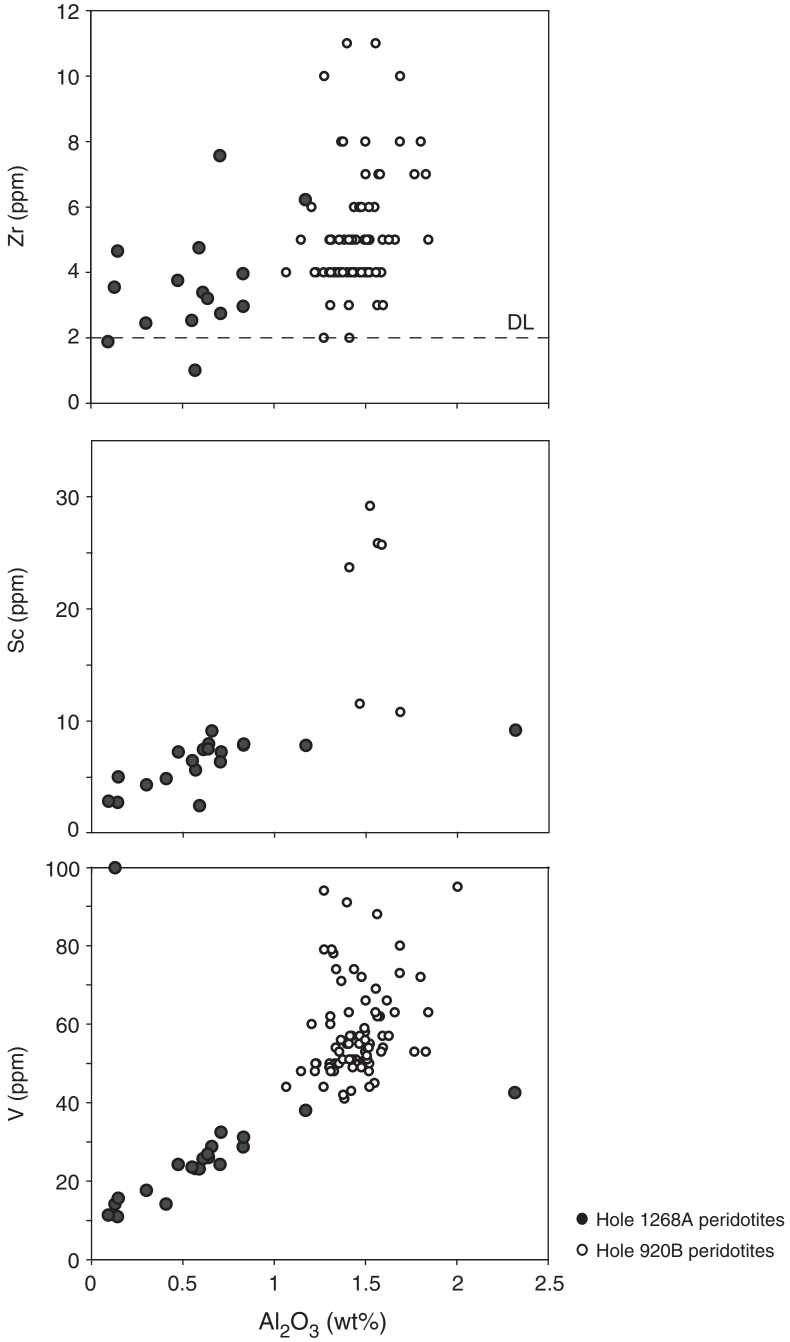

Figure F83. Cr, MgO, and LOI vs. SiO_2 in gabbroic rocks from Site 1268. Compositions of chlorite, talc, albite (Deer et al., 1992), the average composition of clinopyroxenes from the Haymiliyah gabbros (Oman ophiolite; Lachize, 1993), and the compilation of Leg 153 gabbros (Agar et al., 1997) are shown for comparison. Cpx = clinopyroxene. Dashed line shows detection limit (DL) for Cr.

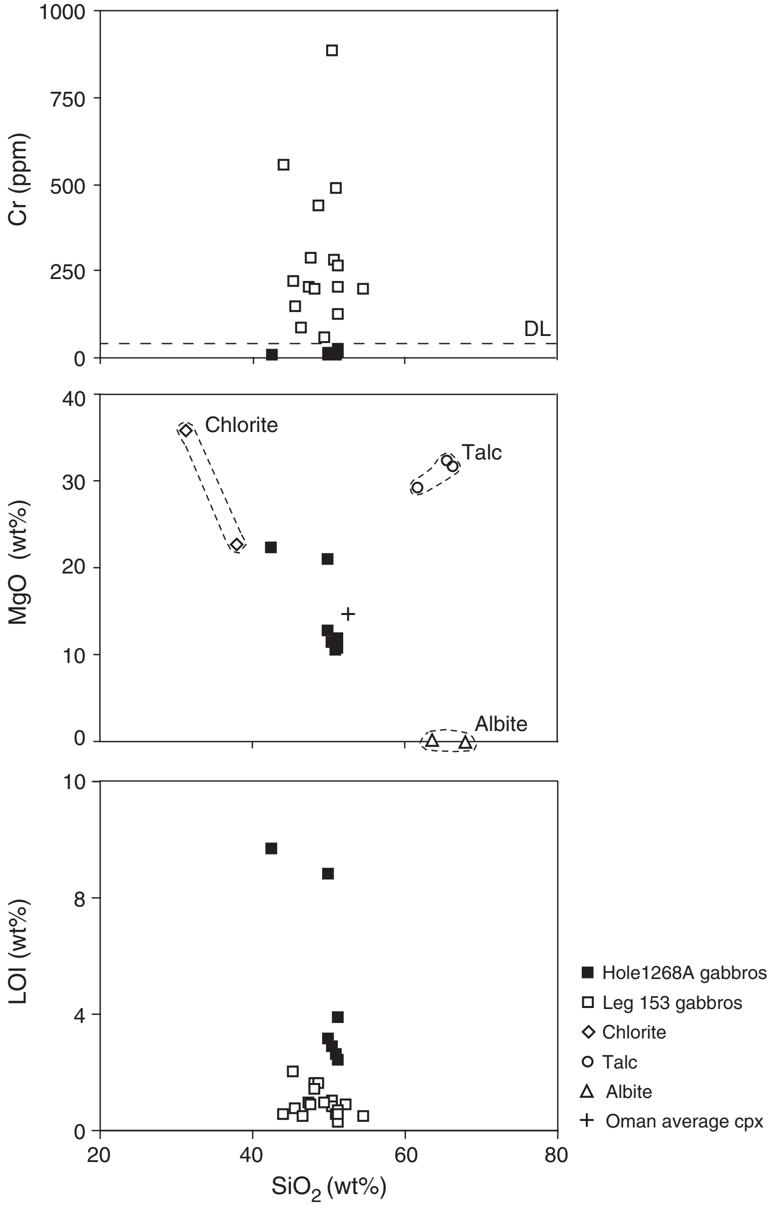

Figure F84. Fe_2O_3 and H_2O for Site 1268 rocks vs. magnetic susceptibility determined by MST.

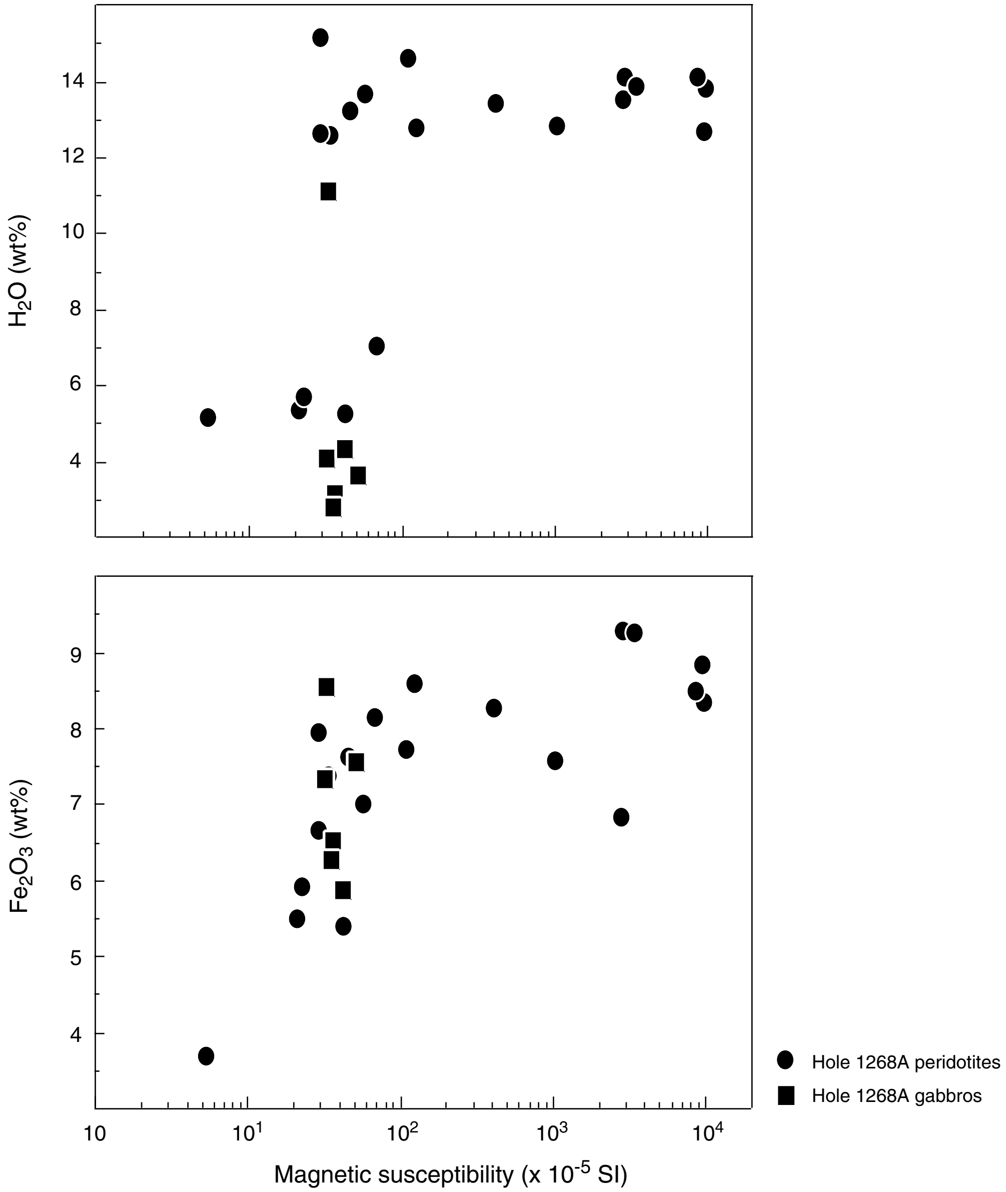

Figure F85. Thermal conductivity, *P*-wave velocity, apparent *P*-wave anisotropy, and bulk density in peridotites and gabbros recovered from Hole 1268A. TD = total depth.

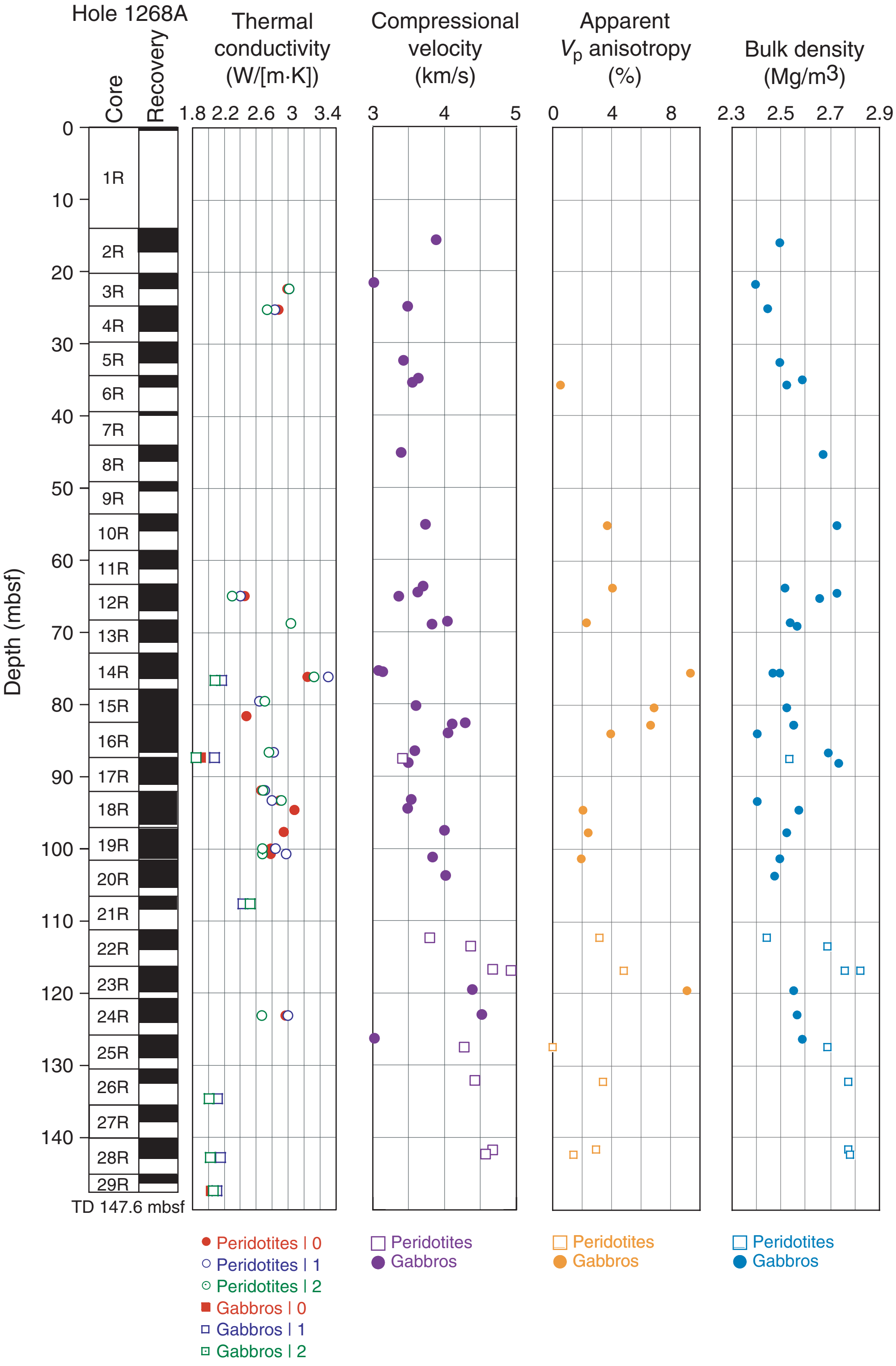

Figure F86. Natural gamma ray (NGR) emission in intervals 209-1268A-5R-2, 30–55 cm, and 16R-1, 102–118 cm. TD = total depth.

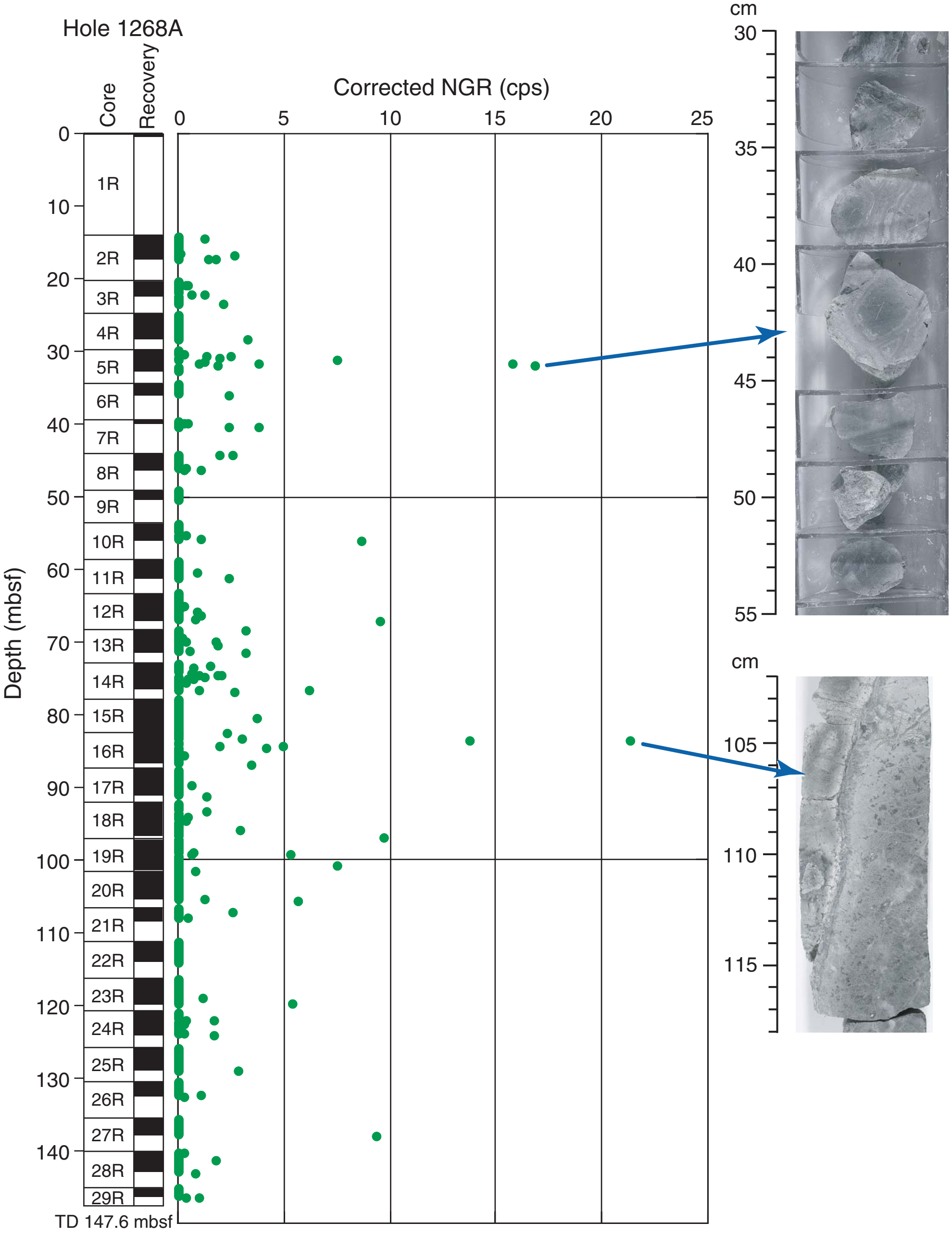

Figure F87. MST magnetic susceptibility in intervals 209-1268A-2R-2, 15–51 cm, and 18R-2, 84–100 cm. The highest susceptibility recorded by the Bartington magnetic susceptibility loop of the MST is 10,000 × 10^{-5} SI. TD = total depth.

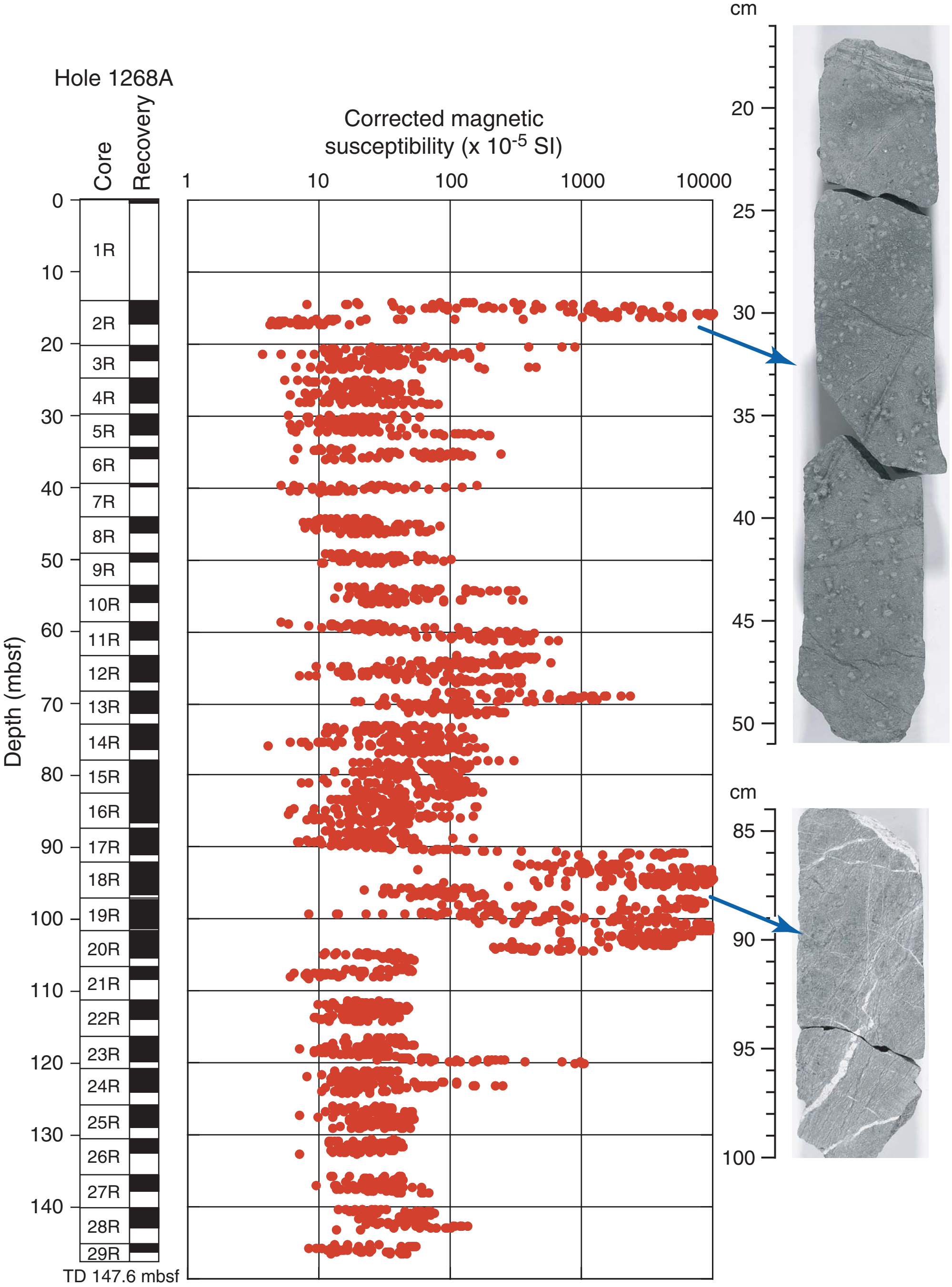

Figure F88. MST magnetic susceptibility of Hole 1268A cores and previous peridotite cores from Legs 147 (Gillis, Mével, Allan, et al., 1993) and 153 (Cannat, Karson, Miller, et al., 1995).

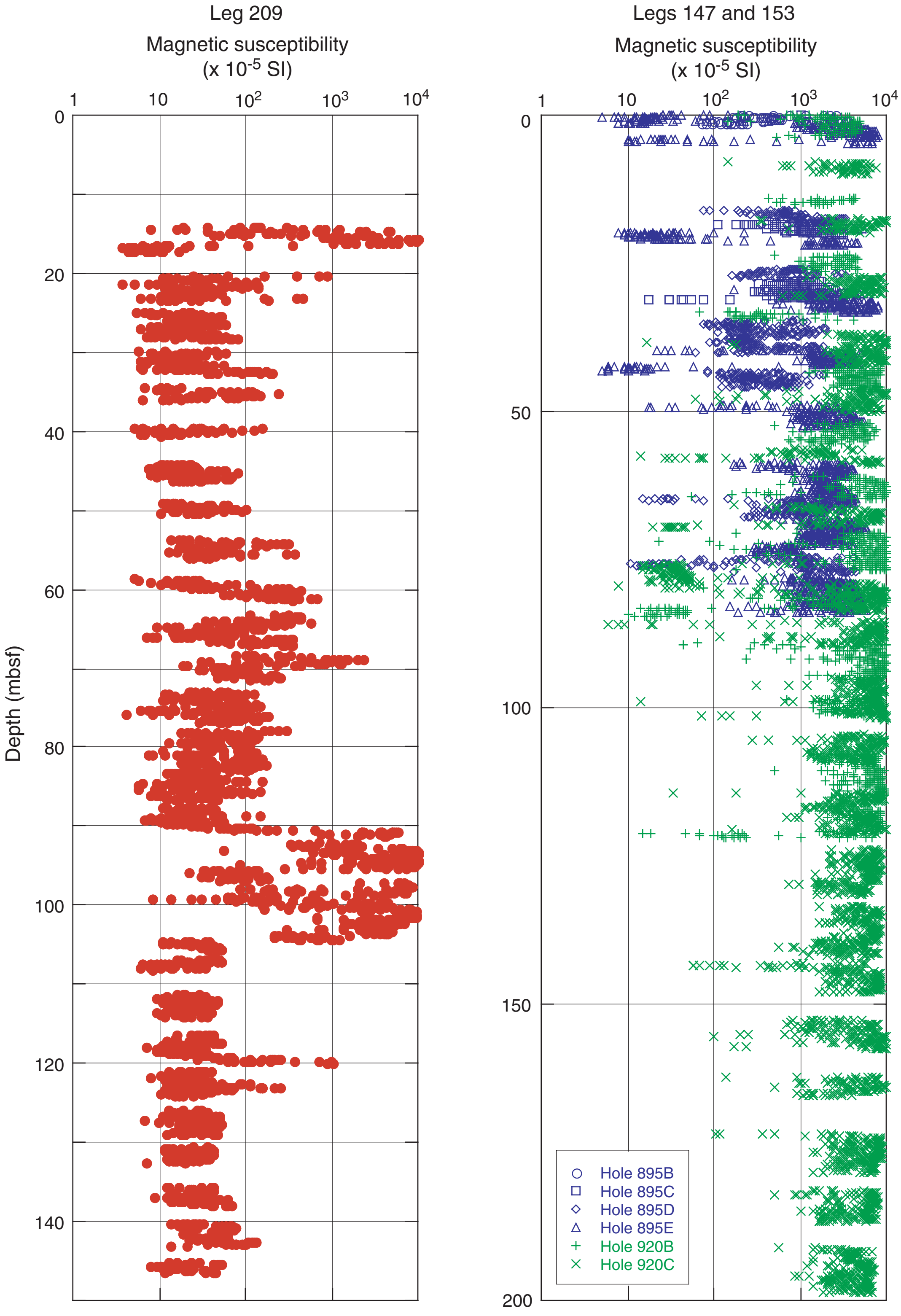

Figure F89. Thermal conductivity in selected samples of peridotite and gabbro from Hole 1268A. Shown for comparison are shipboard data from Legs 118 (Robinson, Von Herzen, et al., 1989), 147 (Gillis, Mével, Allan, et al., 1993), 153 (Cannat, Karson, Miller, et al., 1995), and 176 (Dick, Natland, Miller, et al., 1999).

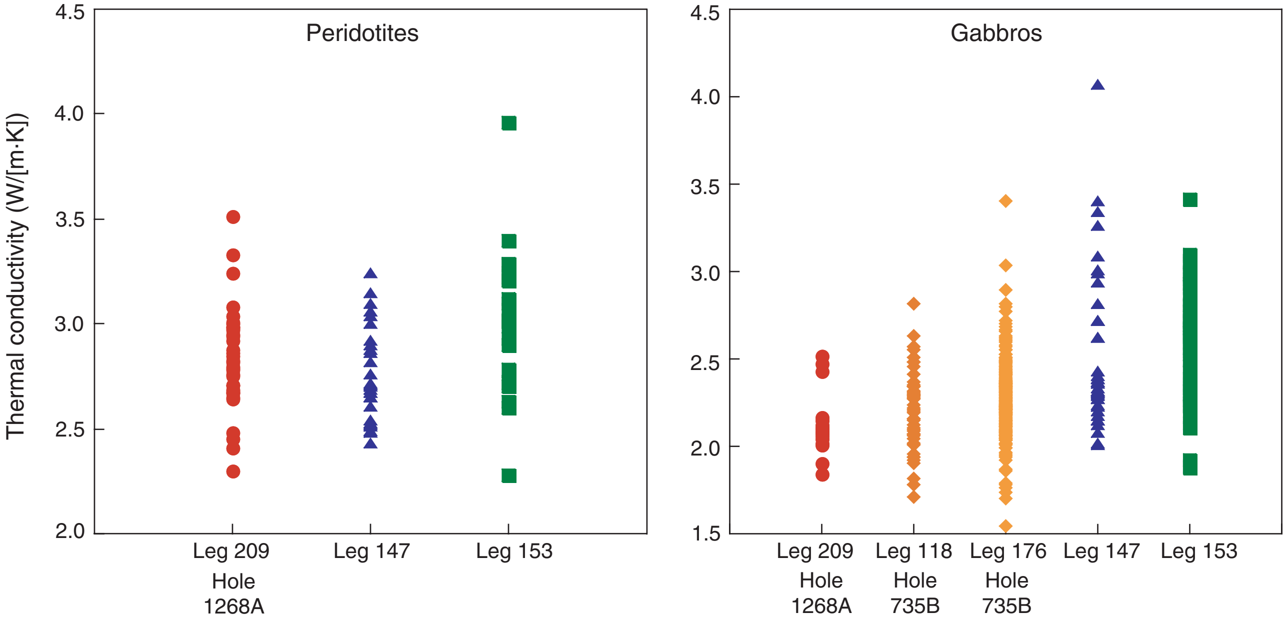

Figure F90. Wet bulk density vs. *P*-wave velocity in selected samples of gabbro and peridotite from Hole 1268A. Shown for comparison are shipboard data from Leg 153 (Cannat, Karson, Miller, et al., 1995).

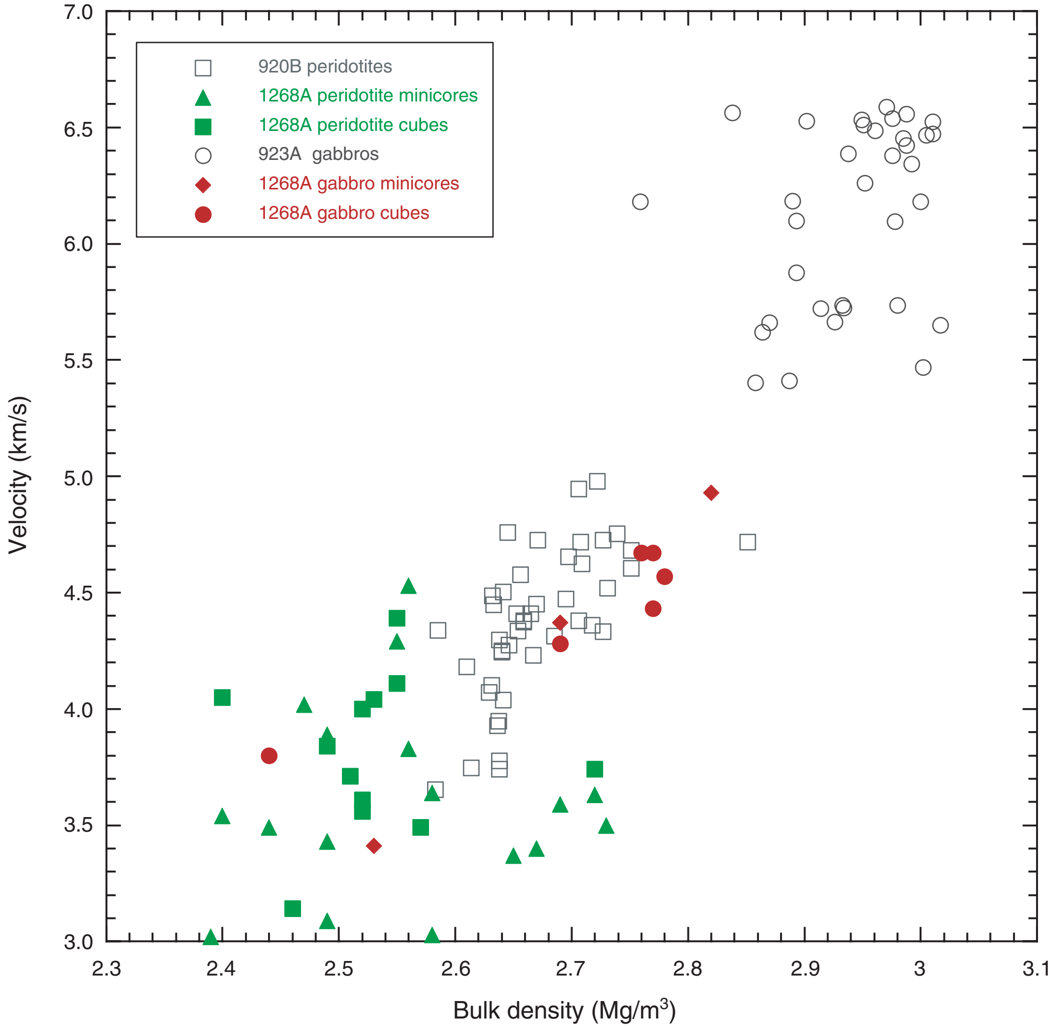

Figure F91. Average *P*-wave velocity in gabbros and peridotites from Hole 1268A, compared with seismic profiles (Vera et al., 1990; J. Collins and R. Detrick, pers. comm., 1998) and velocity-depth profiles for oceanic gabbros and ultramafic rocks inferred from laboratory studies. MAR = Mid-Atlantic Ridge, EPR = East Pacific Rise.

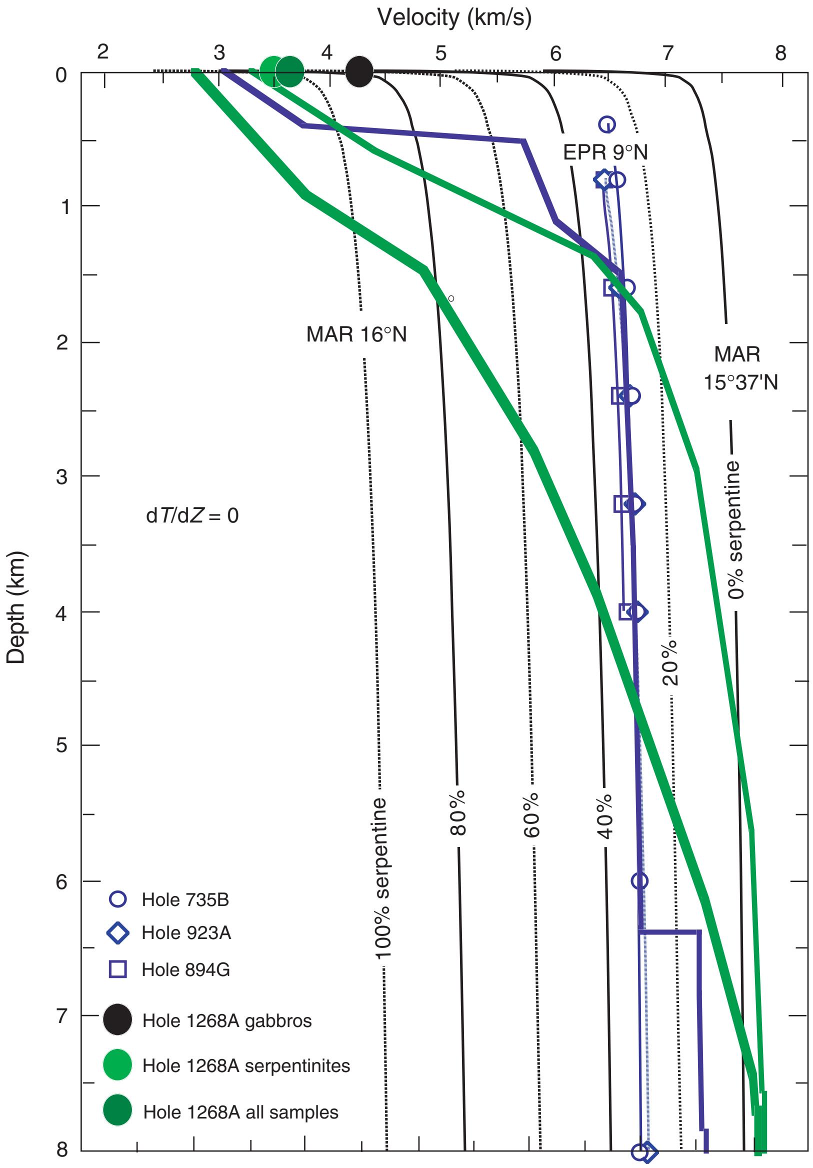

Figure F92. Long-core magnetic measurements from Hole 1268A. From left: volume magnetic susceptibility; intensity of the natural remanent magnetization (NRM) (red open circles) and remanence after 20-mT AF demagnetization (black solid circles); inclination of the NRM and at 20 mT (same symbols); percent of NRM remaining after 20-mT demagnetization step (lower values indicate higher degree of low-stability overprint, higher values indicate stable remanence).

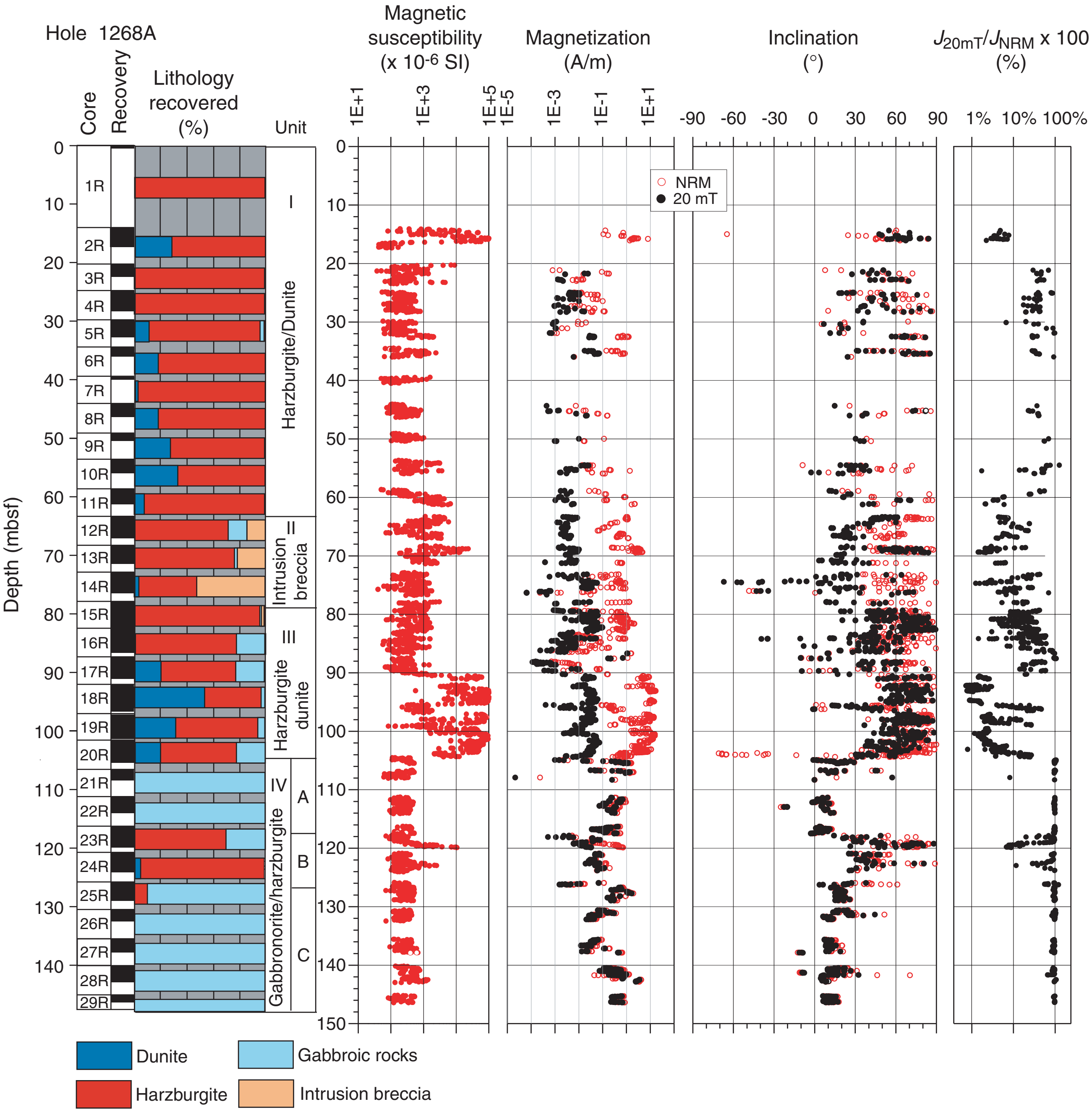

Figure F93. Vector endpoint demagnetization diagrams from a set of discrete samples of different lithologies. **A, B.** AF demagnetization of talc-altered ultramafics with variable degrees of drilling-related overprint; (A) Sample 209-1268A-20R-2, 117 cm; (B) Sample 209-1268A-8R-1, 123 cm. **C.** Thermal demagnetization of ultramafic rock with high degree of talc alteration (Sample 209-1268A-10R-2, 87 cm). **D, E.** AF and thermal demagnetization of gabbroic samples; (D) Sample 209-1268A-77R-1, 18 cm; (E) Sample 209-1268A-28R-2, 51 cm. NRM = natural remanent magnetization. Solid circles are projections onto the horizontal plane and open circles are projections onto the vertical plane.

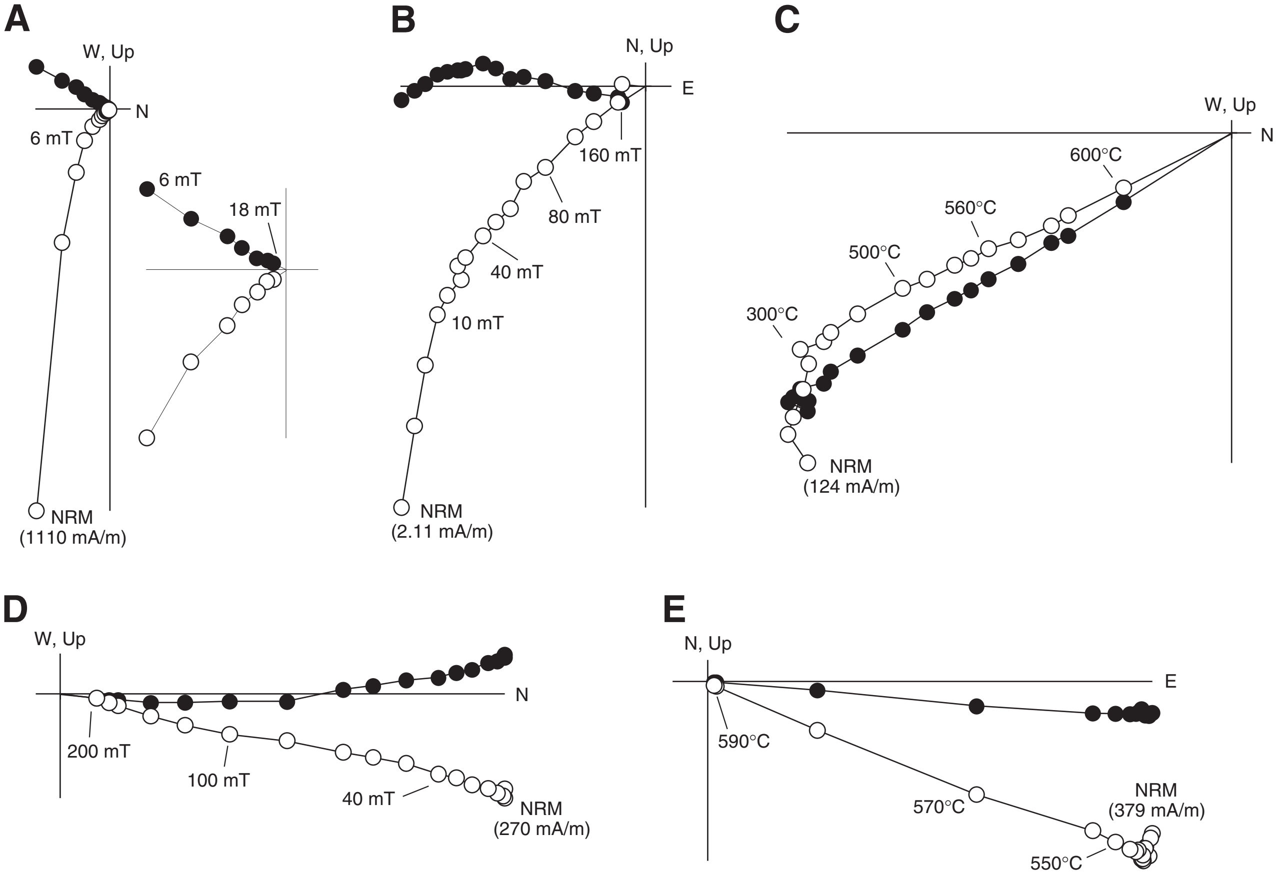

Figure F94. **A.** Median destructive field derived from AF NRM demagnetization of discrete samples of ultramafics (white bars) and gabbros (shaded bars). **B.** NRM unblocking temperature distribution from ultramafics with variable degrees of alteration (dashed lines) and gabbros (solid lines). Increasing degree of talc alteration of the serpentinized peridotite samples correlates with higher unblocking temperatures.

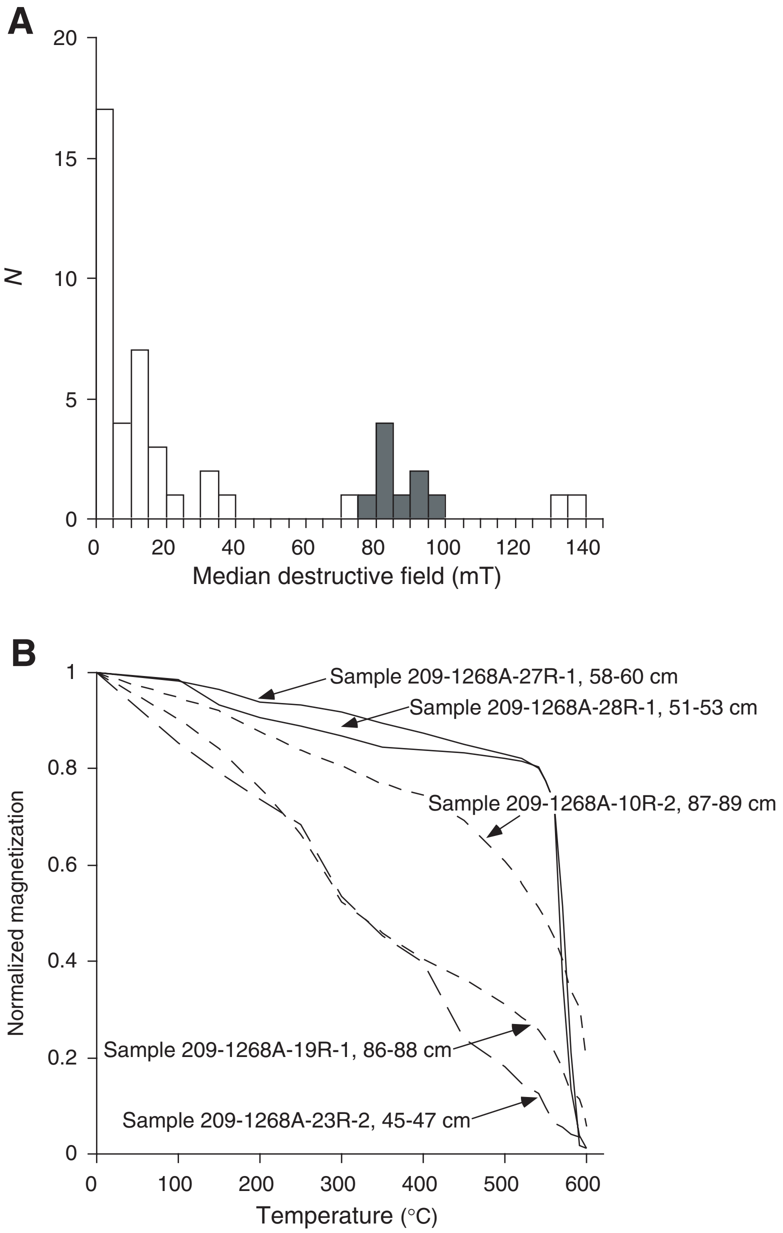

Figure F95. Example of an artifact caused by a core piece with order of magnitude variation in remanent intensity. Apparent reversal transition in Section 209-1268A-21R-1 (Piece 1) was recorded in continuous measurement of archive half. **A.** Vector endpoint diagrams from the two sides of the piece and stereonet projection of directions obtained at 2-cm intervals (top: Section 209-1268A-20R-2, 8 cm; bottom: Section 209-1268A-20R-2, 20 cm). **B.** Measurement of the remanence declination, inclination, and intensity of the same piece alone after 80-mT AF step. The core piece was measured alone so that header and trailer signals were recorded. The transitional directional trend at 12 cm (in the middle of the piece) has a mirror image at 28 cm, 8 cm away from the piece end. This demonstrates that the antipodal directions reflect the negative response function along x- and y- magnetometer axes at distances of 10 cm from the SQUID center. NRM = natural remanent magnetization.

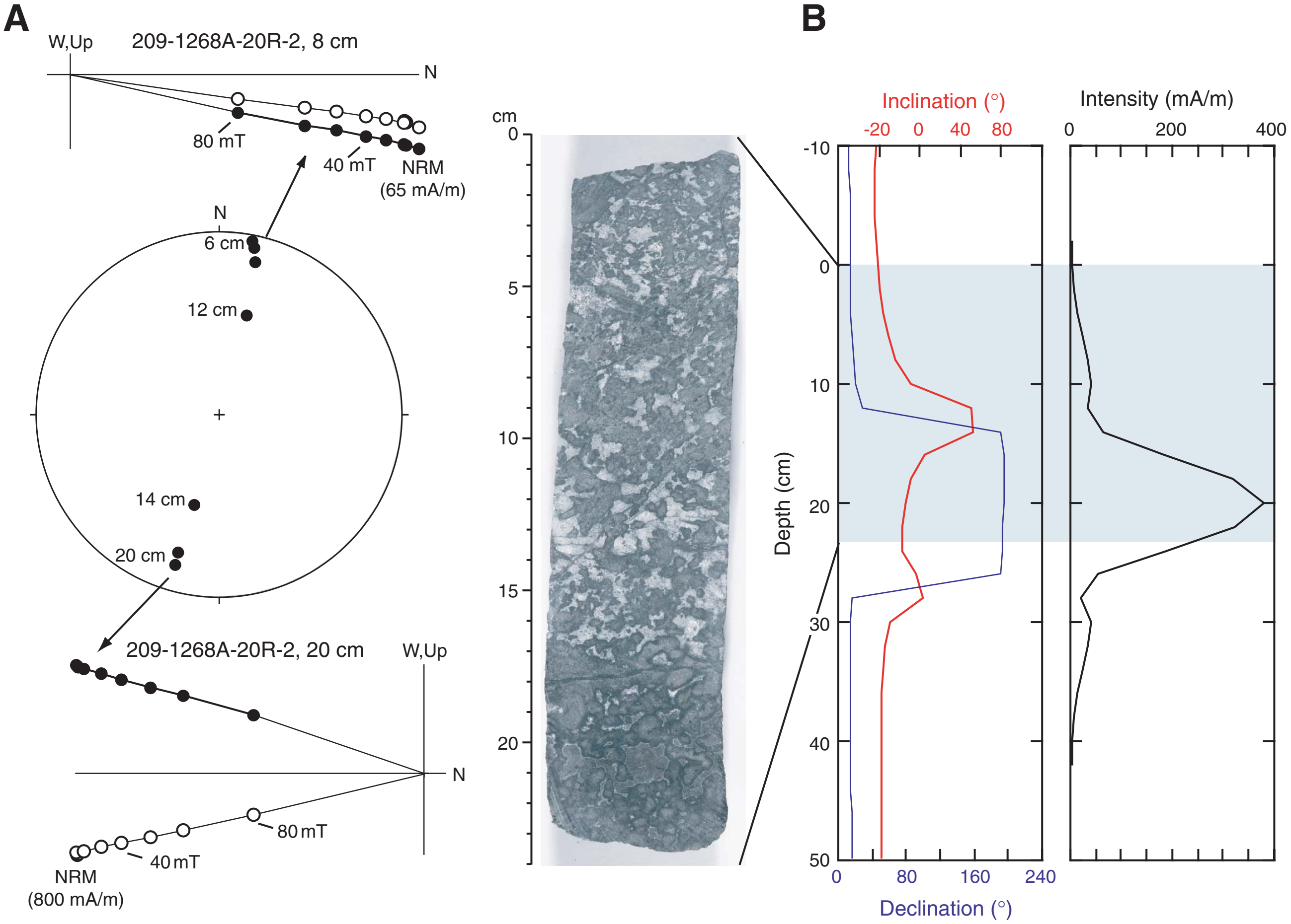

Figure F96. Standard curve for the perfluorocarbon tracer (PFT) and sample concentrations.

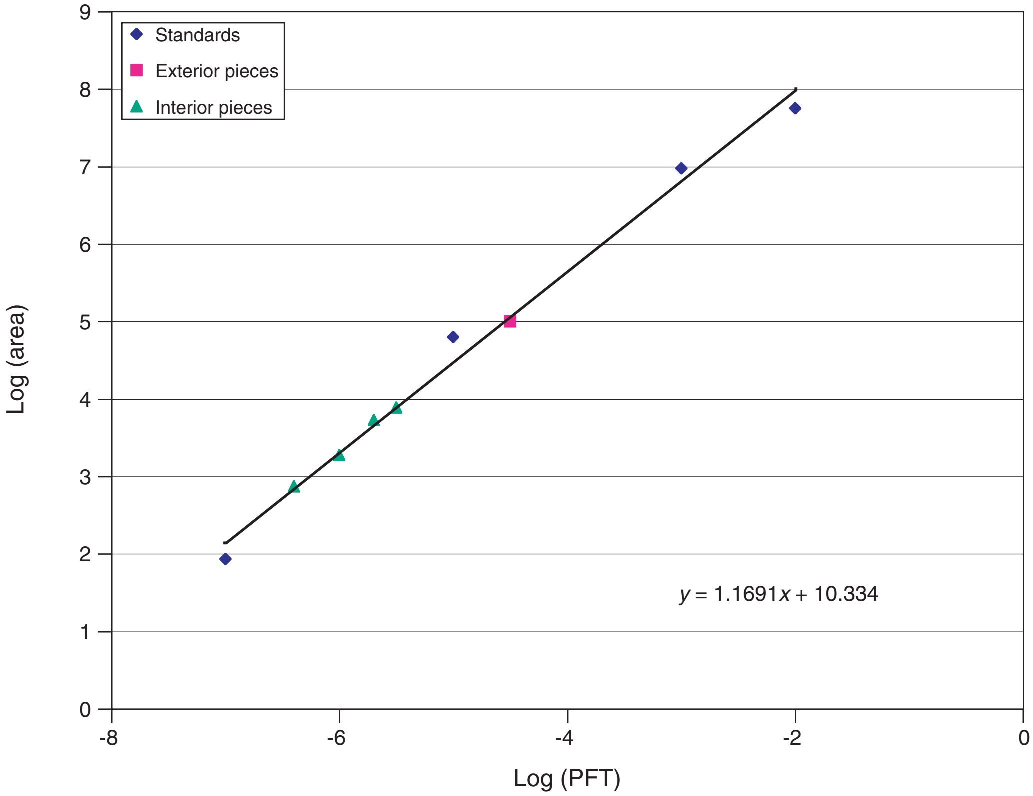

Figure F97. Temperature results of ocean bottom water from the WSTP deployment prior to drilling operations in Hole 1268A. **A.** Entire temperature-time series showing the temperature response of the WSTP prior to, during, and after the deployment. **B.** Expanded section of the temperature changes while the WSTP was lowered to a depth of 2 m above seafloor. This profile shows the rising temperatures before collecting a water sample, the time when the water-sampling valve opened (VO), when the valve closed (VC), and a thermal anomaly after the valve closed. **C.** A linear fit to the temperature time-series data before the water-sampling valve opened.

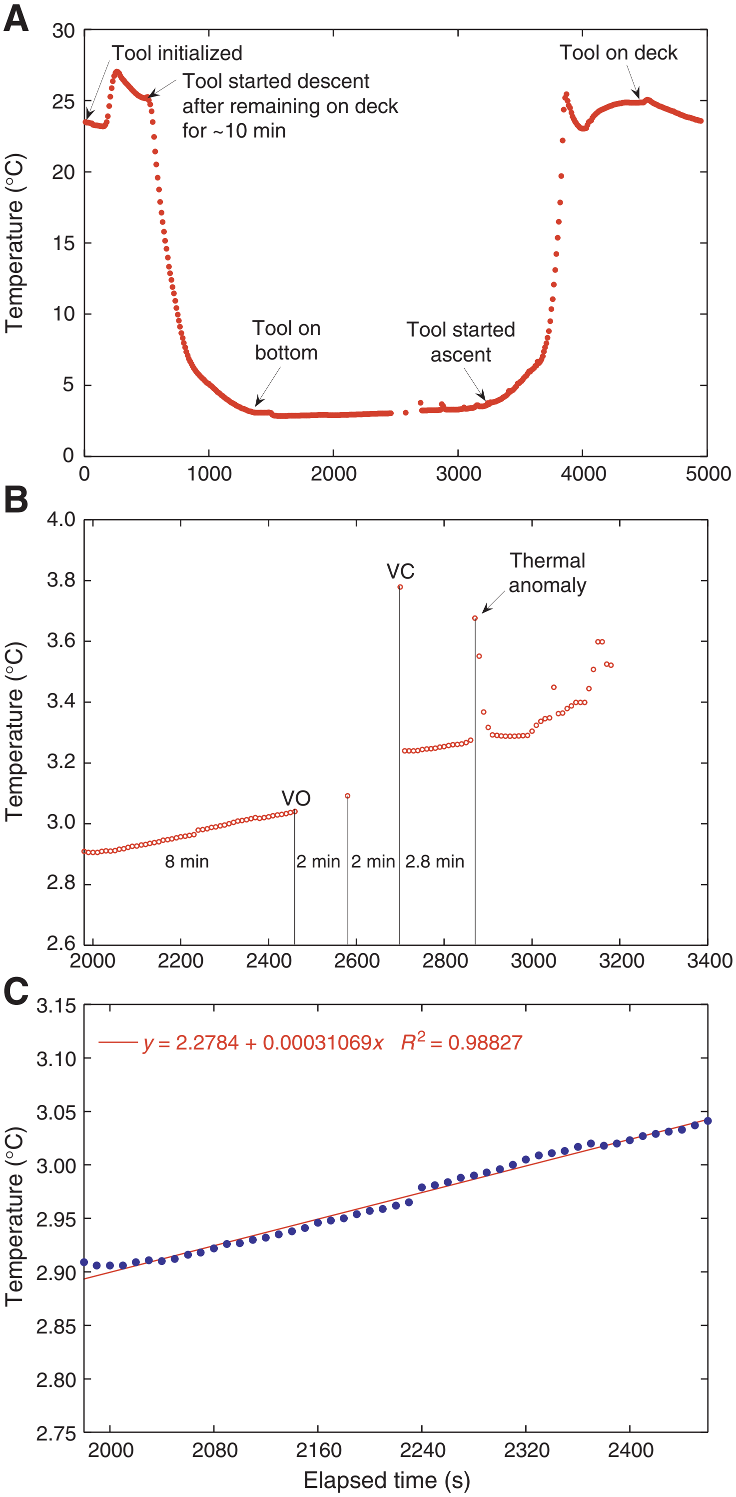

Table T1. Coring summary, Site 1268.

Hole 1268A

Latitude: 14°50.7552′N
Longitude: 45°4.6409′W
Time on site: 109.75 (0545 hr, 22 May–1930 hr, 26 May 2003)
Seafloor (drill pipe measurement from rig floor, mbrf): 3018.0
Distance between rig floor and sea level (m): 11.0
Water depth (drill pipe measurement from sea level, m): 3007.0
Total depth (drill pipe measurement from rig floor, mbrf): 3165.6
Total penetration (meters below seafloor, mbsf): 147.6
Total length of cored section (m): 147.6
Total core recovered (m): 78.69
Core recovery (%): 53.3
Total number of cores: 29

Core	Date (May 2003)	Local time (hr)	Depth (mbsf)		Length (m)		Recovery (%)	Remarks
			Top	Bottom	Cored	Recovered		
209-1268A-								
1R	23	1115	0.0	14.0	14.0	0.80	5.7	WSTP @ 3016 m; AHC on
2R	23	1410	14.0	20.2	6.2	3.00	48.4	
3R	23	1640	20.2	24.8	4.6	2.84	61.7	
4R	23	1940	24.8	29.8	5.0	3.15	63.0	
5R	23	2200	29.8	34.4	4.6	2.47	53.7	
6R	23	2355	34.4	39.4	5.0	1.38	27.6	
7R	24	0140	39.4	44.0	4.6	1.04	22.6	
8R	24	0325	44.0	49.0	5.0	1.90	38.0	
9R	24	0500	49.0	53.6	4.6	1.36	29.6	
10R	24	0635	53.6	58.6	5.0	2.11	42.2	
11R	24	0835	58.6	63.2	4.6	2.53	55.0	
12R	24	1045	63.2	68.2	5.0	3.35	67.0	
13R	24	1310	68.2	72.8	4.6	2.94	63.9	
14R	24	1540	72.8	77.8	5.0	3.58	71.6	
15R	24	1910	77.8	82.4	4.6	4.56	99.1	
16R	24	2220	82.4	87.4	5.0	4.11	82.2	
17R	25	0030	87.4	92.0	4.6	3.61	78.5	
18R	25	0315	92.0	97.0	5.0	4.33	86.6	
19R	25	0530	97.0	101.6	4.6	4.19	91.1	
20R	25	0730	101.6	106.6	5.0	3.57	71.4	
21R	25	0845	106.6	111.2	4.6	1.61	35.0	
22R	25	1010	111.2	116.2	5.0	2.57	51.4	
23R	25	1205	116.2	120.8	4.6	3.47	75.4	
24R	25	1415	120.8	125.8	5.0	2.90	58.0	
25R	25	1620	125.8	130.5	4.7	2.94	62.6	
26R	25	1855	130.5	135.5	5.0	2.00	40.0	
27R	25	2045	135.5	140.1	4.6	2.36	51.3	
28R	25	2230	140.1	145.1	5.0	2.74	54.8	
29R	26	0300	145.1	147.6	2.5	1.28	51.2	
				Cored totals:	147.6	78.69	53.3	

Notes: WSTP = Water Sampling Temperature Probe. AHC = active heave compensation.

Table T2. XRD results, Hole 1268A.

Core, section, interval (cm)	Depth (mbsf)	Piece	Rock type	Mineralogy			ICP-AES analyses	Thin section
				Major	Minor	Trace		
209-1268A-								
2R-2, 41–44	15.8	4C	Harzburgite	Lizardite	Talc, magnetite		Yes	Yes
2R-2, 73–76	16.1	8	Harzburgite	Lizardite	Magnetite		Yes	Yes
2R-3, 11–13	16.9	4	Harzburgite	Talc			Yes	Yes
3R-2, 107–111	22.7	20A	Harzburgite	Chrysotile, talc		Pyrite	Yes	Yes
4R-1, 122–127	26.0	20A	Harzburgite	Lizardite	Talc		Yes	Yes
4R-2, 92–94	27.2	15	Harzburgite	Talc			—	—
5R-2, 60–63	31.9	14	Harzburgite	Talc			Yes	Yes
6R-1, 109–112	35.5	15	Harzburgite	Lizardite	Talc		Yes	Yes
10R-2, 5–7	55.1	1	Dunite	Talc			Yes	Yes
10R-2, 82–85	55.9	14	Harzburgite	Talc			Yes	Yes
12R-1, 50–52	63.7	3	Harzburgite	Lizardite		Talc	Yes	Yes
13R-1, 33–37	68.5	6A	Harzburgite	Lizardite		Talc	Yes	Yes
13R-1, 71–76	68.9	6B	Harzburgite	Lizardite		Talc	Yes	Yes
14R-2, 130–133	75.6	16	Harzburgite	Talc	Lizardite		Yes	Yes
15R-3, 132–135	81.7	5A	Harzburgite	Lizardite			Yes	Yes
16R-1, 36–42	82.8	3B	Dunite	Lizardite			Yes	Yes
16R-2, 36–40	84.0	1	Harzburgite	Lizardite	Talc	Amphibole	Yes	Yes
16R-4, 9–13	86.7	1	Gabbro	Albite	Chlorite	Amphibole	Yes	Yes
18R-2, 118–121	94.5	11A	Dunite	Lizardite	Magnetite		Yes	Yes
18R-3, 0–5	94.6	1A	Dunite	Lizardite	Magnetite		Yes	Yes
19R-1, 54–57	97.5	2B	Harzburgite	Lizardite	Magnetite		Yes	Yes
19R-3, 0–6	99.8	1	Harzburgite/Dunite	Lizardite	Magnetite		Yes	Yes
19R-2, 127–135	99.7	16	Vein	Lizardite			—	—
21R-1, 31–35	106.9	3	Gabbro	Albite, chlorite, quartz			Yes	Yes
21R-2, 21–24	108.3	5	Gabbro	Plagioclase, chlorite		Amphibole? Lizardite?	Yes	Yes
23R-1, 53–57	116.7	4C	Gabbro	Plagioclase	Clinopyroxene	Lizardite	Yes	Yes
26R-2, 16–22	132.1	2	Gabbro	Plagioclase	Clinopyroxene	Chlorite, amphibole?	Yes	Yes
28R-2, 28–32	141.7	1B	Gabbro	Plagioclase	Chlorite, amphibole		Yes	Yes
29R-1, 115–120	146.3	14	Gabbro	Plagioclase	Chlorite, amphibole		Yes	Yes

Notes: Due to peak overlap, samples with identified lizardite may also contain chrysotile. Sample 209-1268A-21R-2, 21–24 cm: poor quality, high noise, low count rates. Qualifiers "major, minor, and trace" indicate relative abundances based on peak heights and do not necessarily reflect true relative proportions. ICP-AES = inductively coupled plasma–atomic emission spectrometry. ICP-AES data are available in Table **T5,** p. 159. This table is also available in **ASCII.**

Table T3. Vein mineralogy, Hole 1268A.

Mineral in vein	Volume (cm^3)	Volume by vein type (cm^3)						Vein minerals in veins (%)	Vein minerals in hole (%)	Volume in vein types (%)					
		MSV	TPV	MTV	SPV	CLV	OTV			MSV	TPV	MTV	SPV	CLV	OTV
Talc	9,511	215	1,857	6,900	492	46		48.0	4.24	1.1	9.37	34.80	2.48	0.23	
Serpentine	7,755		37	335	7,331	15	37	39.1	3.46		0.19	1.69	36.97	0.07	0.19
Sulfides	1,602	903	359	316	16	9		8.1	0.71	4.55	1.81	1.59	0.08	0.04	
Iron oxides (others)	488	344	117	24	2	1		2.5	0.22	1.74	0.59	0.12	0.01	0.003	
Chlorite	402		38	120	165	79		2.0	0.18		0.19	0.60	0.83	0.40	
Magnetite	44			1	5	1	37	0.2	0.02			0.00	0.03	0.01	0.19
Amphibole	26			12	3	12		0.1	0.01			0.06	0.01	0.06	
Volume in site by vein type (%)									8.85	0.65	1.07	3.44	3.58	0.07	0.03
Relative volume of vein types (%)										7.4	12.1	38.9	40.4	0.8	0.4
Total	19,829	1,463	2,407	7,707	8,015	163	74								

Notes: MSV = massive sulfide veins; TPV = talc-pyrite veins; MTV = massive talc veins; SPV = serpentine veins; CLV = chlorite veins; OTV = other veins. Vein volumes are based on macroscopic observations of vein mineralogy and vein percentage. We computed volume percentages of veins by using the volume weighted average of macroscopic estimates on the reported length scale of observation (i.e., piece, section, etc.) using relative curated length and assuming a constant core radius throughout the hole. This table is also available in ASCII.

Table T4. Crystal-plastic deformation intensities, Hole 1268A.

Lithology	Cores				Thin sections	
	Average CPf	*N*	Total core (m)*	Percent of core	Average CPf	*N*
Harzburgite	0.9	593	78.9	55.5	1.1	40
Dunite	0.3	80	12	8.4	0	5
Gabbro Cores 209-1268A-1R to 19R	0.4	67	11.3	7.9		
Gabbro Cores 209-1268A-20R to 29R	0	212	34.6	24.3		
Gabbro (all)	0.2	315	45.9	32.3	0.3	13
Harzburgite-gabbro breccia	1.3	55	5.4	3.8		
Average	0.67				0.8	61

Note: CPf = crystal-plastic deformation intensity index (0 = no deformation through 5 = extreme deformation). *N* = number of measurements. * = recovery expanded to fill the cored intervals for each lithology. This table is also available in **ASCII.**

Table T5. Major and trace element compositions of rocks, Hole 1268A. (Continued on next page.)

Core, section, interval (cm)	Depth (mbsf)	Piece	Unit	Major element oxides (wt%)										LOI	Volatiles (wt%)	
				SiO_2	TiO_2	Al_2O_3	Fe_2O_3	MgO	MnO	CaO	Na_2O	K_2O	Total		CO_2	H_2O
209-1268A-																
2R-2, 41–44	15.81	4C	I	48.83	<0.01	0.66	8.85	42.53	0.06	0.00	0.09	0.01	101.04	11.80	<0.04	12.71
2R-2, 73–76	16.13	8	I	49.10	<0.01	0.57	6.84	43.81	0.08	<0.06	0.07	0.01	100.48	13.10	<0.04	13.55
2R-3, 11–13	16.94	4	I	63.71	<0.01	0.14	3.69	30.53	0.02	<0.06	0.06	<0.01	98.16	4.84	<0.04	5.17
3R-2, 107–111	22.70	20A	I	50.21	<0.01	0.64	7.39	40.04	0.07	<0.06	0.08	0.01	98.45	12.00	<0.04	12.57
4R-1, 122–127	26.02	20A	I	50.00	<0.01	0.59	7.96	41.51	0.07	<0.06	0.08	0.01	100.23	11.90	<0.04	12.66
5R-2, 60–63	31.90	14	I	66.03	<0.01	0.41	5.51	29.86	0.06	<0.06	0.10	0.01	101.98	4.70	<0.04	5.36
6R-1, 109–112	35.49	15	I	49.34	<0.01	0.55	7.00	44.59	0.04	0.06	0.07	0.01	101.66	12.33	0.15	13.68
10R-2, 5–7	55.09	1	I	65.80	<0.01	0.09	5.41	31.36	0.07	<0.06	0.02	<0.01	102.78	4.55	0.03	5.29
10R-2, 82–85	55.86	14	I	61.85	<0.01	0.30	5.92	31.22	0.10	0.07	0.08	0.01	99.54	5.25	0.03	5.69
12R-1, 50–52	63.70	3	II	47.15	0.01	0.71	8.27	43.44	0.10	<0.06	0.08	0.01	99.81	12.44	0.06	13.45
13R-1, 33–37	68.53	6A	II	47.41	0.22	2.32	8.60	40.98	0.17	0.12	0.12	0.02	99.95	12.31	0.06	12.81
13R-1, 71–76	68.91	6B	II	48.12	<0.01	0.61	7.59	43.69	0.07	<0.06	0.08	0.01	100.20	12.35	0.05	12.83
14R-2, 130–133	75.59	16	II	59.60	0.01	0.70	8.15	31.69	0.07	0.11	0.22	0.01	100.56	6.27	0.07	7.07
15R-3, 132–135	81.72	5	III	48.94	0.01	0.83	6.66	44.21	0.12	0.08	0.07	0.01	100.93	13.32	0.19	15.15
16R-1, 36–42	82.76	3B	III	47.44	<0.01	0.83	7.73	43.24	0.14	0.19	0.07	0.01	99.66	12.75	0.14	14.64
16R-2, 36–40	83.97	1	III	48.45	0.07	1.17	7.64	39.96	0.22	0.45	0.08	0.01	98.04	11.89	0.13	13.24
16R-4, 9–13	86.70	1	III	51.35	0.24	17.90	5.88	11.88	0.36	7.85	3.24	0.06	98.76	3.89	0.11	4.31
18R-2, 118–121	94.46	11A	III	44.14	<0.01	0.13	8.34	44.85	0.06	<0.06	0.08	0.01	97.63	12.82	0.20	13.83
18R-3, 0–5	94.59	1A	III	43.93	<0.01	0.15	9.30	44.17	0.06	<0.06	0.08	<0.01	97.71	12.72	0.10	14.11
19R-1, 54–57	97.54	2B	III	44.81	0.01	0.47	8.50	44.36	0.08	0.07	0.06	0.01	98.35	12.75	0.12	14.15
19R-3, 0–6	99.82	1	III	44.75	<0.01	0.64	9.25	41.99	0.10	0.07	0.09	0.01	96.90	12.58	0.09	13.87
21R-1, 31–35	106.91	3	IVA	50.12	0.29	19.01	8.54	20.78	0.08	1.99	0.83	0.04	101.68	8.80	0.11	11.13
21R-2, 21–24	108.31	5	IVA	42.56	0.37	23.74	9.24	22.31	0.18	2.28	2.02	0.07	102.78	9.70	0.07	13.10
23R-1, 53–57	116.73	4C	IVA	51.12	0.25	18.18	6.52	10.52	0.15	13.42	2.31	0.04	102.52	2.62	0.09	3.15
26R-2, 16–22	132.10	2	IVC	51.22	0.24	18.39	6.28	10.62	0.16	13.37	2.14	0.04	102.46	2.38	0.09	2.81
28R-2, 28–32	141.70	1B	IVC	50.61	0.33	18.26	7.57	11.41	0.17	11.28	2.24	0.07	101.93	2.90	0.10	3.64
29R-1, 115–120	146.25	14	IVC	49.93	0.25	18.29	7.33	12.71	0.16	11.24	2.07	0.09	102.07	3.13	0.08	4.08

Note: LOI = loss on ignition. This table is also available in **ASCII.**

Table T5 (continued).

Core, section, interval (cm)	Depth (mbsf)	Piece	Unit	Trace elements (ppm)								
				S	Cr	Ni	Sr	V	Y	Zr	Sc	Co
209-1268A-												
2R-2, 41–44	15.81	4C	I	1,168	2,451	2,869	<5	29	<2	<2	9.1	82
2R-2, 73–76	16.13	8	I	15,899	3,379	2,816	<5	23	<2	<2	5.7	93
2R-3, 11–13	16.94	4	I	6,285	1,127	1,923	<5	11	<2	<2	<4.0	50
3R-2, 107–111	22.70	20A	I	9,028	2,473	2,641	<5	26	<2	<2	8.0	73
4R-1, 122–127	26.02	20A	I	9,392	2,248	2,787	<5	23	2	5	<4.0	78
5R-2, 60–63	31.90	14	I	1,094	1,998	1,878	<5	14	<2	<2	4.9	51
6R-1, 109–112	35.49	15	I	6,366	2,180	2,276	<5	24	<2	3	6.5	103
10R-2, 5–7	55.09	1	I	4,443	834	1,930	<5	11	<2	<2	<4.0	86
10R-2, 82–85	55.86	14	I	3,453	1,190	1,758	<5	18	<2	2	4.3	78
12R-1, 50–52	63.70	3	II	8,476	2,861	2,570	<5	33	<2	3	7.3	119
13R-1, 33–37	68.53	6A	II	4,448	3,849	2,357	<5	43	9	50	9.2	112
13R-1, 71–76	68.91	6B	II	1,735	2,320	2,477	<5	26	<2	3	7.5	115
14R-2, 130–133	75.59	16	II	8,232	2,025	2,207	<5	24	<2	8	6.4	93
15R-3, 132–135	81.72	5	III	1,377	2,775	2,542	<5	29	<2	4	7.9	101
16R-1, 36–42	82.76	3B	III	5,434	3,281	2,246	<5	31	<2	3	8.0	91
16R-2, 36–40	83.97	1	III	2,585	2,108	2,378	<5	38	<2	6	7.8	95
16R-4, 9–13	86.70	1	III		<41	<165	145	161	6	9	39.3	40
18R-2, 118–121	94.46	11A	III	1,420	893	3,499	<5	14	<2	4	4.9	135
18R-3, 0–5	94.59	1A	III	1,482	1,136	3,286	<5	16	<2	5	5.0	128
19R-1, 54–57	97.54	2B	III	1,307	1,926	2,666	<5	24	<2	4	7.2	120
19R-3, 0–6	99.82	1	III	4,048	2,720	2,364	<5	27	<2	3	7.5	94
21R-1, 31–35	106.91	3	IVA	<400	<41	<165	51	201	6	5	45.7	40
21R-2, 21–24	108.31	5	IVA	<400	<41	<165	66	251	8	10	58.4	47
23R-1, 53–57	116.73	4C	IVA	<400	<41	<165	128	177	7	9	43.9	36
26R-2, 16–22	132.10	2	IVC	<400	<41	<165	121	166	5	6	40.2	37
28R-2, 28–32	141.70	1B	IVC	<400	<41	<165	120	158	8	24	33.5	41
29R-1, 115–120	146.25	14	IVC	<400	<41	<165	115	161	6	7	38.5	42

Table T6. Thermal conductivity measurements, Hole 1268A.

Core, section, interval (cm)	Depth (mbsf)	Piece	Thermal conductivity* (W/[m·K])	Standard deviation	Standard error	Needle orientation	Apparent anisotropy (%)	Primary lithology
209-1268A-								
3R-2, 0–14	22.3	1	2.99	0.047	0.024	0	0.8	Harzburgite
3R-2, 0–14	22.3	1	3.01	0.043	0.022	1		Harzburgite
3R-2, 0–14	22.3	1	3.02	0.015	0.008	2		Harzburgite
4R-1, 22–31	25.2	5B	2.88	0.020	0.010	0	5.0	Harzburgite
4R-1, 22–31	25.2	5B	2.83	0.043	0.022	1		Harzburgite
4R-1, 22–31	25.2	5B	2.74	0.015	0.008	2		Harzburgite
12R-1, 124–136	64.9	14	2.45	0.039	0.020	0	6.3	Harzburgite
12R-1, 124–136	64.9	14	2.41	0.045	0.022	1		Harzburgite
12R-1, 124–136	64.9	14	2.30	0.010	0.005	2		Harzburgite
13R-1, 31–39	68.7	6A	3.04	0.047	0.023	1		Harzburgite
14R-2, 106–116	76.1	15	3.24	0.027	0.014	0	7.9	Harzburgite
14R-2, 106–116	76.1	15	3.51	0.094	0.047	1		Harzburgite
14R-2, 106–116	76.1	15	3.33	0.045	0.023	2		Harzburgite
14R-3, 20–30	76.6	4	2.12	0.037	0.018	0	3.8	Gabbroic breccia
14R-3, 20–30	76.6	4	2.17	0.018	0.009	1		Gabbroic breccia
14R-3, 20–30	76.6	4	2.08	0.054	0.027	2		Gabbroic breccia
15R-2, 35–45	79.5	2B	2.65	0.027	0.014	0	2.6	Harzburgite
15R-2, 35–45	79.5	2B	2.64	0.030	0.015	1		Harzburgite
15R-2, 35–45	79.5	2B	2.71	0.102	0.051	2		Harzburgite
15R-3, 132–141	81.6	5A	2.48	0.074	0.037	0		Harzburgite
16R-3, 84–94	86.6	8	2.78	0.083	0.042	0	2.1	Harzburgite
16R-3, 84–94	86.6	8	2.82	0.100	0.050	1		Harzburgite
16R-3, 84–94	86.6	8	2.76	0.076	0.038	2		Harzburgite
16R-4, 4–12	87.3	1	1.90	0.023	0.011	0	12.0	Gabbro
16R-4, 4–12	87.3	1	2.08	0.027	0.014	1		Gabbro
16R-4, 4–12	87.3	1	1.84	0.016	0.008	2		Gabbro
17R-3, 64–77	91.9	6	2.67	0.103	0.051	0	1.8	Dunite/Harzburgite
17R-3, 64–77	91.9	6	2.71	0.022	0.011	1		Dunite/Harzburgite
17R-3, 64–77	91.9	6	2.69	0.113	0.056	2		Dunite/Harzburgite
18R-1, 116–126	93.3	5E	2.90	0.155	0.077	0	3.9	Harzburgite
18R-1, 116–126	93.3	5E	2.80	0.088	0.044	1		Harzburgite
18R-1, 116–126	93.3	5E	2.92	0.105	0.053	2		Harzburgite
18R-2, 112–122	94.6	11A	3.08	0.121	0.060	0		Harzburgite
19R-1, 50–60	97.6	1B	2.95	0.020	0.010	0		Harzburgite
19R-3, 0–6	99.9	1	2.79	0.048	0.024	0	6.1	Dunite
19R-3, 0–6	99.9	1	2.85	0.015	0.008	1		Dunite
19R-3, 0–6	99.9	1	2.68	0.011	0.005	2		Dunite
19R-3, 82–97	100.7	6	2.93	0.034	0.017	0	5.3	Dunite
19R-3, 82–97	100.7	6	2.98	0.080	0.040	1		Dunite
19R-3, 82–97	100.7	6	2.83	0.060	0.030	2		Dunite
21R-1, 34–43	107.6	3	2.47	0.015	0.008	0	3.6	Gabbro
21R-1, 34–43	107.6	3	2.43	0.015	0.007	1		Gabbro
21R-1, 34–43	107.6	3	2.52	0.079	0.040	2		Gabbro
24R-2, 21–29	123.1	1C	2.97	0.018	0.009	0	11.5	Harzburgite
24R-2, 21–29	123.1	1C	3.00	0.076	0.038	1		Harzburgite
24R-2, 21–29	123.1	1C	2.67	0.113	0.056	2		Harzburgite
26R-2, 13–23	134.6	2	2.09	0.024	0.012	0	4.9	Gabbronorite
26R-2, 13–23	134.6	2	2.11	0.052	0.026	1		Gabbronorite
26R-2, 13–23	134.6	2	2.01	0.033	0.017	2		Gabbronorite
28R-2, 20–31	142.8	1B	2.08	0.015	0.007	0	6.4	Gabbronorite
28R-2, 20–31	142.8	1B	2.15	0.029	0.014	1		Gabbronorite
28R-2, 20–31	142.8	1B	2.02	0.056	0.028	2		Gabbronorite
29R-1, 117–130	147.4	14	2.04	0.022	0.011	0	3.5	Gabbronorite
29R-1, 117–130	147.4	14	2.11	0.017	0.008	1		Gabbronorite
29R-1, 117–130	147.4	14	2.06	0.044	0.022	2		Gabbronorite

Notes: * = average of four measurements. 0 = parallel to core axis, 1 = oblique to core axis (~35°), 2 = oblique to core axis (~35°) in opposite direction. This table is also available in **ASCII.**

Table T7. Porosity, density, and velocity on discrete samples, Hole 1268A.

		Volume measured in pycnometer				Volume measured with caliper				
		Density (Mg/m^3)				Density (Mg/m^3)				
Core, section, interval (cm)	Depth (mbsf)	Bulk	Grain	Porosity (%)	Sample size	Bulk	Grain	Porosity (%)	V_P (km/s)	Primary lithology
209-1268A-										
2R-2, 37–39	15.77	2.66	2.82	8.9	Chip	2.49	2.54	3.3	3.89	Harzburgite
3R-2, 4–6	21.67	2.51	2.86	19.2	Chip	2.39	2.48	6.2	3.02	Harzburgite
4R-1, 16–18	24.96	2.57	2.76	10.8	Chip	2.44	2.49	3.8	3.49	Harzburgite
5R-2, 119–121	32.49	2.49	2.68	11.7	Minicore	2.49	2.57	4.7	3.43	Dunite
6R-1, 49–51	34.89	—	—	—	—	2.58	2.63	3.1	3.64	Harzburgite
8R-1, 123–125	45.23	—	—	—	—	2.67	2.71	2.2	3.40	Harzburgite
10R-2, 87–89	55.91	2.70	2.81	6.2	Chip	—	—	—	—	Harzburgite
12R-1, 130–132	64.50	2.70	2.83	7.4	Minicore	2.72	2.77	2.7	3.63	Harzburgite
12R-2, 40–42	65.10	2.64	2.84	11.0	Chip	2.65	2.70	2.8	3.37	Harzburgite
13R-1, 77–79	68.97	2.69	2.81	6.7	Chip	2.56	2.60	2.3	3.83	Harzburgite
14R-2, 112–114	75.41	2.46	2.74	16.2	Chip	2.49	2.58	5.5	3.09	Harzburgite
15R-4, 73–75	82.59	2.55	2.63	4.8	Minicore	2.55	2.58	1.9	4.29	Harzburgite
16R-3, 133–135	86.44	2.81	2.91	5.4	Chip	2.69	2.73	2.2	3.59	Harzburgite
17R-1, 18–20	87.58	2.60	2.81	11.5	Chip	2.53	2.62	5.1	3.41	Gabbro
17R-1, 69–71	88.09	—	—	—	—	2.73	2.77	2.2	3.50	Harzburgite
18R-1, 123–125	93.23	2.55	2.87	17.3	Chip	2.40	2.40	2.5	3.54	Dunite
19R-1, 86–88	97.86	2.45	2.58	8.7	Chip	—	—	—	—	Harzburgite
20R-2, 66–68	103.69	2.50	2.67	10.4	Chip	2.47	2.47	4.1	4.02	Harzburgite
22R-2, 81–82	113.51	2.71	2.85	7.7	Minicore	2.69	2.73	2.8	4.37	Gabbro
23R-1, 63–65	116.83	2.88	2.91	1.4	Minicore	2.82	2.83	0.5	4.93	Gabbronorite
23R-2, 45–47	118.09	2.67	2.86	10.3	Chip	—	—	—	—	Gabbro
24R-2, 90–92	122.95	2.49	2.54	3.0	Minicore	2.56	2.57	1.2	4.53	Harzburgite
25R-1, 45–47	126.25	2.67	2.86	10.8	Chip	2.58	2.66	5.0	3.03	Harzburgite

Note: This table is also available in **ASCII.**

Table T8. Bulk density and velocity measured on cube samples, Hole 1268A.

Core, section, interval (cm)	Depth (mbsf)	Bulk density (Mg/m^3)	V_P (km/s)				V_P apparent anistropy (%)	Primary lithology
			x	y	z	Mean		
209-1268A-								
6R-1, 106–108	35.46	2.52	3.57	3.55	3.56	3.56	0.42	Harzburgite
10R-2, 8–10	55.12	2.72	3.80	3.66	3.76	3.74	3.69	Dunite
12R-1, 47–49	63.67	2.51	3.77	3.75	3.62	3.71	3.96	Harzburgite
13R-1, 33–35	68.53	2.53	4.00	4.05	4.08	4.04	2.20	Harzburgite
14R-2, 128–130	75.57	2.46	3.26	2.97	3.18	3.14	9.25	Harzburgite
15R-2, 104–106	80.26	2.52	3.65	3.47	3.71	3.61	6.79	Harzburgite
16R-1, 37–39	82.77	2.55	4.24	3.97	4.13	4.11	6.54	Harzburgite
16R-2, 34–36	83.95	2.40	4.02	3.99	4.15	4.05	3.85	Harzburgite
18R-2, 116–118	94.44	2.57	3.46	3.50	3.53	3.49	2.03	Dunite
19R-1, 51–53	97.51	2.52	3.95	4.01	4.04	4.00	2.35	Harzburgite
19R-4, 36–38	101.17	2.49	3.81	3.83	3.88	3.84	1.88	Dunite
22R-1, 114–116	112.34	2.44	3.85	3.81	3.73	3.80	3.16	Gabbro
23R-1, 53–55	116.73	2.76	4.81	4.59	4.61	4.67	4.80	Gabbronorite
23R-3, 61–63	119.52	2.55	4.56	4.44	4.16	4.39	9.05	Harzburgite
25R-2, 25–27	127.48	2.69	4.28	4.29	4.28	4.28	0.05	Gabbro
26R-2, 20–22	132.14	2.77	4.51	4.36	4.43	4.43	3.45	Gabbronorite
28R-2, 28–30	141.70	2.77	4.75	4.62	4.65	4.67	2.89	Gabbronorite
28R-2, 87–89	142.29	2.78	4.55	4.61	4.55	4.57	1.44	Gabbronorite

Note: This table is also available in ASCII.

Table T9. Paleomagnetic discrete sample data, Hole 1268A.

Core, section, interval (cm)	Depth (mbsf)	Piece	Lithology	Talc index	*N*	Decay type	MAD (°)	Remanence direction (°)		Demagnetization			*J* (A/m)	PCA (%)
								Declination	Inclination	Low	High	Unit		
209-1268A-														
2R-2, 24	15.64	4B	2	1	2	A	1.8	330.7	57.4	20	30	mT	0.0664	0.6
2R-2, 37	15.77	4C	2	1	4	A	6.0	7.0	26.7	10	30	mT	0.4313	5.4
3R-2, 4	21.67	1	2	1	3	A	3.7	206.1	31.5	15	30	mT	0.0419	46.7
4R-1, 16	24.96	5A	2	1	12	F	3.6	300.6	23.5	15	180	mT	0.0082	61.2
5R-2, 119	32.49	26A	1	1	4	A	10.6	349.5	44.3	20	50	mT	0.0973	22.1
5R-2, 124	32.54	26A	1	1	7	F	3.7	338.1	63.9	4	20	mT	0.1918	44.1
6R-1, 49	34.89	10	2	1.5	4	F	6.1	35.5	22.3	5	20	mT	0.0486	36.3
6R-1, 55	34.95	10	1	1.5	9	A	9.5	13.5	50.4	2	30	mT	0.0963	66.0
6R-1, 106	35.46	15	2	1.5	3	A	2.1	172.1	37.9	18	30	mT	0.1259	50.4
8R-1, 123	45.23	26	2	2	9	F	3.7	282.3	45.2	30	160	mT	0.0010	47.4
10R-1, 94	54.54	16B	2	1.5	10	A	3.4	301.4	30.2	20	120	mT	0.0256	84.8
10R-2, 8	55.12	1	1	2	5	F	4.2	191.9	42.7	16	50	mT	0.0120	46.5
10R-2, 87	55.91	14	2	2	13	F	1.9	149.7	23.2	300	600	°C	0.0834	67.3
12R-1, 33	63.53	2D	2	1	6	F	2.6	180.2	38.9	8	30	mT	0.4948	26.3
12R-1, 130	64.50	14	2	1	8	F	2.0	342.9	32.1	10	60	mT	0.1375	41.0
12R-2, 40	65.10	7	2	2	6	F	2.1	233.6	14.9	10	40	mT	0.0488	58.7
13R-1, 44	68.64	6B	2	1	5	F	3.8	336.3	35.6	10	30	mT	0.0909	28.0
13R-1, 77	68.97	6B	2	1	6	F	2.9	341.2	36.1	10	40	mT	0.2078	16.0
14R-2, 112	75.41	15	2	2	6	F	8.5	330.5	13.2	5	30	mT	0.3979	68.4
15R-2, 37	79.59	2B	2	1	11	F	16.4	116.1	34.6	4	30	mT	0.1946	71.5
15R-3, 28	80.68	1	2	1	3	A	6.8	299.1	67.0	20	30	mT	0.0506	32.9
15R-4, 70	82.56	4	2	1	2	A	1.4	220.0	12.5	25	30	mT	0.0775	37.6
15R-4, 73	82.59	4	2	1	3	A	5.0	243.9	–12.4	30	50	mT	0.0736	28.0
16R-1, 62	83.02	5	2	1				†						
16R-3, 120	86.31	11	2	1.5	6	A	2.0	296.2	61.3	14	30	mT	0.0048	44.4
16R-3, 133	86.44	11	2	1.5	14	F	2.7	234.1	41.0	10	180	mT	0.0023	86.5
17R-1, 18	87.58	2	10	1	7	F	2.5	0.8	13.0	80	200	mT	0.1155	42.8
17R-1, 69	88.09	8A	2	2	10	F	7.4	147.6	36.2	15	120	mT	0.0003	68.6
17R-1, 78	88.18	8B	2	2	8	A	2.0	147.4	47.2	10	30	mT	0.0006	92.0
18R-1, 120	93.20	5E	1	1	7	F	3.4	89.4	55.0	8	20	mT	0.3339	4.0
18R-1, 123	93.23	5E	1	1				†						
18R-2, 57	93.85	3	1	1	4	+	9.1	281.6	37.9	20	30	mT	0.0558	0.8
18R-3, 29	94.88	1B	1	1	7	F	4.9	312.8	57.9	8	20	mT	0.3751	8.3
19R-1, 86	97.86	2D	2	1	11	F	3.7	72.5	58.9	400	600	°C	0.2269	38.7
19R-2, 112	99.50	15	2	1	6	F	4.0	81.5	51.3	8	18	mT	0.1320	8.9
19R-4, 59	101.40	1	1	1	8	F	2.9	351.5	35.2	6	20	mT	1.230	13.6
20R-2, 66	103.69	1D	2	1	11	F	3.4	10.0	31.1	10	120	mT	0.1748	19.3
20R-2, 117	104.20	5	1	2	8	F	5.6	212.5	40.7	10	30	mT	0.0400	3.6
22R-2, 81	113.51	13	10	1	13	F	0.7	108.7	8.0	10	200	mT	0.2301	94.3
23R-1, 53	116.73	4C	16	1	16	F	1.9	43.4	4.5	10	200	mT	0.0990	92.5
23R-1, 63	116.83	4C	12	1	13	F	1.1	43.6	6.0	10	200	mT	0.2485	94.5
23R-2, 45	118.09	6	2	2	8	F	11.7	138.5	20.3	500	590	°C	0.0014	16.4
24R-2, 90	122.95	7C	2	1	6	F	4.0	155.6	31.7	60	200	mT	0.0668	13.0
25R-1, 45	126.25	4B	2	2	7	F	2.2	197.1	48.3	50	200	mT	0.0003	37.3
25R-2, 25	127.48	4	12	1	16	F	2.2	215.3	27.2	10	200	mT	2.006	87.6
26R-2, 20	132.14	2	12	1	16	F	1.7	108.9	15.7	10	200	mT	0.0169	94.4
27R-1, 58	136.08	5B	12	1	16	F	3.7	235.6	7.3	100	590	°C	0.0631	95.2
28R-2, 28	141.70	1B	12	1	16	F	2.2	46.6	19.0	10	200	mT	0.5930	96.6
28R-2, 51	141.93	1D	12	1	16	F	3.3	94.0	20.6	100	590	°C	0.3684	97.2
28R-2, 51	141.93	1D*	12	1	17	A	1.0	105.2	33.1	10	80	mT	0.3640	97.8
28R-2, 87	142.29	5	12	1.5	16	F	2.3	217.8	11.9	10	200	mT	0.2669	92.0

Notes: Lithology: 1 = dunite, 2 = harzburgite, 10 = gabbro, 12 = gabbronorite, 16 = microgabbro. Talc alteration index: 1 = least talc, 2 = pervasive talc alteration. MAD = maximum angular deviation. *N* = number of points. Decay type: A = anchored to origin, F = free of origin, + = includes origin as point. PCA = principal component analysis; percentage of natural remanent magnetization intensity. * = small chip of thermal sample. † = no stable direction. This table is also available in **ASCII.**

Table T10. Anisotropy of magnetic susceptibility, Hole 1268A.

Core, section, interval (cm)	Depth (mbsf)	Piece	Susceptibility (SI)	1σ	Maximum*			Intermediate*			Minimum*			Total anisotropy	F12	F23	*P*	*F*	*L*
					Value	Dec (°)	Inc (°)	Value	Dec (°)	Inc (°)	Value	Dec (°)	Inc (°)						
209-1268A-																			
2R-2, 37	15.77	4C	1.04×10^{-1}	0.00031	0.3488	319.5	35.3	0.3482	51.7	3.1	0.3030	146.1	54.6	5677.7	1.5	9999.9	1.151	1.149	1.002
3R-2, 4	21.67	1	6.77×10^{-4}	0.00096	0.3403	88.1	49.6	0.3332	297.4	36.6	0.3265	196.1	14.8	41.8	27.4	24.9	1.042	1.021	1.021
4R-1, 16	24.96	5A	2.24×10^{-4}	0.00195	0.3371	158.6	17.5	0.3346	63.4	16.0	0.3284	293.4	65.9	4.2	0.8	5.1	1.027	1.019	1.008
5R-2, 119	32.49	26A	1.65×10^{-3}	0.00027	0.3367	170.8	59.5	0.3329	313.8	25.2	0.3304	51.6	16.1	109.6	97.9	42.8	1.019	1.008	1.011
6R-1, 49	34.89	10	4.92×10^{-4}	0.00075	0.3506	54.2	35.2	0.3488	153.0	12.2	0.3006	259.1	52.1	1140.0	2.8	2058.5	1.166	1.160	1.005
8R-1, 123	45.23	26	2.93×10^{-4}	0.00156	0.3377	68.3	6.9	0.3359	334.3	30.1	0.3264	170.0	58.9	12.2	0.7	18.7	1.035	1.029	1.005
10R-1, 94	54.54	16B	6.24×10^{-4}	0.00067	0.3415	222.8	0.7	0.3330	313.7	54.8	0.3255	132.3	35.2	114.1	81.2	61.9	1.049	1.023	1.026
10R-2, 87	55.91	14	4.32×10^{-4}	0.00076	0.3382	350.3	12.8	0.3336	84.0	15.7	0.3282	222.9	69.5	34.7	17.9	25.7	1.030	1.017	1.014
12R-1, 130	64.50	14	5.12×10^{-3}	0.00075	0.3808	88.3	45.1	0.3466	344.8	13.0	0.2727	242.8	42.0	4303.8	1031.8	4810.1	1.396	1.271	1.099
12R-2, 40	65.10	7	5.47×10^{-4}	0.00076	0.3422	359.8	42.1	0.3368	95.5	6.3	0.3210	192.4	47.2	168.3	25.2	216.4	1.066	1.049	1.016
13R-1, 77	68.97	6B	3.86×10^{-3}	0.00043	0.3687	89.7	62.3	0.3510	333.3	13.1	0.2804	237.4	23.9	9339.4	838.5	9999.9	1.315	1.252	1.050
14R-2, 112	75.41	15	1.05×10^{-3}	0.00047	0.3448	73.9	84.3	0.3314	231.1	5.2	0.3239	321.3	2.2	397.6	399.3	123.8	1.064	1.023	1.040
15R-4, 73	82.59	4	1.37×10^{-3}	0.00057	0.3589	62.2	56.7	0.3524	205.3	27.7	0.2888	304.5	17.0	3674.0	64.3	6193.6	1.243	1.220	1.018
16R-3, 133	86.44	11	2.71×10^{-4}	0.00187	0.3367	345.6	43.3	0.3322	100.6	24.1	0.3311	210.4	37.0	1.9	2.8	0.2	1.017	1.003	1.013
17R-1, 18	87.58	2	4.70×10^{-4}	0.00122	0.3448	310.4	18.0	0.3376	184.4	61.0	0.3176	47.9	21.9	107.5	17.3	135.8	1.086	1.063	1.021
17R-1, 69	88.09	8A	2.69×10^{-4}	0.00161	0.3363	289.8	3.2	0.3349	191.8	68.0	0.3288	21.1	21.7	5.0	0.4	7.3	1.023	1.019	1.004
18R-1, 123	93.23	5E	1.23×10^{-1}	0.00029	0.3591	347.8	4.5	0.3379	81.8	41.2	0.3030	252.6	48.5	7878.9	2751.3	7483.9	1.185	1.115	1.063
19R-1, 86	97.86	2D	2.85×10^{-3}	0.00026	0.3427	38.9	16.0	0.3387	299.7	29.1	0.3186	154.1	56.1	2028.5	121.9	3069.9	1.076	1.063	1.012
20R-2, 66	103.69	1D	3.28×10^{-3}	0.00014	0.3440	177.1	11.6	0.3337	272.6	25.0	0.3224	64.3	62.1	4777.4	2721.4	3258.5	1.067	1.035	1.031
22R-2, 81	113.51	13	4.11×10^{-4}	0.00078	0.3409	53.9	11.8	0.3321	316.0	33.3	0.3270	160.7	54.2	64.7	63.4	21.2	1.042	1.016	1.026
23R-1, 63	116.83	4C	3.69×10^{-4}	0.00094	0.3431	0.7	0.9	0.3307	267.9	71.5	0.3262	91.0	18.5	69.7	87.4	11.6	1.052	1.014	1.038
23R-2, 45	118.09	6	3.21×10^{-4}	0.00146	0.3391	72.8	24.0	0.3365	336.7	13.5	0.3244	219.8	62.0	22.9	1.6	33.9	1.045	1.037	1.008
24R-2, 90	122.95	7C	3.25×10^{-3}	0.00019	0.3379	216.2	30.2	0.3331	330.7	35.4	0.3290	97.1	39.8	457.6	330.0	244.1	1.027	1.013	1.014
25R-1, 45	126.25	4B	2.89×10^{-4}	0.00126	0.3393	268.4	40.4	0.3338	173.4	5.9	0.3269	76.6	49.0	19.4	9.6	14.8	1.038	1.021	1.017
27R-1, 58	136.08	5B	4.62×10^{-4}	0.00065	0.3443	250.9	14.9	0.3374	155.1	20.9	0.3183	13.9	63.9	342.9	57.2	429.2	1.082	1.060	1.021
28R-2, 51	141.93	1D	5.76×10^{-4}	0.00053	0.3401	256.2	13.7	0.3376	354.1	29.2	0.3223	144.1	57.2	263.9	11.6	414.2	1.055	1.048	1.008

Notes: σ = 1 standard deviation for normalized eigenvalues. * = ODP core coordinates (double line on working half = 360°, inclination positive down). Dec = declination, inc = inclination. Total anisotropy critical value = 3.4817). F12 = max, min eigenvalues, F23 = int, min eigenvalues (critical value = 4.2565 for F12 and F23). *P* (degree of anisotropy) = max/min eigenvalues, *F* (magnetic foliation) = int/min eigenvalues, *L* (magnetic lineation) = max/int eigenvalues. This table is also available in **ASCII.**

Table T11. Piece orientations from archive-half data, Hole 1268A. (**See table notes.** Continued on next page.)

Core, section, interval (cm)	Piece	Length (cm)	PCA interval (cm)	Depth (mbsf)	*N*	Decay type	MAD (°)	Remanence direction (°)		Demagnetization (mT)		*J* (A/m)	PCA (%)
								Declination	Inclination	Low	High		
209-1268A-													
3R-1, 115.1–126.8	19	11.7	122	21.42	6	F	2.6	18.7	36.5	10	50	0.088	47.8
4R-1, 12.0–30.6	5	18.6	20	25.00	7	A	2.1	301.1	25.9	15	70	0.0063	81.6
4R-3, 45.2–58.0	9	12.8	52	28.30	5	F	7.2	311.0	34.2	15	50	0.0057	17.9
5R-1, 52.1–59.2	10	7.1	56	30.36	6	F	4	303.2	15.8	15	60	0.0045	34.4
5R-1, 124.1–131.3	11	7.2	126	31.06	8	F	6.7	173.0	27.0	10	70	0.0012	61.9
5R-2, 54.7–63.7	14	9	58	31.88	8	A	3.8	201.1	19.9	10	70	0.0009	97.6
6R-2, 8.6–14.7	2	6.1	10	35.96	10	A	1.9	297.8	25.8	2	70	0.0059	93.4
8R-1, 28.0–35.0	8	7	32	44.32	7	F	1.6	310.6	14.4	15	70	0.0033	44.4
8R-2, 11.0–22.0	3	11	16	45.66	8	F	3.5	311.8	40.5	10	70	0.0259	44.3
8R-2, 47.0–54.0	9	7	50	46.00	7	F	2.4	355.8	30.6	5	50	0.0981	60.9
9R-1, 94.0–99.0	23	5	96	49.96	8	F	0.8	202.8	31.1	10	70	0.097	85.1
10R-2, 0.0–13.0	1	13	8	55.12	5	F	3.8	109.5	29.3	15	50	0.0108	42.4
10R-2, 21.0–29.0	4	8	26	55.30	7	F	1.3	340.6	28.5	10	60	0.0952	45.3
10R-2, 66.5–73.0	11	6.5	68	55.72	6	F	2.3	317.7	–2.7	15	60	0.0227	63.6
10R-2, 82.0–91.0	14	9	86	55.90	7	F	1	138.8	20.9	10	60	0.0736	74.1
11R-1, 21.0–22.0	5	1	28	58.88	7	F	1.8	2.5	13.1	10	60	0.022	80.9
11R-1, 78.0–86.0	16	8	82	59.42	7	F	0.7	103.4	24.4	15	70	0.0354	29.3
11R-1, 126.0–136.0	24	10	132	59.92	9	F	1.8	84.1	24.8	5	70	0.5933	65.3
11R-2, 115.0–124.0	20	9	120	61.23	5	F	0.6	354.7	42.9	10	40	0.4584	28.5
12R-1, 6.0–37.5	2	31.5	24	63.44	5	F	0.8	165.4	53.1	10	40	0.2839	26.0
12R-1, 39.5–61.5	3	22	54	63.74	4	F	1.7	150.0	48.8	15	40	0.1459	13.1
12R-2, 24.0–32.5	6	8.5	30	65.00	5	F	1.6	340.5	33.5	10	40	0.0497	28.1
12R-2, 34.0–43.5	7	9.5	40	65.10	5	F	1.6	221.8	23.2	10	40	0.0432	41.5
12R-2, 45.0–47.0	8	2	54	65.24	5	F	1	319.4	14.2	10	40	0.0412	41.9
12R-2, 90.0–102.0	17	12	96	65.66	5	F	0.8	264.8	19.4	10	40	0.0355	48.8
12R-3, 0.0–25.0	1	25	10	66.20	5	F	2.2	13.3	29.9	10	40	0.1448	24.3
12R-3, 38.0–52.0	5	14	46	66.56	5	F	1.7	195.9	20.9	10	40	0.1439	32.8
12R-3, 54.0–60.0	6	6	58	66.68	5	F	2.3	68.8	41.5	10	40	0.1439	26.2
12R-3, 61.0–74.0	7	13	68	66.78	5	F	2.1	90.3	25.1	10	40	0.162	38.9
13R-2, 0.0–7.5	1	7.5	4	69.61	5	F	3.8	101.4	36.0	10	40	0.0807	31.4
13R-2, 19.0–30.0	4	11	24	69.81	5	F	1.5	219.2	19.8	10	40	0.1326	39.0
13R-2, 63.0–70.5	10	7.5	68	70.25	5	F	1.3	334.8	20.1	10	40	0.0377	29.5
13R-2, 129.0–143.0	21	14	136	70.93	5	F	1.8	330.2	22.5	10	40	0.2807	43.6
13R-3, 8.0–26.0	3	18	18	71.19	5	F	1.3	4.1	27.6	10	40	0.1696	27.0
14R-1, 29.0–49.0	7	20	38	73.18	5	F	2.5	31.2	25.8	10	40	0.185	51.0
14R-3, 19.0–32.0	4	13	26	75.99	4	F	2.2	308.8	–40.7	10	30	0.0074	18.5
15R-2, 0.0–14.0	1	14	8	79.30	6	F	5.5	67.5	55.5	10	50	0.003	45.7
15R-2, 74.0–117.0	7	43	98	80.20	5	F	2.4	347.2	37.3	10	40	0.2087	42.5
16R-2, 80.0–96.0	4	16	88	84.49	7	F	8.9	98.3	49.3	10	60	0.0016	34.0
16R-2, 125.0–142.0	7	17	138	84.99	7	F	11.3	332.0	54.0	10	60	0.0028	36.3
16R-3, 102.0–111.0	10	9	108	86.19	6	F	4.5	294.7	20.1	15	60	0.0007	55.1
16R-4, 0.0–12.0	1	12	8	86.69	7	A	0.5	103.9	10.2	10	60	1.5099	101.3
17R-1, 0.0–8.0	1	8	6	87.46	7	A	0.3	192.4	–10.4	10	60	1.07	97.3
17R-1, 10.0–17.0	2	7	16	87.56	7	A	0.3	8.4	4.6	10	60	0.311	101.3
17R-2, 67.0–74.0	3	7	72	89.62	7	F	2.5	75.4	6.6	10	60	0.0022	62.1
17R-2, 130.0–137.0	4	7	136	90.26	7	F	2.5	10.5	29.9	10	60	0.0902	54.7
18R-3, 95.0–111.0	10	16	102	95.61	4	F	2	142.0	16.3	15	40	0.0398	18.1
18R-3, 111.0–129.0	11	18	122	95.81	4	F	1.4	251.2	32.0	10	30	0.0644	31.0
18R-4, 1.0–28.0	1	27	18	96.07	4	F	1.1	26.0	43.5	10	40	0.1347	54.1
20R-1, 86.0–110.0	8	24	100	102.60	6	F	0.5	350.2	50.9	10	50	1.0065	28.7
20R-2, 0.0–71.0	1	71	32	103.35	5	F	0.8	338.8	62.9	15	50	0.3306	6.3
20R-2, 72.0–79.0	2	7	76	103.79	3	F	3.2	355.6	35.4	30	50	0.0109	2.0
20R-2, 80.0–89.0	3	9	86	103.89	4	F	3.8	9.6	44.7	20	50	0.047	6.1
20R-2, 90.0–114.0	4	24	98	104.01	4	F	0.1	338.5	36.5	20	50	0.1026	17.8
20R-2, 125.0–137.0	6	12	134	104.37	5	F	1.4	223.8	33.2	20	60	0.0908	14.7
20R-3, 54.0–74.0	11	20	68	105.13	4	A	0.2	341.7	11.2	30	60	0.303	92.1
20R-3, 75.0–82.5	12	7.5	80	105.25	4	A	0.6	154.4	14.7	30	60	0.7069	89.5
20R-3, 83.0–107.0	13	24	98	105.43	4	A	0.4	106.9	17.5	30	60	1.49	94.9
21R-1, 0.0–23.0	1	23	20	106.80	6	A	0.5	197.4	12.4	20	80	0.784	98.0
21R-1, 32.0–47.0	3	15	38	106.98	6	A	0.7	82.8	13.5	20	80	1.92	98.0
22R-1, 10.0–18.0	2	8	16	111.36	6	A	0.2	134.6	5.7	20	80	0.358	98.1
22R-1, 39.5–48.5	6	9	44	111.64	6	A	0.4	96.6	2.1	20	80	0.855	98.7
22R-1, 55.0–62.5	8	7.5	58	111.78	6	A	0.3	172.8	4.8	20	80	0.249	100.0
22R-1, 69.5–77.5	10	8	72	111.92	6	A	0.9	105.4	6.9	20	80	0.276	96.5
22R-1, 85.0–98.5	12	13.5	94	112.14	6	A	0.2	139.5	–0.1	20	80	0.701	95.4
22R-1, 112.0–119.5	15	7.5	116	112.36	6	A	0.3	258.2	10.3	20	80	0.17	92.9

Table T11 (continued).

Core, section, interval (cm)	Piece	Length (cm)	PCA interval (cm)	Depth (mbsf)	*N*	Decay type	MAD (°)	Remanence direction (°)		Demagnetization (mT)		*J* (A/m)	PCA (%)
								Declination	Inclination	Low	High		
22R-1, 128.5–139.5	17	11	134	112.54	6	A	1.2	268.7	6.1	20	80	0.132	99.2
22R-2, 4.0–10.5	2	6.5	8	112.78	6	A	0.4	41.3	5.2	20	80	0.152	96.2
22R-2, 19.0–27.5	5	8.5	24	112.94	6	A	0.6	208.2	–20.4	20	80	0.51	97.0
22R-2, 54.0–63.5	11	9.5	60	113.30	6	A	0.9	308.9	7.3	20	80	0.407	97.8
22R-2, 68.0–82.5	13	14.5	80	113.50	6	A	0.2	124.3	7.6	20	80	0.226	98.3
22R-2, 119.0–129.0	21	10	126	113.96	6	A	0.4	113.6	12.1	20	80	0.395	99.2
23R-1, 7.0–17.0	3	10	12	116.32	6	A	0.7	108.7	4.6	20	80	0.454	96.6
23R-1, 17.5–71.0	4	53.5	38	116.58	6	A	0.7	56.2	1.2	20	80	0.241	100.0
23R-1, 72.5–97.0	5	24.5	90	117.10	6	A	0.4	30.7	7.1	20	80	0.169	96.6
23R-1, 107.0–115.0	7	8	112	117.32	6	A	0.4	6.6	5.3	20	80	0.157	92.4
23R-1, 116.0–131.0	8	15	124	117.44	6	A	0.5	157.4	–0.9	20	80	0.53	95.8
24R-1, 24.5–41.0	4	16.5	32	121.12	5	+	0.8	334.3	44.9	40	80	0.052	78.5
24R-1, 106.0–117.0	15	11	114	121.94	3	+	0.2	196.6	30.4	60	80	0.0386	87.3
24R-2, 0.0–30.0	1	30	26	122.31	3	+	0.8	352.6	39.7	60	80	0.0263	50.6
24R-2, 129.0–136.0	14	7	134	123.39	3	+	1	214.2	27.2	60	80	0.118	59.9
24R-2, 139.0–147.0	15	8	142	123.47	3	+	0.4	219.2	35.6	60	80	0.0874	81.7
24R-3, 21.0–31.0	3	10	26	123.78	3	+	0.4	203.4	24.9	60	80	0.0616	105.1
25R-1, 8.0–15.5	2	7.5	14	125.94	8	+	0.5	182.4	27.1	10	60	0.111	98.2
25R-1, 85.5–98.0	12	12.5	92	126.72	8	+	0.3	195.1	14.8	10	60	0.716	98.2
25R-1, 117.0–133.0	16	16	126	127.06	8	+	0.3	176.2	17.3	10	60	0.614	95.8
25R-2, 14.5–31.5	4	17	26	127.49	8	+	0.1	212.9	19.6	10	80	1.27	99.2
25R-2, 35.0–43.5	6	8.5	40	127.63	8	+	0.1	59.4	17.4	10	80	1.59	99.4
25R-2, 44.5–53.0	7	8.5	50	127.73	8	+	0.2	325.5	17.5	10	80	1.88	97.9
25R-2, 75.3–82.7	13	7.4	80	128.03	8	+	0.3	207.6	21.3	10	80	0.369	96.6
25R-2, 91.8–100.5	15	8.7	96	128.19	8	+	0.5	188.5	19.2	10	80	0.8959	97.7
25R-2, 118.5–129.0	19	10.5	124	128.47	8	+	0.2	82.7	22.2	10	80	0.213	100.0
25R-2, 134.2–142.8	21	8.6	138	128.61	8	+	0.4	264.5	18.6	10	80	0.287	100.7
25R-3, 0.0–11.0	1	11	6	128.73	8	+	0.2	48.1	21.5	10	80	0.372	101.4
25R-3, 20.5–32.8	4	12.3	26	128.93	8	+	0.3	324.7	17.4	10	80	0.407	99.3
26R-1, 0.0–5.7	1	5.7	4	130.54	8	+	0.2	184.6	13.9	10	80	0.148	96.7
26R-1, 6.2–22.0	2	15.8	14	130.64	8	+	0.5	111.9	18.1	10	80	0.121	104.3
26R-1, 42.7–53.3	6	10.6	48	130.98	8	+	0.3	119.4	14.4	10	80	0.281	98.3
26R-1, 54.2–65.0	7	10.8	60	131.10	8	+	0.3	104.8	23.6	10	80	0.303	104.8
26R-1, 80.2–102.2	11	22	88	131.38	8	+	0.5	316.6	24.9	10	80	0.0946	99.4
26R-1, 114.0–125.0	14	11	120	131.70	8	+	0.5	23.5	8.9	10	80	0.0574	98.3
26R-1, 125.7–136.2	15	10.5	132	131.82	8	+	0.5	320.7	7.6	10	80	0.0478	97.0
26R-2, 9.0–26.0	2	17	20	132.14	8	+	0.4	110.9	12.5	10	80	0.0401	99.3
27R-1, 9.0–32.0	3	23	22	135.72	7	+	0.3	79.9	11.8	20	80	0.0567	176.1
27R-1, 39.0–83.0	5	44	62	136.12	7	+	0.6	244.7	10.0	20	80	0.0576	95.8
27R-1, 102.0–129.0	8	27	122	136.72	7	+	0.5	248.7	8.6	20	80	0.0458	92.3
27R-2, 13.0–20.0	4	7	16	137.14	7	+	0.7	82.2	10.3	20	80	0.183	92.4
27R-2, 59.0–70.5	12	11.5	64	137.62	7	+	0.5	47.2	8.3	20	80	0.0328	92.9
27R-2, 80.0–94.5	14	14.5	88	137.86	7	+	0.3	41.7	–9.6	20	80	0.638	95.7
28R-1, 34.0–67.0	15	33	60	140.70	8	+	0.5	295.8	10.3	10	80	0.652	98.8
28R-1, 68.0–106.0	16	38	80	140.90	7	+	1	95.6	9.7	20	80	0.6469	92.2
28R-1, 111.0–124.0	17	13	120	141.30	7	+	0.7	305.2	–7.7	20	80	0.319	92.5
28R-2, 100.0–115.0	18	15	108	142.50	7	+	1.6	115.5	6.3	20	80	4.2992	104.6
28R-2, 121.0–127.0	19	6	124	142.66	7	+	1	80.3	5.3	20	80	3.4091	98.8
28R-2, 128.0–143.0	10	15	136	142.78	7	+	0.9	153.3	8.9	20	80	3.3299	97.1
29R-1, 15.0–37.0	11	22	26	145.36	7	+	0.6	347.6	14.1	20	80	0.533	94.7
29R-1, 100.0–112.0	12	12	108	146.18	7	+	1	60.0	8.7	20	80	0.3479	97.7
29R-1, 115.0–133.0	13	18	124	146.34	7	+	1	194.2	12.7	20	80	0.5959	98.5

Notes: Principal component analysis (PCA) interval = level at which PCA analysis was performed. *N* = number of points. Decay type: A = anchored to origin, F = free of origin, + = includes origin as point. MAD = maximum angular deviation. PCA (%) = percentage of natural remanent magnetization intensity. This table is also available in **ASCII.**

Table T12. GC analysis of PFT contamination, Hole 1268A.

Standard PFT curve					Samples			
Dilution (vol:vol)	PFT (g)	Peak area (counts)	Log (PFT)	Log (area counts)	Location	Peak area (counts)	Log (PFT)	Log (area counts)
1×10^{-2}	8.8×10^{-7}	5.62×10^{7}	–2	7.75	Exterior 1	101,000	–4.5	5.00
1×10^{-3}	8.8×10^{-8}	9.53×10^{6}	–3	6.98	Interior 1	5,334	–5.7	3.73
1×10^{-5}	8.8×10^{-10}	6.31×10^{4}	–5	4.80	Interior 2	7,803	–5.5	3.89
1×10^{-7}	8.8×10^{-12}	85.81	–7	1.93	Interior 3	740	–6.4	2.87
1×10^{-9}	8.8×10^{-14}	8.83×10^{4}	–9	4.95	Interior 4	1,899	–6	3.28

Notes: GC = gas chromatography. PFT = perfluorocarbon tracer. Sample from Section 209-1268A-2R-1 (Piece 7B) run on 24 May 2003.

Table T13. Fluorescent microsphere contamination, Hole 1268A.

Section	Exterior of core	Interior of core	Thin section
209-1268A-2R-1 (Piece 7B)	Yes ($N = 5.7 \times 10^4$)	No	Yes*

Notes: * = microspheres are on the exterior of the thin section and are believed to be an artifact of making the thin section. N = number.

Table T14. Bacteria and viruses in a bottom water sample.

Sample	Bacteria (counts/mL)	Virus (counts/mL)
Bottom water	8.5×10^5	3.7×10^6

Table T15. Surface water and atmospheric microbiology results, 22–28 May 2003.

Sample	Date (May 2003)	Surface water (counts/mL)		Air growth* (CFU)		Atmospheric condition[†]
		Bacteria	Virus	Bacteria	Fungi	
a	22	6.98×10^5	3.01×10^6	0/0	0/0	8.1: light cloud
b	23	5.09×10^5	4.67×10^6	0/0	0/0	7.6: light cloud
c	24	6.04×10^5	5.41×10^6	0/0	0/0	No data
d	25	1.17×10^6	5.41×10^6	0/2	0/3	9.1: light dust
e	26	5.28×10^5	5.09×10^6	0/1	0/2	12.25: light/heavy dust
f	27	6.41×10^5	5.23×10^6	0/1	0/0	9.89: light dust
g	28	5.09×10^5	5.09×10^6	0/0	0/0	8.0: light cloud

Notes: * = colony-forming units (CFU) growth is measured at 48/96 hr. † = SeaWiFS image values.